Detection of lower hybrid waves at the plasma edge of a diverted tokamak

by

Seung Gyou Baek

Submitted to the Department of Nuclear Science and Enginnering
in partial fulfillment of the requirements for the degree of
Doctor of Philosophy in Nuclear Science and Engineering
at the
MASSACHUSETTS INSTITUTE OF TECHNOLOGY
February 2014

Author .....
Department of Nuclear Science and Enginnering
January 15, 2014

Certified by .....
Ronald R. Parker
Professor, Department of Nuclear Science and Engineering
Thesis Supervisor

Certified by .....
Paul T. Bonoli
Senior Research Scientist, MIT Plasma Science and Fusion Center
Thesis Reader

Certified by .....
Earl S. Marmar
Senior Research Scientist, MIT Plasma Science and Fusion Center
Thesis Reader

Accepted by .....
Mujid S. Kazimi
TEPCO Professor of Nuclear Engineering
Chair, Department Committee on Graduate Students

Detection of lower hybrid waves at the plasma edge of a diverted tokamak

by

Seung Gyou Baek

Submitted to the Department of Nuclear Science and Enginnering
on January 15, 2014, in partial fulfillment of the
requirements for the degree of
Doctor of Philosophy in Nuclear Science and Engineering

Abstract

In this thesis, two experimental investigations are presented in an attempt to understand the loss of lower hybrid current drive (LHCD) efficiency in reactor-relevant, high-density plasmas on the diverted Alcator C-Mod tokamak. While the previous work has identified that edge interactions, such as collisional absorption and excessive up-shift of the parallel refractive index due to full-wave effects, could potentially explain the observed loss of LHCD efficiency in a wide range of line-averaged densities, these simulations still over-predict the fast electron population generated by LHCD above line-averaged densities of $1 \times 10^{20}\,\mathrm{m}^{-3}$. It is critical to identify remaining mechanisms in order to demonstrate advanced tokamak operation at reactor-relevant densities.

The first investigation is to perform microwave backscattering experiments to detect electrostatic lower hybrid (LH) waves in the scrape-off layer (SOL), where a significant amount of the injected LH power may be deposited due to a number edge loss mechanisms. An existing ordinary-mode (O-mode) reflectometer system has been modified to measure the backscattered O-mode wave as a result of Bragg backscattering of the incident O-mode wave off the LH wave. The detection of LH waves in a region that is not magnetically connected to the launcher implies a weak single pass absorption of LH waves in high density plasmas. The observed spectral width of the backscattered signals indicates the presence of non-linear effects on the propagation of LH waves, but no experimental evidence is found to confirm whether the non-linear mechanism that is responsible for the observed spectral broadening is responsible for the observed loss of LHCD efficiency.

The second investigation is to examine the change in LH frequency spectra due to density-dependent non-linear effects, such as parametric decay instability (PDI) above the line-averaged density of $1 \times 10^{20}\,\mathrm{m}^{-3}$, using the probes installed on the launcher, outer divertor, and inner wall. Ion cyclotron PDI is found to be excited above line-averaged densities of $1 \times 10^{20}\,\mathrm{m}^{-3}$, suggesting that ion cyclotron PDI may be a remaining mechanism to understand the loss of LHCD efficiency. Ion cyclotron PDI is observed to be excited not only at the low-field-side edge but also at the

high-field-side (HFS) edge of Alcator C-Mod, further corroborating that LH waves are weakly absorbed on their first pass. Evidence of pump depletion is found with the onset of ion cyclotron PDI at the HFS edge in lower-single-null plasmas. However, no apparent pump depletion is seen when the magnetic geometry is switched to an upper-single-null. Moreover, ion cyclotron PDI is excited at the LFS edge in this case. Thus, the role of the observed ion cyclotron PDI on the loss of LHCD efficiency needs further experimental investigation to be conclusive due to the different ion cyclotron PDI strength and excitation location, depending on magnetic configurations.

A summary of the new findings of this thesis is as follows:

- First measurements of PDI below the classical threshold ($\omega_0/\omega_{LH}(0) \approx 2$).
- First ever observation of PDI on HFS of a tokamak and its relationship to being in a multi-pass damping regime.
- Advancement of PDI as a candidate mechanism for the LHCD density limit.

Thesis Supervisor: Ronald R. Parker
Title: Professor, Department of Nuclear Science and Engineering

Thesis Reader: Paul T. Bonoli
Title: Senior Research Scientist, MIT Plasma Science and Fusion Center

Thesis Reader: Earl S. Marmar
Title: Senior Research Scientist, MIT Plasma Science and Fusion Center

Acknowledgments

Looking back the past six and half years, this thesis is completed with support from numerous people.

First of all, I would like to thank my advisor, Professor Ron Parker, who has supported my research since the beginning of my study at MIT. With his patience that allowed me to explore different research topics, his guidance and insights helped me to finish the PhD course. I do not think I could have arrived at this stage of writing a thesis without his constant support. I learned from him how to think independently. I will not also forget his sincere considerations for my family.

Besides my advisor, I would like to thank Dr. Syun'ichi Shiraiwa, who taught me not to be afraid of new approaches. In particular, I was fortunate that he was deeply involved in backscattering experiments. He was willing to spend his time on this project and showed me how to develop electronics from the scratch, while answering my numerous questions. He has also been a good friend of mine. I enjoyed the afternoon coffee break with him.

I would also like to thank my thesis supervision committee members, Dr. Paul Bonoli, Dr. Earl Marmar, and Prof. Anne White for their constructive feedback at the regular committee meetings. Furthermore, their constructive comments improved the overall quality of this thesis. Dr. Bonoli taught me how to perform random scattering calculations using the GENRAY/CQL3D codes. Dr. Marmar supported the modification of the existing ordinary-mode reflectometer system for my thesis research. Professor White constantly expressed her interests on my research.

My sincere thanks goes to the Alcator C-Mod members. Dr. Greg Wallace was there whenever I had questions on the lower hybrid current drive system. He had also examined lower hybrid frequency spectra, which has motivated this research. He corrected my English a number of times. Dr. Amanda Hubbard supported my first project on the feasibility study on the use of non-thermal electron cyclotron emission in diagnosing the fast electron distribution. Dr. Gerrit Kramer and Dr. Arturo Dominguez were the ones who showed me how reflectometry works. Dr. Jim

Terry agreed to share his re-entrant tube when I initiated a design study of a new scattering diagnostic. Dr. Brian LaBombard and Dr. Dan Brunner provided useful insights into the physics of edge plasmas. Dr. Brian LaBombard also allowed me to use his probes to measure lower hybrid frequency spectra. Prof. Miklos Porkolab answered my questions on parametric decay instability. Professor. Yuichi Takase at the University of Tokyo replied to my numerous e-mails and provided me a code to study parametric decay instability. I thank Dr. Yijun Lin, Dr. Steve Wukitch, and Dr. Steve Wolfe for being physics operators during my run days.

This thesis would not have been possible without the support of the PSFC engineers. The lower hybrid group, including Atma Kanojia, David Johnson, and David Terry, helped me prepare for my run days. It was a great pleasure working with Bill Parkin, Ed Fitzgerald, William Burke, and Andy Pfeiffer when designing and fabricating spectral recorders. Rick Murray and Alan Binus allowed me to use their spectrum analyzers and signal analyzers. Rui Vieira and Ned Mucic supported my design study of a new scattering diagnostic.

I would like to thank the fellow graduate students at the PSFC. I enjoyed talking with Dr. Yunxing Ma, Dr. Peng Xu, Dr. Orso Meneghini, Dr. Nathan Howard, Dr. Roman Ochoukov, Dr. Dan Brunner, Chi Gao, Ted Golfinopoulos, Ian Faust, and Mike Churchill. Dr. Jinseok Ko helped me settle at MIT when I arrived at MIT. I enjoyed the lunch with Jungpyo and Choongki.

My undergraduate advisor, Prof. Han-Gyu Joo, encouraged my study at MIT and has been my mentor.

Outside the academia, numerous friends and families made me feel at home. Talking to Fr. Clancy and Kristelle has always been inspiring. I appreciate Korean mothers at MIT, who took care of my son when my wife was in a hospital. Thanks to my mother-in-law, Haesook, who did not mind to stay with us whenever needed, I was able to manage all the hardships. Thank you. Sarah and Grant, Julie and Edwin, and Sarah and Ben have been good neighbors. Naomi supported our stay at Westgate. I have been fortune to get to know them.

Thank you to my parents, Taehyun and Gilsung, who taught me how to love

myself. My brothers, Seungwhan and Seungil, have always believed in me in the past several years. I wish that Seungwhan and Sunyoung will enjoy their time in Colorado in the next two years. Thank you to my son, Jongwoo, who always brightened my evenings after the work. He once told me that "you won't know unless you try". I like that saying, although, at that moment, we were trying to find an animation on YouTube. Thank you to my newborn daughter, Jiyoo, who came to the world to start the journey with us. Finally, thank you to my wife, Nayoung, who has always been next to me and supported my study at MIT.

This work is supported by the Plasma Science and Fusion Center at MIT and Kwanjeong Educational Foundation.

THIS PAGE INTENTIONALLY LEFT BLANK

Contents

THIS PAGE INTENTIONALLY LEFT BLANK

List of Figures

THIS PAGE INTENTIONALLY LEFT BLANK

List of Tables

THIS PAGE INTENTIONALLY LEFT BLANK

Chapter 1

Introduction

A tokamak [1] is a magnetic confinement fusion device whose stability partly relies on a poloidal magnetic field that is generated by a toroidal plasma current. One of the inherent limitations of the tokamak comes from the fact that the plasma current is inductively driven through the use of an ohmic transformer. The current ramp in the central solenoid induces a change in the magnetic flux, which then induces a toroidal electric field that drives the plasma current around the torus. However, the current in the solenoid cannot be increased indefinitely to maintain a constant current swing in the solenoid due to the engineering limitations. Thus, the conventional tokamak is inherently a pulsed device.

To realize steady-state tokamak operation, non-inductive current drive has been proposed and demonstrated using neutral beam or radio frequency waves with a wide range of operating frequencies [2]. Of the several possibilities, lower hybrid current drive (LHCD) is known to have the highest efficiency (i.e., the highest driven current per watt of applied power). The wave-electron interaction that occurs at the tail of the electron distribution transfers both wave momentum and energy to the electrons with a phase speed that is about three times the thermal speed, generating current-carrying fast electrons as well as an asymmetric (in velocity space) resistivity in the plasma. This process is efficient because the electrons in this range are relatively collisionless. On the other hand, it has been shown that LHCD is not economical enough to drive the entire plasma current ($\sim 20\,\mathrm{MA}$) in a reactor-relevant tokamak [3].

Fortunately, the tokamak is known to create a self-generated toroidal plasma current known as the bootstrap current [1]. Thus, the present approach is to develop a new mode of the tokamak operation known as the advanced tokamak operation by controlling the pressure and current profiles in order to maximize the bootstrap current fraction and minimize the demand for external inductive current drive. Since LHCD minimizes the particle trapping effect at the edge, it is particularly useful in driving off-axis current for the purpose of current profile control. While both JET [4] and JT60U [5] successfully demonstrated advanced tokamak operating modes using LHCD, such operation remain to be explored at reactor-relevant plasma parameters.

Unfortunately, a number of tokamaks [6] report lower-than-expected LHCD efficiency in the reactor-relevant high-density plasmas. A number of mechanisms responsible for this reduction in current drive efficiency have been proposed and validated through detailed modeling work. For example, simulations on Alcator C-Mod [7] show that collisional absorption and full-wave effects can explain the observed loss of current drive efficiency across a wide range of densities, and these may be the dominant mechanisms. But, additional loss mechanisms may also play a role in plasmas with line-averaged density above $\overline{n}_e \gtrsim 1.0 \times 10^{20}\,\mathrm{m}^{-3}$, given that the synthetic diagnostics based on those models begin to over-predict the number of fast electrons generated by the LHRF power.

It is critical to understand the loss mechanisms and if possible to mitigate them in order to realize advanced tokamak operation at reactor-relevant densities. A successful advanced tokamak regime could be economically achieved only if LHCD exhibits the expected current drive efficiency in reactor-relevant high-density plasmas. For example, a recent modeling study [8] indicates that advanced tokamak operation in ITER requires LHCD in order to reach its Q=5 steady-state target. Moreover, LHCD plays an important role in driving off-axis plasma current in advanced reactor design studies such as ARIES [9]. Since these studies are based on the expected LHCD efficiency without any loss mechanisms considered, it is crucial to identify any hidden power loss mechanisms, which need to be properly

incorporated into the models that are used to predict the performance of the tokamak and LHCD.

This thesis describes two experimental investigations on Alcator C-Mod in an attempt to identify lower hybrid (LH) power loss mechanisms, in order to understand the steep decrease of non-thermal hard X-ray count rates in the density range of $\overline{n}_e \approx 1.0 \sim 1.5 \times 10^{20}\,\mathrm{m}^{-3}$ during lower hybrid current drive (LHCD) experiments [10]. The loss of efficiency above $\overline{n}_e \approx 1.0 \times 10^{20}\,\mathrm{m}^{-3}$ [7] cannot be fully explained by previously studied loss mechanisms, such as collisional power loss [7] and full-wave effects [11]. In this thesis, non-linear effects, such as parametric decay instability (PDI), have been hypothesized as a loss mechanism because PDI is known to be a density dependent loss mechanism [12]. PDI can result in the loss of efficiency as a result of the decay of the launched LH waves (pump) into low-frequency ion-modes and sideband LH waves with high $n_\parallel$ that would be inefficient to drive current (see Chapter 2 and 4). The first experimental approach (see Chapter 3) is the detection of LH waves in the scrape-off layer (SOL) using the microwave backscattering technique [13, 14]. The other approach (see Chapter 5) is the measurement of LH frequency spectra using probes to characterize the onset of ion cyclotron PDI [15, 16, 17].

1.1 Outline

This thesis consists of six chapters and four appendices. In the remainder of this chapter, the Alcator C-Mod tokamak and the LHCD system in Alcator C-Mod are discussed. In the next chapter, a review of lower hybrid and relevant physics is presented. In Chapter 3, results of the microwave back-scattering experiments to detect LH waves in the scrape-off layer are presented. In Chapter 4, the theory and numerical studies of ion sound and ion cyclotron parametric decay instabilities are presented, which will form a basis to understand the LH frequency spectra presented in Chapter 5. The measured LH frequency spectra are analysed by considering the homogeneous growth rate and convective growth. Finally, in Chapter 6 conclusions and future work are presented. Appendix A presents the

mode coupling calculation to derive the coupling coefficient that is used in developing an 1D backscattering model in Chapter 3. Appendix B develops the 1D backscattering model in the presence of a linear density gradient. Appendix C presents a preliminary 2D full wave simulation to better understand the backscattering process. Appendix D summarizes the development of a power detector that is used in the two experiments presented.

1.2 Alcator C-Mod Tokamak and Lower Hybrid Current Drive System

1.2.1 Alcator C-Mod

Alcator C-Mod [18, 19] is a tokamak located at the Plasma Science and Fusion Center at MIT. Table 1.1 summarizes the engineering and plasma parameters of Alcator C-Mod and compares them to those of ITER, which will be a flagship facility for the world's magnetic fusion research in the next several decades. The goal of ITER is to demonstrate the viability of the fusion power generation, which will be an important milestone toward the development of a commercial fusion power reactor. Although Alcator C-Mod is a small tokamak, it operates with ITER-relevant plasma parameters, such as the high magnetic field and plasma densities. The presence of a divertor and the solid metal walls addresses a number of physics issues arising from such structures that are relevant to ITER. Experimental results from Alcator C-Mod will be readily applicable to ITER. Further details of the Alcator C-Mod tokamak can be found in [19].

The LHCD program in Alcator C-Mod is also relevant to ITER. Although LHCD will not be operational in the first phase of ITER plasma operation, a 20 MW LHCD system may be installed before the second phase of ITER operation to demonstrate a steady state plasma with current drive [20, 21]. As shown in Table 1.1, both the plasma conditions (the magnetic field and the density) and the LH source frequency of Alcator C-Mod are similar to those of ITER, which primarily determine the LH

Table 1.1: Comparison of engineering parameters between Alcator C-Mod and ITER.

Parameter	Alcator C-Mod	ITER
Major radius (m)	0.67	6.2
Minor radius (m)	0.22	2.6
Pulse length (second)	2	400 – 1000
Central toroidal magnetic field (T)	3 – 8	5
Plasma current (MA)	0.6 – 1.4	15
Line-averaged density ($10^{20}\,\mathrm{m}^{-3}$)	1 – 3	1
Central temperature (keV)	2 – 8	20 – 25
Elongation	$\lesssim 1.9$	~ 1.7
Magnetic configurations	LSN, USN, IWL	LSN
Ion cyclotron RF power (MW)	6	20
LH power (MW)	1	40 (upgrade)
LH frequency (GHz)	4.6	5 (upgrade)

propagation physics.

Meanwhile, in terms of LH propagation and absorption physics, there is one major difference between Alcator C-Mod and ITER. In ITER, it is expected that the energy propagation path of the launched LH waves will be much shorter than that in Alcator C-Mod due to the higher plasma temperature of ITER. Lower hybrid waves are expected to be efficiently absorbed in the plasma as soon as they pass the last closed flux surface, contrary to the C-Mod case where LH waves propagate toward the high-field side edge without being absorbed and make reflections there at least once in typical L-mode plasmas due to the relatively low electron temperature.

However, due to the small machine size, the ratio of the pulse length to the current relaxation time is long enough in Alcator C-Mod to allow the study of steady state plasma conditions in the sense of fully relaxed current density profiles. Here, the current relaxation time [22] is defined as $\tau_{CR} = 1.4 a^2 \kappa T_e^{1.5}(\mathrm{keV})/Z_{eff}$ where a is the minor radius, κ is the elongation, T_e is the electron temperature, and Z_{eff} is the effective ion charge. For typical Alcator C-Mod plasma parameters with $\kappa \approx 1.7$, $T_e \approx 2\,\mathrm{keV}$, and $Z_{eff} \approx 2$, one finds $\tau_{CR} \approx 160\,\mathrm{ms}$, which is much shorter than the typical LH pulse length (> 0.5 second) and plasma pulse length (> 2 second) of Alcator C-Mod.

One important goal of the LHCD program in Alcator C-Mod is to develop the

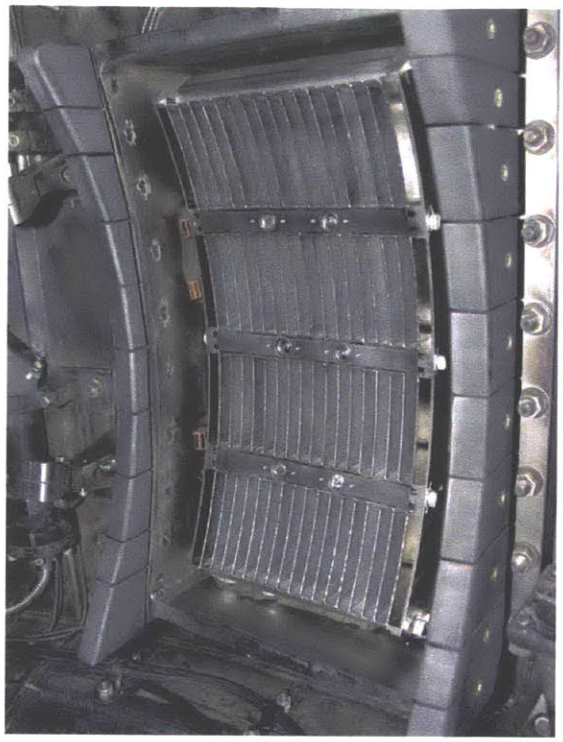

Figure 1-1: LH launcher of Alcator C-Mod

advanced tokamak target plasma using LHCD to supplement the bootstrap current for several τ_{CR}. A previous scoping study [23] with Alcator C-Mod plasma parameters indicated that a majority of plasma current can be sustained by the naturally occurring pressure driven bootstrap current in high temperature ($T_{e0} \approx 5\,\mathrm{keV}$), high density ($\overline{n}_e \approx 1.5 \times 10^{20}\,\mathrm{m}^{-3}$) plasmas. It was observed that 3 MW of LHCD can supplement the bootstrap current at the outer radial region with on-axis fast wave current drive to eliminate the need for inductive plasma current. High density plasmas were found to be necessary to ensure not only good confinement but also a significant amount of bootstrap current fraction ($\gtrsim 50$ %), which is critical for achieving steady state tokamak operation. Thus, LHCD experiments on Alcator C-Mod explore the feasibility of advanced tokamak operation with the reactor-relevant plasma parameters.

1.2.2 Lower hybrid current drive system

The LHCD system [24] of Alcator C-Mod delivers radio frequency waves at 4.6 GHz to the plasma. The current launcher [25] has been installed on Alcator C-Mod since the 2010 campaign and has been reliable in the past three years of physics operations. The launcher consists of four rows, each of which is a phased array of 16 rectangular waveguides, as shown in Figure 1-1. The dimension of each waveguide is 7 mm in width and 60 mm in height. There is a septum with a thickness of 1.5 mm between the waveguides. Each row of the waveguides is separated by 21 mm. On each side of the launcher there are four passive waveguides. Between the rows, there are two Langumuir probes that measure plasma density and temperature at the coupler. This probe can be used to monitor LH frequency spectra as well. The launcher is protected from the plasma by the presence of the poloidal molybdenum limiters on each side of the launcher. While the limiter is a fixed structure, the launcher itself can be radially moved to maximize the coupling during the experiments.

A four-way splitter system [25] at the front end of the LHCD system splits the power evenly into each row of waveguides and increases transmission efficiency up to $\sim$ 75%, as compared to the previously installed launcher where the transmission efficiency was up to 50% at best. Another feature of the four-way splitter system is that the launcher is resilient to poloidal variations in plasma loading.

Using this system, the launched antenna spectrum can be dynamically controlled in the range of a peak parallel refractive index ($n_{\parallel}$) from 1.5 to 3.0, which can be controlled by adjusting the relative phase between the adjacent columns of the wave-guides. Figure 1-2 shows an example of analytic $n_{\parallel}$ spectra with the relative phasing of 60°, 75°, 90°, 110° and 180° using a geometry of the single row of the current launcher. As the relative phasing increases, the directionality decreases. It also shows the negative spectra. While the 180° phasing case is not available with the existing launcher, it serves an example of the wavenumber spectrum when LH waves are used for the plasma heating instead of current drive.

A set of 12 klystrons provides 3 MW of source power. Standard WR-187

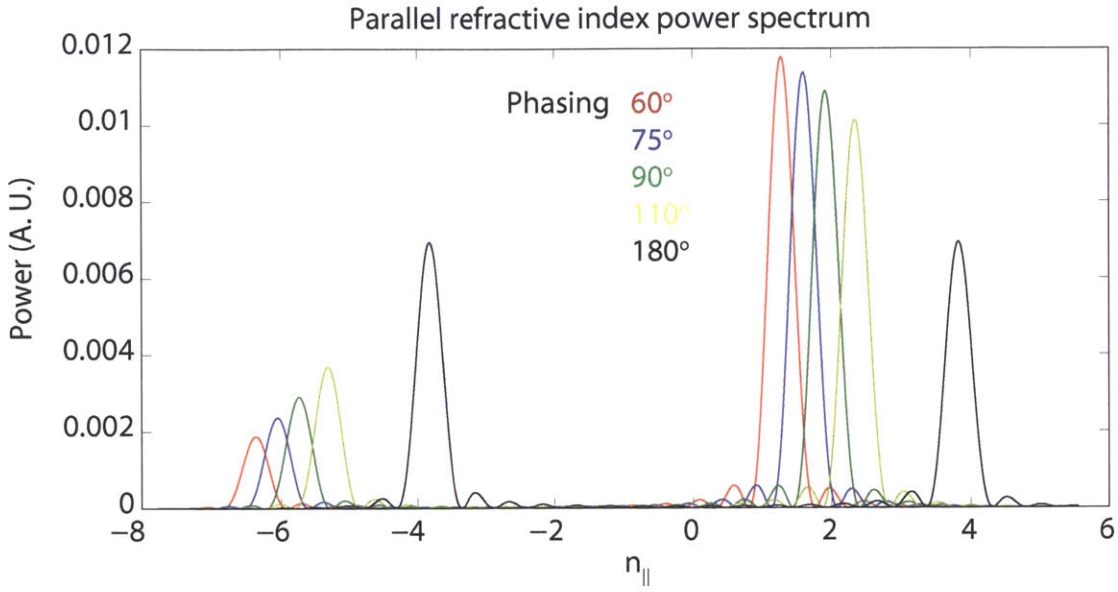

Figure 1-2: Simulated $n_{\parallel}$ spectra of the Alcator C-Mod LH launcher.

wave-guides are used to feed source power to the launcher. Up to 1.2 MW of net power has been coupled to plasmas with a wide range of magnetic fields ($3 \sim 8\,\mathrm{T}$), densities ($\overline{n}_e = 0.3 \sim 2 \times 10^{20}\,\mathrm{m}^{-3}$), and plasma currents ($300 \sim 1000\,\mathrm{kA}$). A recent upgrade of the transmitter protection system has also allowed the pulse length to be extended to as long as one second [26].

Chapter 2

Review of Lower Hybrid Waves and Lower Hybrid Current Drive

In this chapter, the physics of lower hybrid (LH) waves and lower hybrid current drive (LHCD) are reviewed. Section 2.1 examines the propagation of electromagnetic waves in a cold magnetized homogeneous plasma and the accessibility condition of LH waves. Section 2.2 discusses LH waves in the limit of electrostatic waves, and Section 2.3 presents the kinetic theory of electrostatic waves. Section 2.4 discusses the effect of toroidicity on LH wave propagation in a toroidal geometry. Section 2.5 presents the theory of LHCD. Section 2.6 discusses the experimental observations of the loss of LHCD efficiency in reactor-relevant high-density plasmas.

2.1 Review of Cold Plasma Wave Theory

2.1.1 General dispersion relation

To describe the propagation of electromagnetic waves in plasmas, one derives the linearized wave equation from the Maxwell equations:

$$\nabla \times \vec{E} = -\frac{\partial \vec{B}}{\partial t}, \tag{2.1}$$

$$\nabla \times \vec{H} = \vec{j} + \frac{\partial \vec{D}}{\partial t}, \tag{2.2}$$

$$\nabla \cdot \vec{B} = 0, \tag{2.3}$$

and

$$\nabla \cdot \vec{D} = \rho, \tag{2.4}$$

where $\vec{E}$ is the electric field intensity, $\vec{B}$ is the magnetic induction, $\vec{j}$ is the current density, ρ is the charge density. $\vec{D} = \bar{\bar{\epsilon}} \cdot \vec{E}$ is the electric displacement vector, where $\bar{\bar{\epsilon}}$ is the effective dielectric permittivity dielectric tensor. The magnetic intensity $\vec{B} = \mu \vec{H}$ is characterized by the magnetic permeability (μ) of the medium. It is generally assumed that $\mu = \mu_0$ in plasma, where μ_0 is the permeability of free space. Note that applying the divergence to both sides of Equation 2.2 (Ampere's Law) leads to the following equation of continuity:

$$\nabla \cdot \vec{j} + \frac{\partial \rho}{\partial t} = 0. \tag{2.5}$$

With the assumption that all field quantities have the form of $\sim e^{i(\vec{k} \cdot \vec{r} - \omega t)}$, the wave equation is found by combining Equations 2.1 and 2.2 as follows:

$$\vec{k} \times (\vec{k} \times \vec{E}) + \frac{\omega^2}{c^2} \vec{E} + i \mu_0 \omega \vec{j} = 0. \tag{2.6}$$

In order to relate $\vec{j}$ to $\vec{E}$, the conductivity tensor $\bar{\bar{\sigma}}$ is defined as follows:

$$\vec{j} = \bar{\bar{\sigma}} \cdot \vec{E}. \tag{2.7}$$

Then, Equation 2.6 can be re-written as

$$\bar{\bar{D}} \cdot \vec{E} = \vec{n} \times \vec{n} \times \vec{E} + \bar{\bar{K}} \cdot \vec{E} = 0, \tag{2.8}$$

where the dielectric tensor $\bar{\bar{K}}$ is

$$\bar{\bar{K}} = \bar{\bar{I}} + \frac{i}{\omega \epsilon_0} \bar{\bar{\sigma}}, \tag{2.9}$$

and $\vec{n} = c\vec{k}/\omega$ is the wave refractive index. The dispersion relation is given by setting the determinant of $\bar{\bar{D}}$ to zero.

$$\det|\bar{\bar{D}}| = 0. \tag{2.10}$$

2.1.2 Cold plasma dispersion relation

To derive the cold plasma dispersion relation, the dielectric tensor is found from the two-fluid cold plasma mode, which assumes no thermal motion of particles. No background electric field is assumed, but the static background magnetic field is assumed to be in the z-direction ($\vec{B}_0 = B_0\hat{z}$). The linearized equation of motion for a single particle of species j in the presence of the electromagnetic field is

$$m_j \frac{\partial \vec{v}_j}{\partial t} = q_j(\vec{E}_j + \vec{v_j} \times \vec{B}_0). \tag{2.11}$$

Because $\vec{j} = \bar{\bar{\sigma}} \cdot \vec{E} = \sum_j n_j q_j \vec{v}_j$, where the sum is over the species, the conductivity tensor can be written as

$$\bar{\bar{\sigma}}_j = \begin{bmatrix} \frac{q_j^2 n_j}{m_j} \frac{i\omega}{\omega^2 - \Omega_j^2} & -\frac{q_j^2 n_j}{m_j} \frac{\Omega_j}{\omega^2 - \Omega_j^2} & 0 \\ \frac{q_j^2 n_j}{m_j} \frac{\Omega_j}{\omega^2 - \Omega_j^2} & \frac{q_j^2 n_j}{m_j} \frac{i\omega}{\omega^2 - \Omega_j^2} & 0 \\ 0 & 0 & \frac{iq_j^2 n_j}{m_j} \frac{1}{\omega} \end{bmatrix}. \tag{2.12}$$

The dielectric tensor in the cold plasma limit becomes

$$\bar{\bar{K}} = \begin{bmatrix} K_{xx} & K_{xy} & 0 \\ K_{yx} & K_{yy} & 0 \\ 0 & 0 & K_{zz} \end{bmatrix} = \begin{bmatrix} S & -iD & 0 \\ iD & S & 0 \\ 0 & 0 & P \end{bmatrix}, \tag{2.13}$$

where

$$S = 1 - \sum_j \frac{\omega_{pj}^2}{\omega^2 - \Omega_j^2}, \tag{2.14}$$

$$D = \sum_j \frac{\Omega_{pj}}{\omega} \frac{\omega_{pj}^2}{\omega^2 - \Omega_j^2}, \tag{2.15}$$

and

$$P = 1 - \sum_j \frac{\omega_{pj}^2}{\omega^2}. \tag{2.16}$$

Here, $\omega_{pj} = \sqrt{\frac{q_j^2 n_j}{\epsilon_0 m_j}}$ is the plasma frequency, and $\Omega_j = \frac{q_j B_0}{m_j}$ is the cyclotron frequency. Finally, combining Equation 2.10 with Equation 2.13 yields the following cold plasma dispersion relation:

$$\det\left|\bar{\bar{D}}\right| = \det \begin{vmatrix} S - n_\parallel^2 & -iD & n_\perp n_\parallel \\ iD & S - n_\parallel^2 - n_\perp^2 & 0 \\ n_\perp n_\parallel & 0 & P - n_\perp^2 \end{vmatrix} = 0, \tag{2.17}$$

where $n_\parallel = n\cos\theta$ is the parallel refractive index, $n_\perp = n\sin\theta$ is the perpendicular refractive index, and θ is the angle between $\vec{n}$ and $\vec{B}_0$.

In the limit of perpendicular propagation to $\vec{B}_0$, two relevant dispersion relations are as follows:

$$\text{Ordinary-mode (O-mode) wave: } n_\perp^2 = P \tag{2.18a}$$

$$\text{Extraordinary-mode (X-mode) wave: } n_\perp^2 = \frac{RL}{S}, \tag{2.18b}$$

with $R = S + D$ and $L = S - D$:

$$R = 1 - \sum_j \frac{\omega_{pj}^2}{\omega(\omega + \Omega_j)} \tag{2.19a}$$

$$L = 1 - \sum_j \frac{\omega_{pj}^2}{\omega(\omega - \Omega_j)}. \tag{2.19b}$$

The edge reflectometer system [27] of Alcator C-Mod uses the O-mode wave that can interact with the LH wave to generate the backscattered O-mode wave. This interaction can be used to study LH waves in the scrape-off layer, and will be discussed further in Chapter 3.

2.1.3 Lower hybrid accessibility

As the LH wave propagates toward a higher density region, it might mode-convert into the Whistler wave and propagate back toward the plasma edge if the accessibility condition is not met. This mode conversion occurs at the radial location where the wave roots of the LH wave and Whistler wave coalesce. To examine the accessibility of LH waves, Equation 2.17 can be re-written in terms of $n_\perp$.

$$An_\perp^4 - Bn_\perp^2 + C = 0, \tag{2.20}$$

where

$$A = S \tag{2.21a}$$

$$B = (S - n_\parallel^2)(P + S) - D^2 \tag{2.21b}$$

$$C = P(n_\parallel^2 - R)(n_\parallel^2 - L) = P[(n_\parallel^2 - S)^2 - D^2] \tag{2.21c}$$

Here, it is assumed that the launched $n_\parallel$ spectrum is fixed by the grill antenna with no toroidal variations in $n_\parallel$. Note the presence of cut-off layers at $n_\perp^2 = 0$: $P = 0$, $n_\parallel^2 = R$, and $n_\parallel^2 = L$. The first is the cut-off layer of the LH wave, the second is the cut-off layer of the Whistler wave, and the third is irrelevant in the regime of interest.

Solving Equation 2.20 yields two roots:

$$n_\perp^2 = \frac{B \pm \sqrt{B^2 - 4AC}}{2A}, \tag{2.22}$$

where the (+) root corresponds to the LH wave and the (−) root is the Whistler wave. The (perpendicular) phase velocity of the LH wave is slower than that of the Whistler wave. The LH wave is often called a slow wave, and the Whistler wave a fast wave.

The dispersion relation of the LH wave can be found from setting $D \to 0$:

$$n_\perp^2 = \left(1 - \frac{n_\parallel^2}{S}\right) P \tag{2.23}$$

The electric field is polarized in the x-z plane: $\vec{E} = E_x\hat{x} + E_z\hat{z}$. Lower hybrid waves can propagate in the region of $\omega_{pe}^2 > \omega^2$ if $n_\parallel^2 > 1$, but they become evanescent in the region of $\omega_{pe}^2 < \omega^2$. The cut-off density is $n_e \approx 2.6 \times 10^{17}\,\mathrm{m}^{-3}$ with the source frequency at 4.6 GHz in Alcator C-Mod. The LH wave needs to tunnel through this evanescent layer from the edge, which is typically on the order of $\sim$ mm for Alcator C-Mod plasmas. The LH launcher is pushed toward the plasma as much as it can be to minimize this layer and thus ensure maximizing coupling.

The dispersion relation of the Whistler wave is found from dividing Equation 2.23 into the last term in the Equation 2.20 that is Equation 2.21c :

$$n_\perp^2 = (S - n_\parallel^2) - \frac{D^2}{S - n_\parallel^2}, \tag{2.24}$$

with the electric field polarized in the y-direction. It can be seen in Equation 2.21c that the Whistler wave is evanescent up to the location of $n_\parallel^2 = R \approx 1 + \omega_{pi}^2/(\omega\omega_{ci})$ where the latter approximation holds for $\omega_{ci} \ll \omega \ll \omega_{ce}$. If $f = 4.6$ GHz, $n_\parallel = 2$, and $f_{ci} = 30\,\mathrm{MHz}$ (corresponding to the deuterium ion cyclotron frequency at the low-field-side edge of the Alcator C-Mod tokamak with $B_{T0} = 5.4\,\mathrm{T}$), then the cut-off density for the Whistler wave is $n_e \approx 2 \times 10^{19}\,\mathrm{m}^{-3}$.

At the mode conversion layer, the dispersion relations of both the LH and Whistler wave become $n_\perp^2 = B/(2A)$. Thus, to avoid mode conversion at any given location, the accessibility condition must satisfy

$$B^2 - 4AC > 0. \tag{2.25}$$

This condition can be rewritten in terms of the minimum $n_\parallel$ of the LH wave. To achieve a simplified expression in the frequency range of interest ($\Omega_i^2 \ll \omega_{pi}^2 \sim \omega^2 \ll$

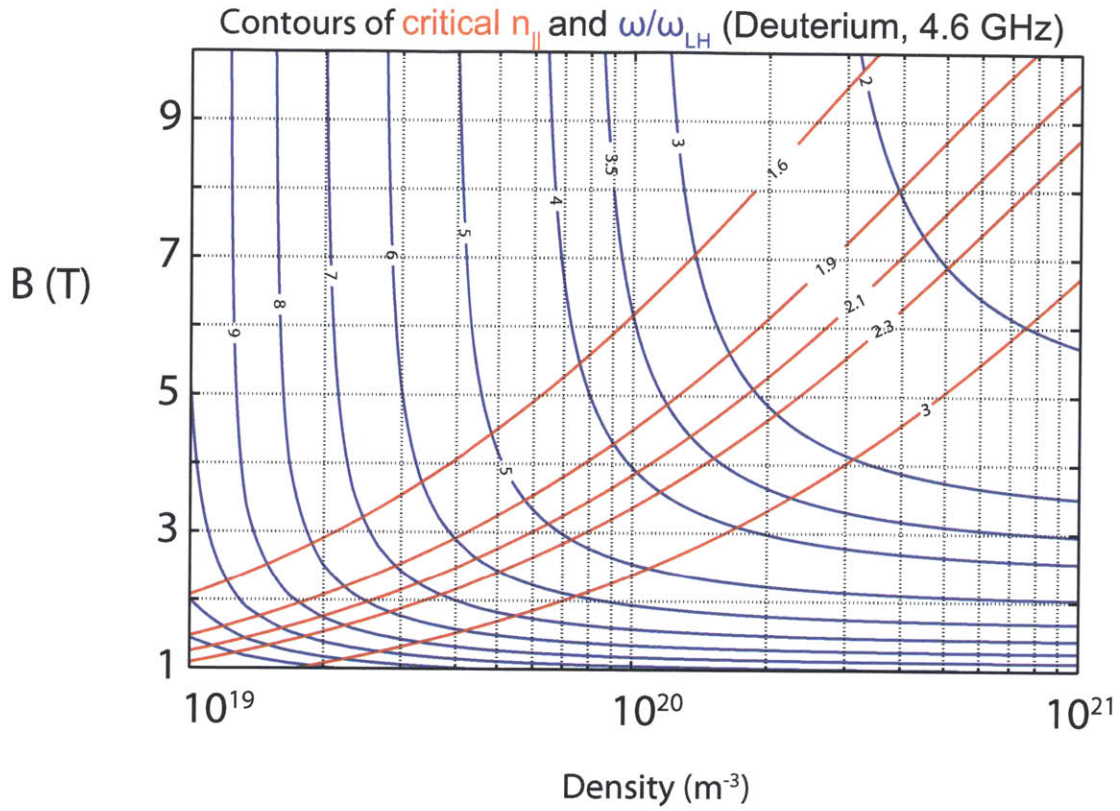

Figure 2-1: Contours of accessible $n_{\parallel}$ (red) and ω_0/ω_{LH} (blue) against density and magnetic field in a deuterium plasma with $\omega_0 = 2\pi f_0$ and $f_0 = 4.6\,\mathrm{GHz}$.

$\omega_{pe}^2 \sim \Omega_e^2$), Equations 2.21a, 2.21b, and 2.21c can be approximated as follows:

$$A = S \approx 1 - \frac{\omega_{pi}^2}{\omega^2} + \frac{\omega_{pe}^2}{\omega_{ce}^2} \tag{2.26a}$$

$$B \approx P(S - n_{\parallel}^2) - D^2 \tag{2.26b}$$

$$C \approx -PD^2. \tag{2.26c}$$

The accessibility condition in terms of $n_{\parallel}$ becomes

$$n_{\parallel} > n_{\parallel,crit} = \sqrt{1 - \frac{\omega_{pi}^2}{\omega^2} + \frac{\omega_{pe}^2}{\omega_{ce}^2}} + \frac{\omega_{pe}}{|\omega_{ce}|}, \tag{2.27}$$

where $n_{\parallel,crit}$ is the minimum $n_{\parallel}$ to avoid mode conversion. Note that higher magnetic field machines have better accessibility than lower magnetic field machines do.

Figure 2-1 shows the contours of the accessibility condition for several $n_\parallel$ as functions of the density and magnetic field in deuterium plasmas with the source frequency at 4.6 GHz. The parameter space only above the (red) contour line is accessible for the given $n_\parallel$. Thus, $n_\parallel \gtrsim 2$ is necessary for accessibility to the core of the typical Alcator C-Mod high-density L-mode plasmas with $n_e(0) \approx 2 \times 10^{20}\,\mathrm{m}^{-3}$ and $B_T(0) = 5.4\,\mathrm{T}$. Note that the contour of ω/ω_{LH} is over-plotted, where $\omega_{LH}^2 = \omega_{pi}^2/[1 + \omega_{pe}^2/\omega_{ce}^2]$ is the lower hybrid frequency (corresponding to $S = 0$), which will be discussed more in the next section.

Note that one of the limitations of the cold plasma wave theory is that it neglects both the thermal motion of the particles and the interactions between the waves and the particles. In particular, the theory breaks down when $n_\parallel \to \infty$ or $n_\perp \to \infty$. Thus, cold plasma theory is valid only when $\omega/k_\parallel > 3v_{tj}$ and $k_\perp^2 r_{cj}^2 \ll 1$. Otherwise, one needs to consider the effects of finite temperature to study kinetic effects, such as Landau damping and the mode conversion from the electromagnetic wave to the electrostatic wave (e.g., the mode conversion into Bernstein waves), which can be thoroughly studied with the kinetic theory, which is presented in Section 2.3.

2.2 Cold plasma electrostatic waves

The LH wave can be described as the electrostatic wave, which is a longitudinal wave with a relatively short wavelength, in the limit when $n^2 \gg |K_{ij}|$. Unlike the electromagnetic wave, the magnetic field component of the electrostatic wave is negligible. This allows one to represent the electric field of the LH wave with the scalar potential ϕ as follows:

$$\vec{E} = -\nabla\phi, \tag{2.28}$$

which indicates that the wave is longitudinal ($\vec{E} = \vec{E}_l \parallel \vec{n} = c\vec{k}/\omega$) and has no transverse component ($\vec{E}_{tr} = 0$). The potential ϕ can be related to the perturbed charge density with Poisson's equation

$$\nabla^2\phi = -\frac{\rho}{\epsilon_0}, \tag{2.29}$$

where ρ is calculated by combining the equations of continuity and momentum in a similar way that was presented in Section 2.1.2. The resulting dispersion relation is

$$1 + \chi_i + \chi_e = 0, \tag{2.30}$$

where the susceptibility χ_j is defined as

$$\chi_j = -\left(\frac{\omega_{pj}^2}{\omega^2 - \Omega_j^2} \frac{k_\perp^2}{k^2} + \frac{\omega_{pj}^2}{\omega^2} \frac{k_\parallel^2}{k^2} \right). \tag{2.31}$$

Another way to examine the dispersion relation of the electrostatic wave is to take the dot product of Equation 2.8 with $\vec{n}$ and assume $\vec{E} = -\nabla\phi$:

$$\vec{n} \cdot \bar{\bar{K}} \cdot \vec{n} = 0. \tag{2.32}$$

In the cold plasma limit, Equation 2.32 is found to be the resonance condition of the electromagnetic wave:

$$S n_\perp^2 + P n_\parallel^2 = 0. \tag{2.33}$$

Within the limit of perpendicular propagation, two hybrid resonances can be predicted. The first is the upper hybrid resonance

$$\omega^2 \simeq \omega_{uh} = \omega_{pe}^2 + \omega_{ce}^2, \tag{2.34}$$

and the second is the lower hybrid resonance

$$\omega^2 \simeq \omega_{lh}^2 = \omega_{ci}^2 + \frac{\omega_{pi}^2}{1 + \omega_{pe}^2/\omega_{ce}^2}. \tag{2.35}$$

In the case of propagating electrostatic waves ($k_\parallel \neq 0$, $k_\perp \neq 0$), a unique solution for $\omega(k)$ can be found. The cold lower hybrid wave (slow wave) exists in the frequency range of $\omega_{ci} \ll \omega_{pi} \lesssim \omega \ll \min(\omega_{pe}, \omega_{ce})$. In this range, the ion contribution becomes important to calculate the perturbed charge, and the resulting dispersion relation

becomes

$$\omega^2 = \omega_{LH}^2 \left(1 + \frac{k_\parallel^2}{k^2}\frac{m_i}{m_e}\right), \tag{2.36}$$

where ω_{LH} is the lower hybrid frequency within the limit of $\sin^2\theta = 1$:

$$\omega_{LH}^2 = \frac{\omega_{pi}^2}{1 + \frac{\omega_{pe}^2 \sin^2\theta}{\omega_{ce}^2}} \simeq \frac{\omega_{pi}^2}{1 + \frac{\omega_{pe}^2}{\omega_{ce}^2}}. \tag{2.37}$$

The parallel and perpendicular group velocities are then

$$v_{g\parallel} = \frac{\partial\omega}{\partial k_\parallel} = \frac{\omega}{k_\parallel}\left(1 - \frac{\omega_{LH}^2}{\omega^2}\right) \tag{2.38a}$$

$$v_{g\perp} = -\frac{\partial\omega}{\partial k_\perp} = \frac{\omega}{k}\left(1 - \frac{\omega_{LH}^2}{\omega^2}\right) \tag{2.38b}$$

with the approximation $k_\parallel^2 \ll k_\perp^2 \simeq k^2$ from $\omega^2 \ll \omega_{pe}^2$. Consequently, the group velocity angle φ, which is the angle between $\vec{v}_g$ and $\vec{B}$, depends only on plasma parameters:

$$\tan\varphi = \frac{v_{g\perp}}{v_{g\parallel}} \simeq -\frac{k_\parallel}{k} = \sqrt{\frac{m_e}{m_i}\left(\frac{\omega^2}{\omega_{LH}^2} - 1\right)}. \tag{2.39}$$

As long as the electrostatic approximation holds, φ is independent of $n_\parallel$. The trajectory of $\vec{v}_g$ is called a resonance cone. Note also that $\vec{v}_g$ is orthogonal to the phase velocity because $\vec{k} \cdot \vec{v_g} = 0$. The LH wave is a backward wave; while the perpendicular component of the resonance cone propagates radially inward, the perpendicular component of the phase velocity propagates radially outward. This characteristic of the LH wave can be exploited for detecting LH waves using O-mode waves, which will be discussed in further detail in Chapter 3.

Note, however, that when the electrostatic approximation does not hold (i.e., $n_\parallel \not\gg 2$), the group velocity should be found from the general dispersion relation as

derived in Section 2.1.2. In this case, the group velocity of the slow LH wave becomes

$$v_{g\parallel} = \frac{\omega}{k_\parallel} = \frac{c}{n_\parallel} \tag{2.40a}$$

$$v_{g\perp} = -v_{g\parallel}\frac{\omega}{\omega_{pe}}\sqrt{1-\frac{1}{n_\parallel^2}}. \tag{2.40b}$$

In contrast to the resonance cone propagation in the electrostatic limit, the group velocity angle φ depends on $n_\parallel$ in this case:

$$\tan\varphi = -\frac{\omega}{\omega_{pe}}\sqrt{1-\frac{1}{n_\parallel^2}} \tag{2.41}$$

In the electrostatic limit, the electric field within the resonance cone can be found with the WKB theory [28, 29]. The electric field at a position x is related to the electric field at the mouth of a launcher at $x = x_{WG}$:

$$|E_\parallel(x)| = |E_\parallel(x_{WG})|\left[\frac{P(x_{WG})S(x_{WG})}{P(x)S(x)}\right]^{1/4} \tag{2.42a}$$

$$|E_\perp(x)| = \frac{|k_\perp(x)|}{|k_\parallel|}|E_\parallel(x)|, \tag{2.42b}$$

where P and S are defined in Equations 2.16 and 2.14. The electric field at the mouth of the launcher on plasma side $E_\perp(x_{WG})$ can be found from the following conservation of power flux across the vacuum-plasma interface:

$$P_{RF} = Wv_{g\perp}A|_{x_{WG},\text{vacuum}} = Wv_{g\perp}A|_{x_{WG},\text{plasma}}, \tag{2.43}$$

where $W = \epsilon_0\vec{E}^*\cdot\partial(\omega\bar{\bar{\epsilon}}_0)/\partial\omega\cdot\vec{E}/4$ is the total energy density in a lossless medium [30, p. 193], and A is the surface area of the wave-guide mouth. Equations 2.42a and 2.42b state that $|E_\parallel|$ decreases and $|E_\perp|$ increases as the LH wave propagates to a higher density region. The electric field calculated from the WKB approach will be used in Chapter 4 to evaluate the local electric field for the given power and plasma density.

2.3 Kinetic Theory of Electrostatic Waves

In the kinetic theory, the charge density in Poisson's equation (2.29) can be written in terms of the integral of the distribution function:

$$\rho(\vec{r},t) = \sum_j Z_j q_j n_j(\vec{r},t) = \sum_j Z_j q_j \int_{-\infty}^{\infty} \mathrm{d}v^3 f_j(\vec{r},\vec{v},t). \tag{2.44}$$

It can be shown that the dispersion relation of the electrostatic wave in a hot magnetized Maxwellian plasma with an isotropic temperature is given by [31, p. 294][1]

$$\epsilon(\omega,k) = 1 + \chi_i + \chi_e = 0, \tag{2.45}$$

with the following susceptibility χ_j

$$\chi_j = \frac{1}{k^2\lambda_{Dj}^2}\left[1 + \zeta_{0j}\sum_{m=-\infty}^{\infty}\Gamma_m(b_j)Z(\zeta_{mj})\right], \tag{2.46}$$

where $\lambda_{Dj} = (\epsilon_0 T_j/e^2 n_0)^{1/2}$ is the Debye length, $v_{tj} = (2T_j[eV]/m_j)^{1/2}$ is the thermal speed, $b_j = k_\perp^2 r_{cj}^2 = k_\perp^2 v_{tj}^2/2\Omega_j^2$ is the Larmor radius factor, $\Gamma_m(b_j) \equiv I_m(b_j)\exp(-b_j)$, $I_m(b_j)$ is the modified Bessel function of the first kind, $\zeta_{mj} \equiv (\omega - m\Omega_j)/k_\parallel v_{tj}$, and $Z(\zeta_{mj})$ is the Fried-Conte plasma dispersion function

$$Z(\zeta_{mj}) = \frac{1}{\sqrt{\pi}}\int_{-\infty}^{\infty} dv_\parallel \frac{e^{-v_\parallel^2/v_{tj}^2}}{v_\parallel - \left(\dfrac{\omega - m\Omega_j}{k_\parallel}\right)}, \tag{2.47}$$

where, for $\omega_{im} > 0$,

$$Z(\zeta_{mj}) = i\sqrt{\pi}\frac{k_\parallel}{|k_\parallel|}\exp(-\zeta_{mj}^2) + \frac{\mathbf{P}}{\sqrt{\pi}}\int_{-\infty}^{\infty} dz \frac{\exp(-z^2)}{z - \zeta_{mj}}, \tag{2.48}$$

where $\mathbf{P}$ is the Cauchy principal value operator. Note that the term $\Gamma_m(b_j)$ results from the integration of the perpendicular velocity term, and the term $Z(\zeta_{mj})$ from

[1] To follow the convention used in Stix, the dimensionless effective dielectric constant is defined as ϵ in the rest of this thesis.

the integration of the parallel velocity term.

As compared to the cold plasma theory, the kinetic theory can describe two additional physical effects. One effect is the wave-particle resonance that is described by the denominator of the integrand in Equation 2.47. The term in the denominator corresponds to Landau resonance if $m = 0$ and cyclotron resonance if $m \neq 0$. The other is the finite Larmor radius effect that is described by the term $\Gamma_m(b_j)$.

2.3.1 Lower hybrid waves

In the frequency range of LH waves($\lambda \sim r_{Li}$), with the relevant approximations and expansions, the approximate (Hermitian part of the) dispersion relation is found to be [32]

$$\omega^2 = \omega_{LH}^2 \left[1 + \frac{k_\parallel^2}{k^2} \frac{m_i}{m_e} + \frac{3k_\perp^2 T_i}{\omega^2 m_i} \left(1 + \frac{1}{4} \frac{T_e}{T_i} \frac{\omega^4}{\omega_{ce}^2 \omega_{ci}^2} \right) \right], \tag{2.49}$$

which is in agreement with the cold plasma dispersion relation (Equation 2.36) except for the finite temperature correction term. Note that Maxwellian plasma is considered in deriving this dispersion relation.

This dispersion relation derived from the kinetic theory shows the possibility of using LH waves for plasma heating or current drive in the following two approaches. The first is ion heating in the limit of $\omega/k_\parallel v_{te} > 3 \sim 4$ to avoid electron Landau damping [33]. Equation 2.49 predicts that the incoming LH wave may transform into an outgoing hot ion plasma wave near the density where $\omega/\omega_{LH} \approx 1$. Near this mode conversion layer, $k_\perp$ becomes large, so ion cyclotron harmonic damping on ions is expected [32]. The imaginary term that is responsible for this process in the dielectric constant is

$$\epsilon_{Im}(\omega, \vec{k})_{ions} = \frac{\sqrt{\pi}}{k^2 \lambda_{Di}^2} \frac{\omega}{k_\parallel v_{ti}} \sum_{-\infty}^{\infty} \Gamma_m(b_i) \exp \left[-\frac{(\omega - m\omega_{ci})^2}{k_\parallel^2 v_{ti}^2} \right]. \tag{2.50}$$

Earlier LH experiments have focused on this ion heating regime, but the results were not reliable [33], and the cause was attributed to non-linear effects at the plasma

edge, such as parametric decay instability (PDI) [34, 35] and low-frequency density fluctuations [36, 37, 38]. The hypothesis was that both mechanisms could scatter incoming LH waves and thus limit the radial penetration.

The second approach is electron heating or current drive in the limit of $\omega/k_{\parallel}v_{te} \lesssim 2.8$, and this approach can result in the strong electron Landau damping of LH waves [33]. The momentum and energy of LH waves are transferred to the electrons that satisfy this condition. In terms of $n_{\parallel}$, the equivalent condition is [33]

$$n_{\parallel} \gtrsim \frac{5.8}{\sqrt{T_e(\mathrm{keV})}}. \tag{2.51}$$

The imaginary term responsible for this process in the dielectric constant is

$$\epsilon_{Im}(\omega, k)_{electrons} = \frac{\sqrt{\pi}}{k^2\lambda_{De}^2}\frac{\omega}{k_{\parallel}v_{te}}\exp\left(-\omega^2/k_{\parallel}^2v_{te}^2\right). \tag{2.52}$$

If the plasma core temperature is $T_{e0} \approx 2\,\mathrm{keV}$, then the LH wave with $n_{\parallel} > 4$ can be effectively Landau damped to heat the electrons. Subsequent bulk ion heating is also expected due to electron-ion collisions. If the phasing of the launched LH waves is controlled in a preferential direction, then electron Landau damping can impart momentum and energy to electrons in that direction only, creating toroidal currents [39, 40]. This will be more discussed in detail in Section 2.5.

The Landau damping condition also states that the LH wave with higher $n_{\parallel}$ can be damped at the plasma edge, which is why non-linear effects, such as PDI and LH wave scattering, are expected to inhibit the radial penetration of incoming LH waves because they can excite the LH waves with a much higher $n_{\parallel}$ than that of the launched LH waves. Those waves will be readily damped at the edge. Note that the launched LH power density in existing tokamaks is high enough to cause undesirable non-linear effects, but the general rule of thumb [34, 35] is that (ion cyclotron) PDI will at least not be problematic as long as the plasma density is low such that $\omega_0/\omega_{lh}(0) > 2$, where $\omega_{lh}(0)$ is ω_{lh} at $r/a = 0$. This condition assumes that LH waves cross the edge region only once when propagating from the launcher to the plasma core, and

keep penetrating radially inward (e.g., Figure 1 in [34]). However, this might not be necessarily the case in the existing tokamaks, including Alcator C-Mod, due to a weaker radial penetration of the LH wave (Equation 2.41) in high density plasmas. Then, LH waves could be susceptible to non-linear effects at the high-field side edge of the tokamak, which will be discussed further in Chapter 5.

2.3.2 Ion sound, ion acoustic, and ion cyclotron waves

In the limit of

$$v_{ti} \ll \frac{\omega}{k_\parallel} \ll v_{te}, \tag{2.53}$$

three types of hot electrostatic waves can be identified by keeping all terms to first order in T_e in the limit of $\omega \ll \omega_{ce}$: ion sound waves, ion cyclotron waves, and ion acoustic waves. In this limit, ions behave as if they were in a fluid-like medium, but electrons behave as if they were in an isothermal medium [30, p. 157]. In addition, for ion sound and ion acoustic waves, it is assumed that $b_e \simeq 0$ so that $\Gamma_{0e} \simeq 1$ and $\Gamma_m(b_e) = 0$ for $m \geq 2$ because $b_e = (T_e m_e / T_i m_i) b_i \ll b_i < 1$. Then, the following dispersion relation is found in this limit:

$$\begin{aligned}
\epsilon(\omega, \vec{k}) &= 0 \\
&= 1 + \frac{1}{k^2 \lambda_{De}^2}\left(1 + \frac{i\sqrt{\pi}\omega}{k_\parallel v_{te}}\right) + i\Gamma_0(b_i)\frac{\sqrt{\pi}}{k^2\lambda_{Di}^2}\frac{\omega}{k_\parallel v_{ti}}\exp\left(-\frac{\omega^2}{k_\parallel^2 v_{ti}^2}\right) \\
&\quad - \frac{\omega_{pi}^2}{\omega^2}\left\{\frac{k_\parallel^2}{k^2}\left(1 + \frac{3}{2}\frac{k_\parallel^2 v_{ti}^2}{\omega^2}\right) + \frac{k_\perp^2}{k^2}\frac{\omega^2}{\omega^2 - \omega_{ci}^2}\left(1 + \frac{b_i 3\omega_{ci}^2}{\omega^2 - 4\omega_{ci}^2}\right)\right. \\
&\qquad \left. - b_i\frac{k_\parallel^2}{k^2}\left[1 - \frac{\omega^3}{2(\omega - \omega_{ci})^3} - \frac{\omega^3}{2(\omega + \omega_{ci})^3}\right]\right\}.
\end{aligned} \tag{2.54}$$

First, when $\omega^2 \ll \omega_{ci}^2$, the dispersion relation of the ion sound wave can be found with:

$$\omega^2 = \frac{k_\parallel^2 c_s^2 (1 + 3T_i/T_e)}{1 + k^2\lambda_{De}^2 + k_\perp^2 v_s^2/\omega_{ci}^2}, \tag{2.55}$$

where $v_s^2 = c_s^2(1 + T_i/T_e) = (T_i + T_e)/m_i$. The damping rate of this wave can be estimated as follows:

$$\gamma = -\frac{\epsilon_{Im}}{\partial\epsilon_R/\partial\omega} \simeq \frac{\sqrt{\pi}}{k^2\lambda_{De}^2}\frac{\omega_R}{k_\parallel v_{te}}\left[1 + \left(\frac{m_i}{m_e}\right)^{1/2}\left(\frac{T_e}{T_i}\right)^{3/2}\exp\left(-\frac{\omega_R^2}{k_\parallel^2 v_{ti}^2}\right)\right] / \left(\frac{\partial\epsilon_R}{\partial\omega}\right)_{\omega_R}, \tag{2.56}$$

where the first term in the bracket is due to electron Landau damping and the second is due to ion Landau damping. When $T_e \approx T_i$, strong ion Landau damping arises because the exponential term becomes

$$\exp\left(-\frac{\omega_R^2}{k_\parallel^2 v_{ti}^2}\right) \Rightarrow \exp\left(-\frac{\frac{T_e}{2T_i} + \frac{3}{2}}{1 + k^2\lambda_{De}^2 + k_\perp^2 v_s^2/\omega_{ci}^2}\right), \tag{2.57}$$

with $|\partial\epsilon/\partial\omega_R| \approx 2/(k^2\lambda_{De}^2\omega_R)$.

Second, when $\omega_{ci}^2 \ll \omega^2 \leq \omega_{pi}^2$, the dispersion relation of the ion acoustic wave can be found [30, p. 158]:

$$\omega^2 \simeq \frac{k^2 c_s^2}{1 + k^2\lambda_{De}^2}\left(1 + \frac{3T_i}{T_e}\right). \tag{2.58}$$

The damping rate of this wave is given by the same functional form as Equation 2.56 with the corresponding ω_R and $\partial\epsilon_R/\partial\omega_R$. Similar to the ion sound wave, this wave is strongly ion Landau damped for $T_i \approx T_e$, unless $k_\parallel^2 \ll k_\perp^2$. However, as long as the wave propagates nearly perpendicular to $\vec{B}$, only electron Landau damping becomes important because the exponential term becomes

$$\exp(-\omega_R^2/k_\parallel^2 v_{ti}^2) \Rightarrow \exp\left[-\frac{k^2}{k_\parallel^2}\left(\frac{T_e}{2T_i} + \frac{3}{2}\right)\right] \rightarrow 0. \tag{2.59}$$

Finally, when $\omega \sim m\omega_{ci}$, the ion cyclotron wave exists in the limit $k_\perp^2 \gg k_\parallel^2$ in order to avoid strong ion cyclotron damping. The dispersion relation is given by [34]

$$\begin{aligned}\epsilon(\omega,\vec{k}) = 1 + \frac{1}{k^2\lambda_{De}^2}\left(1 + \frac{i\sqrt{\pi}\omega}{k_\parallel v_{te}}\right) - \frac{1}{k^2\lambda_{Di}^2}\sum_{m=1}^{\infty}\frac{2\Gamma_m(b_i)m^2\omega_{ci}^2}{\omega^2 - m\omega_{ci}^2} \\ + \frac{i\sqrt{\pi}}{k^2\lambda_{Di}^2}\frac{\omega}{k_\parallel v_{ti}}\sum_{m=1}^{\infty}\Gamma_m(b_i)\exp\left[-\frac{(\omega - m\omega_{ci})^2}{k_\parallel^2 v_{ti}^2}\right]\end{aligned} \tag{2.60}$$

Note the presence of harmonics of the ion cyclotron wave, in addition to the fundamental wave. When keeping only the term with $m = 1$, the dispersion relation of the fundamental ion cyclotron waves is given by the

$$\begin{aligned}\omega^2 &= \omega_{ci}^2\left[1 + \frac{T_e 2\Gamma_1(b_i)}{T_i(1 + k^2\lambda_{De}^2)}\right] \\ &\approx \begin{cases}\omega_{ci}^2\left(1 + \frac{T_e}{T_i}b_i\right) & \text{for } b_i \ll 1 \ : \text{forward waves,} \\ \omega_{ci}^2\left(1 + \frac{T_e}{T_i}\frac{2}{\sqrt{2\pi b_i}}\right) & \text{for } b_i \gg 1 \ : \text{backward waves,}\end{cases}\end{aligned} \tag{2.61}$$

using $2\Gamma_1(b_i) \simeq b_i(1 - b_i)$ for $b_i \ll 1$ and $\Gamma_1(b_i) \simeq 1/\sqrt{2\pi b_i}$ for $b_i \gg 1$. Note the maximum value of $\Gamma_1(b_i) \approx 0.22$ at $b_1 \approx 1.5$. The damping rate of the fundamental ion cyclotron wave is given by

$$\frac{\gamma}{\omega_R} = \frac{\sqrt{\pi}}{k^2\lambda_{De}^2}\left\{\frac{\omega}{k_\parallel v_{te}} + \frac{T_i}{T_e}\Gamma_1(b_i)\frac{\omega}{k_\parallel v_{ti}}\exp\left[-\frac{(\omega - \omega_{ci})^2}{k_\parallel^2 v_{ti}^2}\right]\right\} \Big/ \left(\omega_R\frac{\partial\epsilon_R}{\partial\omega_R}\right), \tag{2.62}$$

which contains the contributions from both electron Landau damping and ion cyclotron harmonic damping. For example, ion cyclotron damping of the forward ion cyclotron wave will be strong when

$$\frac{(\omega - \omega_{ci})}{k_\parallel v_{ti}} \approx \frac{\omega_{ci}}{k_\parallel v_{ti}}\frac{T_e}{T_i}\Gamma_1(b_i) < 3, \tag{2.63}$$

or

$$k_\parallel > \frac{T_e}{T_i}\frac{\Gamma_1(b_i)}{3}\frac{1}{\sqrt{2}r_{ci}}. \tag{2.64}$$

For Alcator C-Mod edge deuterium plasmas with $T_e \approx T_i \approx 60\,\mathrm{eV}$, $B = 4\,\mathrm{T}$, and $\Gamma_1(b_i) \approx 0.22$, r_{ci} is about $0.027\,\mathrm{cm}$ and strong ion cyclotron damping sets in for $k_\parallel \gtrsim 192\,\mathrm{m}^{-1}$. The corresponding normalized $n_\parallel$ is about $ck_\parallel/\omega_0 \approx 2$ with respect to the LH source frequency $f_0 = 4.6\,\mathrm{GHz}$. In studying the parametric dispersion relation, it is generally considered that the low-frequency ion cyclotron (quasi) mode has a short wavelength ($ck_\parallel/\omega_0 \gg 2$), and it is expected to be heavily ion cyclotron damped. Furthermore, the contribution of electron Landau damping may be significant depending on the frequency of the ion mode (i.e. $\omega_R \approx k_\parallel v_{te}$ [34]), which is called non-linear electron Landau damping because the resulting ion mode is a consequence of the beating of the two LH waves. These will be discussed more in Chapter 4.

2.4 Effects of Toroidicity on Lower Hybrid Wave Propagation

A resonance cone propagation of the LH wave in toroidal geometry can be described by the following ray equations [38]:

$$\frac{dr}{dt} = -\frac{\partial D/\partial k_r}{\partial D/\partial \omega} \tag{2.65a}$$

$$\frac{d\theta}{dt} = -\frac{\partial D/\partial m}{\partial D/\partial \omega} \tag{2.65b}$$

$$\frac{d\phi}{dt} = -\frac{\partial D/\partial n}{\partial D/\partial \omega} \tag{2.65c}$$

$$\frac{dk_r}{dt} = -\frac{\partial D/\partial r}{\partial D/\partial \omega} \tag{2.65d}$$

$$\frac{dm}{dt} = -\frac{\partial D/\partial \theta}{\partial D/\partial \omega} \tag{2.65e}$$

$$\frac{dn}{dt} = -\frac{\partial D/\partial \phi}{\partial D/\partial \omega} = 0 \tag{2.65f}$$

where the toroidal coordinate $\vec{r} = (r, \theta, \phi)$ is shown in Figure 2-2, and (k_r, m, n) are wave momenta, which are canonically conjugate to (r, θ, ϕ). Here, $n \equiv Rk_\phi$ is

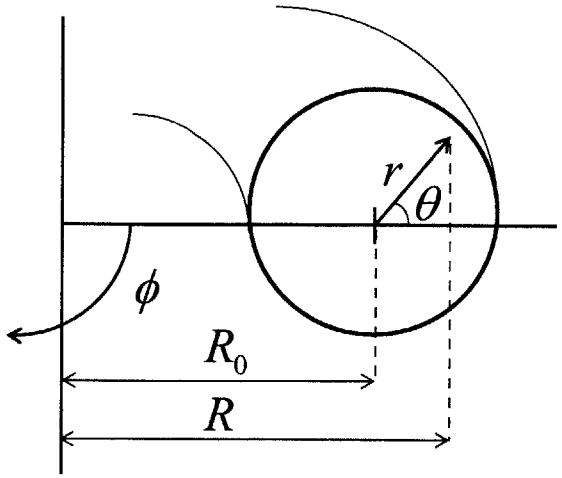

Figure 2-2: Toroidal geometry and variables (r, θ, ϕ) discussed in this section. Here, R_0 is the major radius of the tokamak.

the toroidal mode number, which is a conserved quantity due to toroidal symmetry $(\partial D/\partial \phi = 0)$. The poloidal mode number is $m \equiv r k_\theta$, which is not a conserved quantity in the toroidal geometry since $\partial D/\partial \theta \neq 0$.

In toroidal geometry, the parallel wavenumber to the magnetic field becomes

$$k_\parallel = \frac{\vec{k} \cdot \vec{B}}{|B|} = \frac{k_r B_r + (m/r) B_\theta + (n/R) B_\phi}{|B|}. \tag{2.66}$$

Therefore, the initial $k_\parallel$ at the launcher is no longer conserved in toroidal geometry due to the variations in both m and B_θ. The former is a toroidal effect, and the latter is a poloidal field effect. The radial component term is typically small as compared to the other two terms, however, its contribution may become important in elongated plasmas [11]. Thus, the accessibility condition derived in slab geometry (Section 1.1.3) does not hold in toroidal geometry, and ray-tracing is necessary to track the evolution of $k_\parallel$ in a toroidal plasma with poloidal inhomogeneity in order to study the propagation and absorption behavior of LH waves.

Figure 2-3 shows an example of the poloidal projection of the ray trajectory in Alcator C-Mod, which is calculated with the ray tracing code, GENRAY [41]. In this particular example, the ray power is lost only due to electron Landau damping, while the model allows the rays to propagate in the scrape-off layer. Note that GENRAY

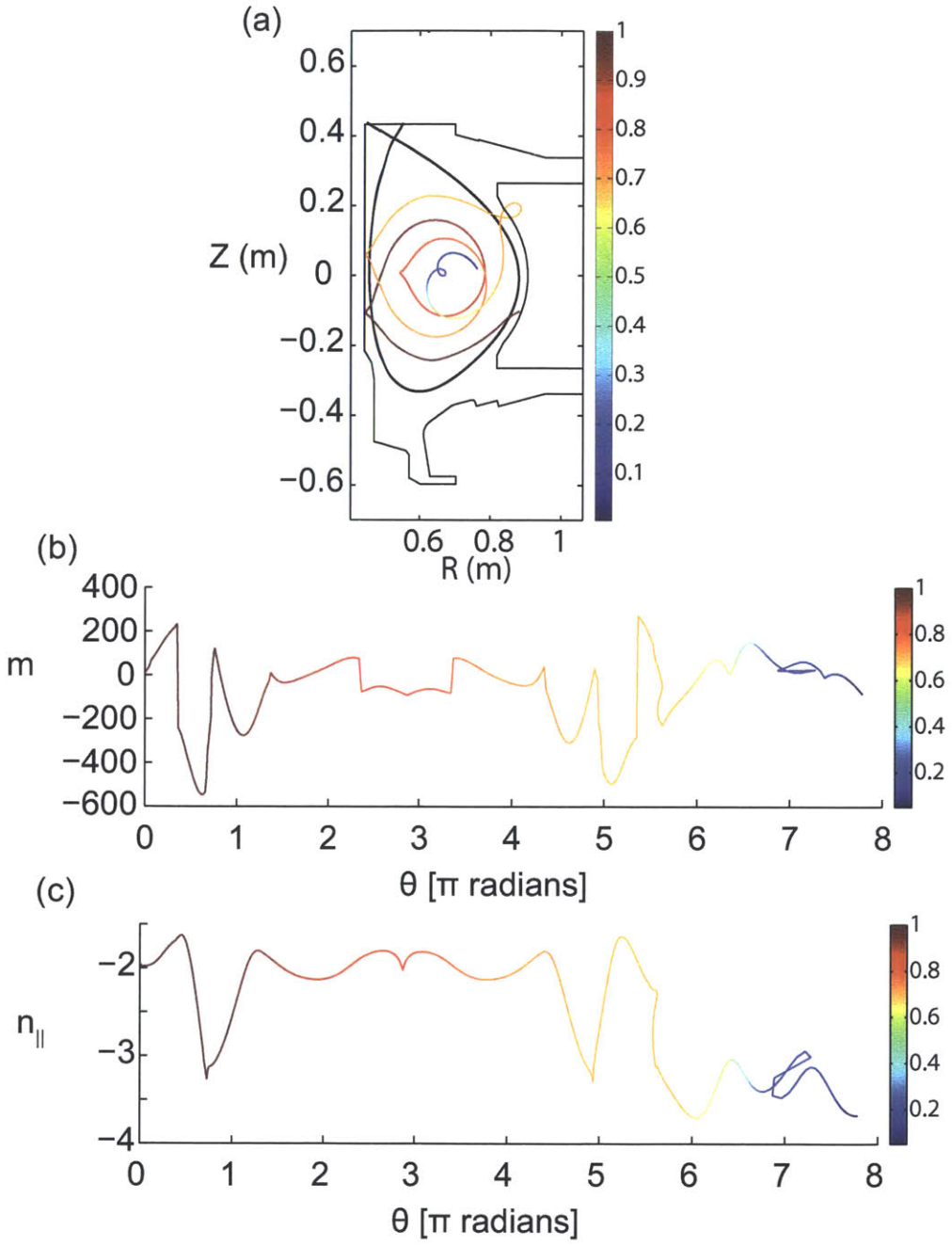

Figure 2-3: (a) Poloidal projection of the ray trajectory. Calculation is performed with the ray-tracing/Fokker-Planck code, GENRAY/CQL3D. Electron Landau damping is the only wave absorption mechanism. The color code is ray power that is normalized to 1 at the initial position. The thick black line shows the last closed flux surface. Plasma parameters are those of the Alcator C-Mod diverted L-mode plasma discharge with $B_{T0} = 5.4\,\mathrm{T}$, $\overline{n}_e = 1.35 \times 10^{20}\,\mathrm{m}^{-3}$, $T_{e0} \approx 1.5\,\mathrm{keV}$, and $I_p = 800\,\mathrm{kA}$. Also shown are the variation of (b) the poloidal mode number m and (c) $n_{\|}$.

is coupled to the Fokker-Planck code, CQL3D [42], in order to self-consistently solve the power absorption problem with the evolution of the electron distribution function. A 1D Fokker-Planck picture will be introduced in the next section. Figures 2-3 (b) and (c) show the variation of m and $n_{\parallel}$ as a function of θ. The toroidal m variation is somewhat reflected in the evolution of $n_{\parallel}$ [38]. This figure shows that the LH ray propagates toward the high-field side edge and across the plasma several times until the phase velocity of the ray significantly slows down (or until $n_{\parallel}$ is significantly up-shifted) at which point Landau damping becomes effective. Since the ray crosses the last closed flux surface multiple times before being fully absorbed, it is said that the ray propagates in a multi-pass regime and is therefore not absorbed in a single pass.

Care should be taken while using the ray-tracing code in multi-pass regimes because the WKB approximation ($|\nabla k|/k^2 \ll 1$) used in the ray-tracing approach can be questionable at the plasma edge where the fractional variation of the wave-number might not be small within a wavelength. Furthermore, up-shift mechanisms other than the torodicity effect may be also effective, which are not trivial to model using only the ray-tracing approach.

2.5 Lower Hybrid Current Drive Efficiency

2.5.1 2D velocity effects and asymmetric resisitivity

Asymmetric resistivity has been found to be an underlying dominant mechanism in determining current drive efficiency [39, 40]. This conclusion comes from the fact that the momentum destruction frequency ν is inversely proportional to the total velocity cubed $v^3 = (v_{\parallel}^2 + v_{\perp}^2)^{3/2}$ rather than to the parallel velocity cubed $v_{\parallel}^3$:

$$\nu = \nu_0 \frac{5 + Z_{eff}}{2} \frac{v_{te}^3}{(v_{\parallel}^2 + v_{\perp}^2)^{3/2}}. \tag{2.67}$$

To describe this effect, consider the displacement of a small number, δf, of electrons from region 1 to region 2 in velocity space due to energy input:

$$\Delta E = (E_2 - E_1)\delta f, \tag{2.68}$$

where E_i is the kinetic energy associated with velocity-space location i.

The displaced electrons lose their parallel momentum at a rate of ν_2, instead of a rate of ν_1. The parallel net current density is then

$$\mathfrak{J} = e\delta f \left[v_{\parallel 1}\exp\left(-\nu_1 t\right) - v_{\parallel 2}\exp\left(-\nu_2 t\right)\right], \tag{2.69}$$

where $v_\parallel$ is the velocity parallel to the magnetic field. The time-averaged current, J, over an interval Δt ($\gg 1/\nu_1, 1/\nu_2$) is given as follows:

$$J_\parallel \equiv \frac{1}{\Delta t}\int_0^{\Delta t} \mathfrak{J}(t)\,\mathrm{d}t \simeq \frac{e\delta f}{\Delta t}\left(\frac{v_{\parallel 1}}{\nu_1} - \frac{v_{\parallel 2}}{\nu_2}\right). \tag{2.70}$$

By defining $\Delta E/\Delta t$ as S_D, this equation leads to the current drive efficiency η:

$$\frac{J}{S_D} = -e\left(\frac{v_{\parallel 1}/\nu_1 - v_{\parallel 2}/\nu_2}{E_1 - E_2}\right) \xrightarrow[\vec{v}_2 \to \vec{v}_1]{} -e\frac{\hat{s}\cdot\nabla(v_\parallel/\nu)}{\hat{s}\cdot\nabla E}, \tag{2.71}$$

where $\hat{s}$ is the velocity displacement vector. When $\nu \propto v^{-3}$, and $\hat{s}$ is taken to be along the parallel direction for the LH wave case, η is shown to be

$$\eta = \frac{J_\parallel}{S_D} \propto \frac{\partial(v_\parallel v^3)/\partial v_\parallel}{\partial v^2/\partial v_\parallel} = \frac{(v_\parallel^2 + v_\perp^2)^{3/2}}{v_\parallel} + 3v_\parallel(v_\parallel^2 + v_\perp^2)^{1/2}, \tag{2.72}$$

where the first term is due to the momentum input and the second term is due to the energy input. In the limit $|v| \approx |v_\parallel|$, the second term is three times larger than the first term, indicating that asymmetric resisitivity is the dominant mechanism in RF current drive in general. By normalizing $J_\parallel$ and S_D to their thermal values, $\tilde{\eta}$ is given by

$$\tilde{\eta} = \frac{\hat{s}\cdot\nabla_s(wu^3)}{\hat{s}\cdot\nabla_s u^2}\frac{4}{5 + Z_{eff}}, \tag{2.73}$$

where $w \equiv v_{\parallel}/v_{te}$ and $u \equiv v/v_{te}$.

2.5.2 1D Fokker-Planck picture

Quasi-linear theory [43] can quantitatively describe the evolution of the electron distribution in the presence of RF waves. By taking into account the effect of quasi-linear diffusion in velocity space, this quasi-linear theory allows one to calculate a more precise expression for $\tilde{\eta}$. In particular, a competition between velocity space diffusion due to the presence of LH waves and collisional diffusion due to electron-electron and/or electron-ion collisions will determine the plateau formation in the electron distribution and, in turn, $\tilde{\eta}$. The evolution of the electron distribution function is studied with the following Fokker-Planck equation [39]:

$$\frac{\partial}{\partial t} f_{e0} = \frac{\partial}{\partial v_{\parallel}} D(v_{\parallel}) \frac{\partial}{\partial v_{\parallel}} f_{e0} + \left(\frac{\partial}{\partial t} f_{e0} \right)_{\text{coll.}} \tag{2.74}$$

where $D(v_{\parallel})$ is the RF quasi-linear diffusion coefficient, and the collision operator is written as

$$\left(\frac{\partial f_{e0}}{\partial t} \right)_{coll.} = \frac{2 + Z_{eff}}{2} \frac{\partial}{\partial v_{\parallel}} \left[\nu(v_{\parallel}) \left(v_e^2 \frac{\partial}{\partial v_{\parallel}} + v_{\parallel} \right) f_{e0} \right]. \tag{2.75}$$

To calculate $D(v_{\parallel})$ as a function of the applied wave electric field, consider the 1D Vlasov equation

$$\frac{\partial}{\partial t} f_e + v_{\parallel} \frac{\partial f_e}{\partial t} - \frac{e}{m_e} E_{\parallel} \frac{\partial}{\partial v_{\parallel}} f_e = 0, \tag{2.76}$$

where the electron distribution function $f_e(v_{\parallel}, z, t)$ is the sum of the spatially averaged function $f_{e0}(v_{\parallel}, t)$ and the perturbed function $f_{e1}(v_{\parallel}, z, t)$:

$$f_e(v_{\parallel}, z, t) = f_{e0}(v_{\parallel}, t) + f_{e1}(v_{\parallel}, z, t). \tag{2.77}$$

Here, it is assumed that $f_{e1} \ll f_{e0}$. The spatially averaged distribution function is defined as follows:

$$f_{e0}(v_{\parallel}, t) = \lim_{L \to \infty} \frac{1}{L} \int_{-L}^{L} \mathrm{d}z \, f_e(v_{\parallel}, z, t) \equiv \langle f_e \rangle. \tag{2.78}$$

It is further assumed that there is no background electric field and only the RF-induced electric field exists: $E_\parallel = E_1(z,t)$.

To solve for f_{e1} and $D(v_\parallel)$ as a function of E_1, Equation 2.76 can be spatially averaged as follows [44, Chap. 10.2]:

$$\frac{\partial}{\partial t} f_{e0} = \frac{e}{m_e} \frac{\partial}{\partial v_\parallel} \langle E_1 f_{e1} \rangle. \tag{2.79}$$

Note that Equation 2.79 shows that the time derivative of the zeroth order distribution function f_{e0} is expressed in terms of the second order quantity $\langle E_1 f_{e1} \rangle$. Rewriting Equation 2.76 using $f_e = f_{e0} + f_{e1}$ yields:

$$\frac{\partial f_{e1}}{\partial t} + v_\parallel \frac{\partial}{\partial z} f_{e1} - \frac{e}{m_e} E_1 \frac{\partial}{\partial v_\parallel} f_{e0} = \frac{e}{m_e} \frac{\partial}{\partial v_\parallel} \left(E_1 f_{e1} - \langle E_1 f_{e1} \rangle \right). \tag{2.80}$$

This equation can be used to solve for f_{e1} by neglecting the second-order terms on the right hand side. When taking a Fourier mode of the form $f_{e1} \sim \exp(ik_\parallel z - i\omega t)$,

$$f_{e1} = \frac{(ie/m_e) E_1}{\omega - k_\parallel v_\parallel} \frac{\partial f_{e0}}{\partial v_\parallel}. \tag{2.81}$$

Finally, using Equation 2.81 in Equation 2.79 yields $D(v_\parallel)$:

$$D(v_\parallel) \equiv \left\langle \frac{ie^2}{m_e^2} \frac{E_1^2(z,t)}{\omega - k_\parallel v_\parallel} \right\rangle \tag{2.82}$$

and

$$\frac{\partial}{\partial t} f_{e0} = \frac{\partial}{\partial v_\parallel} D(v_\parallel) \frac{\partial f_{e0}}{\partial v_\parallel}. \tag{2.83}$$

Note that $D(v_\parallel)$ is second-order in the perturbed electric field E_1.

A steady state solution f_{e0} of Equation 2.74 can be found with the assumption that f_{e0} is Maxwellian outside the RF interaction region and is time-independent ($\partial f_{e0}/\partial t = 0$):

$$f_{e0} = f_{e0}(v_\parallel) = \frac{1}{2\sqrt{\pi} v_{te}} \exp(-v_\parallel^2 / 2v_{te}^2) \tag{2.84}$$

Integrating Equation 2.74 over $v_\parallel$ and rearranging the terms to obtain $\partial f_{e0}/\partial v_\parallel$ yields:

$$\frac{\partial f_{e0}}{\partial v_\parallel} = -\frac{v_\parallel f_{e0}/v_e^2}{1+\tilde{D}(v_\parallel)}, \tag{2.85}$$

where $\tilde{D}(v_\parallel) = D(v_\parallel)/D_{coll}$ is the ratio of the RF quasi-linear diffusion to the collisional diffusion

$$D_{coll} \equiv \nu(v_\parallel) v_{te}^2 (2 + Z_{eff})/2. \tag{2.86}$$

When $\tilde{D}(v_\parallel) \gg 1$, the RF diffusion will be much greater than the collisional diffusion, and a plateau will form on the distribution f_{e0} in the velocity space between v_1 and v_2 where resonant particles reside because $\partial f_{e0}/\partial v_\parallel \approx 0$ in that range. Integrating Equation 2.85 yields

$$f_{e0}(v_\parallel) = \sqrt{\frac{1}{2\pi}}\frac{1}{v_{te}} \exp\left[-\int \frac{(v_\parallel/v_e)\, d(v_\parallel/v_e)}{1+\tilde{D}(v_\parallel)}\right], \tag{2.87}$$

where $f_{e0}(v_\parallel)$ has been normalized such that $\int_{-\infty}^{\infty} f_{e0}(v_\parallel)\, dv_\parallel = 1$.

Now, $\tilde{\eta} = \tilde{J}/\tilde{S_D}$ can be calculated using Equation 2.87 with the assumption that the LH wave spectrum is uniformly distributed such that

$$\begin{aligned} &\tilde{D}(v_\parallel) \gg 1 \qquad \text{for } v_1 \le v_\parallel \le v_2 \\ &\tilde{D}(v_\parallel) = 0 \qquad \text{for } v_\parallel < v_1 \text{ and } v_\parallel > v_2 \end{aligned} \tag{2.88}$$

and that $f_{e0}(v_\parallel) \simeq f_{e0}(v_1) =$ constant for $v_1 \le v_\parallel \le v_2$. The resulting RF current density $J_\parallel$ is

$$\begin{aligned} J_\parallel &= n_e e \int_{-\infty}^{\infty} f_{e0}(v_\parallel) v_\parallel \, \mathrm{d}v_\parallel \\ &= \frac{n_e e v_{te}}{\sqrt{2\pi}} \exp\left(-\frac{v_1^2}{2v_{te}^2}\right)\left[\left(\frac{v_2}{\sqrt{2}v_{te}}\right)^2 - \left(\frac{v_1}{\sqrt{2}v_{te}}\right)^2\right]. \end{aligned} \tag{2.89}$$

The power dissipated per unit volume S_D is given by

$$\begin{aligned} S_D &= \int_{-\infty}^{\infty} \frac{1}{2} n_e m_e v_\parallel^2 \left(\frac{\partial f_{e0}}{\partial t} \right)_{RF} \mathrm{d}v_\parallel \\ &= \frac{n_e \nu_0 T_e}{\sqrt{2\pi}} \left(\frac{2 + Z_{eff}}{2} \right) \exp\left(\frac{v_1^2}{2v_{te}^2} \right) \log\left(\frac{v_2}{v_1} \right). \end{aligned} \tag{2.90}$$

Finally, the normalized $\tilde{\eta}$ is then given by

$$\tilde{\eta} = \frac{\tilde{J}}{\tilde{S}_D} = \left(\frac{2}{2 + Z_{eff}} \right) \frac{\left(\frac{v_2}{\sqrt{2}v_e} \right)^2 - \left(\frac{v_1}{\sqrt{2}v_e} \right)^2}{\log\left(v_2 / v_1 \right)}. \tag{2.91}$$

The current drive efficiency decreases with the increase in Z_{eff}. Note also that $\tilde{\eta}$ increases with the higher phase velocity v_2 of the RF wave, which is limited by the accessibility condition. v_1 is set by the minimum phase velocity for the quasi-linear electron Landau damping, i.e., $v_1/(\sqrt{2}v_{te}) \approx 2.3$.

It is interesting that the contribution of the plateau height is canceled out and only the spectral width of the plateau remains in determining $\tilde{\eta}$. Given that the phase velocity of the launched LH waves with $n_\parallel \approx 2$ is about 10 times faster than the electron thermal velocity in the plasma with $T_e \approx 2\,\mathrm{keV}$, several mechanisms have been proposed to explain this extended plateau formation in the electron distribution function because there are not enough electrons to explain the experimentally observed driven current only by considering the population of the electrons in the velocity space region $v_{ph}/v_{te} \approx 10$. In a tokamak geometry, the toroidal and poloidal $n_\parallel$ up-shift presented in Section 2.4 is the leading mechanism that can lower the phase velocity of the injected LH waves and thus fill the spectral gap [45]. In addition, full-wave effects [46, 47] (e.g., diffraction, refraction, and focusing) and non-linear effects (e.g., scattering by turbulence [48] and ion sound parametric decay instabilities [49, 50]) have been studied as well to understand this mechanism.

2.5.3 Engineering efficiency

To calculate the total driven plasma current per applied total LH power in a cylindrical plasma, one should consider the geometrical effect. Providing that all of the injected LH power is dissipated in an annular plasma volume ($\triangle V \cong 2\pi R \triangle A$), the driven current I in the area $\triangle A$ associated with this volume is $I \simeq J_{\|} \triangle A$, and the power dissipated within this volume is $P_{RF} \simeq \triangle A 2\pi R S_D$. By applying the ratio of these two expressions, one finds that

$$\frac{IR}{P_{RF}} = \frac{1}{2\pi} \frac{J_{\|}}{S_D} = \frac{e}{2\pi m_e v_{te} \nu_0} \frac{\tilde{J}}{\tilde{S}_D}. \tag{2.92}$$

The engineering current drive efficiency is often defined as

$$\frac{n_e\,(10^{14}\mathrm{cm}^{-3})\, I\,(\mathrm{MA})\, R\,(\mathrm{m})}{P_{RF}\,(\mathrm{MW})} = \frac{T_e\,(10\,\mathrm{keV})}{50} \frac{\tilde{J}}{\tilde{S}_D}. \tag{2.93}$$

Note that $n_e IR/P$ is a constant value with the constant T_e, R, and $n_{\|}$. Lower hybrid current drive experiments in Alcator C confirm [51] this scaling up to $\overline{n}_e \approx 1.0 \times 10^{20}\,\mathrm{m}^{-3}$, which is also found to be consistent with the ray-tracing/1D Fokker-Planck simulations [45] that include the 2D velocity space effects discussed in Section 2.5.1. This expression can be rearranged in the following form to calculate the driven current:

$$I_{LH}(\mathrm{MA}) \simeq 0.02 \frac{\tilde{J}}{\tilde{S}_D} \frac{P_{RF}\,(\mathrm{MW})\, T_e\,(10\ \mathrm{keV})}{n_e\,(10^{20}\,\mathrm{m}^{-3})\,\mathrm{R\,(m)}} \tag{2.94}$$

I_{LH} is inversely proportional to the major radius R. By applying Alcator C-Mod parameters with $n_{\|} = 2$, $P_{RF} = 1\,\mathrm{MW}$, $n_e = 10^{20}\,\mathrm{m}^{-3}$, $T_e = 2\,\mathrm{keV}$, and $R = 0.67\,\mathrm{m}$, one finds that the normalized efficiency of $\tilde{\eta} \approx 63$ from Equation 2.91 and the corresponding driven current of $I_{LH} \approx 376\,\mathrm{kA}$ from Equation 2.94. Nevertheless, one should be careful while interpreting this value because no variations in $n_{\|}$ are considered. Power reduction mechanisms, such as collisional absorption and ionization, can lower the effective LH power as well.

2.6 Loss of Current Drive Efficiency

In low density Alcator C-Mod plasmas with up to $\overline{n}_e \lesssim 7 \times 10^{19}\,\mathrm{m}^{-3}$, the engineering efficiency is found to be $\eta \equiv n_e IR/P \approx 2.5 \pm 0.2 \times 10^{19}\,\mathrm{A/m^2/W}$ [22], which is consistent with the value that is calculated based on the ray tracing/Fokker-Planck code GENRAY-CQL3D. The loop voltage is observed to decrease with increasing LH power. Plasma discharges with full non-inductive LHCD have been also demonstrated with the expected current drive efficiency [52]. EFIT reconstructions, constrained by internal magnetic field measurements with a motional Stark effect diagnostic, indicate a weak shear reversal with $q(0) \sim 2$, demonstrating the current profile modification using LHCD at reactor-relevant plasma densities.

However, when $\overline{n}_e$ increases above $1.0 \times 10^{20}\,\mathrm{m}^{-3}$, all experimental signatures of current drive effects disappear [10], although the accessibility is not lost and the density ($\omega_0/\omega_{lh}(0) \approx 3$) remains above the classical ion cyclotron PDI limit ($\omega_0/\omega_{lh}(0) \approx 2$), as shown in Figure 2-1. No change in the loop voltage is seen, and non-thermal electron cyclotron emission generated by fast electrons vanishes. In addition, non-thermal hard X-ray emission rapidly decreases compared with the emission predicted in GENRAY-CQL3D simulations. No heating effects are reported, either. LH power modulation experiments [52] show that negligible core heating occurs for $\overline{n}_e > 1.0 \times 10^{20}\,\mathrm{m}^{-3}$, suggesting that most of the LH power is deposited near the plasma edge.

Extensive modeling work [7] on Alcator C-Mod plasmas has identified two possible loss mechanisms by including the scrape-off layer (SOL) in the simulation domain. The first mechanism is collisional absorption [10] at the plasma edge. The LH rays are weakly damped on a single pass due to the relatively low plasma temperature and have a limited radial penetration in high density plasmas. Consequently, simulations with GENRAY-CQL3D indicate that the rays are susceptible to electron-ion collisional absorption before being fully Landau damped. The simulations that include collisional loss show that up to 50% of the launched power can be lost through collisions, while the power loss is found to be sensitive to

the SOL parameters. This study also reveals that the inclusion of electron-neutral collisions would intensify the collisional power loss. One important remaining question is the validity of the WKB approximation when the rays make reflections at the plasma edge.

The second mechanism is full-wave effects [11] as studied with the full-wave/Fokker-Planck code LHEAF/VERD. This approach can account for the effects that are not properly treated by the ray-tracing approach, such as diffraction, focusing, and interference. The wavelet analysis on the calculated electric field shows that strong up-shift of the $n_{\parallel}$ spectrum occurs after the first reflection at the inner wall region, resulting in Landau damping with reduced current drive efficiency. This wave propagation is clearly different from that predicted in GENRAY/CQL3D. The responsible up-shift mechanism is thought to be due to the change in $n_{\parallel}$ after reflection from a layer that is not parallel to the poloidal magnetic field.

The LHEAF/VERD calculations also show that the collisional power loss is less than 10% of the launched power as compared to the GENRAY/CQL3D results because the energy propagation path is significantly shortened in the full-wave picture. Nonetheless, different SOL models are used between LHEAF/VERD and GENRAY/CQL3D simulations; moreover, these models have different Fokker-Planck solvers. More detailed model comparisons of different results are necessary to better characterize the different SOL models that are used in the two codes.

Figure 2-4 compares two different LH power deposition profiles calculated by GENRAY/CQL3D and LHEAF/VERD for the same high-density ($\overline{n}_e = 1.3 \times 10^{20}\,\mathrm{m}^{-3}$) L-mode discharge. In both cases, most of the power is deposited in the radial region $r/a > 0.8$, although the GENRAY/CQL3D model predicts that most of the power is deposited outside the last closed flux surface (LCFS) due to collisional damping, whereas the LHEAF/VERD model predicts that the power is deposited inside the LCFS due to Landau damping.

Figure 2-5 compares the experimentally measured hard X-ray count rates and the numerically calculated hard X-ray count rates based on the GENRAY/CQL3D and

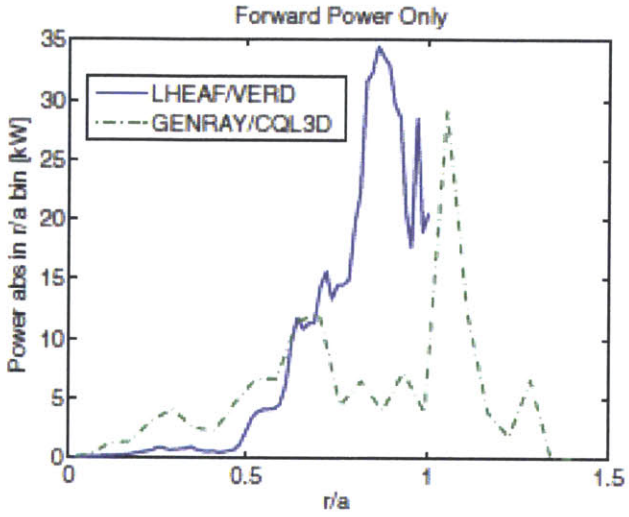

Figure 2-4: Comparison of LH power deposition profiles calculated by GENRAY/CQL3D (green dashed-dotted line) and by LHEAF/VERD (blue) for a diverted Alcator C-Mod L-mode plasma at $\overline{n}_e = 1.3 \times 10^{20}\,\mathrm{m}^{-3}$. Figure is reproduced from [7].

LHEAF/VERD calculations. Compared to the $1/n_e$ dependence predicted by the GENRAY/CQL3D results without SOL, the measured hard X-ray count rates show an exponential decrease as a function of $\overline{n}_e$. Both models with SOL can reproduce the reduction in hard X-ray count rates in a wide range of densities, and this behavior is consistent with the experimental trend. However, there remains a discrepancy in the high density plasmas above $\overline{n}_e \gtrsim 1.2 \times 10^{20}\,\mathrm{m}^{-3}$, which suggests that additional loss mechanisms might play a role.

The anomalous loss of LHCD efficiency has been also observed on previously operated tokamaks, and it was reported that the maximum density at which lower hybrid current drive was observed correlates with the source frequency [33, 53]. Figure 2-6 shows the maximum density where the wave-electron interactions occur. The crosses indicate the density limit of electron heating, and the circles indicate the density limit of the current drive. Note that the density limit of the LH heating appears to be higher than the density limit of the LH current drive. A number of mechanisms have been listed [53] as possible causes: weak single pass absorption of LH waves, focusing effects, scattering of LH waves by turbulence, wave instabilities,

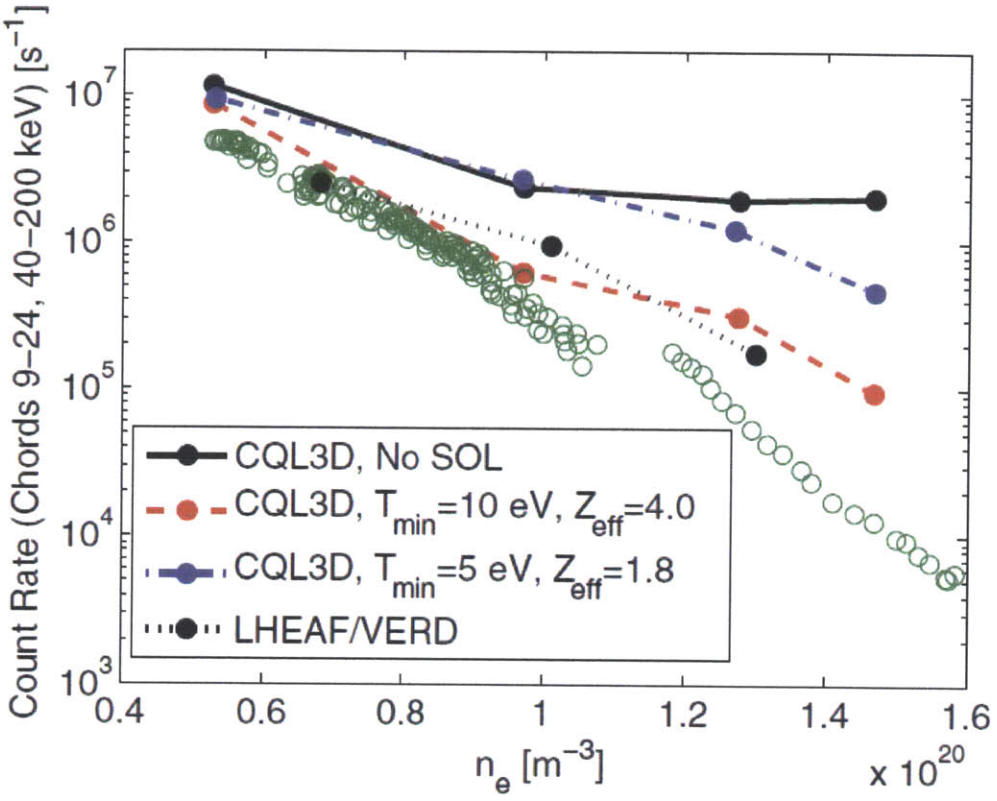

Figure 2-5: Experimental non-thermal hard X-ray count rates (green circles) as a function of the line-averaged density. Overplotted are simulated non-thermal hard X-ray count rates with no collisional losses (solid black line) and two different finite collisional loss (blue and red dashed line) from the ray-tracing/Fokker-Plank code GENRAY/CQL3D. Full-wave results from the full-wave/Fokker-Planck code LHEAF/VERD are also shown (dotted black line). Figure is reproduced from [7].

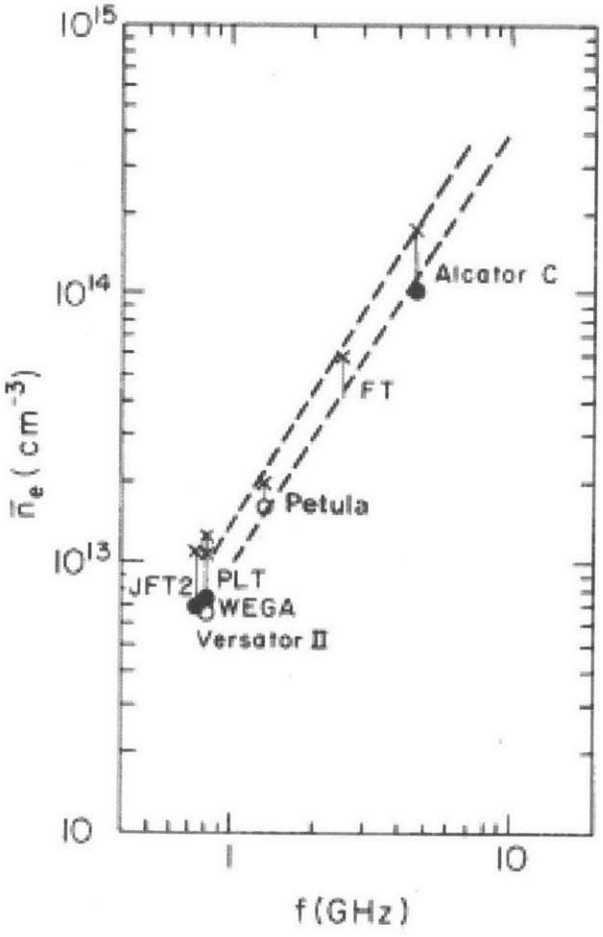

Figure 2-6: Frequency scaling of the density limit of the LH current drive (circles) and of the LH heating (crosses). Figure is reproduced from [33].

or the onset of ion absorption. Alcator C results indicate that LH current drive effects are observed up to $\overline{n}_e \approx 1.0 \times 10^{20}\,\mathrm{m}^{-3}$ at a frequency of 4.6 GHz with the RF power of 1 MW. It was speculated [33] that the Alcator C result is due to the limited source power. While this scaling appears to hold for the Alcator C-Mod tokamak, this scaling might not hold for the FTU tokamak with a source frequency of 8 GHz. It was reported [54, 55, 56] that the current drive effects are seen only up to the $\overline{n}_e \approx 1.0 \sim 1.3 \times 10^{20}\,\mathrm{m}^{-3}$ in their so-called standard regime plasmas.

In addition to FTU, existing limited and diverted tokamaks have also reported weaker-than-expected LH effects. A summary of the recent multi-machine assessment of this phenomenon can be found in Tuccillo [6]. Enhanced non-linear scattering due to ion sound PDI [34, 49, 57, 58] that leads to the excessive spectral broadening has been hypothesized in FTU [56] and JET [59], and has been supported by modeling [50, 56, 59, 60]. At the same time, it was pointed out [6] that the concurrent contributions from both collisional loss [61] and scattering by density fluctuations [62] cannot be excluded due to the limited accuracy of the data. Meanwhile, the prompt LH power loss near a LH launcher due to fast electron generation [63] might also contribute to the loss of current drive efficiency. Based on the prediction that higher temperature can diminish the LH spectral broadening due to ion sound PDI, FTU [56] demonstrated effective LH penetration on ITER-relevant high-density plasmas up to $\overline{n}_e \approx 2.0 \times 10^{20}\,\mathrm{m}^{-3}$ by raising the edge temperature in their so-called new regime discharges. The change in edge temperature at r/a $\sim$0.8 is reported to be from $\sim$ 100 eV to $\sim$ 200 eV. The density profile is very peaked with the central density $n_e \approx 4 \times 10^{20}\,\mathrm{m}^{-3}$ and central temperature $T_e \approx 1\,\mathrm{keV}$. It is not clear whether the LH waves have undergone multiple passes as the accessibility condition may have limited the radial penetration in such a high density plasma. Since the important parameter appears to be the edge temperature, similar attempts have been made in Alcator C-Mod I-mode plasmas that exhibit a higher edge temperature than L-mode plasmas; however, no such drastic improvement was reported [64].

In summary, Alcator C-Mod results suggest that multiple parasitic loss mechanisms play a role to degrade the LHCD performance at reactor-relevant

densities, if single-pass absorption is not guaranteed. Meanwhile, the leading mechanism of the loss of LHCD efficiency is not well agreed upon in the LH community. One of the active research areas in the LH community is to identify the presence of additional and excessive spectral broadening mechanisms and their significance, in addition to the toroidicity effect. In this thesis, non-linear effects, such as wave scattering by turbulence, ion sound PDI, and ion cyclotron PDI will be experimentally examined in the following chapters.

Chapter 3

Microwave Backscattering Experiments

3.1 Introduction

The direct detection of LH waves in the plasma is desirable to better understand the propagation and absorption behavior of LH waves. In particular, it is important to measure the LH wave field in the scrape-off layer (SOL) where a significant amount of LH power may be deposited in high density plasmas, as indicated by the several power loss mechanisms that are particularly exacerbated at the plasma edge.

To detect LH waves within plasmas, earlier experiments adopted small angle laser- [65, 66, 67] or microwave- [68, 69, 70, 71] scattering techniques. However, these techniques have limited spatial resolution due to small scattering angle [12], which makes it difficult to probe only the plasma periphery. Moreover, material probes cannot be reliably used to probe Alcator C-Mod edge plasmas due to the relatively high SOL density and temperature.

To overcome this limitation, microwave backscattering experiments have been performed on the Alcator C-Mod tokamak using ordinary-mode (O-mode) reflectometry. This technique [13] can measure the radially localized LH wave field in the SOL. The interaction between the launched O-mode wave and LH wave occurs at a scattering layer where the wave-matching condition is satisfied among

the three waves: the incident O-mode wave (60 GHz), the LH wave (4.6 GHz), and the backscattered O-mode wave with a finite frequency shift (60±4.6 GHz). The scattering layer is different from the cut-off layer in conventional reflectometry where the incident O-mode wave is reflected back to the plasma edge. Previous reports [72, 73] on the detection of the RF waves in the ion cyclotron range of frequencies relies on the modulation of the cut-off layer due to the relatively long wavelength of the RF waves of interest. However, in our case, resonant Bragg scattering is the responsible mechanism because the radial wavelength of the LH wave is shorter than that of the incident O-mode wave [74, 75, 76, 77, 78].

In addition to the radial localization of the LH wave detection, the finite frequency-shift of the resulting O-mode signals allow us to distinguish the backscattered O-mode signals (at 60±4.6 GHz) from the reflected O-mode signals (at 60 GHz). Furthermore, the use of a microwave source enables us to measure the spectral amplitude and width of the backscattered signals with good spatial and temporal resolution.

The purpose of this chapter is to use the microwave backscattering diagnostic [13, 79] to study the propagation of LH waves by examining the response of the backscattered signals under different plasma conditions. To understand our observations, we also present an 1D scattering model based on mode-mode coupling interactions in the presence of a linear density gradient.

The organization of this chapter is as follows. In Section 3.2, the 1D backscattering model is discussed in terms of three-wave coupling. In Section 3.3 the experimental set-up is described. In Section 3.4, experimental observations in terms of the spectral amplitude and width of scattered signals are presented and discussed. Section 3.5 discusses the relation of the observed signals to previously studied LH power loss mechanisms. Section 3.6 is a summary of this chapter.

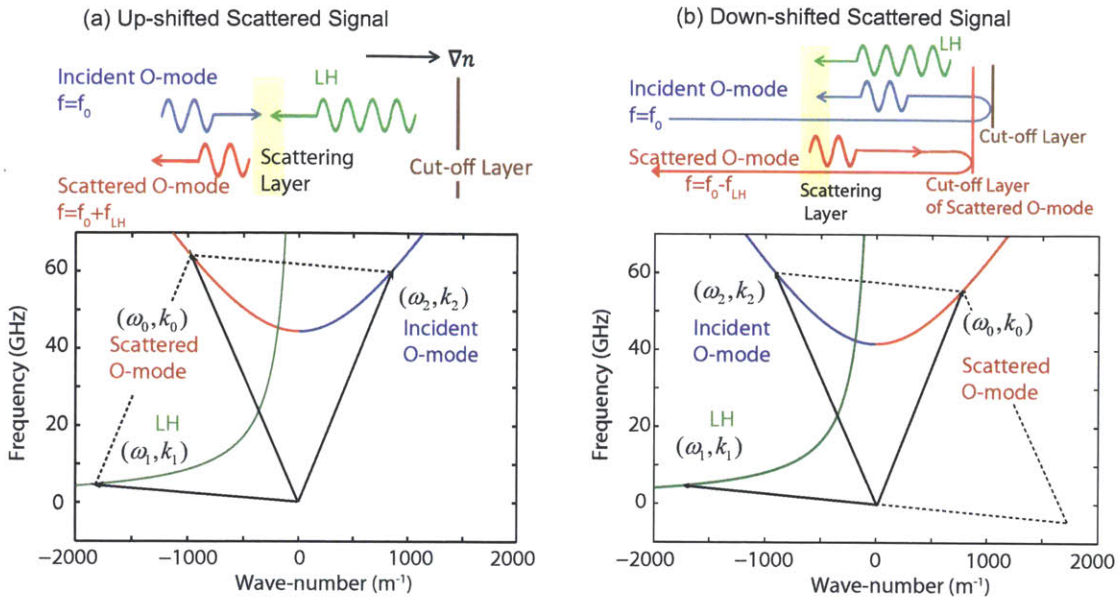

Figure 3-1: Parallelogram constructions show the frequency and wave-number matching for three waves: incident O-mode wave at 60 GHz (blue), LH wave at 4.6 GHz (green), and scattered O-mode wave (red). Depending on the propagation direction of the incident O-mode wave, the scattered O-mode wave can be either (a) frequency up-shifted or (b) frequency down-shifted. The $n_{||}$ of LH wave is set to 2.

3.2 Physical Model

3.2.1 Wave matching condition

To describe the backscattering of the incident O-mode wave by the LH wave, a 1D plasma slab geometry is considered with a density gradient along the x-axis and with a background magnetic field along the z-axis ($\vec{B}_0 = B_0\hat{z}$). The incident O-mode wave propagates in the $\hat{x}$-direction (towards the cut-off layer) and in the $-\hat{x}$ direction (towards the plasma edge) after a reflection at a cut-off layer. Given that the LH wave is a backward wave, its perpendicular phase velocity (to $\vec{B}_0$) is in the $-\hat{x}$ direction. The incident O-mode wave, propagating along the x-axis, can be backscattered by the LH wave at a location x' where the following resonant matching condition is satisfied

$$\vec{k}_0(x') = \pm\vec{k}_1(x') + \vec{k}_2(x') \tag{3.1a}$$

$$\omega_0 = \pm\omega_1 + \omega_2 \tag{3.1b}$$

where $\vec{k}_0$, $\vec{k}_1$, and $\vec{k}_2$ are the perpendicular wave-vectors of the backscattered O-mode wave, LH wave, and incident O-mode wave, respectively; and ω_0, ω_1, and ω_2 are the respective frequencies of the backscattered O-mode wave, LH wave, and incident O-mode wave. Note that the parallel component of the LH wave-number produces a negligible effect on the parallel wave-number matching because the frequency of the LH wave is much lower than the frequency of the O-mode waves in our case.

Figure 3-1 shows the dispersion curves of the three waves in the frequency and wave-number space based on the dispersion relation of the O-mode wave

$$c^2k_j^2 = \omega_j^2 - \omega_{pe}^2; \quad j = 0, 2 \tag{3.2}$$

and the electrostatic dispersion relation of the LH wave relevant at the plasma edge

$$k_1 \approx -k_{\|}\frac{\omega_{pe}}{\omega_1}, \tag{3.3}$$

where ω_{pe} is the electron plasma frequency. While obeying the dispersion relation of each wave, two parallelograms can be constructed, which can satisfy the resonant wave-matching condition. The first scattering process occurs when the incident O-mode wave propagates towards the cut-off layer. In this case, the frequency up-shifted backscattered O-mode wave can satisfy the resonant condition ($\vec{k}_0 = -\vec{k}_1 + \vec{k}_2$, $\omega_0 = -\omega_1 + \omega_2$), as shown in Figure 3-1 (a). The scattered O-mode wave propagates towards the plasma edge directly. Note that the forward-scattering does not occur because this cannot satisfy the wave matching condition. The second scattering process occurs when the incident O-mode wave propagates back towards the plasma edge, after the reflection at the cutoff layer. In this case, the frequency down-shifted scattered O-mode wave can satisfy the resonant condition

($\vec{k}_0 = \vec{k}_1 - \vec{k}_2$, $\omega_0 = \omega_1 - \omega_2$), as shown in Figure 3-1 (b). The resultant backscattered O-mode wave propagates towards its own cut-off layer before traveling to the plasma edge.

3.2.2 1-D scattering power

The scattered power can be evaluated in the context of three wave coupling [80] in the 1-D space. Of the two possible scattering cases, the case when the backscattered wave can directly travel towards the plasma edge (Figure 3-1 (a)) is only considered because the other case can be studied in a similar manner. In the Wentzel–Kramers–Brillouin limit, the coupled mode equations in 1D inhomogeneous plasma can be expressed as follows [80]:

$$[\frac{\partial}{\partial t} + \vec{v}_{g0} \cdot \nabla]a_0 = K a_1 a_2 \exp \int^x -i\kappa(x')\,\mathrm{d}x', \tag{3.4a}$$

$$[\frac{\partial}{\partial t} + \vec{v}_{g1} \cdot \nabla]a_1 = -K^* a_0 a_2^* \exp \int^x i\kappa(x')\,\mathrm{d}x', \tag{3.4b}$$

$$[\frac{\partial}{\partial t} + \vec{v}_{g2} \cdot \nabla]a_2 = -K^* a_0 a_1^* \exp \int^x i\kappa(x')\,\mathrm{d}x', \tag{3.4c}$$

where $a_0(x,t)$, $a_1(x,t)$ and $a_2(x,t)$ are the slowly varying mode amplitudes of the scattered wave, LH wave, and incident wave; $v_{g0}(x)$, $v_{g1}(x)$, and $v_{g2}(x)$ are the group velocities of the scattered wave, LH wave, and incident wave; and $K(x)$ is a coupling coefficient. The phase mismatch at a given location is represented by $\kappa(x) = \vec{k}_0(x) - \vec{k}_1(x) - \vec{k}_2(x)$, and, without loss of generality, the phase mismatch is assumed to be zero at $x = 0$, where the resonant matching condition holds. At this location, by constructing the three coupled equations as shown in Appendix A, $K(0)$ can be identified as follows:

$$K(0) \simeq \omega_{pe}\sqrt{\frac{\omega_1}{\omega_0\omega_2}}\frac{|k_1|}{\sqrt{n_0 m_e}}\frac{1}{2\sqrt{2 + 2\omega_{pe}^2/\omega_{ce}^2}}. \tag{3.5}$$

In calculating this, the O-mode dispersion relation for the scattered mode with finite $k_\parallel$ is approximated to be $n_{0,\perp}^2 \approx P(1 - n_{0,\parallel}^2/S) \approx P$, where $S \approx 1 - \omega_{pe}^2/(\omega_0^2 - \omega_{ce}^2)$

and $P \approx 1 - \omega_{pe}^2/\omega_0^2$ in Stix notation. If $n_{1,\parallel} \approx 2$, then $n_{0,\parallel} \approx 0.14$ from the parallel matching condition with the assumption that the incident mode is purely an O-mode. Then the latter approximation is justified since $n_{0,\parallel}^2/S \approx 2\,\%$ with $n_e \approx 2 \times 10^{19}\, m^{-3}$ where scattering occurs. Neglected are the terms which arise from the fact that with finite $n_\parallel$ the O-mode polarization develops small components perpendicular to the background magnetic field. With $n_{0,\parallel} \approx 0.14$, $|\vec{E}_{0,\perp}|/|\vec{E}_{0,\parallel}| \approx 10\,\%$. Thus, the contributions of $|\vec{E}_{0,\perp}|$ to the coupling coefficient, as well as terms of order $\omega_1/\omega_{0,2}$, have been neglected.

In addition, the magnitude of $\vec{E}_j$, $\vec{H}_j$, and $\vec{v}_j$ are normalized such that $4\langle W_{j,norm}\rangle = \omega_j$, where $\langle W_{j,norm}\rangle$ is the normalized time-averaged energy density:

$$4\langle W_{j,norm}\rangle = \epsilon_0|\vec{E}_j|^2 + \mu_0|\vec{H}_j|^2 + m_i n_0|\vec{v}_{i,j}|^2 + m_e n_0|\vec{v}_{e,j}|^2. \tag{3.6}$$

Here, n_0 is the background density, and m_j and v_j are the mass and velocity of species j. Then the action density of mode j with the mode amplitude a_j is given by $\langle W_j\rangle/\omega_j = |a_j|^2/4$.

To analytically treat these coupled mode equations, the following three assumptions are made. First, the LH wave is unaffected by the nonlinear interaction and its mode amplitude is constant in the whole domain. Second, the mode amplitudes for all three waves have a steady state time dependence, $\partial/\partial t = 0$. Finally, the phase mismatch is linear in space $\kappa(x) = \frac{\mathrm{d}\kappa}{\mathrm{d}x}x = \kappa' x$, and its scale length is longer than the wavelengths of each linear mode, and shorter than the scale length of inhomogeneity. Then, it is justified [80] that both the coupling coefficient and the group velocities are constant ($K = K(0)$, $\vec{v}_{gj} = \vec{v}_{gj}(0)$) within the region where strong nonlinear interaction occurs. These approximations reduce Equations 3.4 (a)-(c) from a nonlinear to a linear problem between the incident O-mode wave and the scattered O-mode wave:

$$-v_{g0}\frac{\mathrm{d}}{\mathrm{d}x}a_0 = K a_1 a_2 \exp(-i\kappa' x^2/2), \tag{3.7a}$$

$$v_{g2}\frac{\mathrm{d}}{\mathrm{d}x}a_2 = -K^* a_1^* a_0 \exp(i\kappa' x^2/2). \tag{3.7b}$$

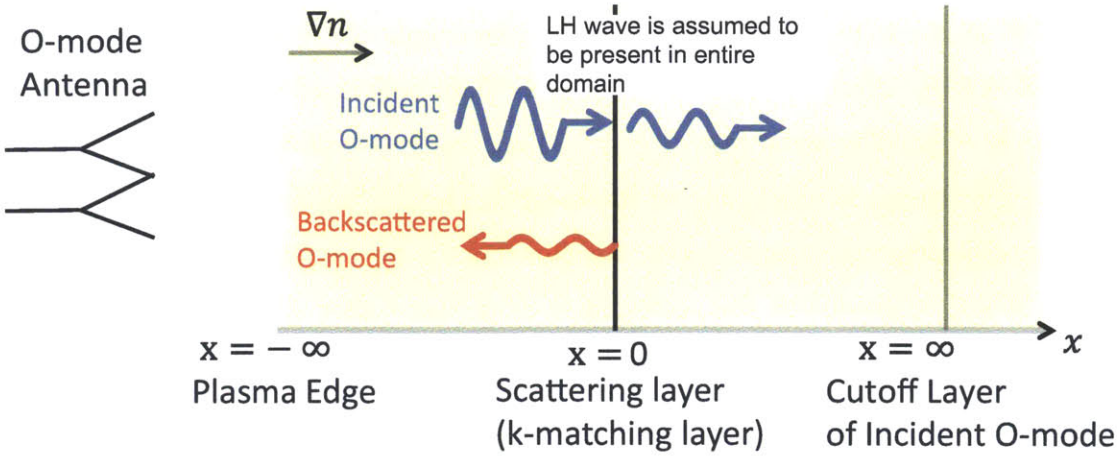

Figure 3-2: 1D description of backscattering problem. While the LH wave is assumed to fill the entire 1D space, the scattering occurs at a radially localized scattering layer where the matching condition is satisfied.

This pair of first-order ordinary differential equations has been used to describe the mode coupling among three waves in inhomogeneous media [81, 82].

Figure 3-2 depicts the 1D scattering problem. Even when the LH wave is assumed to be present in the entire problem domain, the matching condition ensures that the scattered O-mode wave is generated at a localized layer where the matching condition is satisfied due to the presence of a density gradient. In this problem, both the plasma edge and the cut-off layer of the incident O-mode wave is assumed to be located sufficiently far away from the scattering layer.

As shown in Appendix B, the analytic solutions of the mode amplitudes that describe the backscattering process are given in terms of parabolic cylinder functions [81, 82, 83] as follows:

$$a_2 = c_2 e^{i\xi^2/2} D_{iZ/2}(\sqrt{2}e^{i\pi/4}\xi), \tag{3.8a}$$

$$a_0 = -c_2 i e^{i\pi/4} e^{-i\xi^2/2} \frac{lKa_1/v_{g0}}{\sqrt{2}} D_{iZ/2-1}(\sqrt{2}e^{i\pi/4}\xi), \tag{3.8b}$$

where $\xi \equiv \sqrt{\kappa'/2}x \equiv x/l$ is a normalized length, $Z = l^2 K K^* a_1 a_1^*/(v_{g0}v_{g2})$, and c_2 is a constant that is determined by the boundary condition. Note that these solutions are determined by the plasma parameters at the layer where the matching condition is

perfectly satisfied. Figure 3-3 shows the complex amplitude of the mode amplitudes when $Z = 0.01$. The magnitude of each mode amplitude is normalized by the mode amplitude of incident wave (a_2) at $\xi = -20$ for illustrative purposes. Figure 3-3 (a) shows that the mode amplitude of the incident O-mode wave reduces as the wave crosses the scattering layer at $\xi = 0$. As shown in Figure 3-3 (b), the sharp decrease in the mode amplitude of the scattered O-mode wave after $\xi > 0$ shows that the backscattered O-mode wave is present in the region to the left of the scattering layer, consistent with the physical picture shown in Figure 3-2.

Appendix B also shows that the ratio of the scattered power density to the incident power density becomes

$$\frac{S_0}{S_2}|_{\xi\to-\infty} \approx \pi r_e^2 \lambda_0^2 l^2 (\delta n)^2, \tag{3.9}$$

where r_e is the classical electron radius, λ_0 is the vacuum wavelength of the incident O-mode, and δn is the electron density fluctuation assoicated with the LH mode. From the cold plasma electrostatic dispersion relation, the magnitude of δn is then estimated as follows:

$$\frac{\delta n}{n_0} \approx \frac{-ie|\vec{k}_1||\vec{E}_1|}{m_e \omega_{pe}^2}, \tag{3.10}$$

where $|\vec{k}_1|$ is the magnitude of the LH wave-vector, m_e is the mass of electron, and ω_{pe} is the electron plasma frequency. Taking $n_\parallel \approx 2$ to estimate k_1 and $E_1 \approx 100\,\mathrm{kV/m}$ (corresponding to the maximum field strength based on the full wave calculation [11]) and assuming the density at the scattering layer to be $n_e \approx 2 \times 10^{19}\,\mathrm{m}^{-3}$, we find the $\delta n/n_0 \approx 5 \times 10^{-4}$. Using this value in Equation 3.9 with $\lambda_0 = 5\,\mathrm{mm}$ (60 GHz) and $l \approx 4\,\mathrm{mm}$ based on X-mode reflectometer measurements [84] of SOL density profiles, we calculate the scattered power to be about 60 dB less than the incident power in the 1-D space. Note that this value is the upper bound that can be expected from the measurements because the primary LH resonance cone might not be passing in front of the O-mode antennas, and 2D and 3D spatial effects on the O-mode wave propagation are not considered. Appendix C presents a preliminary time-dependent full wave simulation with an aim to examine spatial effects on the propagation of O-mode waves.

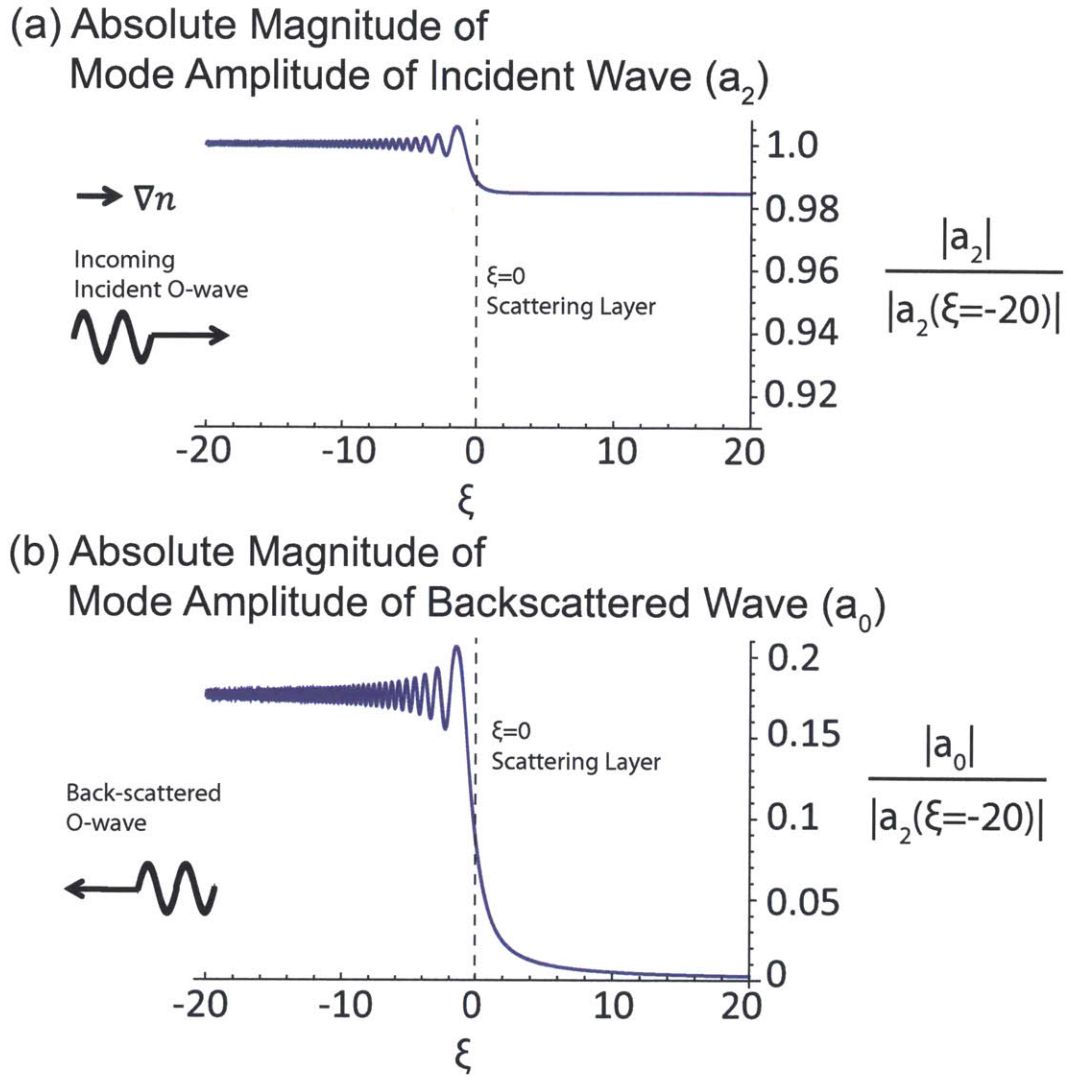

Figure 3-3: (a) Absolute magnitude of the mode amplitude of incident wave $|a_2|$. (b) Absolute magnitude of the mode amplitude of backscattered wave $|a_0|$. The magnitude of each mode amplitude is normalized by the absolute magnitude of a_0 at $\xi = -20$. In this particular case, $a_1 = 1$, $|lK/v_{g0}| = |lK^*/v_{g2}| = \sqrt{Z}$, and $Z = 0.01$. Thus, the contribution of the scale length term l is embedded in Z. These are the results of the analytic solutions, Equations 3.8 (a) and (b). They have been also verified by numerical integrations of Equations 3.7 (a) and (b).

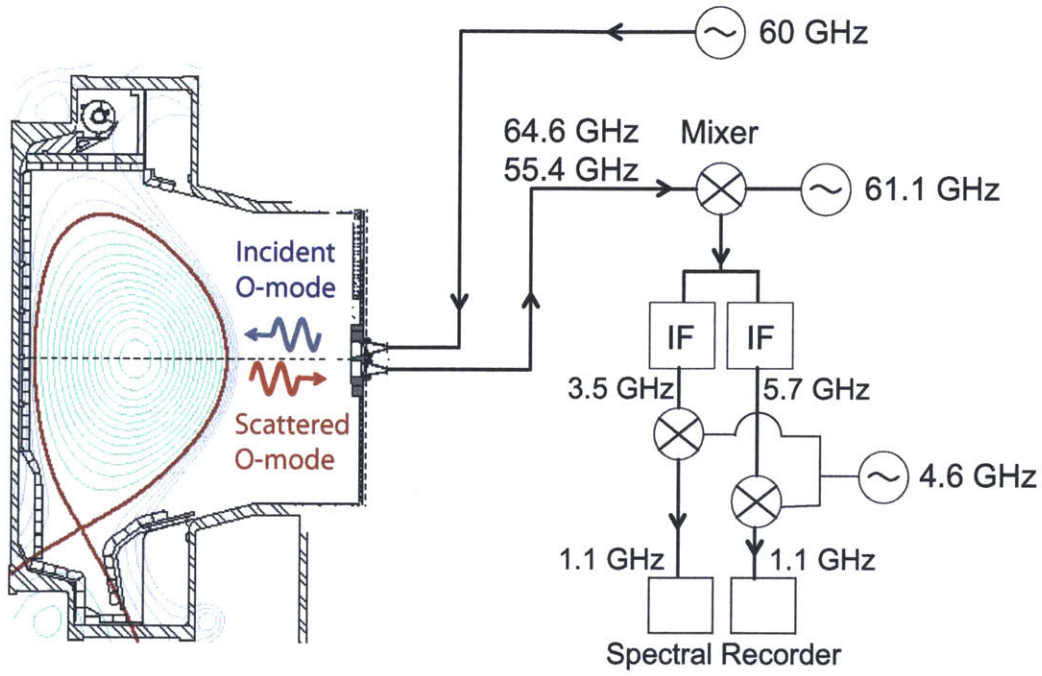

Figure 3-4: The high frequency stage and the intermediate frequency stage is shown with the vacuum vessel (not to scale) and plasma equilibrium in typical L-mode plasmas. The frequency of the backscattered signals at 64.6 and 55.4 GHz are both converted down to 1.1 GHz in two separate channels.

3.3 Experimental Setup

One of the goals of the hardware modification was to develop a system that can handle frequency-shifted backscattered signals, while maintaining the existing capability of detection low frequency density fluctuations(< 1 MHz) by plasma turbulence and to develop a power detection system that can perform as a spectrum analyzer to avoid the direct digitization of backscattered signals, given the limit of the sampling rate (2 MHz) of the available digitizer.

Figure 3-4 shows the experimental setup of the backscattering measurement system. The 60 GHz channel of the O-mode reflectometry system [85, 86] has been used with the bi-static antennas and the waveguides connecting between the antennas and the high frequency (HF) stage. Figure 3-5 shows a detailed block diagram of the modified system. The antennas of the O-mode reflectometry system

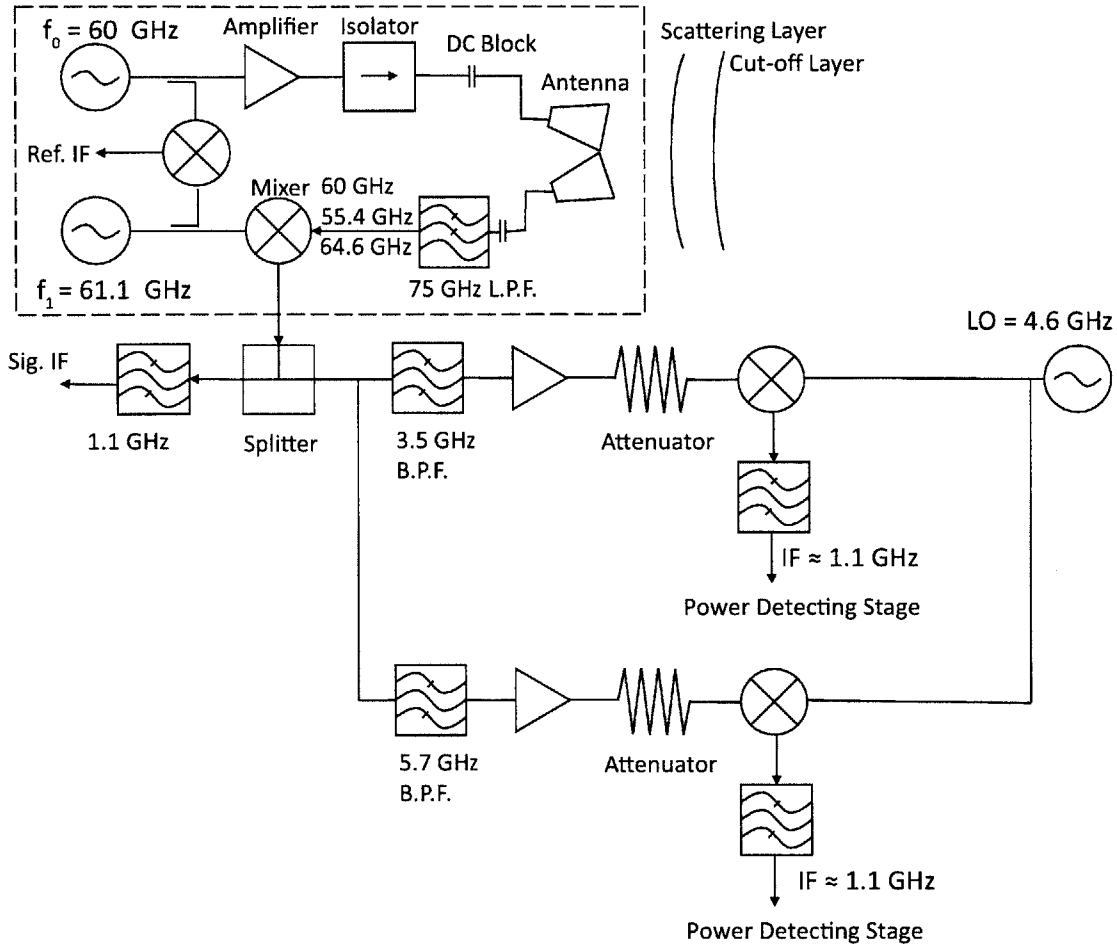

Figure 3-5: A detailed block diagram of the 60 GHz reflectometry system with an heterodyne detection approach. The dashed rectangle encloses the microwave parts in the high-frequencys stage.

are located at the mid-plane of A-port. In the transmitter section of the HF stage, a power amplifier was installed to increase the incident wave up to +25 dBm. A 2D beam pattern calculation using a commercial finite element solver (COMSOL [87]) indicates that the incident O-mode beam pattern is concentrated vertically within ±5 cm from the mid-plane near the LCFS.

In the receiver section, two mixing stages have been added. After the frequencies of the scattered signals are mixed down from 64.6 and 55.4 GHz to 3.5 and 5.7 GHz at the first mixing stage, the signal is split in two different intermediate frequency stages. At the second mixing stage, the final frequency of both signals becomes 1.1

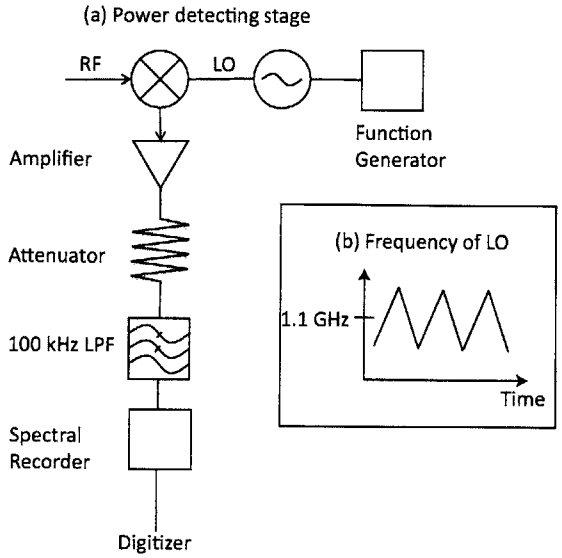

Figure 3-6: (a) A block diagram of the power detecting stage. (b) The frequency of LO as a function of time.

GHz. Because the final IF of the scattered signals is the same as that of the reflected signals, care was taken to prevent leakages due to finite isolation in the mixers by using a set of filters and amplifiers.

To perform continuous spectral measurements of the scattered signals, power detecting stages have been designed and built that can provide amplitude spectra. As shown in Figure 3-6 (a), each power detecting stage consists of a frequency-tunable LO, a mixer, an amplifier, a low pass filter, and a spectral recorder built in-house. Figure 3-6 (b) shows the LO frequency, which is continuously swept across a frequency range around (1.1 ± 0.1) GHz in a triangular shape with a repetition rate of $10 \sim 20$ Hz to generate an IF signal at different frequencies to perform spectral measurements. Then, the 10-pole low-pass Bessel filter with a cut-off frequency at 100 kHz[1] selects a spectral component of the signals. The stop-band of this filter extends from 410 kHz to 10 MHz with attenuation of -60 dBc to eliminate any unwanted signals fed into the spectral recorder.

The spectral recorders, tuned at 1.1 GHz with a resolution bandwidth of 100 kHz,

[1]TTE, Incorporated, Model: LT10-20K-50-720A

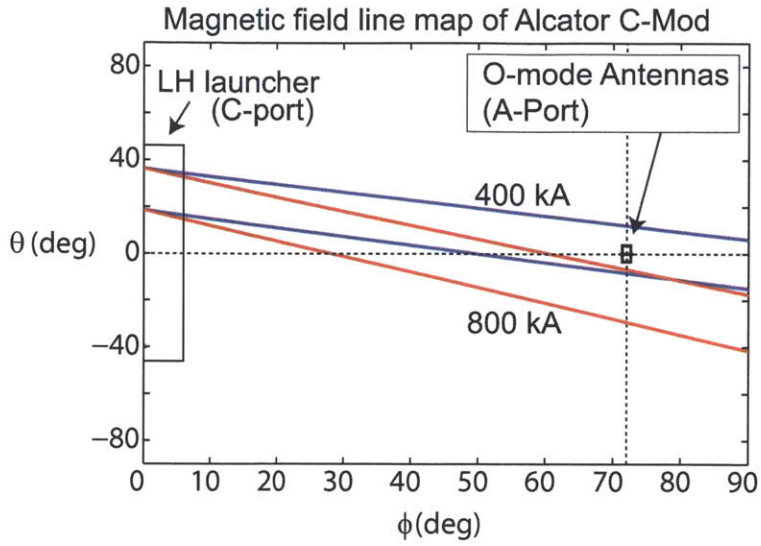

Figure 3-7: Magnetic field line mapping of Alcator C-Mod for 800 kA (red) and 400 kA (blue) plasmas. The LH launcher is located at C-port and the antennas for scattering diagnstics are located at the mid-plane of A-port.

are connected to both channels to measure the spectral power [13], which can measure the spectral power in the frequency range of interest with the repetition rate of 10∼20 Hz. The details of the power detector are discussed more in Appendix B.

Figure 3-7 shows the magnetic field line mapping in the toroidal- and poloidal-space of Alcator C-Mod when the plasma current is 400 kA (blue) and 800 kA (red) in typical plasma discharges. Figure 3-7 indicates that the incident O-mode wave is most likely to interact with the LH waves that are leaving the top part of the LH launcher, if it interacts with LH waves directly leaving the LH launcher, because LH waves propagate along the resonance cone, which is almost aligned to the background magnetic field.

3.4 Scattering Results

3.4.1 General observations

Scattered signals that are frequency-shifted by ± 4.6 GHz with respect to the frequency of the incident wave (60 GHz) have been observed in L-mode and H-mode

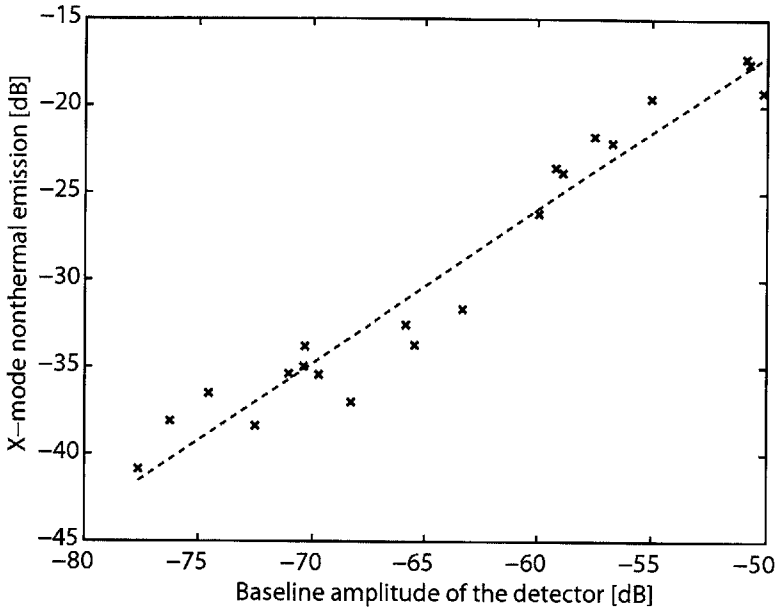

Figure 3-8: The strength of the X-mode non-thermal electron cyclotron emission at 220 GHz as a function of the baseline power amplitude of the spectral recorder. The dotted line shows a linear fit with a correlation coefficient of 0.97.

plasmas with line-averaged densities above $\overline{n}_e \approx 0.9 \times 10^{20}\,\mathrm{m}^{-3}$. Below this density, the noise floor of the spectral recorder increases up to 20 dB, and no scattered signals can be identified during the injection of LH waves. The change of noise floor is highly correlated with the strength of non-thermal X-mode electron cyclotron (EC) emission, suggesting that O-mode non-thermal EC emission is responsible for the increase in baseline [13].

Figure 3-8 shows that, during the LH power injection, the increased level in the baseline of the spectral recorder measuring the spectral power at 64.6 GHz is highly correlated to the X-mode non-thermal electron cyclotron emission (ECE) strength at frequency 220 GHz, corresponding to the peak amplitude of the second harmonic down-shifted ECE. This suggests that the increased background emission at these frequency ranges originates from O-mode first harmonic down-shifted non-thermal ECE. The energy range of the fast electrons responsible for this enhanced emission is estimated to be 0.73 MeV, as calculated by taking a ratio between the fundamental frequency (114 GHz) at the last closed flux surface (LCFS) and the target frequency (64.6 GHz). Due to this enhanced plasma emission, no clear backscattered signals

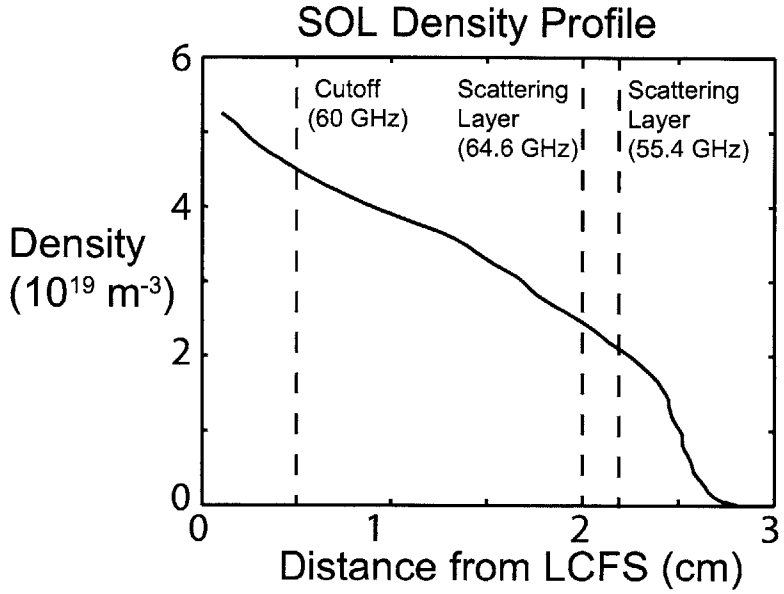

Figure 3-9: Example of a SOL density profile measured in a high-density L-mode plasma at $\overline{n}_e = 1.4 \times 10^{20} m^{-3}$ with the X-mode reflectometer [84].

were observed over the baseline when the plasma was lowered below $\overline{n}_e \approx 0.9 \times 10^{20}\,\mathrm{m}^{-3}$. When the density was raised above $\overline{n}_e \approx 1.3 \times 10^{20}\,\mathrm{m}^{-3}$ the baseline level does not change noticeably with and without LH injection, suggesting that the LH waves were not able to generate enough fast electrons, which is consistent with the observation of decreased current drive efficiency in high density plasmas [10].

At higher densities, the cut-off layer of the 60 GHz incident O-mode wave is typically located near the LCFS, indicating that the scattering signals are generated in the scrape-off layer (SOL). Figure 3-9 shows an example of a SOL density profile measured with the X-mode reflectometer when $\overline{n}_e = 1.4 \times 10^{20}\,\mathrm{m}^{-3}$. In this case, the cut-off layer of the 60 GHz incident O-mode wave is about 0.5 cm outside of the LCFS and the scattering layers for both up-shifted and down-shifted scattered signals are further outside by 1.5 cm from the cut-off layer. To calculate the scattering layers, the $n_{\|}$ of LH waves is assumed to be 2, which is a typical peak $n_{\|}$ at the launcher.

Figure 3-10 shows the simultaneous measurements of both frequency up-shifted (64.6 GHz) and down-shifted (55.4 GHz) signals. When LH waves are applied to the plasma, five coherent scattered signals are observed with a slight increase in baseline.

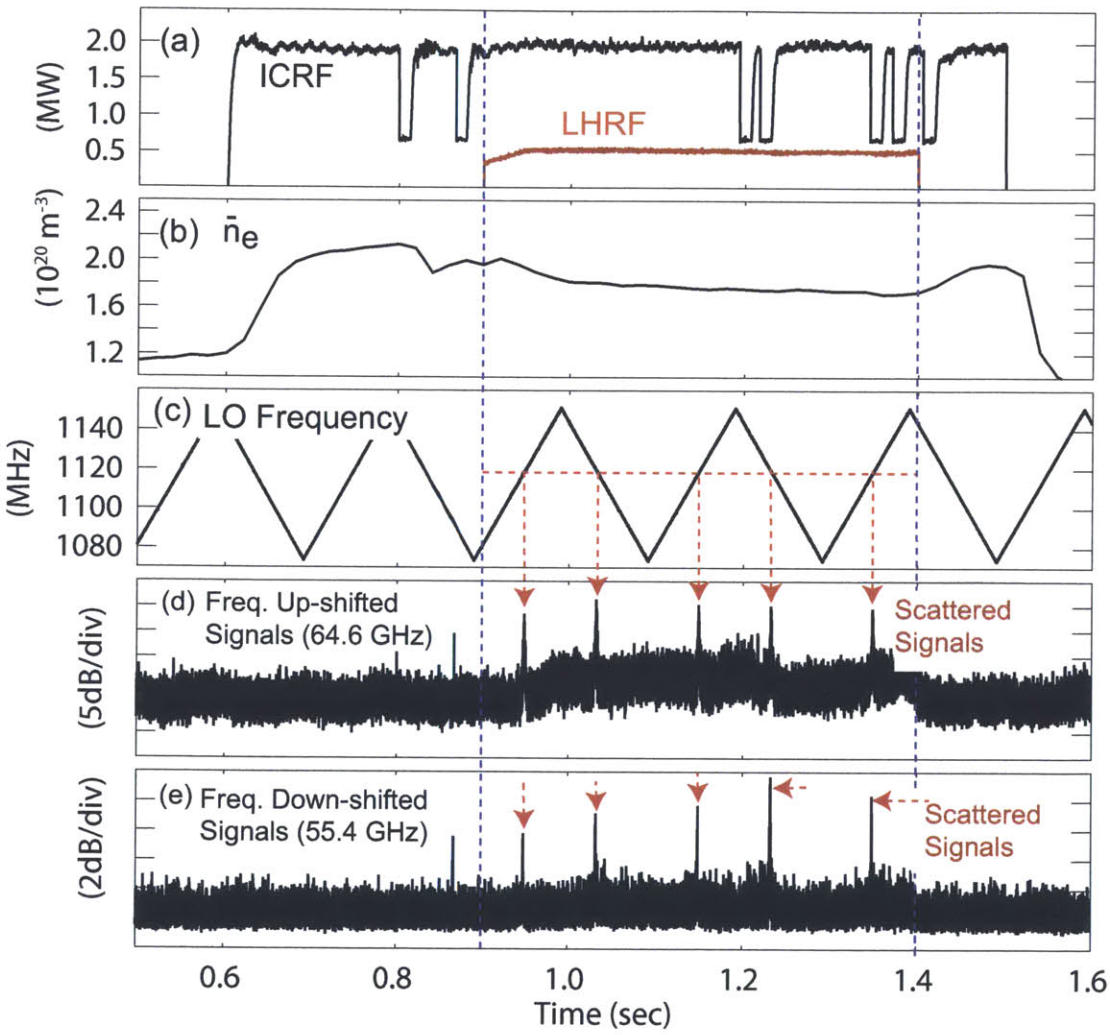

Figure 3-10: Time traces for a H-mode discharge with the injection of LH waves: (a) coupled LH and ICRF power, (b) line-averaged electron density, (c) frequency of the local oscillator of the power detector, (d) detected frequency up-shifted signals, and (e) detected frequency down-shifted signals. Note that the two power spectra have different relative scales.

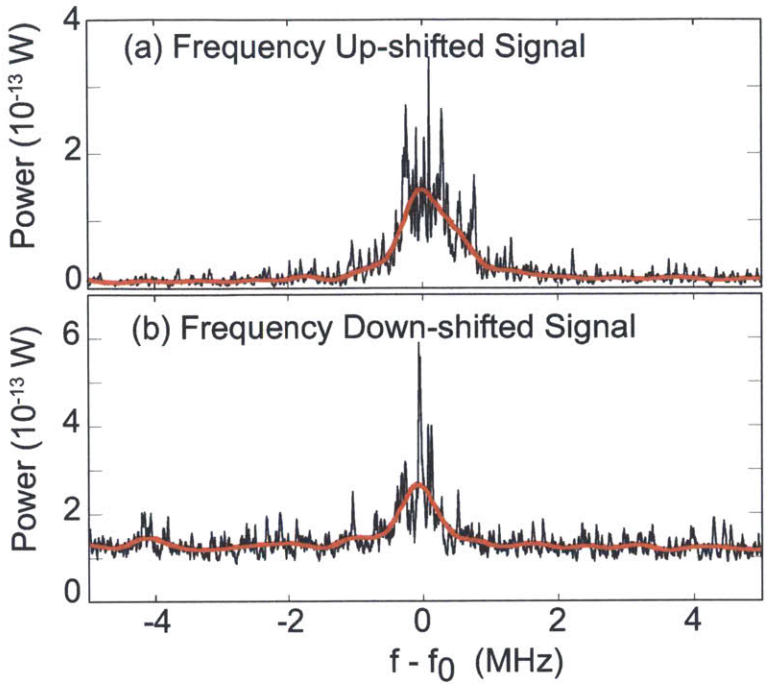

Figure 3-11: Frequency spectrum of the scattered signals measured between 1.14 and 1.16 second of the discharge from Figure 3-10: (a) frequency up-shifted and (b) frequency down-shifted signals. Digitally filtered signals (red lines) are overlaid over the raw signals.

The measured power in Figures 3-10 (d) and (e) denote the power that is fed to the IF stage shown in Figure 3-4. Figures 3-11 (a) and (b) show the detailed spectra of the frequency up-shifted and down-shifted signals that are measured between 1.14 sec and 1.16 sec of the discharge shown in Figure 3-10. To eliminate background fluctuations at frequencies over 1 kHz, post-processing with digital low pass filters is applied to the raw signals. The offset in power denotes the noise floor. The data presented in the rest of the chapter have been post-processed in this way to calculate the peak amplitude of the scattered signals. The focus will be given to the frequency up-shifted scattered signals due to the relatively shorter travel distance than that of the frequency down-shifted signals.

Based on available data, the effective scattered power is estimated to be about -55 dBm when taking into account the approximate power loss (-45 dB) in the wave-guide system and the antenna gain. Note that this power loss is estimated by measuring the

returned 60 GHz incident power at its own cutoff layer during the plasma discharge. Thus, in general, the ratio of the scattered power to the incident power is about -80 dB. We can then use Equation 3.10 to evaluate the electron density fluctuation δn by the LH wave, obtaining $\delta n/n_0 \approx 5 \times 10^{-5}$ with the relevant parameters: $\lambda_0 = 5\,\mathrm{mm}$, $n_0 = 2 \times 10^{19}\,\mathrm{m}^{-3}$, and $l \approx 4\,\mathrm{mm}$. Using Equation 3.10, we find that $|\vec{E}_1| \approx 10\,\mathrm{kV/m}$, which is about one tenth of the maximum strength of the electric field based on full wave calculations [11]. This calculation suggests that we might not be detecting the central part of the resonance cone. This will be discussed more in the next subsection by examining the radial spread of the launched LH waves that have a different $n_\parallel$ and thus a different spectral amplitude. Another possibility is scattering of the LH waves from drift wave turbulence, which could destroy the LH resonance cone and weaken the LH electric field. This will be also discussed more in the next subsection.

It should be noted that 2D and 3D spatial effects have not been properly taken into account in the previously presented 1D model. While this can be a source of the discrepancy between the expected level of density fluctuations and the calculated level of density fluctuations, one of the major uncertainties also comes from the assumed strength of the LH electric field. Together with the radial propagation of the LH waves, the poloidal variation in the magnetic field line pitch angle with the plasma current needs to be considered because LH resonance cones propagate mainly along the field line. This is supported by the observations that the scattered power increases when the plasma current is lowered, which is discussed in the next subsection.

3.4.2 Plasma current dependence of scattering power

Figure 3-12 shows the measured peak amplitudes of the frequency up-shifted signals in six discharges with different plasma currents from 300 kA to 800 kA, which affects the field line mapping. At the fixed plasma density $\overline{n}_e = 0.9 \times 10^{20}\,\mathrm{m}^{-3}$, the plasma current is varied to examine the dependence of the scattered power on plasma current. In all six discharges, the peak $n_\parallel$ is 1.6, the LH power is 800 kW and the central toroidal magnetic field is 5.4 T.

The enhanced scattered power in lower current plasmas is due to the field line

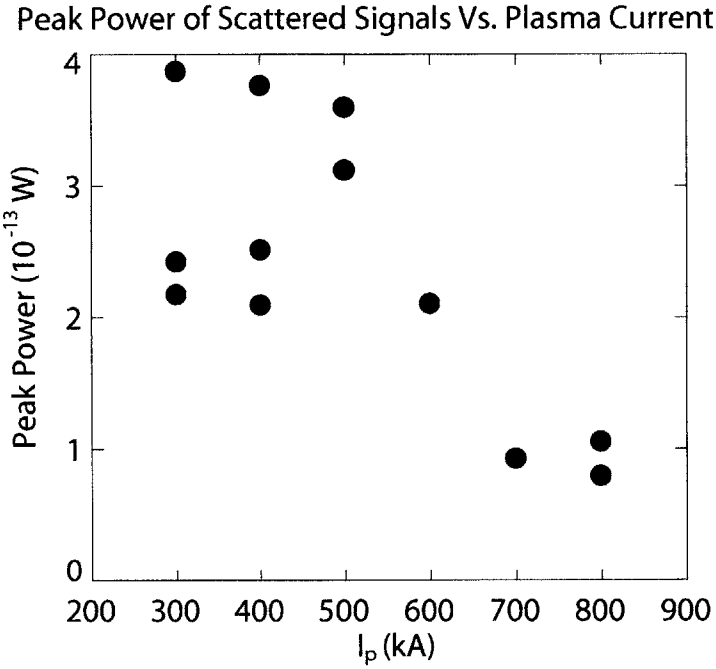

Figure 3-12: Measured peak power of frequency up-shifted signals as a function of plasma current. Experimental plasma parameters are $B_{T0} = 5.4$ T and $\overline{n}_e = 0.9 \times 10^{20}\,\mathrm{m}^{-3}$, and the launched peak $n_{\|} = 1.6$.

mapping between the incident O-mode wave and the LH wave leaving the LH launcher. As shown in Figure 3-7, when the plasma current is lowered, more LH waves pass by the mid-plane at A-port where the incident O-mode wave exits, resulting in stronger scattered power. Therefore, the increase in scattered power is evidence that LH waves propagate along the resonance cone, which predominantly follows the magnetic field line at angle $\theta \approx v_{g\perp}/v_{g\|} \approx -\omega/\omega_{pe}$.

Another possible way to interpret the observed data is to examine the contribution of the scattered LH waves by non-linear effects in the plasmas with different plasma current. For example, FTU [56] uses a higher plasma current as a way to increase edge temperature, which is then reported to reduce the LH spectral broadening driven by non-linear effects. This approach will not be pursued further in this thesis because the change of edge temperature at outside r/a $\sim$ 0.8 between the 300 kA and 800 kA Alcator C-Mod plasmas is not observed to be significant. In both cases, the edge temperature at r/a $\sim$ 0.8 is in the range 250 to 300 eV.

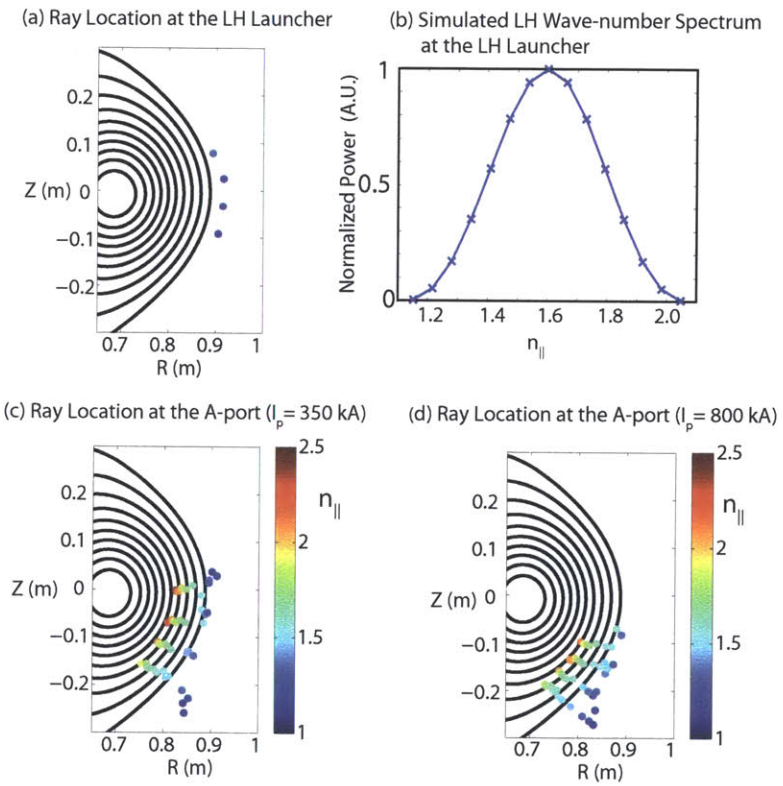

Figure 3-13: Ray tracing simulation results. (a) ray locations at the LH launcher, (b) initial LH wave-number power spectrum (peak $n_{\|} = 1.6$) at the launcher, (c) ray positions at A-port when $I_p = 350\,\mathrm{kA}$, (d) ray positions at A-port when $I_p = 800\,\mathrm{kA}$.

In lower current plasmas, LH ray tracing simulations using GENRAY [41] indicate that the LH rays with lower $n_{\parallel}$ dominantly interact with the incident O-mode waves and have weaker spectral power, assuming that the interaction between the incident O-mode wave and the LH wave dominantly occurs on the first pass of the LH wave from the launcher to the plasma core. Figure 3-13 shows the results of LH ray tracing simulations with two different plasma currents. As shown in Figure 3-13 (b), the launched LH spectrum consists of 15 different $n_{\parallel}$ with maximum peak power at $n_{\parallel} = 1.6$. In the simulation, this spectrum is launched at four different poloidal locations to simulate the actual geometry of the LH launcher, as shown in Figure 3-13 (a). By the time these rays pass by A-port on the first pass, the spatial spread of the rays due to their different initial $n_{\parallel}$ is observed. Regardless of plasma current, the rays with higher $n_{\parallel}$ penetrate more radially inward. Note that GENRAY solves the ray equations using the general cold plasma dispersion relation instead of Equation 3.3, and that the weaker radial penetration of the rays with lower $n_{\parallel}$ is due to the $n_{\parallel}$ dependency of the group velocities ($v_{g\perp}/v_{g\parallel} \approx -\sqrt{1 - 1/n_{\parallel}^2}\omega/\omega_{pe}$) when the electrostatic approximation ($n_{\parallel} \gg 1$) does not hold (e.g., Equations 2.43 (a) and (b)). Thus, this simulation suggests that the increase in the measured scattered power in lower current plasmas is due to the LH waves with lower $n_{\parallel}$ (e.g., Figure 3-13 (c)) near the mid-plane. It can be also seen that these rays outside the LCFS are not the central part of the wavenumber spectrum and have much weaker spectral power as shown in Figure 3-13 (b). As mentioned previously, this spatial broadening of the rays with different $n_{\parallel}$ can partly explain why the observed scattered power is weaker than the power predicted by the 1D model, even when the primary resonance cone of the LH wave is seen by the incident O-mode wave in the lower plasma current case.

3.4.3 Detection of scattered signals in high current, high density plasmas

The detection of the scattered power in higher current plasmas indicates the presence of LH waves in a region that is not magnetically connected to the LH

launcher on the first pass. As shown in Figure 3-13 (d), in a high current plasma (800 kA) LH waves are well below the mid-plane by the time they pass A-port mid-plane because of a higher poloidal magnetic field. Thus, it is not expected to detect the backscattered signals when the plasma current is increased even in high density plasmas. Nonetheless, these observations are consistent with the previous scanning probe measurements of LH wave fields in the SOL [88]. In the latter case, the radial and poloidal locations where the probe measurements were made also did not intersect the resonance cone directly leaving the LH launcher.

One possibility to explain the presence of the LH wave at the outer mid-plane in the SOL near A-port is the multiple toroidal turns of un-damped LH waves. In Alcator C-Mod, the central core temperature of high-density L-mode plasmas is about $\sim$2 keV, resulting in a multi-pass absorption regime of LH waves. Ray tracing simulations indicate that rays can propagate more than 3 times toroidally with multiple reflections at the plasma edge before being completely absorbed by plasma either by Landau-damping or collisional damping. In this process, it is possible that LH waves propagate out to the SOL near the mid-plane of A-port.

Note that care should be taken when using ray-tracing codes in multi-pass regimes because the WKB approximation may not hold at the plasma edge. Reflections at the edge may not be adequately treated by the ray-tracing approach. In this view, full-wave simulations could be ideal to calculate the local LH electric field.

The other possibility is that the change in LH wave propagation due to non-linear effects, which is supported by broadened scattered signals. For example, Figure 3-14 shows the full width at half maximum (FWHM) of scattered signals collected in four discharges. The spectral widths of the frequency up-shifted (64.6 GHz) signals are measured at higher density plasmas over $\overline{n}_e = 1.2 \times 10^{20}\,\mathrm{m}^{-3}$ at which the signal to noise ratio of scattered signals is over 10 dB. The measured FWHM is about 1 MHz, which is broader than the FWHM of the incident waves (0.6 MHz). The latter was measured by examining the reflected 60 GHz incident wave at the cut-off layer with the same spectral recorder. Since the spectral profile of the scattered O-mode wave is the convolution of two spectral profiles (the incident O-mode wave and the LH

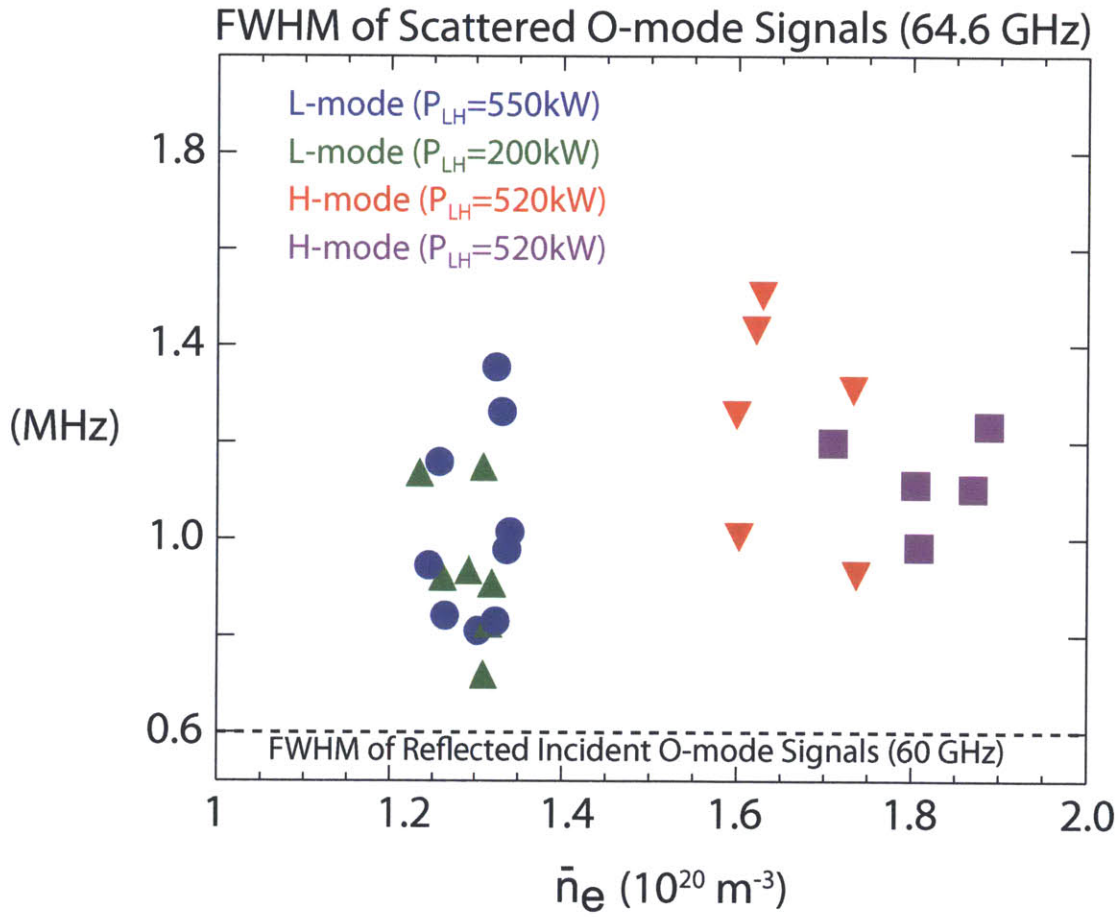

Figure 3-14: Measured full width at half maximum of the frequency up-shifted scattered signals versus the line-averaged density.

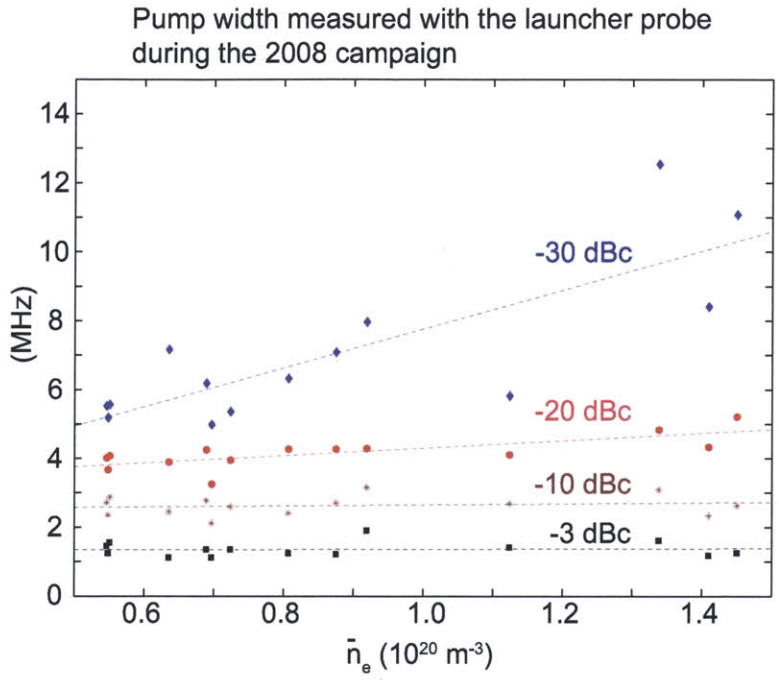

Figure 3-15: Measured full width of the LH wave with a launcher probe during the 2008 campaign as a function of the line-averaged density at 3 dB, 10 dB, 20 dB, and 30 dB below the LH peak power in L-mode USN plasmas (B_{T0} = 5.4 or 7 T, I_p=0.8 or 1.1 MA, and $n_{\|}$=1.9 or 2.3).

wave), the spectral width of the scattered signal $\triangle_{sc}$ can be expressed in terms of the spectral width of the incident signal $\triangle_{inc}$ and the LH wave $\triangle_{LH}$: $\triangle_{sc}^2 = \triangle_{inc}^2 + \triangle_{LH}^2$, assuming all spectral profiles are Gaussian shapes [89]. Thus, the FWHM of LH waves is inferred to be on the order of 0.6 MHz or higher.

This broadening is consistent with the observations that LH spectra are generally broadened in high density plasmas, when measured with edge probes [10, 16]. Figure 3-15 shows an example of the spectral width of the LH wave measured with a probe installed at the LH launcher during the 2008 campaign. A commerical spectrum analyzer is used. No clear trend of the spectral broadening of the LH wave at 3 dB below the peak power is observed across a wide range of densities. It remains on the order of 1 MHz even in the low density plasmas.

In general, spectral broadening of LH waves indicates undesirable non-linear

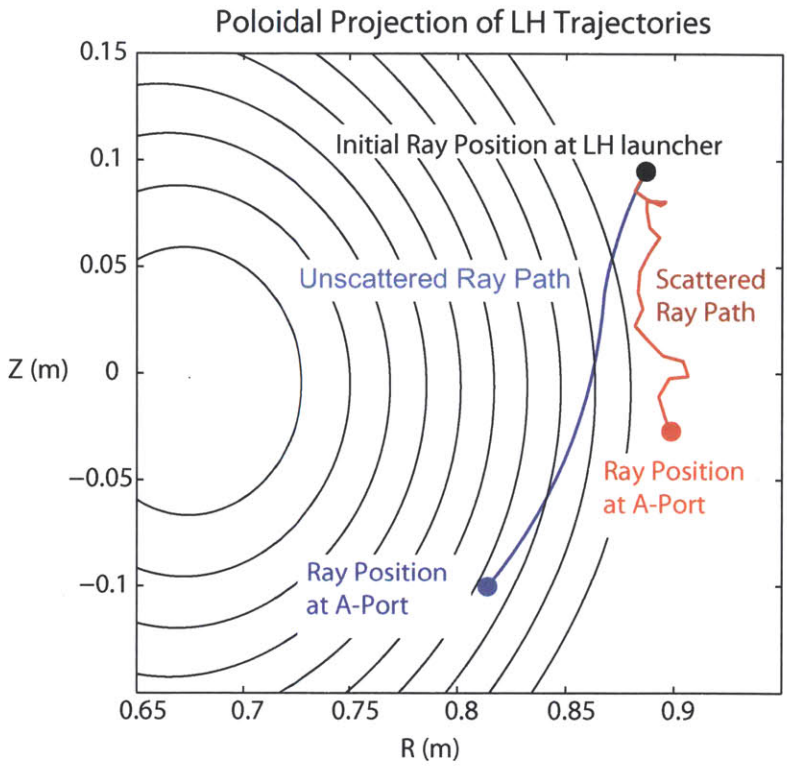

Figure 3-16: Poloidal projection of a LH ray with (red) and without (blue) scattering effect. Initial $n_{\parallel} = 2$.

interactions between LH waves and plasma because non-linear effects are known to degrade LH current drive efficiency. Two models exist to explain this spectral broadening: the scattering of LH waves by plasma turbulence [36, 37, 38] and by ion sound parametric decay instability (PDI) [34, 49, 60]. Although it is difficult to study the origin of the observed broadening partly due to the relatively low signal-to-noise ratio, our measurements of broadened scattered signals indicate that non-linear effects may play a role in understanding LH propagation in high density plasmas.

To examine the possible role of scattering of LH waves by turbulence on the propagation of LH waves, a numerical study was conducted using GENRAY: when LH rays passed by pre-defined radial locations in the SOL, the perpendicular wave-number was randomly rotated to simulate the scattering process. Figure 3-16 shows that, depending on the case, LH rays can be displaced from the unperturbed

propagation path, and they can be present near the mid-plane of A-port on the first pass, even when the plasma current is 800 kA. The observed LH waves could arrive at A-port as a result of this process. This simulation result also indicates that turbulence in the SOL may scatter incoming LH waves, which can limit the radial penetration of LH waves beyond the LCFS. A more complete study of the scattering effect on the loss of current drive efficiency can be found in Bertelli [48]. Similar consequences result via ion sound parametric decay PDI [49], which can redistribute the incident wave-number spectrum and change propagation directions as well.

Nonetheless, $n_{\|}$ scan experiments suggest that the resonance cone of the launched LH wave is not completely destroyed in high density plasmas. Figure 3-17 shows the time traces of the line-averaged density, launched peak $n_{\|}$, and measured peak power of the scattered signals for three discharges, in which both the line-averaged density $\overline{n}_e$ ($\approx$ 1.3, 1.35 and 1.4 $\times 10^{20}\,\mathrm{m}^{-3}$) and the peak $n_{\|}$ (=1.9 and 2.3) are controlled while other plasma parameters remain fixed. In these three experiments, the plasma current is 800 kA and toroidal magnetic field is 5.4 T. At fixed $\overline{n}_e$, in all three discharges, the peak power is consistently reduced by approximately 30 % when the peak $n_{\|}$ is increased from 1.9 to 2.3. This $n_{\|}$ dependence implies that the propagation path of LH waves has been changed because both density and magnetic field, which primarily determine the propagation path of LH waves, are kept constant. If the resonance cone is completely destroyed, then it is not expected that the change in scattered power with the change in initial $n_{\|}$ at the launcher would be observed.

The decrease of peak scattered power with higher peak $n_{\|}$ is qualitatively in agreement with the ray tracing simulations. As shown in Figure 3-13, LH rays with higher $n_{\|}$ generally penetrate more radially inside the LCFS on arriving at A-port on their first pass. This will result in weaker density fluctuations associated with the LH waves in the scattering layer, which is located outside of the LCFS. However, it is not clear whether the presence of LH waves in the SOL near the mid-plane of A-port is due to the undamped LH waves or due to the LH waves directly leaving the LH launcher then experiencing random scattering processes (e.g., Figure 3-16).

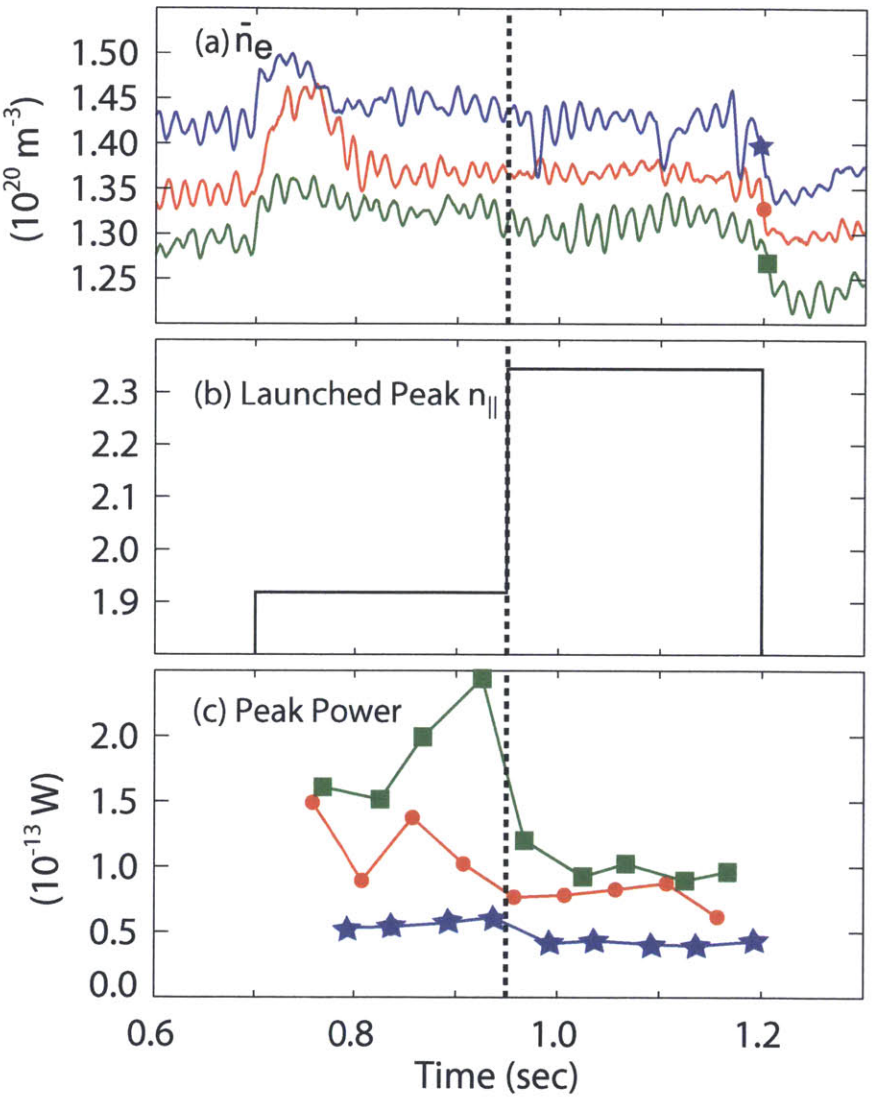

Figure 3-17: Three discharges with slightly different line-averaged densities to study scattering signal response. Shown are the time traces of (a) line-averaged density, (b) peak $n_{||}$ of launched LH wave, and (c) peak power of the frequency up-shifted signals. The vertical dashed lines mark the time when the launched peak $n_{||}$ increased from 1.9 to 2.3

3.5 Relation to LH Power Loss Mechanisms

Although the present experimental work is the first attempt to detect the LH wave in the SOL using the microwave backscattering technique, the data are not yet extensive enough to provide a clear picture on the loss of LHCD efficiency. Nonetheless, it is worthwhile discussing our two experimental observations from the viewpoint of identifying possible LH power loss mechanisms.

First, the observed decrease of the backscattered O-mode power with the increase in the plasma density may be an indication that the LH electric field becomes weaker due to possible LH power loss mechanisms, which become aggravated with the increase in the plasma density. Figure 3-17 shows that, at fixed peak $n_{\parallel}$, the peak power is reduced by 30 % when the plasma density is raised by 10 %, implying a decrease in the amplitude of the LH wave field in the scattering layer. This observation is in line with the findings of previous studies that parasitic loss mechanisms degrade the LHCD performance by dissipating the launched LH power at the plasma edge. Examples of these mechanisms include collisional absorption [10, 61, 64], full-wave effects [11], ionization [90], fast electron generation [63], ion sound PDI [56, 59] and wave scattering by density fluctuations [48, 62].

However, based on the presented results, it is difficult to identify the most responsible power loss mechanism because several edge loss mechanisms might concurrently contribute to dissipate the launched LH power. While it is also critical to identify whether or not the dominant mechanism is one that occurs near the LH launcher, it cannot be concluded from our observations because the measurements shown in Figure 3-17 are made in the region that is not magnetically mapped to the launcher.

Second, the broadened backscattered signals shown in Figure 3-14 indicate the presence of non-linear effects on the propagation of LH waves. The estimated spectral width (FWHM) of the LH wave is $\lesssim$ 1 MHz and is consistent with the probe measurements on Alcator C-Mod [10, 16]. There are two known spectral broadening mechanisms, such as ion sound PDI and wave scattering by turbulence,

and this observation raises two questions: the first is which mechanism is responsible for the observed spectral broadening, and the second is whether this broadening mechanism is responsible for the loss of LHCD efficiency. One example of such efforts to address these questions is the study conducted in FTU [56] and JET [59]. The observed spectral broadening on these tokamaks led to an investigation of how much ion sound PDI can degrade the LHCD performance.

Nonetheless, based on our measurements, the link between the observed spectral broadening and the loss of LHCD efficiency is not conclusive for the following three reasons. First, the limited signal-to-noise ratio ($\lesssim$ 15 dB, as shown in Figure 3-8) makes it difficult to distinguish the experimental signature of ion sound PDI from that of wave scattering by turbulence. It is reported that a clear experimental signature [56] of ion sound PDI is seen from the asymmetric LH spectral broadening at 30 dB below the peak power.

Second, even if the responsible spectral broadening mechanism is the ion sound PDI near the launcher, those non-linearly excited LH waves are not likely to arrive at the detection region that is not magnetically connected to the launcher. This is because they are expected [56] to have a much higher $n_{\parallel}$ than that of the launched LH waves and thus to be Landau-damped on their first pass.

Third and finally, while wave scattering might explain the observed spectral broadening, it may not necessarily be the primary mechanism that degrades the LHCD performance on Alcator C-Mod. Using a model by Andrews and Perkins [36, 37], the spectral broadening is evaluated to be $\lesssim$ 1 MHz with the assumption that the LH wave crosses the turbulent ($\delta n/n = 50\,\%$) SOL region ($\sim$ 2 cm). This spectral width is similar to the observed spectral broadening. However, a recent simulation study [48] shows that no additional decline of non-thermal hard X-ray count rates is seen due to the additional wave scattering effect.

Therefore, it cannot be concluded at the moment whether the observed spectral broadening is an experimental indication that the LHCD performance is degraded by the mechanism that is responsible for the observed spectral broadening.

3.6 Chapter Summary

The backscattering experiment to directly measure the LH waves in the SOL is described in Chapter 3. Detection of LH waves at a location that is not directly mapped to the LH launcher implies that LH power is not fully dissipated near the launcher. 1D scattering power is evaluated using mode-mode coupling equations and is compared to the experimentally measured backscattered power in order to evaluate the strength of LH electric field at the backscattering layer. The increase in scattered power with decreasing plasma current indicates the presence of LH resonance cones, based on the fact that LH waves propagate mostly along the magnetic field lines and that the LH launcher and the detecting antenna are magnetically connected only at lower plasma currents.

Nonetheless, contrary to the predictions based on the magnetic field line mapping and LH ray tracing simulations, LH waves have been also observed in high current, high density plasmas. To understand this, two possible mechanisms have been discussed. One is weak single pass absorption of LH waves owing to relatively low core temperature. The other is non-linear effects that can result in partially scattered LH waves, as evidenced by the spectrally broadened signals (FWHM $\sim$ 1 MHz).

Two known pump broadening mechanisms are ion sound PDI [49, 56] and LH wave scattering by turbulence [37, 36]. While the latter can result in the spectral broadening to be $\lesssim$ 1 MHz with the assumption that the LH wave crosses the turbulent ($\delta n/n = 50\,\%$) SOL region ($\sim$ 2 cm) using the available analytic model [37, 36], recent simulations on Alcator C-Mod [48] indicate that LH wave scattering causes an insignificant effect on the loss of efficiency. Meanwhile, the role of ion sound PDI on the loss of efficiency is not clear. For example, LH spectral measurements using probes indicate that the LH spectral width (FWHM) exhibits no apparent threshold behavior across $\overline{n}_e \approx 1.0 \times 10^{20}\,\mathrm{m}^{-3}$. The FWHM of the measured LH spectra remains approximately 1.5 MHz below and above $\overline{n}_e \approx 1.0 \times 10^{20}\,\mathrm{m}^{-3}$. Thus, it has not been possible to conclude that the pump

broadening mechanisms (i.e., LH wave scattering and ion sound PDI) are responsible for the loss of LHCD efficiency.

THIS PAGE INTENTIONALLY LEFT BLANK

Chapter 4

Parametric Decay Instability

4.1 Introduction

The parametric dispersion relation of the LH wave in the framework of the linear parametric decay instability (PDI) theory was originally studied by Porkolab [34, 91] in the dipole pump limit. Later, Tripathi [57, 92] approached this problem with a finite pump wave-number vector. Takase [49] and Liu [93] demonstrated that Tripathi's dispersion relation can be obtained with the fluid approach for LH waves, while ion modes are treated are treated kinetically. Although Porkolab did not consider the effects of finite pump wave-vector, his model is considered to be fully kinetic than those derived later because his model retained the higher order terms of Bessel functions. In fact, Porkolab showed [34] that the two models have the same form in the limit $\mu \ll 1$, where μ is the coupling coefficient. While the difference in the growth rate between two models becomes significant in the limit $\mu \to 1$, in the range of LH power densities relevant to Alcator C-Mod experiments, the two models agree well with one another.

In this chapter, the parametric dispersion relation is first reviewed by following Liu's approach, which can provide physical insights into the parametric dispersion relation. However, unlike the original derivation, the contribution of the parallel coupling term in the coupling coefficient will be added, in addition to the perpendicular coupling term. In the classical PDI limit, the perpendicular coupling

term was thought to be dominant because it was considered that PDI occurs relatively inside of the last closed flux surface (LCFS), where the contribution of the parallel coupling will be minimized and that of the perpendicular coupling term will be maximized as the perpendicular LH electric field is enhanced. The potential importance of the parallel coupling term to explain the observed LH spectra was later pointed out by Takase [12].

The organization of this chapter is as follows. Section 2 derives the parametric dispersion relation of the LH wave with the addition of the parallel coupling term, by extending the Liu's approach [93]. Section 3 presents the numerical solutions of the parametric dispersion relation for Alcator C-Mod edge plasmas. Section 4 examines convective losses in the perpendicular and parallel coupling limit.

4.2 Parametric Dispersion Relation of LH Waves

4.2.1 Derivation of parametric dispersion relation

Consider the propagation of pump LH waves with a potential $\phi_0 = \phi_0 e^{i\vec{k}_0\cdot\vec{x}-i\omega_0 t} + c.c.$. The linear response of electrons to these LH waves is calculated by solving the equation of motion and the equation of continuity in the cold plasma limit:

$$\vec{v}_{0\perp} = -\frac{ei\phi_0}{m\omega_c^2}(\vec{k}_0 \times \vec{\omega}_c + i\omega_0 \vec{k}_{0\perp}), \tag{4.1a}$$

$$v_{0\parallel} = -\frac{ek_{0\parallel}\phi_0}{m\omega_0}, \tag{4.1b}$$

$$n_0 = -n_0^0 \frac{e\phi_0}{m}\left(\frac{k_{0\parallel}^2}{\omega_0^2} - \frac{k_{0\perp}^2}{\omega_c^2}\right), \tag{4.1c}$$

where n_0^0 is the unperturbed background electron density. Note that the first term on the right-hand-side (RHS) of Equation 4.1a is due to the $\vec{E}\times\vec{B}$ motion, which is larger by ω_c/ω_0 than the second term that is due to the polarization drift. Thus, the contribution of the polarization drift will be neglected in the remainder of the derivation.

Consider now the case when the pump LH wave excites PDI, which will result in the sideband LH wave and the low-frequency ion mode, while satisfying the following frequency and wave-number matching condition:

$$\omega_{1,2} = \omega \mp \omega_0 \tag{4.2a}$$

$$\vec{k}_{1,2} = \vec{k} \mp \vec{k}_0, \tag{4.2b}$$

where the subscript 0 refers to the pump, the subscript 1 refers to the LH lower-sideband wave, the subscript 2 refers to the LH upper-sideband wave, and variables without any subscripts refer to low-frequency ion mode. The relevant low-frequency ion modes are either an ion sound quasi-mode and/or ion cyclotron quasi-mode, which will be discussed in more detail in Section 4.2.2. In the weak coupling limit, higher order coupling terms are neglected. In the following derivation of the parametric dispersion relation, the upper sideband is neglected until the end of this section.

Due to the frequency-dependent ponderomotive force, the dominant non-linear force that acts on the sideband LH wave arises from the $\nabla \cdot (n\vec{v})$ term in the equation of continuity. For the electrostatic LH wave, the non-linearity arising from the term $\vec{v} \times \vec{B}$ in the equation of motion can be neglected because modes are electrostatic ($\vec{B} \approx 0$). The ion contribution in the non-linear terms can generally be neglected due to the larger ion mass than the electron mass.

The dominant non-linear force that acts on the low-frequency ion mode comes from the parallel ponderomotive force $\vec{F}_{p\|} = -m\vec{v} \cdot \nabla\vec{v}_{\|}$. In general, the non-linear coupling between the pump and sideband LH waves produces the ponderomotive force $\vec{F}_p = -m\vec{v} \cdot \nabla\vec{v}$ on the low-frequency ion mode, consisting of two components: the component ($F_{p\|}$) along the background magnetic field ($\vec{B}_0$) and another component ($F_{p\perp}$) perpendicular to $\vec{B}_0$. However, the latter contribution is strongly suppressed by the presence of $\vec{B}_0$, and this term is neglected here and after.

To evaluate the contribution of the parallel ponderomotive potential on the electron density fluctuation of low-frequency ion mode, in addition to the

self-consistent potential ϕ, the parallel ponderomotive force term can be decomposed into two terms[1]:

$$\vec{F}_{p,\parallel} = \vec{F}_{p,\parallel 1} + \vec{F}_{p,\parallel 2} = e\nabla_{\parallel}(\phi_{p1} + \phi_{p2}), \tag{4.3}$$

where the first term on the RHS is due to the perpendicular coupling

$$\vec{F}_{p\parallel,1} = -\frac{m_e}{2}(\vec{v}_{0\perp} \cdot \nabla_{1\perp} v_{1\parallel} + \vec{v}_{1\perp} \cdot \nabla_{0\perp} v_{0\parallel}), \tag{4.4}$$

because it includes perpendicular velocity components of pump and sideband LH waves, and the second term is due to the parallel coupling

$$\vec{F}_{p\parallel,2} = -\frac{m_e}{2}(\vec{v}_{0\parallel} \cdot \nabla_{1\parallel} v_{1\parallel} + \vec{v}_{1\parallel} \cdot \nabla_{0\parallel} v_{0\parallel}) \tag{4.5}$$

because it includes parallel velocity components of pump and sideband LH waves. Here, a factor of $1/2$ is introduced because

$$\mathrm{Re}A\mathrm{Re}B = \frac{1}{2}\mathrm{Re}\left[AB + (AB)^*\right], \tag{4.6}$$

where $A = A_0 e^{i\vec{k}_A \cdot \vec{x} - i\omega_A t} + c.c.$ and $\mathrm{Re}A = 2A_0 \cos(\vec{k}_A \cdot \vec{x} - i\omega_A t)$. Using the notation of Equation 4.3, ϕ_{p1} and ϕ_{p2} can be expressed in terms of $\vec{k}$ as follows:

$$\phi_{p1} = \frac{e\phi_0\phi_1}{2m\omega_c^2}\frac{\vec{k}_{\perp} \cdot \vec{k}_{0\perp} \times \vec{\omega}_c}{ik_{\parallel}\omega_0\omega_1}(\omega_0 k_{\parallel} - \omega k_{0\parallel}), \tag{4.7a}$$

$$\phi_{p2} = \frac{-e\phi_0\phi_1}{2m\omega_0\omega_1}k_{0\parallel}k_{1\parallel}, \tag{4.7b}$$

where the wave-matching condition (i.e., Equation 4.2) and the vector identity $\vec{a} \times \vec{b} \cdot \vec{c} = \vec{c} \cdot \vec{a} \times \vec{b} = \vec{b} \cdot \vec{c} \times \vec{a}$ are used. Then, the electron density fluctuation of the

[1] In Liu's paper, only the 1st term on the RHS was retained. Porkolab and Takase retained this term in their derivation, but this term was typically neglected due to their small contribution. In thesis, this term is retained because this term can lead to stronger convective growth at the plasma edge, as discussed further in Section 4.4.

low-frequency ion mode due to both ϕ and $\phi_p = (\phi_{p1} + \phi_{p2})$ is obtained as follows:

$$n = \frac{\epsilon_0 k^2}{e} \chi_e (\phi + \phi_p), \tag{4.8}$$

where χ_e is the electron susceptibility. Here, as mentioned cariler, the non-linear contribution from the $n_0 v_1 + n_1 v_0$ term in the equation of continuity is smaller by ω/ω_0 than that due to the ponderomotive potential term, and is neglected.

Substituting Equation 4.8 into Poisson's equation, the equation that governs the response of the low-frequency ion mode potential ϕ in the presence of the ponderomotive potential ϕ_p becomes [34, 91]

$$\epsilon \phi = -\chi_e \phi_p, \tag{4.9}$$

where $\epsilon = 1 + \chi_e + \chi_i$ is the low-frequency ion mode dielectric function.[2] This expression allows one to write the density fluctuation of the low-frequency ion mode in terms of ϕ only:

$$n = n^{linear} + n^{nonlinear} = \frac{\epsilon_0 k^2}{e} \chi_e (\phi + \phi_p) = \frac{\epsilon_0 k^2}{e} (\chi_e - \epsilon) \phi \tag{4.10}$$

Consider now the equation that governs the response of the LH sideband potential ϕ_1 in the presence of ϕ. The non-linear response of the LH sideband arises through the term $\nabla \cdot (n\vec{v})$ in the continuity equation. The dominant drive term is the product of the electron density fluctuation of the low-frequency ion mode and the electron velocity of the pump LH wave:

$$\frac{\partial n_1^{nl}}{\partial t} + \nabla \cdot (n v_0) = 0 \Rightarrow n_1^{nl} = n \frac{\vec{k}_1 \cdot \vec{v}_0^*}{2\omega_1}. \tag{4.11}$$

Here, the contributions from both the $n_0 v$ term in the continuity equation and the ponderomotive force term ($n_0^0 v_{pondero}$) are smaller by ω/ω_0 than the term retained.

[2] As discussed in Chapter 2.3, to follow the convention used in Stix, the dimensionless effective dielectric constant is defined as ϵ.

Substituting Equation 4.10 and Equation 4.11 in Possion's equation leads to

$$\epsilon_1\phi_1 = -\frac{e}{\epsilon_0 k_1^2}\frac{\vec{k}_1\cdot\vec{v}_0^*}{2\omega_1}n \tag{4.12a}$$

$$= (\epsilon-\chi_e)\frac{k^2}{k_1^2}\frac{\vec{k}_{1\perp}\cdot\vec{v}_{0\perp}^* + \vec{k}_{1\parallel}\cdot\vec{v}_{0\parallel}^*}{2\omega_1}\phi, \tag{4.12b}$$

where $\epsilon_1 = 1+\chi_{i1}+\chi_{e1}$ is the LH sideband dielectric function. The susceptibilities in the kinetic limit is given in Equation 4.35.

By combining the equations for ϕ and ϕ_1, the parametric dispersion relation can be constructed

$$\epsilon_1\phi_1 = \frac{\chi_e-\epsilon}{\epsilon}\chi_e\frac{k^2}{k_1^2}\frac{1}{2\omega_1}(\vec{k}_{1\perp}\cdot\vec{v}_{0\perp}^* + \vec{k}_{1\parallel}\cdot\vec{v}_{0\parallel}^*)(\phi_{p1}+\phi_{p2}). \tag{4.13}$$

In order to simplify the RHS of this equation, the expression for the pump velocity $\vec{v}_0$ is substituted, and the first term can be evaluated as follows:

$$(\vec{k}_{1\perp}\cdot\vec{v}_{0\perp}^*)\phi_{p1} \approx \phi\frac{1}{2\omega_1}\frac{e^2}{m^2}\frac{k_{1\perp}^2k_{0\perp}^2\phi_0^2\sin^2\delta}{\omega_{ce}^2}\left(1-\frac{\omega}{\omega_0}\frac{k_{0\parallel}}{k_\parallel}\right) \tag{4.14a}$$

$$\approx \phi\frac{1}{2\omega_1}\frac{e^2}{m^2}\frac{k_{1\perp}^2k_{0\perp}^2\phi_0^2\sin^2\delta}{\omega_{ce}^2} \tag{4.14b}$$

where the term $\triangle \equiv 1-\frac{\omega}{\omega_0}\frac{k_{0\parallel}}{k_\parallel}$ is assumed to be 1 because the LH wave satisfies $\omega_0/k_{0\parallel} \gg v_{te}$ (i.e., fluid limit) and the low-frequency ion mode turns out to satisfy $\omega/k_\parallel \lesssim v_{te}$ (i.e., kinetic limit). In a similar manner, the remaining terms on the RHS of Equation 4.13 are evaluated as follows:

$$(\vec{k}_{1\perp}\cdot\vec{v}_{0\perp}^*)\phi_{p2} + (\vec{k}_{1\parallel}\cdot\vec{v}_{0\parallel}^*)\phi_{p1} = -\frac{ie^2\phi_0^2\phi_1}{2m^2\omega_c^2}k_{1\perp}k_{0\perp}\omega_c\frac{k_{0\parallel}k_{1\parallel}}{\omega_0\omega_1}(1-\triangle) \tag{4.15a}$$

$$\approx 0 \tag{4.15b}$$

$$(\vec{k}_{1\parallel}\cdot\vec{v}_{0\parallel}^*)\phi_{p2} = \phi_1\frac{1}{2\omega_1}\frac{e^2}{m^2}\frac{k_{1\parallel}^2k_{0\parallel}^2\phi_0^2}{\omega_0^2} \tag{4.16}$$

With this manipulation, the parametric dispersion relation is reduced to a simple-looking form:

$$\epsilon\epsilon_1 + \frac{(1+\chi_i)\chi_e}{4}(\mu^-)^2 = 0, \tag{4.17}$$

with the coupling coefficient μ^-

$$(\mu^-)^2 = \frac{e^2}{m^2}\frac{\omega_0^2}{\omega_1^2}\frac{k^2}{k_1^2}\left(\frac{[(\vec{E}_{0\perp}\times\vec{k}_{1\perp})\cdot\hat{z}]^2}{\omega_{ce}^2\omega_0^2} + \frac{k_{1\parallel}^2 E_{0\parallel}^2}{\omega_0^4}\right) \tag{4.18a}$$

$$\approx \frac{e^2}{m^2}\frac{k^2}{k_1^2}\left(\frac{[(\vec{E}_{0\perp}\times\vec{k}_{1\perp})\cdot\hat{z}]^2}{\omega_{ce}^2\omega_0^2} + \frac{k_{1\parallel}^2 E_{0\parallel}^2}{\omega_0^4}\right). \tag{4.18b}$$

Here, the first term on the right-hand side is due to the $\vec{E}\times\vec{B}$ motion of electrons (i.e., perpendicular coupling) and the second term is due to the parallel motion of electrons driven by $\vec{E}_\parallel$ (i.e., parallel coupling). The contribution of the parallel coupling becomes important at the plasma edge [34, 12]. The ratio of the parallel coupling term to the perpendicular coupling term can be approximated to be

$$\frac{(k_{1\parallel}E_{0\parallel}/\omega_0)^2}{[(\vec{E}_{0\perp}\times\vec{k}_{1\perp})\cdot\hat{z}/\omega_{ce}]^2} \approx \frac{k_{0\parallel}^4\omega_{ce}^2}{k_{0\perp}^4\omega_0^2} \approx \frac{\omega_0^2\omega_{ce}^2}{\omega_{pe}^4} \tag{4.19}$$

with the use of the LH dispersion relation relevant at the plasma edge ($k_{0\perp} \approx -k_{0\parallel}\omega_{pe}/\omega_0$). For typical Alcator C-Mod edge plasmas at the low-field side ($B \approx 4\,\mathrm{T}$), parallel coupling becomes comparable to perpendicular coupling below the density $n_e \approx 6.3\times10^{18}\,\mathrm{m}^{-3}$. Near the high-field side edge ($B \approx 8\,\mathrm{T}$), parallel coupling becomes dominant below $n_e \approx 1.3\times10^{19}\,\mathrm{m}^{-3}$.

This dispersion relation can be extended to include the contribution of the upper sideband LH wave, and the resulting dispersion relation becomes [34, 91]

$$\epsilon + \frac{(1+\chi_i)\chi_e}{4}\left[\frac{(\mu^-)^2}{\epsilon_1} + \frac{(\mu^+)^2}{\epsilon_2}\right] = 0, \tag{4.20}$$

where $\epsilon_2 = 1+\chi_{i2}+\chi_{e2}$ is the dielectric function of the upper sideband LH wave with the susceptibilities defined in Equation 4.35. and μ^+ is the relevant coupling

coefficient

$$(\mu^+)^2 \approx \frac{e^2}{m^2}\frac{k^2}{k_2^2}\left(\frac{[(\vec{E}_{0\perp}\times\vec{k}_{2\perp})\cdot\hat{z}]^2}{\omega_{ce}^2\omega_0^2}+\frac{k_{2\parallel}^2E_{0\parallel}^2}{\omega_0^4}\right). \tag{4.21}$$

4.2.2 Analytic estimates of growth rates

In the case of the LH parametric decay, two relevant low-frequency ion modes are ion sound quasi-mode and ion cyclotron quasi-mode. Quasi-modes refer to the modes that are not supported by the plasma without the non-linear drive. Thus, these modes are generally heavily damped either due to ion/electron Landau damping, or ion cyclotron Landau damping, depending on the dominant imaginary term of the electron/ion susceptibilities. For quasi-modes, the wave-matching condition depends mainly on $k_\parallel$ [34], and the resulting quasi-modes may possess a finite growth rate for an extended perpendicular wave-number space. Note that the lower sideband LH wave is still expected to be nearly resonant (i.e., $\epsilon_R(\omega_1)\approx 0$).

The decay into resonant ion cyclotron (acoustic) mode is only possible in the low density regime. It is interesting to note [91] that the resonant decay of the pump LH wave into another LH wave and ion acoustic (cyclotron) wave is not easily achievable unless the density is low enough that an electron plasma wave can be assumed $[(k_\parallel^2/k^2)(m_i/m_e)\gtrsim 10]$. This can be thought of in the limit of the dipole pump case so that the magnitudes of the wave-vectors of the sideband LH wave and the low-frequency ion mode are the same ($|\vec{k}_1|=|\vec{k}|$). When the frequency of the sideband LH wave is close to ω_{lh}, it needs to satisfy

$$\frac{m_i}{m_e}\frac{k_\parallel^2}{k^2}\approx O(1), \tag{4.22}$$

while the resonant ion acoustic wave needs to satisfy

$$\frac{\omega}{k_\parallel v_{te}}\ll 1. \tag{4.23}$$

However, these conditions cannot be easily satisfied at the same time because

$$\frac{\omega}{k_{\|}v_{te}} \approx \frac{kC_s}{k_{\|}v_{te}} = \frac{k}{k_{\|}}\sqrt{\frac{m_e}{m_i}} \approx O(1). \tag{4.24}$$

, where $C_s = \sqrt{T_e/m_i}$ is the acoustic speed. Thus, in this case, $\mathrm{Im}[Z(\zeta)] \simeq O(1)$, $|\epsilon_R| \simeq |\epsilon_I|$, and strong Landau damping occurs.

Ion cyclotron quasi-mode

In this section, Porkolab's treatment [34] is reviewed to characterize different kinds of ion cyclotron quasi-modes. Based on the assumption that the lower-sideband LH wave is resonant $[\epsilon_{1R}(\omega_1) \approx 0]$ with $\omega_1 = \omega_0 - \omega > 0$, the dielectric function of the lower-sideband LH wave can be Taylor-expanded as

$$\epsilon_1(\omega_1) \simeq -i\gamma \left|\frac{\partial \epsilon_{1R}}{\partial \omega^-}\right|_{\omega^- = \omega_1} + i\epsilon_{1I}(\omega_1) \tag{4.25a}$$

$$\cong -i(\gamma + \Gamma_1)\left|\frac{\partial \epsilon_{1R}}{\partial \omega^-}\right|_{\omega^- = \omega_1}, \tag{4.25b}$$

where the real term of the frequency and the growth rate γ are introduced in the frequencies of the lower-sideband LH wave $\omega_1 = \omega_{1R} + i\gamma$ and the low-frequency ion mode $\omega = \omega_R + i\gamma$, and $\Gamma_1 = -\epsilon_{1I}(\omega_1)/|\partial\epsilon_{1R}/\partial\omega_1|$ is the linear damping rate of the lower sideband LH wave. Substituting Equations 4.25 (a) and (b) in the parametric dispersion relation (i.e., Equation 4.20), the growth rate is explicitly written as

$$\gamma = -\Gamma_1 - \frac{\mu^2}{4|\partial\epsilon_{1R}/\partial\omega_1|}\mathrm{Im}\left(\frac{\chi_e(\omega)\chi_i(\omega)}{\epsilon(\omega)}\right) \tag{4.26a}$$

$$= -\Gamma_1 - \frac{\mu^2}{4}\frac{\epsilon_I(\chi_{eR}\chi_{iR} - \chi_{eI}\chi_{iI}) - \epsilon_R(\chi_{eI}\chi_{iR} + \chi_{iI}\chi_{eR})}{\left|\frac{\partial\epsilon_{1R}}{\partial\omega_1}\right|(\epsilon_I^2 + \epsilon_R^2)} \tag{4.26b}$$

In the decay channel with the ion cyclotron (quasi-) mode, Porkolab's analytic study considered three different low-frequency ion mode regimes (i.e., resonant ion cyclotron waves, ion cyclotron quasi-modes, and nonresonant quasi-modes) in the limit of perpendicular coupling, depending on the values of $\mathrm{Im}(\chi_i\chi_e/\epsilon)$ [34]. The

sideband LH mode is assumed to be resonant in all cases.

1. Resonant decay into ion cyclotron waves and LH waves

   (a) Ion mode: $\epsilon_R \approx 0$ and $\epsilon_I \simeq (\gamma + \Gamma)(\partial\epsilon_R/\partial\omega)$

   (b) Sideband LH mode: $\epsilon_{1R} \approx 0$ and $\epsilon_{1I} \simeq (\gamma + \Gamma_1)(\partial\epsilon_{1R}/\partial\omega_1)$

2. Ion cyclotron quasi-modes and LH waves: ion modes are strongly damped modes.

   (a) Ion mode: $|\epsilon_R| \ll |\epsilon_I|$ and $\omega_R/k_\parallel v_{te} \approx 1$ (electron Landau damping) or/and $(\omega_R - n\omega_{ci})/k_\parallel v_{ti} \approx 1$ (ion cyclotron damping)

   (b) Sideband LH mode: $\epsilon_{1R} \approx 0$ and $\epsilon_{1I} \simeq (\gamma + \Gamma_1)(\partial\epsilon_{1R}/\partial\omega_1)$

3. Nonresonant quasi-modes and LH waves: ion modes have no resemblance to any normal modes.

   (a) Ion mode: $|\epsilon_R| \gg |\epsilon_I|$ and $\omega_R \approx k_\parallel v_{te}$

   (b) Sideband LH mode: $\epsilon_{1R} \approx 0$ and $\epsilon_{1I} \simeq (\gamma + \Gamma_1)(\partial\epsilon_{1R}/\partial\omega_1)$

First, in the case of the resonant decay into ion cyclotron (acoustic) waves (i.e., $\epsilon_R(\omega, \vec{k}) \simeq 0$, $\epsilon_I(\omega, \vec{k}) \simeq (\gamma + \Gamma)(\partial\epsilon_R/\partial\omega)$, the analytic growth rate is given by

$$(\gamma + \Gamma)(\gamma + \Gamma_1) = -\frac{\mu^2 \chi_{eR}(\omega)\chi_{iR}(\omega)}{4(\partial\epsilon_R/\partial\omega)|\partial\epsilon_{1R}/\partial\omega_1|}, \tag{4.27}$$

where $\Gamma = \epsilon_I(\omega)/(\partial\epsilon_R/\partial\omega)$. Assuming $\omega_R \approx \Omega_i$ and only keeping the first-cyclotron resonance term, the real term of the dielectric function of low frequency ion mode is found to be

$$\epsilon_R(\omega) = 1 + \frac{1}{k^2\lambda_{De}^2} - \frac{1}{k^2\lambda_{Di}^2}\frac{T_e}{T_i}\frac{\Omega_i^2}{\omega^2 - \Omega_i^2} 2I_1(b_i)e^{-b_i} - \frac{\omega_{pi}^2}{\omega^2}\frac{k_\parallel^2}{k^2}. \tag{4.28}$$

Note that solving for $\epsilon_R = 0$, while neglecting the $k_\parallel$ term, leads to the electrostatic ion cyclotron wave:

$$\omega^2 = \Omega_{ci}^2 \left[1 + \frac{2T_e\Gamma_1(b_i)}{T_i(1 + k^2\lambda_{De}^2)}\right]. \tag{4.29}$$

Substituting $\partial\epsilon_R/\partial\omega$ into Equation 4.27 leads to the growth rate in terms of plasma parameters

$$(\gamma+\Gamma)(\gamma+\Gamma_1)=\frac{U^2}{16C_s^2}\frac{\omega_{lh}^2}{\omega_0^2}\frac{\Omega_i^2\omega_1}{\omega}\frac{T_e}{T_i}2I_1(b_i)e^{-b_i}, \tag{4.30}$$

where $U=E_{0x}/B_0$ is the $\vec{E}\times\vec{B}_0$ velocity. Thus, for $\gamma\gg\Gamma$ and $\gamma\gg\Gamma_1$, $\gamma\propto E_0$. The numerical study showed that the condition $\gamma>\Gamma$ can be satisfied for typical parameters if $\omega_0>2\omega_{lh}$ and $U\gtrsim C_s$.

Second, in the case of the decay into (resistive) ion cyclotron quasi-modes, the low-frequency wave is strongly damped (i.e., $\Gamma>\gamma>\Gamma_1$) so that $|\epsilon_R|\ll|\epsilon_I|$ and $\gamma\left[\partial\epsilon_R(\omega)/\partial\omega\right]<\epsilon_I(\omega)$. It was pointed out that this is the case for higher densities or for $U<C_s$, and that it is appropriate to treat low-frequency ion modes as quasi-modes. In this case, the approximate expression of the growth rate becomes

$$\frac{\gamma}{\omega_0}\simeq-\frac{\Gamma_1}{\omega_0}+\frac{U^2}{8C_s^2}\frac{\omega_{lh}^2}{\omega_0^2}\frac{\omega_1}{\omega_0}\frac{\left(-\dfrac{\chi_{iR}(\omega)}{\epsilon_I(\omega)}\right)}{1+\dfrac{3}{2}\dfrac{\omega_{lh}^2}{\omega_1^2}\dfrac{k_\perp^2v_{ti}^2}{\omega_1^2}}, \tag{4.31}$$

where

$$\epsilon_I(\omega)=\frac{\pi^{1/2}}{k^2\lambda_{De}^2}\left[\frac{\omega}{k_\parallel v_{te}}\exp\left(-\frac{\omega^2}{k_\parallel^2v_{te}^2}\right)+\frac{T_e}{T_i}\frac{\omega}{k_\parallel v_{ti}}\Gamma_1(b_i)\exp\left(-\frac{(\omega-\omega_{ci})^2}{k_\parallel^2v_{ti}^2}\right)\right]. \tag{4.32}$$

Here ϵ_I is due to the electron Landau damping ($\omega_R/k_\parallel v_{te}\approx1$) and ion cyclotron damping [$(\omega_R-n\omega_{ci})/k_\parallel v_{ti}\approx1$] at the beat frequency ($\omega=\omega_0-\omega_1$).

Finally, in the case of the decay into non-resonant quasi-modes when $|\epsilon_R|\gg|\epsilon_I|$, the low-frequency mode has no resemblance to any normal modes. Its presence is completely due to the pump, and the drive mechanism is nonlinear electron Landau damping at the beat frequency. This decay channel is particularly important for short wavelengths if $T_e\simeq T_i$, $1\lesssim\omega_0/\omega_{lh}\lesssim3$. The analytic expression of the growth rate in this case is

$$\gamma\simeq-\Gamma_1+\frac{\mu^2}{4}\frac{\chi_{eI}(1-\delta)}{|\partial\epsilon_{1R}/\partial\omega_1|}, \tag{4.33}$$

where δ is due to hot-ion plasma effects and its typical value is $\delta>0.5$. Note that

$\gamma \propto E_0^2$ well above the threshold. The growth rate is maximized for $\omega_R \simeq k_\parallel v_{te}$. Since the maximum value of χ_{eI} is roughly $1/k\lambda_{De}^2$, the maximum growth rate is approximately

$$\frac{\gamma}{\omega_0} \simeq -\frac{\Gamma_1}{\omega_0} + \frac{U^2}{8C_s^2}\frac{\omega_{lh}^2}{\omega_0^2}\frac{\omega_1}{\omega_0}\frac{(1-\delta)}{1+\frac{3}{2}\frac{\omega_{lh}^2}{\omega_1^2}\frac{k_\perp^2 v_{ti}^2}{\omega_1^2}}. \tag{4.34}$$

This growth rate is comparable to that of ion cyclotron quasi-modes. This mode may couple to short wavelength hot-ion plasma waves and/or ion Bernstein waves. Since this instability exists for the shortest wavelength, it may have a lower convective threshold due to its relatively slow group velocity ($\omega_0/\omega_{lh} \lesssim 3$) of the sideband LH wave.

Ion sound quasi-mode

In the decay channel with the ion sound quasi-mode, the ion sound quasi-mode is heavily ion damped ($\omega_R \approx k_\parallel v_{ti}$) when $T_e \approx T_i$. Takase's analytic study [32, 49] showed that the growth rate of this mode increases like $\gamma + \Gamma_1 \propto E_0^2$ for pump powers just above the collisional threshold and the growth rate increases like $\gamma \propto E_0^{2/3}$ well above the threshold. Takase named the former the dissipative quasi-mode and the later the reactive quasi-mode. His numerical study showed that the transition from the decay into dissipative quasi-mode to the decay into reactive quasi-mode occurs for $\gamma \gtrsim \omega_R \gtrsim 2k_\parallel v_{ti}$ when $|\chi_{eI}|$ dominates over $|\chi_{iI}|$. The growth rate of this mode is generally found to be smaller than that of ion cyclotron quasi-mode and is finite only at the edge. This mode is thought to be responsible for the observed down-shifted LH frequency spectra in Alcator A LH heating experiments [49, 94].

4.3 Numerical Results

While the previous mode classification is useful in understanding the underlying non-linear drive, numerical simulations for tokamak plasma parameters show that a clear classification of the resulting modes is rather difficult [34, 49]. It is often found that $|\epsilon_R| \approx |\epsilon_I|$ and $|\chi_{eI}| \approx |\chi_{iI}|$. Since both electron Landau damping and ion

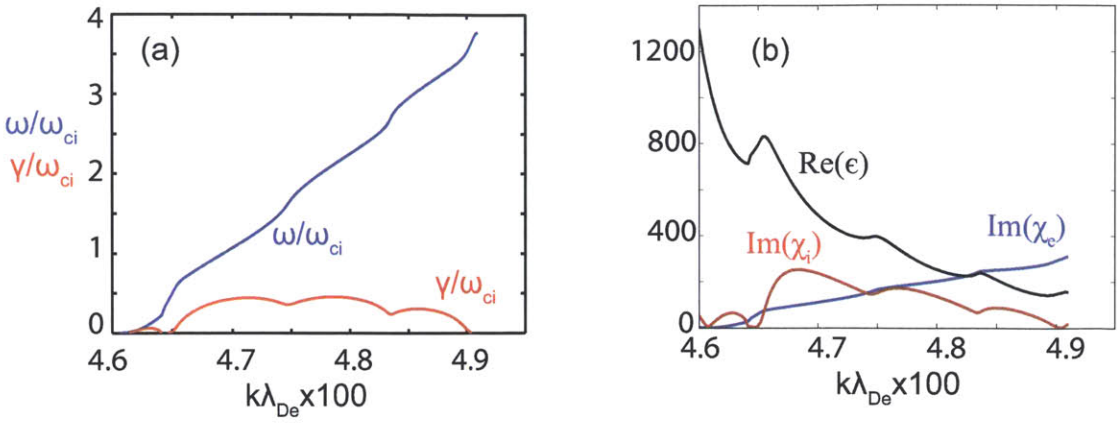

Figure 4-1: (a) Numerical solution of the parametric dispersion relation. Both ω_R/ω_{ci} (blue) and γ/ω_{ci} (red) are plotted against $k\lambda_{De}$. Parameters used are $B = 8\,\mathrm{T}$, $n_e = n_i = 10^{20}\,\mathrm{m}^{-3}$, $T_e = T_i = 40\,\mathrm{eV}$, $f_0 = 4.6\,\mathrm{GHz}$, $ck_{0\|}/\omega_0 = 2$, $ck_{\|}/\omega_0 = 7$, $E_\perp = 500\,\mathrm{kV/m}$, and $E_\| = 0\,\mathrm{kV/m}$. (b) Absolute magnitude of the real term of the dielectric function of the low-frequency mode $\mathrm{Re}(\epsilon)$, the imaginary term of the ion susceptibility $\mathrm{Im}(\chi_i)$, and electron susceptibility $\mathrm{Im}(\chi_e)$ of the low-frequency mode are plotted in black, blue, and red against $k\lambda_{De}$ for the same conditions as in (a).

cyclotron damping contribute in determining the growth rate for tokamak plasma parameters, these modes were generally referred to as ion cyclotron quasi-modes without making a distinction between resistive ion cyclotron quasi-modes and non-resonant ion cyclotron quasi-modes [32]. In this thesis, the same convention is adopted and only the distinction between ion sound quasi-mode and ion cyclotron quasi-mode will be made. Given the parametric dispersion relation, the parametric dependencies of the growth rate are examined for Alcator C-Mod plasmas.

Figure 4-1 shows an example of the solution of the parametric dispersion relation with parameters relevant to the Alcator C-Mod edge plasmas at the high-field side edge (deuterium, $B = 8\,\mathrm{T}$, $n_e = n_i = 10^{20}\,\mathrm{m}^{-3}$, and $T_e = T_i = 40\,\mathrm{eV}$) with the following parameters: $f_0 = 4.6\,\mathrm{GHz}$, $ck_{0\|}/\omega_0 = 2$, $ck_{\|}/\omega_0 = 7$, $E_\perp = 500\,\mathrm{kV/m}$, and $E_\| = 0\,\mathrm{kV/m}$. In this particular case[3], the contribution from the parallel coupling term is neglected, which is relatively small compared to that from the perpendicular coupling term at the assumed density. To include hot plasma effects in the simulations, such as Landau damping and finite Larmor radius effects, the following

[3]By taking $E_\| = 0\,\mathrm{kV/m}$, another purpose of this numerical study was to compare results to the results based on Alcator C parameters [12].

electron and ion susceptibilities are used in the numerical code:

$$\chi_e(\omega,k) = \frac{1}{k\lambda_{De}^2} \frac{1 + \dfrac{\omega + i\nu_e}{k_\parallel v_{te}} \Gamma_0(b_e) Z\left(\dfrac{\omega + i\nu_e}{k_\parallel v_{te}}\right)}{1 + \dfrac{i\nu_e}{k_\parallel v_{te}} \Gamma_0(b_e) Z\left(\dfrac{\omega + i\nu_e}{k_\parallel v_{te}}\right)}, \tag{4.35a}$$

$$\chi_i(\omega,k) = \frac{1}{k^2\lambda_{Di}} \left[1 + \frac{\omega}{k_\parallel v_{ti}} \sum_{n=-100}^{100} \Gamma_n(b_i) Z\left(\frac{\omega - n\Omega_i}{k_\parallel v_{ti}}\right)\right], \tag{4.35b}$$

where ν_e is the effective electron collision frequency due to electron-neutral and electron-ion collisions. Thus, the homogeneous threshold is determined by the collisional damping of the daughter waves. Nonetheless, it is found that the power threshold to overcome collisional damping is quite low ($P_{RF} \lesssim 10\,\mathrm{kW}$).

For given plasma parameters, $k_\perp$ is scanned to look for the frequencies of low-frequency ion modes ($\omega = \omega_R + i\gamma$) that satisfy the parametric dispersion relation. Note that wave-vectors are assumed to have only real terms. The usual way to display the solutions is to plot the numerically found ω_R/ω_{ci} and γ/ω_{ci} against $k\lambda_{De}$, as shown in Figure 4-1 (a). The small peak at near $k\lambda_{De} \times 100 = 4.63$ is due to ion sound quasi-mode ($\omega/\omega_{ci} \approx 0.1$). The multiple peaks up to third ion cyclotron-harmonics are also seen because the ion susceptibility is maximized at each cyclotron harmonic. These peaks generally exhibit higher growth rates than that of ion sound quasi-mode. This is due to relatively higher density plasmas even at the plasma edge of the Alcator C-Mod tokamak, unlike the cases in low density tokamaks such as JET [59, 60]. Figure 4-1 (b) shows that the low-frequency ion modes are quasi-modes since $\mathrm{Re}(\epsilon) \neq 0$. It also shows that the ion sound quasi-mode is driven by ion Landau damping and the ion cyclotron quasi-modes are driven by a combination of ion cyclotron and electron Landau damping. Although not shown here, the lower-sideband LH wave is found to be resonant ($\epsilon_{1R} \approx 0$), while the upper-sideband LH wave is off-resonant.

Figure 4-2 (a) shows γ/ω_{ci} as a function of ω/ω_{ci} for three different amplitudes of the perpendicular pump electric field: $E_{0\perp} = 150$, 300, and 600 kV/m. Other plasma parameters are fixed. As $E_{0\perp}$ increases, ion cyclotron harmonic features are washed

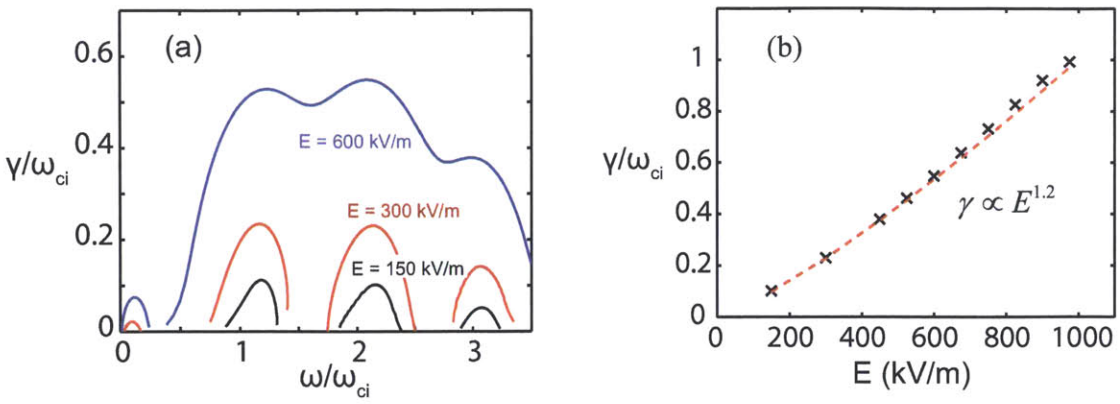

Figure 4-2: (a) Numerical solutions of the parametric dispersion relation for a deuterium plasma at three different perpendicular pump electric fields: $E_{0\perp} =$ 150, 300, and 600 kV/m. Other plasma parameters are $B = 8\,\mathrm{T}$, $n_e = n_i = 10^{20}\,\mathrm{m}^{-3}$, $T_e = T_i = 40\,\mathrm{eV}$, $f_0 = 4.6\,\mathrm{GHz}$, $ck_{0\|}/\omega_0 = 2$, $ck_{\|}/\omega_0 = 7$, and $E_{\|} = 0\,\mathrm{kV/m}$. (b) Dependence of the growth rate of the first ion cyclotron quasi-mode on $E_{0\perp}$. Other plasma parameters are the same as in (a).

out. Figure 4-2 (b) shows the maximum γ and the corresponding ω_R as a function of $E_{0\perp}$. The numerical scaling $\gamma \propto E^{1.2}$ is found well above threshold, contrary to the analytic scaling $\gamma \propto E^2$ that is shown in Equations 4.31 and 4.34.

Figure 4-3 (a) shows γ/ω_{ci} as a function of ω/ω_{ci} for three different densities, while other plasma parameters are fixed. The growth rate of ion cyclotron quasi-modes increases with the density, whereas the growth rate of ion sound quasi-modes remain nearly the same. As the density increases, ion cyclotron harmonic features are washed out. Figure 4-3 (b) shows the maximum γ and the corresponding ω_R as a function of n_e. While γ increases to ω_{ci} with the increasing density, the real frequency of the ion cyclotron quasi-mode remains more or less the same up to $n_e \approx 1.5 \times 10^{20}\,\mathrm{m}^{-3}$.

Figure 4-4 (a) shows γ/ω_{ci} as a function of ω/ω_{ci} for two different temperatures: $T_e = T_i = 40\,\mathrm{eV}$ and $T_e = T_i = 200\,\mathrm{eV}$. Other plasma parameters are fixed. Higher local temperature lowers the peak growth rate and shifts the peak growth rate to the higher ω_R, consistent with the theory that $\omega_R \approx k_{\|} v_{te}$. Figure 4-4 (b) shows the maximum growth rate and the corresponding ω_R as function of $v_{te}/c \propto \sqrt{T_e}$. Due to the presence of the ion cyclotron harmonic peaks, ω_R exhibits discrete jumps, but one can scale the dependence of ω_R on the temperature as $\omega_R \approx 0.3 k_{\|} v_{te}$.

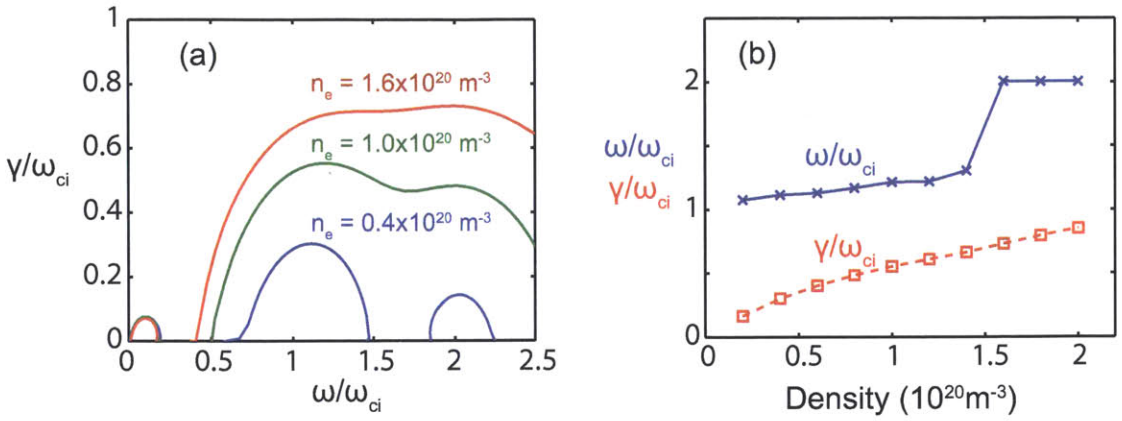

Figure 4-3: (a) Numerical solutions of the parametric dispersion relation for a deuterium plasma at three different densities: $n_e = 0.4$, 1.0, and $1.6 \times 10^{20}\,\mathrm{m}^{-3}$. Other plasma parameters are $B = 8\,\mathrm{T}$, $T_e = T_i = 25\,\mathrm{eV}$, $f_0 = 4.6\,\mathrm{GHz}$, $ck_{0\|}/\omega_0 = 2$, $ck_\|/\omega_0 = 7$, $E_\| = 0\,\mathrm{kV/m}$, and $E_\perp = 525\,\mathrm{kV/m}$. (b) Dependence of the maximum growth rate and the corresponding real frequency of the ion cyclotron quasi-modes on local plasma densities. Other plasma parameters are the same as in (a).

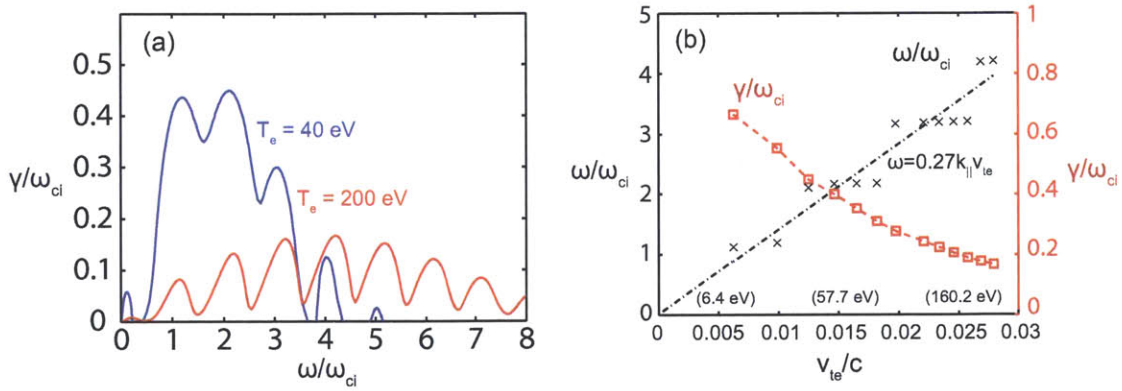

Figure 4-4: (a) Numerical solutions of the parametric dispersion relation for a deuterium plasma with two different temperatures: $T_e = 40$ and 200 eV. Other plasma parameters are $B = 8\,\mathrm{T}$, $n_e = n_i = 10^{20}\,\mathrm{m}^{-3}$, $T_e = T_i$, $f_0 = 4.6\,\mathrm{GHz}$, $ck_{0\|}/\omega_0 = 2$, $ck_\|/\omega_0 = 7$, $E_\| = 0\,\mathrm{kV/m}$, and $E_\perp = 525\,\mathrm{kV/m}$. (b) Dependence of the maximum growth rate and the corresponding real frequency of the ion cyclotron quasi-modes on local temperature. The dashed-dot line corresponds to $\omega_{R,max} \approx 0.27 k_\| v_{te}$. Other plasma parameters are the same as in (a).

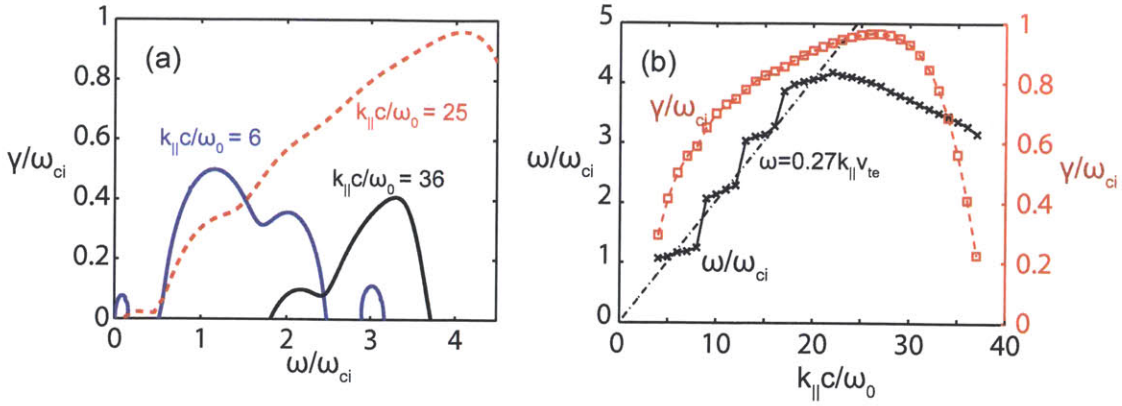

Figure 4-5: (a) Numerical solutions of the parametric dispersion relation for a deuterium plasma with three different parallel wave-numbers of the low-frequency ion mode: $k_{\|}c/\omega_0 = 6$, 25, and 36. Other plasma parameters are $B = 8\,\mathrm{T}$, $n_e = n_i = 10^{20}\,\mathrm{m}^{-3}$, $T_e = T_i = 25\,\mathrm{eV}$, $f_0 = 4.6\,\mathrm{GHz}$, $ck_{0\|}/\omega_0 = 2$, $E_{\|} = 0\,\mathrm{kV/m}$, and $E_{\perp} = 525\,\mathrm{kV/m}$. (b) Dependence of the maximum growth rate and the corresponding real frequency of the ion cyclotron quasi-modes on the parallel wave-numbers of the low-frequency ion mode. The straight line corresponds to $\omega_{R,max} \approx 0.27 k_{\|} v_{te}$. Other plasma parameters are the same as in (a).

Experimentally, the peaking of the higher harmonics in the LH spectra was observed in Alcator C [12] and FTU [58]. In Alcator C, in the limit $\omega_0/\omega_{lh}(0) \to 2$ the observed ion cyclotron harmonic peaks did not monotonically decrease, but there was a second peaking around $|\omega_1/\omega_0 \simeq 0.85|$. The measured spectra in FTU showed that the dominant peaking was around the 10^{th} ion cyclotron harmonics. Two different mechanisms were proposed. In Alcator C, it was thought to be due to ion cyclotron PDI that was excited at a region where the temperature was higher. On the one hand, the observed peaking in FTU was explained by the presence of the higher $n_{\|}$ components that are thought to be excited by ion sound quasi-modes at the plasma edge right in front of the launcher. It can be seen that the two different explanations are grounded in the different views not only on the fundamental mechanism but also on the radial location where the responsible PDI is excited.

Figure 4-5 (a) shows γ/ω_{ci} as a function of ω/ω_{ci} for three different $k_{\|}$: $k_{\|} = 6$, 25, and 36. Other plasma parameters are fixed. Higher $k_{\|}$ shifts the peak γ to higher ω_R, again consistent with the theory that $\omega_R \approx k_{\|} v_{te}$. Figure 4-5 (b) shows the maximum γ and the corresponding ω_R as function of $k_{\|}c/\omega_0$. The γ increases until

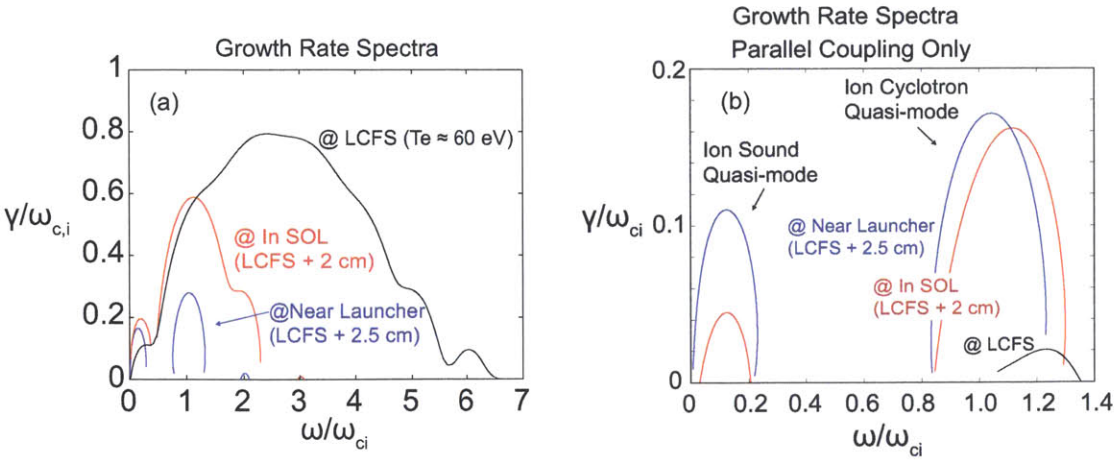

Figure 4-6: (a) Numerical solutions of the parametric dispersion relation for a deuterium plasma at the three different radial locations: (1) at the LCFS ($R = R_{LCFS}$, $n_e = 5.58\times10^{19}\,\mathrm{m}^{-3}$, and $T_e = 64.3\,\mathrm{eV}$), (2) at the scrape-off layer ($R = R_{LCFS}+2\,\mathrm{cm}$, $n_e = 1.99\times10^{19}\,\mathrm{m}^{-3}$, and $T_e = 14.9\,\mathrm{eV}$), and (3) at the mouth of the launcher ($R = R_{LCFS}+2.5\,\mathrm{cm}$, $\mathrm{n_e} = 0.77\times10^{19}\,\mathrm{m}^{-3}$, and $T_e = 10.0\,\mathrm{eV}$). The density and temperature are determined from the fitted profiles based on the measurements shown in Figure 4-7. Other parameters are $f_0 = 4.6\,\mathrm{GHz}$, $ck_{0\|}/\omega_0 = 2$, $ck_{\|}/\omega_0 = 7$, and $P_{RF} = 100\,\mathrm{kW}$.

Landau damping of the sideband LH wave becomes significant $|\omega_1/k_{1,\|}v_{te}|\approx 3$. In this particular case, this critical value approximately corresponds to $k_{\|}c/\omega_0 = 25$, corresponding to $|\omega_1/k_{1,\|}v_{te}|\approx 4$. Up to this value, the scaling $\omega_R \approx 0.3k_{\|}v_{te}$ is numerically found. This result shows that the LH sideband with the higher $n_{1,\|}$ is likely to have a higher mode amplitude than the LH sideband with the lower $n_{1,\|}$. Note, however, Landau damping will be also strong at the same time. Note also that, to match the growth rate spectra to the experimentally observed LH frequency spectra that show the peaking at the first ion cyclotron harmonic (e.g., See Chapter 5), it is assumed that $k_{\|}c/\omega_0 \approx 7$ in the rest of this chapter so that the growth rate is peaked at around the first ion cyclotron harmonic.

Figure 4-6 (a) shows the growth rate spectra at three different radial locations based on the fitted edge profiles in high density L-mode plasmas ($\overline{n}_e \approx 1.2\times10^{20}\,m^{-3}$), as shown in Figure 4-7. The edge density is measured with a Thomson scattering diagnostic and X-mode reflectometer. The core profile inside the LCFS is smoothly connected to the SOL profile. Note that the density profile

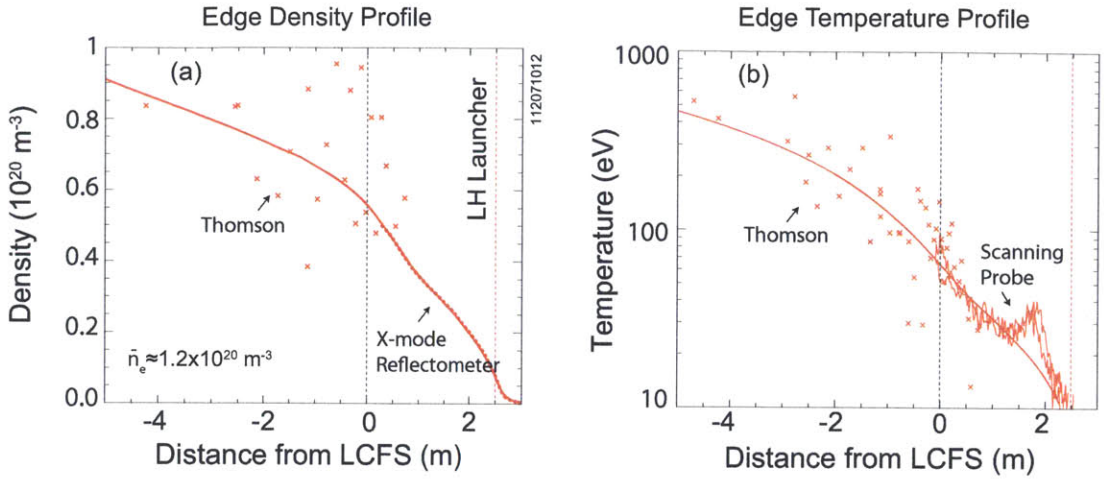

Figure 4-7: (a) Measured edge density profile with a Thomson scattering diagnostic and X-mode reflectometer in front of the launcher in a USN L-mode plasma at $\overline{n}_e \approx 1.2 \times 10^{20}\,\mathrm{m}^{-3}$. The line shows the fitted edge density profile. (b) Measured edge temperature profile. The line shows the fitted edge temperature profile. The reason for the bump in the SOL temperature profile is not clear.

measured with a scanning probe matches well with that measured with the X-mode reflectometer, although not shown here. The edge electron temperature is measured with the scanning probe. $T_e = T_i$ is assumed. The competition between the local density and temperature determines the local growth rate. In calculating this, the local electric field is estimated from the WKB theory, assuming the resonance cone propagation as shown in Chapter 2. This assumption is expected to be valid, at least, on the first-pass toward the plasma core. The typical temperature at the LCFS is around at $60 \sim 70$ eV, which results in the peaking of the maximum growth rate at higher harmonics ($\omega_R = 2 \sim 3\,\omega_{ci}$).

The homogeneous growth rate spectra due to the parallel coupling term only at the three different radial locations are shown in Figure 4-6 (b). The homogeneous growth rate is significantly reduced as compared to the case when both coupling terms are retained. In addition, the growth rate decreases away from the launcher due to both the decrease in density (and $|E_{0\|}|$) and the increase in temperature.

Two important PDI characteristics can be inferred from the presented homogeneous growth rate spectra. First, regardless of the coupling types, ion cyclotron PDI is dominant over ion sound PDI for the Alcator C-Mod edge plasma

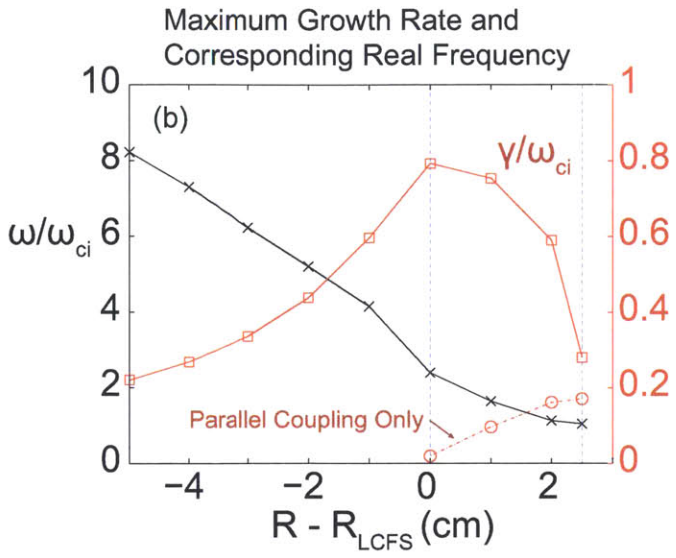

Figure 4-8: Dependence of the maximum growth rate (red) and the corresponding real frequency (black) of the ion cyclotron quasi-modes on the radial locations for a typical Alcator C-Mod high density USN L-mode plasma. The red solid curve is the maximum growth rate when both the perpendicular and parallel coupling terms are retained. The red dashed curve is the maximum growth rate when only the parallel coupling term is retained. The local density and temperature are taken from the measurements shown in Figure 4-7. Other parameters are $f_0 = 4.6\,\mathrm{GHz}$, $ck_{0\|}/\omega_0 = 2$, $ck_{\|}/\omega_0 = 7$, and $P_{RF} = 100\,\mathrm{kW}$.

due to a relatively higher edge density compared to that of other tokamaks [56, 59]. Second, the observed ion cyclotron PDI is expected to be excited at the plasma periphery, where the local temperature is relatively low ($T_e < 60 \sim 70\,\mathrm{eV}$). This is because the observed dominant peak is at the first harmonic. Thus, the focus will be given to the ion cyclotron PDI that is excited at the plasma periphery.

Figure 4-8 shows the maximum growth rate and the corresponding real frequency of the low-frequency ion modes as a function of radial locations. Two growth rate curves are shown. When both the perpendicular and parallel coupling terms are retained, the growth rate is peaked at the LCFS and decreases inside the LCFS with the increase in the local temperature. Inside the LCFS, the real frequency that corresponds to the maximum growth rate is peaked at higher harmonics. When only the parallel coupling term is kept, the growth rate is maximized near the launcher and its magnitude is noticeably weaker than that due to perpendicular coupling. Thus,

the growth rate due to the parallel coupling term is expected to be finite only at the plasma edge.

4.4 Convective Growth

The finite extent of the pump is considered to be one of the limiting mechanisms that determine the amplitude of the sideband LH waves. Since PDI can occur only in the presence of the pump LH wave, the resonance cone propagation of the pump introduces a spatial structure where PDI can grow in space. While low-frequency ion modes are heavily damped, the amplitude of resonant sideband LH modes can grow in space if they propagate within the pump resonance cone. Nonetheless, they will convect out of the pump resonance cone due to the different propagation directions determined by the coupling types. Even in the parallel coupling limit, a slightly lower frequency of the sideband LH wave than that of the pump LH wave will make the sideband propagate at an angle to the pump resonance cone.

The two limiting factors that determine the amplification factor ($A \equiv \gamma\Delta t$) of the sideband LH wave, other than the growth rate, are the distance ($\Delta\xi$) that the sideband LH mode propagates across the pump resonance cone and the group velocity ($\vec{v}_{1g,\xi}$) of the sideband LH mode in that direction:

$$\Delta t = \frac{\Delta\xi}{|v_{1g,\xi}|} \tag{4.36}$$

These will determine the time (Δt) that the sideband LH waves stay within the pump resonance cone before convecting out, and thus the amplitude of the sideband LH waves [$\sim \exp(\gamma\Delta t)$].

In the following, the convective losses are examined in the perpendicular and parallel coupling limit. The purpose of this examination is to justify that the convective loss is minimized in the parallel coupling limit at the plasma edge, especially near the launcher where a well-defined pump resonance cone is expected. For simplicity, a spatially homogeneous plasma is assumed and only the lower

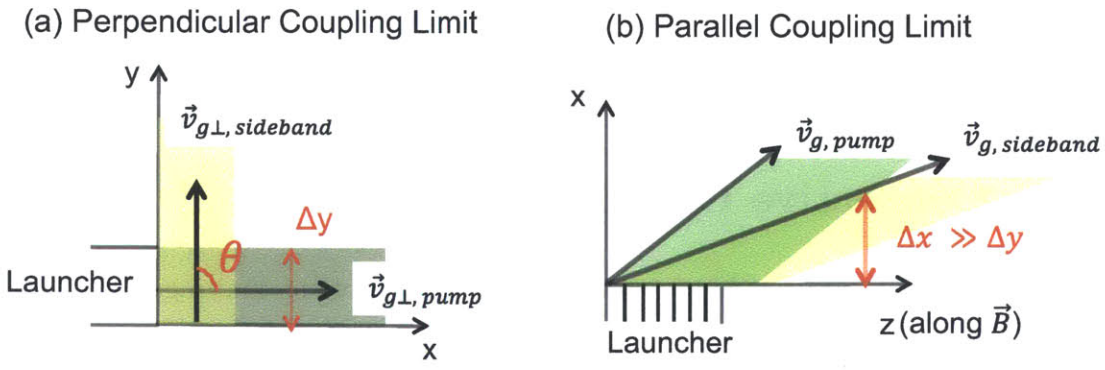

Figure 4-9: (a) Side view of the resonance cone trajectories of the pump (green) and sideband (yellow) LH waves near the launcher in the perpendicular coupling limit ($\theta = \pi/2$). (b) Top view of the resonance cone trajectories of the pump (green) and sideband (yellow) LH waves near the launcher in the parallel coupling limit ($\theta = 0$).

sideband LH wave is considered. At the plasma edge where $\omega_0 \gg \omega_{lh}(0)$, the electrostatic LH dispersion relation can be approximated by that of electron plasma waves $k_\perp^2 = (\omega_{pe}^2/\omega_j^2)k_\parallel^2$ from which the group velocity can be calculated:

$$\vec{v}_{j,g} = \frac{\omega_j}{k_\parallel}\left(\frac{\omega_j}{\omega_{pe}}\hat{k}_\perp + \hat{k}_\parallel\right) \tag{4.37}$$

It is assumed that the pump resonance cone mainly propagates in the radial and toroidal direction near the launcher

$$\vec{v}_{g0} = \frac{\omega_0}{k_{0\parallel}}\left(\frac{\omega_0}{\omega_{pe}}\hat{x} + \hat{z}\right), \tag{4.38}$$

while the group velocity of the sideband LH wave can be generally written as

$$\vec{v}_{g1} = \frac{\omega_1}{k_{1\parallel}}\left(\frac{\omega_1}{\omega_{pe}}\cos\theta\hat{x} + \frac{\omega_1}{\omega_{pe}}\sin\theta\hat{y} + \hat{z}\right), \tag{4.39}$$

where θ is the angle between $\vec{k}_{1\perp}$ and the x-axis.

At the edge, the convective loss is expected to be strong for the perpendicular coupling case. In the perpendicular coupling limit ($\theta = \pi/2$), the group velocity of the LH sideband is perpendicular to that of the pump, as shown in Figure 4-10

(a). Thus, the distance that the sideband LH wave stays inside the pump resonance cone is simply set by the height of the launcher ($\Delta y = h$). Assuming a growth rate on the order of ω_{ci}, the amplification factor is $A \sim (k_{1\parallel}h)\omega_{ci}\omega_{pe}/\omega_1^2$, which shows that the perpendicular coupling is not likely to result in strong amplification $A > \pi$ for typical edge plasma parameters. Note that in the classical ion cyclotron PDI limit $\omega_0/\omega_{lh}(0) \to 2$, ion cyclotron PDI is dominated by the perpendicular coupling term, and the slow group velocity ($v_g \propto 1/\sqrt{n_e}$) maximizes the amplification factor. Experimentally, in the limit of $\omega_0/\omega_{lh}(0) \to 2$, ion cyclotron PDI is expected to occur at $0.5 \lesssim r/a \lesssim 0.8$ in the ATC tokamak [35], and $r/a \gtrsim 3/4$ in the Alcator C tokamak [49].

On the other hand, in the parallel coupling limit ($\theta = 0$), the convective loss is minimized at the plasma edge [12]. In this case, the group velocity of the sideband LH wave is nearly aligned with that of the pump LH wave, as shown in Figure 4-9 (b). Note that the group velocity of the sideband LH wave is more aligned to the background magnetic field direction (z-direction) due to the relatively lower frequency of the sideband LH wave than that of the pump LH wave. Its lower frequency will make the sideband LH wave eventually convect out of the pump region. Taking one of the trajectories of the pump LH wave to be $z = \frac{v_{gz,0}}{v_{gx,0}}x + L_z$ and one of the trajectories of the sideband LH wave to be $z = \frac{v_{gz,1}}{v_{gx,1}}x$, where L_z is the length of the launcher in the z-direction, the maximum distance Δx that the sideband LH wave propagates across the pump resonance cone is [95]

$$\Delta x = \frac{L_z}{\left|\frac{v_{gz,1}}{v_{gx,1}} - \frac{v_{gz,0}}{v_{gx,0}}\right|}, \tag{4.40}$$

which is found to be much larger than the height of the typical launcher. Therefore, the resulting amplification factor is much larger than that of the perpendicular coupling limit ($\theta = 90°$), as shown in Figure 4-10, although the homogeneous growth rate is found to be smaller by an order of magnitude.

Since the parallel propagation of the sideband resonance cone along the pump

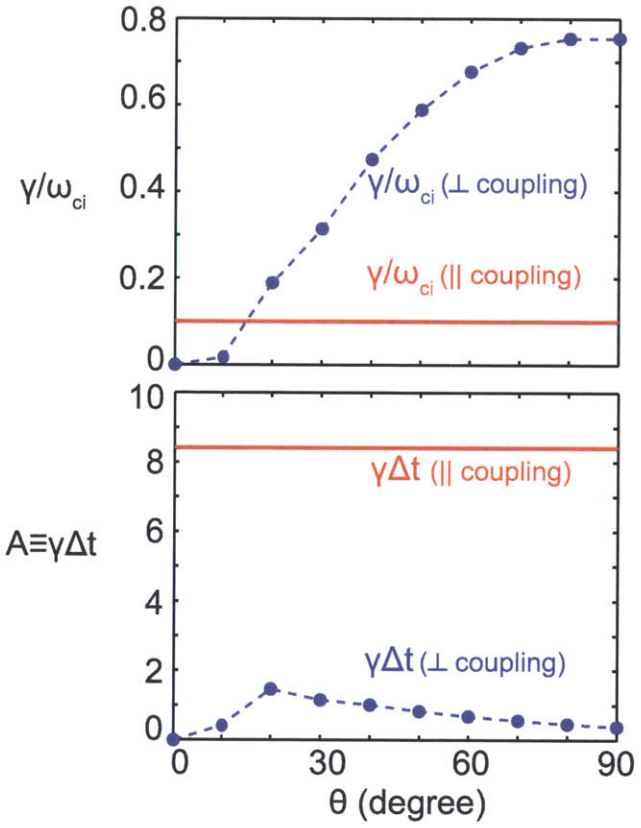

Figure 4-10: (a) Dependence of the maximum growth of the ion cyclotron quasi-mode on θ, which is the angle between $\vec{k}_{1\perp}$ and $\vec{k}_{\perp}$. (b) Dependence of the amplification factor ($A = \gamma\Delta t$) on θ. Two cases are shown. The dashed blue curve is the case when only the perpendicular term is retained in the parametric dispersion relation. The solid red curve is the case when only the parallel coupling term is retained, which is θ independent. Homogeneous plasma is assumed.

resonance cone ensures a longer residence time, one way to increase the residence time of the sideband LH wave, which is excited by the perpendicular coupling, is to consider its propagation with a smaller θ. Then, the sideband LH wave will pick up a finite group velocity along the radial direction. However, in this case, the perpendicular coupling is lost due to the presence of $\sin\theta$ term in the coupling coefficient and the growth rate decreases. As shown in Figure 4-10, the competition between the homogeneous growth rate and the residence time results in the peaking of the amplification factor near $\theta \approx 20°$. However, it is found to be smaller than π, and this particular coupling is not expected to play an important role either at the plasma edge.

While the parallel coupling term is expected to play an important role at the plasma edge, care should be taken when it comes to estimating the amplification factor to interpret the experimental data because the calculated Δx can be larger than the minor radius of the plasma. For example, one finds $\Delta x \approx \frac{\omega_0\omega_2}{\omega_{pe}\omega_{ci}} \approx 1.8\,\mathrm{m}$ with $n_e = 3.6 \times 10^{19}\,\mathrm{m}^{-3}$, which is longer than the major radius of the Alcator C-Mod tokamak. Moreover, the inhomogeneity in density and temperature could further affect the growth rate [34]. Previously, the use of ray-tracing codes [60, 96] was attempted to track the path of pump LH waves and spatial evolution of sideband LH waves, but this approach in general cannot be reliable in tracking all the possible paths of sideband LH waves because the excited modes will have a range of different parallel and perpendicular wave-vectors.

Furthermore, the presented model assumes fixed pump power and the physics of pump depletion cannot be discussed in the linear PDI theory. While analytic [93, 95] or ray-tracing [60, 96] calculations on the pump depletion (or saturation mechanism) have been previously treated, many of them are based on linear PDI theory. For example, in a similar way presented in Section 2, in which the coupled mode equations of the low-frequency ion mode and the sideband LH wave are solved, an attempt [95] was made by solving the coupled mode equations of the pump and the sideband LH mode. The power flow into the low-frequency ion mode was neglected. This is justified because the power redistribution is proportional to the frequency of the mode,

according to the Manley-Rowe relations. Another approach to explain the saturated non-linear sideband frequency spectrum is to perform power-cascading calculations that are studied by Liu [93]. This approach can explain a saturation mechanism other than the convective loss mechanism. However, this approach may not satisfactorily explain the observed peaking of the frequency spectra at higher harmonics.

4.5 Chapter Summary

In this chapter, the parametric dispersion relation relevant to LH waves [34] and convective growth mechanism are reviewed and studied.

By extending an approach by Liu [93], the parallel coupling term is added in the parametric dispersion relation, which can play an important role to ensure the convective growth of the excited LH sideband wave at the plasma edge. The relevant two low-frequency ion modes are ion sound quasi-mode ($\omega_R \approx k_\parallel v_{ti}$) [49] and ion cyclotron quasi-mode ($\omega_R \approx n\,\omega_{ci}$) [34]. To better characterize the nature of ion cyclotron quasi-modes, based on Porkolab's approach [34], three ion modes [i.e., resonant ion cyclotron mode ($\epsilon_R \approx 0$, where ϵ is the dielectric constant of the ion mode), resistive ion cyclotron quasi-mode ($|\epsilon_R| \ll |\epsilon_I|$, and $(\omega_R - n\omega_{ci})/k_\parallel v_{ti} \approx 1$ and/or $\omega_R/k_\parallel v_{te} \approx 1$), and non-resonant quasi-mode ($|\epsilon_R| \gg |\epsilon_I|$, and $\omega_R \approx k_\parallel v_{te}$)] in the range of ion cyclotron frequencies are reviewed.

Numerical studies with Alcator C-Mod plasmas show that the ion cyclotron quasi-mode has higher homogeneous growth rate over the ion sound quasi-mode and that the resulting mode in the range of ion cyclotron frequencies is a mixture of resistive ion cyclotron quasi-mode and non-resonant quasi-mode. Thus, in this thesis, no distinction between resistive ion cyclotron quasi-mode and non-resonant quasi-mode is made, and both are called as ion cyclotron quasi-modes [34]. Guided by the experimentally measured LH spectra that exhibit multiples of ion cyclotron down-shifted LH sidebands with the peaking at the first down-shifted LH sideband (e.g., See LH spectra presented in Chapter 5), the homogeneous growth rate calculation suggests that observed ion modes are excited at the relatively cold

region ($T_e \lesssim 60 \sim 70\,\mathrm{eV}$) with $k_\parallel c/\omega_0 \lesssim 10$. This is required to minimize the effect of non-resonant quasi-modes, which can shift the peak of the growth rate to higher ion cyclotron harmonics due to its characteristic mode frequency ($\omega_R \approx k_\parallel v_{te}$).

Regarding convective growth mechanisms, at the plasma edge, the parallel coupling term, rather than the perpendicular coupling term, is found to be important because it can result in a stronger convective growth as the sideband LH wave can propagate along the pump LH wave for a prolonged time before convecting out of the pump resonance cone.

In summary, it is shown that the dominant PDI process in Alcator C-Mod experiments is decay into ion cyclotron quasi-modes driven by the parallel coupling term.

THIS PAGE INTENTIONALLY LEFT BLANK

Chapter 5

Characterization of Onset of Parametric Decay Instability of Lower Hybrid Waves

5.1 Introduction

The purpose of this chapter is to understand the observed onset of ion cyclotron PDI in Alcator C-Mod high-density plasmas. Although local plasma parameters are more relevant in determining the characteristics of PDI, $\overline{n}_e$ is taken as a representative plasma parameter in interpreting PDI behavior, consistent with the observations [10] that the decrease in HXR emission rate is clearly correlated with the increase in $\overline{n}_e$. More focus is given to the observed ion cyclotron LH sidebands than pump broadening because the former exhibits a threshold-like behavior as a function of $\overline{n}_e$.

Based on these two arguments, the following two topics are discussed. First, the dependence of ion cyclotron PDI on the magnetic configuration is reported. Second, it is also attempted to identify mechanisms that can lead to the onset of ion cyclotron PDI by examining the homogeneous growth rate and convective growth mechanism.

The organization of this chapter is as follows. Section 2 describes the experimental setup and diagnostics used to measure the LH frequency spectra. Section 3 presents

the observations of LH frequency spectra in lower single null (LSN), inner wall limited (IWL), and upper single null (USN) plasmas. Section 3 correlates the scrape-off layer (SOL) densities with the strength of the ion cyclotron PDI that is excited at the low-field-side (LFS) edge. Section 4 discusses the possible role of ion cyclotron PDI on the loss of LHCD efficiency. Section 5 summarizes this chapter.

5.2 Experimental Setup

To continuously monitor LH frequency spectra using probes in a single plasma discharge at various locations simultaneously, a multi-channel spectrum analyzer has been developed. Figures 5-1 (a) and (b) show the schematic diagram of the developed heterodyne detection system and a picture of the corresponding system. Input signals at 4.6 GHz are first down-converted to 1.1 GHz by a fixed local oscillator (LO) at 3.5 GHz using a voltage control oscillator. At the second mixing stage, by controlling the frequency of the second LO, it is possible to select the input signals at a certain frequency. A waveform generator is connected to this second LO, which allows sweeping of the relevant frequency range in a similar way described in Appendix B. For example, the use of a triangular wave-form allowed conducting the spectral measurements with a repetition rate of 10$\sim$20 Hz and frequency bandwidth of $\sim$ 250 MHz. The low pass filter after the two mixing stages selects the spectral component and mainly determines the resolution bandwidth of this system. It is found that the use of a 100 kHz low pass filter is sensitive enough to resolve the changes in the LH frequency spectra. At the final stage, the power detector, which is discussed further in Appendix D, converts the input power into an output voltage that is proportional to the input power. Figure 5-2 shows a photo of the developed heterodyne detection system.

Figures 5-3 (a) and (b) show the poloidal and toroidal locations of the Langmuir probes installed at the various locations in the Alcator C-Mod tokamak. The electrical connection from the probes to the spectral recorders is made via 50 Ω coaxial cables, which minimizes transmission losses and parasitic pickup around the

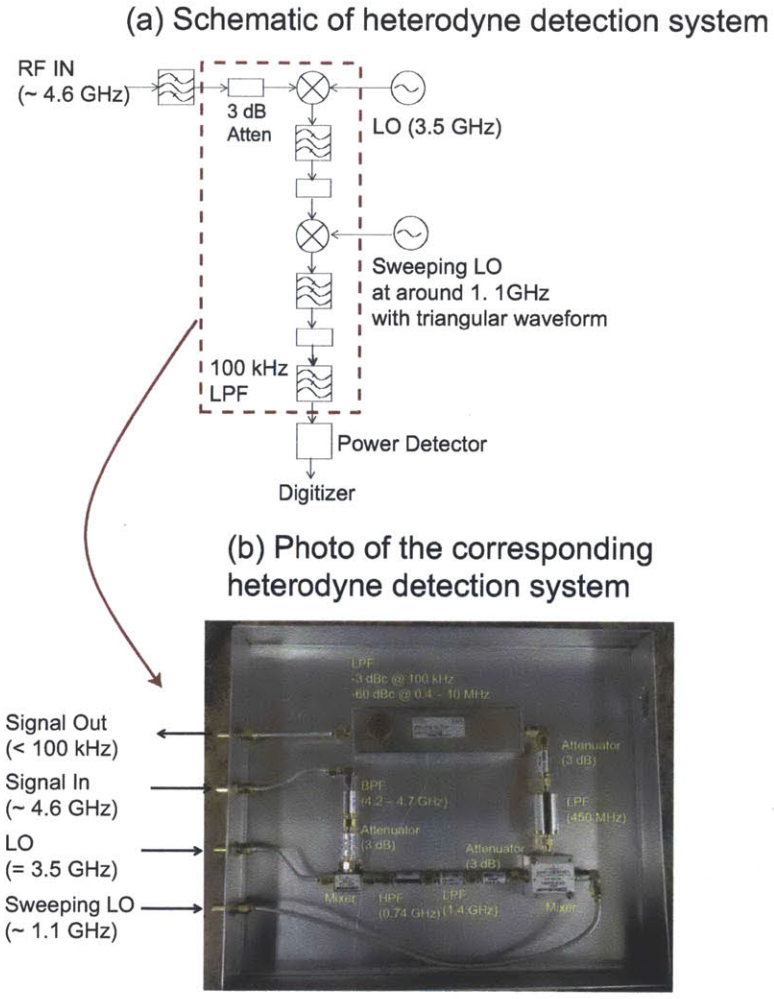

Figure 5-1: (a) Schematic diagram of the heterodyne detection system. Input RF power is converted into DC voltage proportional to the input power through the use of a logarithmic amplifier in a power detecting stage, which is described more in Appendix D. (b) Photo of the corresponding heterodyne detection system

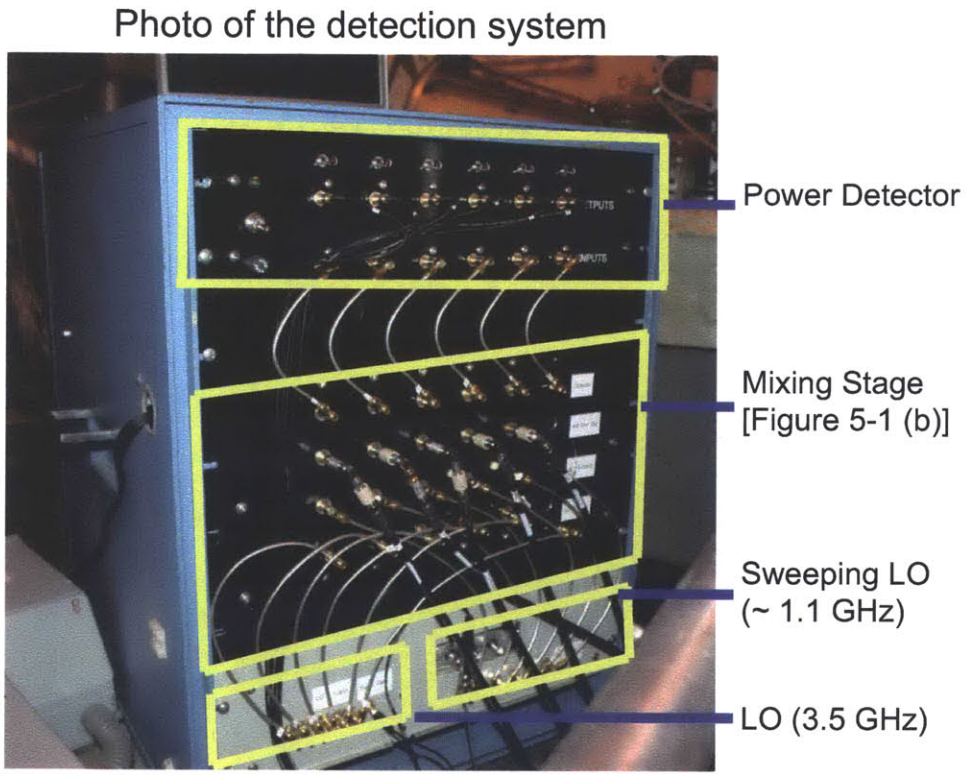

Figure 5-2: Photo of the six channel heterodyne detection system.

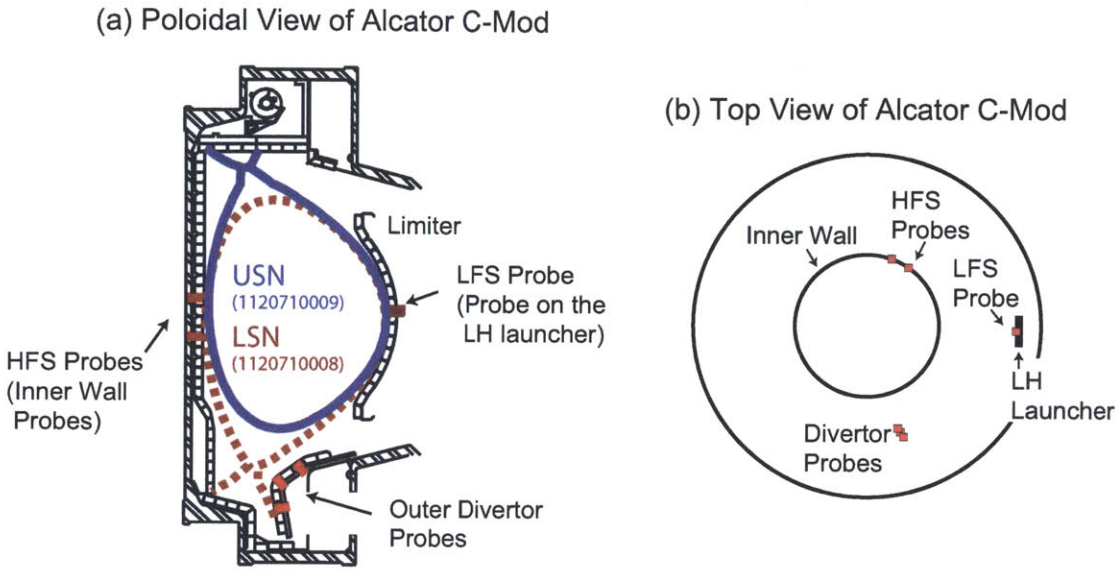

Figure 5-3: (a) Poloidal and (b) toroidal cross-section of the Alcator C-Mod tokamak showing the location of Langmuir probes: LFS probes (the probe on the LH launcher), HFS Probes (the probes on the inner wall), and outer divertor probes. Plots of the LCFS for USN (Shot No. 1120710009) and LSN (1120710008) plasmas are overlaid in red and blue, respectively.

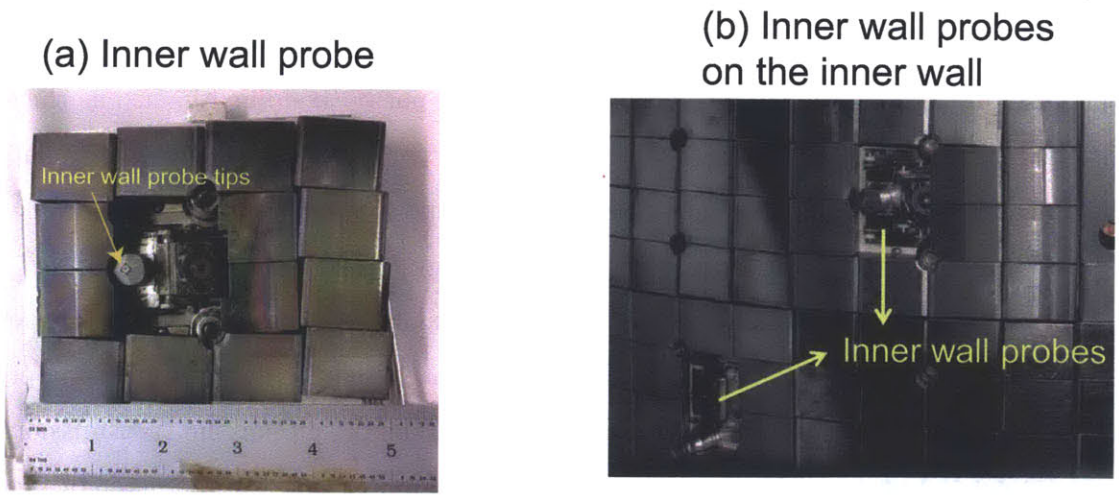

Figure 5-4: (a) Picture of the top view of the inner wall probe. (b) Picture of the two inner wall probes that are mounted in the inner wall at $(R, Z) = (0.44\,\mathrm{m}, 0.054\,\mathrm{m})$ and $(R, Z) = (0.44\,\mathrm{m}, -0.054\,\mathrm{m})$.

LH operating frequency (4.6 GHz). One of the probes on the launcher, which is at the top-row D-port side, is used. This one has been used to measure LH frequency spectra since the 2009 campaign. The absolute response of this probe is measured to be $\sim -50\,\mathrm{dBm/1mW}$ with a dipole antenna and a WR-187 waveguide with the aperture to simulate an irradiating 4.6 GHz (vacuum) electric field.

In addition to the probe on the launcher, three probes on the outer divertor and two probes on the inner wall are used. Details of these inner wall probes can be found in [97]. They are shown in Figures 5-4 (a) and (b). One of the inner wall probes is located below the mid-plane by 5 cm and the other is above the mid-plane by 5 cm. These two probes are toroidally separated by 11.25°. From the LH launcher, they are approximately 72° toroidally away in the counter current direction, as shown in Figure 5-3 (b).

The location of the inner wall probes is important because it allows examining whether the loss of current drive efficiency is due to the prompt loss near the launcher and whether any non-linear effects are present at the HFS plasma edge. Although the inner wall probes can be radially scanned, they remained 2 mm behind the inner wall tiles during the experiments. Since the measured density at the inner wall is typically above the slow LH wave cutoff ($n_e = 2.6 \times 10^{17}\mathrm{m}^{-3}$), the signals measured with the inner wall probes are due to the LH waves propagating toward them. While the absolute response of the inner wall probes could not be examined in-situ as they are under repair during the tokamak opening, these probes showed a relatively flat frequency response when examined ex-situ using a dipole antenna irradiating 4.6 GHz (vacuum) electric field.

Due to the different probe sensitivities and coaxial cable lengths among the probe systems, it is not meaningful to directly compare measured absolute spectral power among different probe measurements. Neither the probe design nor the transmission loss among the probe systems is the same. For example, the active diameter of the probe tip on the inner wall is 1.5 mm, while that on the launcher and on the outer divertor is 3 mm. Furthermore, the length of the 50 Ω coaxial cables connecting the probe and the spectral recorders is not the same. In addition, the inner wall probe

Table 5.1: The shot numbers, magnetic configurations, mid-plane mapped distance between the primary and secondary X-points (SSEP), central magnetic field(B_{T0}), plasma current (I_p), right gap (R.G.), left gap (L.G.), and coupled LH power (P_{LH}) of the four discharges. SSEP represents the location of a X-point in a plasma, which is the distance between the primary and secondary X-points mapped to the outer midplane. When SSEP is negative, the plasma has a LSN; when positive, the plasma has a USN.

Shot	Mag. Config.	SSEP (cm)	B_{T0} (T)	I_p (kA)	R.G. (cm)	L.G. (cm)	P_{LH} (kW)
1120710008	LSN	-1.77	5.4	550	0.89	0.79	620
1120710009	USN	2.57	5.4	550	1.38	1.27	660
1120710013	IWL	—	5.4	550	2.21	0.00	560
1120601014	USN	0.96	5.25	800	2.32	1.10	440

system is designed to have about 70 mm of noncoaxial wire between the coaxial cable and the probe in order to allow radial scanning motions, which can lower transmission coefficient as well. In the rest of this thesis, only the spectral shape will be compared among the probes.

Using these probes and high-repetition spectral recorders, the change in LH spectra at the multiple locations has been monitored with the change in $\overline{n}_e$ and magnetic configuration. Table 5.1 lists experimental parameters of the four discharges that will be discussed in the next section. By examining both the relative strength of the sidebands to that of the pump wave and the frequency separation between the sidebands and pump, the radial region where dominant ion cyclotron PDI occurs can be inferred.

5.3 Spectral Measurements of Lower Hybrid Waves and PDI Analysis

In general, ion cyclotron PDI is found to be excited when $\overline{n}_e > 1.0 \times 10^{20}\,\mathrm{m}^{-3}$. It is also found that ion cyclotron PDI is generally dominant over ion sound PDI in terms of the apparent pump depletion, consistent with the modeling presented in Chapter 4. In addition, no significant pump broadening is observed with the launcher probe

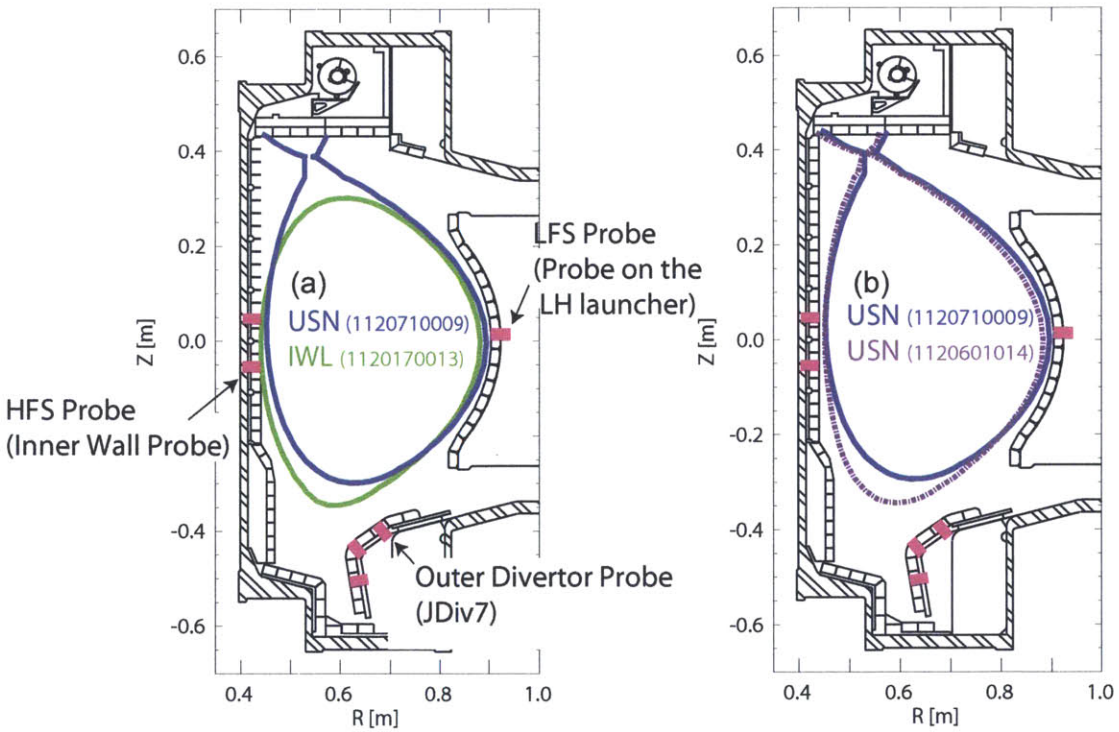

Figure 5-5: (a) LCFS of USN (Shot No. 1120710009) and IWL (112071013) plasmas. (b) LCFS of two USN plasmas (1120710009 and 1120601014).

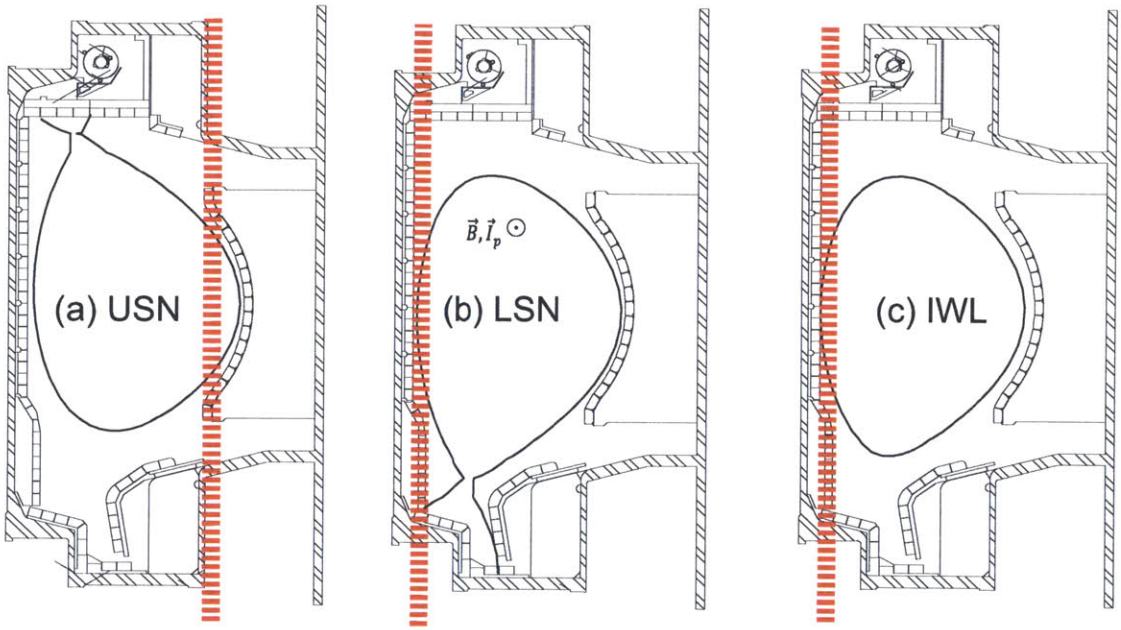

Figure 5-6: Summary of the radial excitation location of ion cyclotron PDI (red chords) of LH waves in different magnetic configurations: (a) USN plasma with $\overline{n}_e \approx 1.2 \times 10^{20}\,\mathrm{m}^{-3}$, (b) LSN plasma with $\overline{n}_e \approx 1.2 \times 10^{20}\,\mathrm{m}^{-3}$, and (c) IWL plasma with $\overline{n}_e \approx 1.3 \times 10^{20}\,\mathrm{m}^{-3}$. This estimation is based on the frequency difference between the pump LH wave and the first ion cyclotron harmonic LH wave.

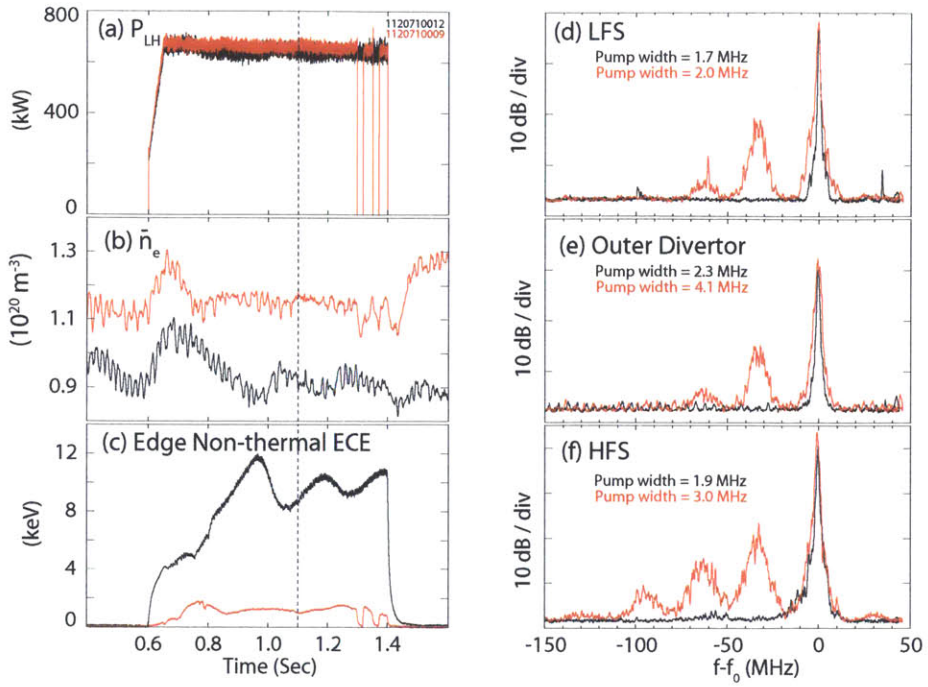

Figure 5-7: Time history of two USN plasmas at $\overline{n}_e \approx 0.9 \times 10^{20}\,\mathrm{m}^{-3}$ (black) and $\overline{n}_e \approx 1.15 \times 10^{20}\,\mathrm{m}^{-3}$ (red): (a) coupled LH power, (b) line averaged density, (c) edge non-thermal electron cyclotron emission, and LH frequency spectra measured at 1.1 second with the (d) LFS probe, (e) outer divertor probe, and (f) HFS probe. In this figure and the rest of figures, the pump width refers to the full width of the pump LH wave below 10 dB from the peak power, and $f_0 = 4.6\,\mathrm{GHz}$.

to date in the density range of $\overline{n}_e \lesssim 1.5 \times 10^{20}\,\mathrm{m}^{-3}$ (e.g., Figures 3-15 and 5-25 (b)).

Nonetheless, depending on magnetic configuration, ion cyclotron PDI is observed to be excited at different radial locations with different strengths. Figure 5-6 summarizes the radial excitation location of the observed ion cyclotron PDI in different magnetic configurations. In USN plasmas, the dominant PDI is observed to be excited at the LFS edge, whereas it is excited at the HFS edge in LSN and IWL plasmas. In the next three subsections, the LH frequency spectra measured in the USN, LSN, and IWL plasmas at $\overline{n}_e$ slightly below and above $1.0 \times 10^{20}\,\mathrm{m}^{-3}$ are discussed.

5.3.1 USN plasma

Figure 5-7 shows the time history of two USN plasmas with $\overline{n}_e \approx 0.9 \times 10^{20}\,\mathrm{m}^{-3}$ and $\overline{n}_e \approx 1.15 \times 10^{20}\,\mathrm{m}^{-3}$. Although the change in $\overline{n}_e$ is less than 30 % in the two discharges, the non-thermal electron cyclotron emission (ECE) drops by an order of magnitude, which indicates the anomalous loss of LHCD efficiency [98]. The ECE channel shown in this thesis measures the relativistically downshifted second harmonic ECE at a frequency of $f/f_{ce0} \approx 1.43$, where f_{ce0} is the central electron cyclotron frequency. Figures 5-7 (d), (e) and (f) show the LH frequency spectra measured at 1.1 second in both discharges. Above $\overline{n}_e \approx 1.0 \times 10^{20}\,\mathrm{m}^{-3}$, all three probes detect the sidebands that are displaced by $31 \sim 33$ MHz, which are absent within the detector sensitivity in the lower density plasma.

The observed ion cyclotron PDI occurs at the LFS edge based on the frequency separation of the sidebands. The fact that the dominant peak is the first ion cyclotron harmonic suggests that ion cyclotron PDI is excited in the relatively cold region ($T_e \lesssim 60\,\mathrm{eV}$) because the real frequency of the ion cyclotron modes corresponding to the maximum growth rate is numerically found to be sensitive to the local temperature, as shown in Chapter 3. However, care should be taken on this argument because the calculated growth rate does not consider any non-linear saturation mechanisms, which may shift the real frequency of the ion cyclotron modes. Furthermore, the excited sideband LH waves may have undergone damping processes while propagating toward the probes, which may affect the relative strength of the sidebands because they have different $n_\parallel$.

These observations are consistent with the previous observations in other tokamaks [12, 99] in the following three ways: first, ion cyclotron PDI is generated at the LFS edge, possibly near the launcher. Second, the broadband features of the observed spectra are independent of the probe locations. Inner-wall probe measurements reveal that the ion cyclotron PDI excited at the LFS edge may generate the sideband LH wave that may have similar $n_\parallel$ to that of the pump in order to propagate from the LFS edge to the HFS edge without being

Landau-damped. This is based on the observation that the relative strength of the observed sidebands is similar between the LFS and HFS edge. Finally, the sideband power remains weak unless the density is further raised to $\overline{n}_e \rightarrow 2 \times 10^{20}\,\mathrm{m}^{-3}$ such that $\omega/\omega_{lh}(0) \rightarrow 2$ for Alcator C-Mod plamsas, which is the classical PDI limit. For example, the observed sideband power is at least weaker by 10 dB than the pump peak power in the density range of interest. Moreover, a nearly unchanged pump strength at the inner wall below and above the threshold density ($\overline{n}_e \approx 1.0 \times 10^{20}\,\mathrm{m}^{-3}$) implies that a significant amount of pump power might not be lost due to ion cyclotron PDI that occurs at the LFS edge at least on the first pass to the HFS. In general, no apparent experimental evidence of pump depletion has been observed due to the ion cyclotron PDI that is excited at the LFS edge in the density range of interest. While it is possible that the existing probes may not be sensitive to PDI, if it is excited relatively inside the LCFS, this experimental work remains as future work, which will be discussed further in Chapter 6.

To understand the observed density threshold in USN plasmas ($\overline{n}_e \approx 1.0 \times 10^{20}\,\mathrm{m}^{-3}$), the homogeneous growth is calculated with the local density and temperature at the LFS edge, which are measured with an edge Thomson scattering diagnostic [100], an X-mode reflectometer [101], and edge scanning probe diagnostics. Figures 5-8 (a) and (b) show the fitted edge density and temperature profiles in the two USN plasmas at $\overline{n}_e \approx 0.9 \times 10^{20}\,\mathrm{m}^{-3}$ and $\overline{n}_e \approx 1.2 \times 10^{20}\,\mathrm{m}^{-3}$. The launcher is located about 2 cm away from the LCFS. In the higher density plasma, the edge density is slightly higher and edge temperature is slightly lower than in the lower density plasma.

The homogeneous growth rate calculations show that the plasma even with $\overline{n}_e < 1.0 \times 10^{20}\,\mathrm{m}^{-3}$ is unstable to ion cyclotron PDI. Figure 5-8 (c) shows the maximum growth rate as a function of radial locations in the two USN plasmas. The growth rates are peaked near the LCFS in the perpendicular coupling limit ($\theta = \pi/2$). On the other hand, in the parallel coupling limit, the growth rate is finite at the plasma edge. One important point of this figure is that the homogeneous growth rates in the two plasmas are comparable to each other. The injected LH power density is high

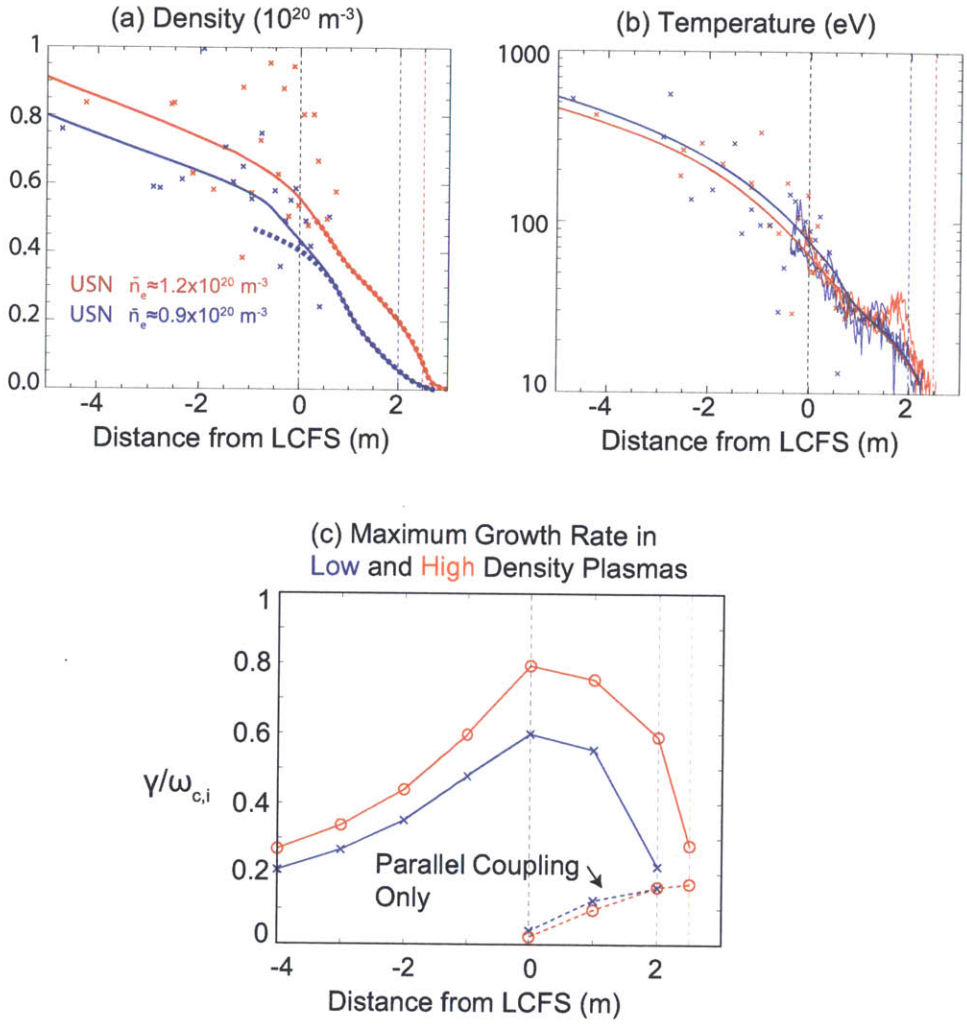

Figure 5-8: (a) Density and (b) temperature profiles in two USN plasmas at $\overline{n}_e \approx 0.9 \times 10^{20}\,\mathrm{m}^{-3}$ and $\overline{n}_e \approx 1.2 \times 10^{20}\,\mathrm{m}^{-3}$. (c) Calculated maximum growth rate, corresponding to the first ion cyclotron harmonic peak, as a function of the radial location. Plasma parameters are $B_0 = 5.4\,\mathrm{T}$, $f_0 = 4.6\,\mathrm{GHz}$, $ck_{0\|}/\omega_0 = 2$, $ck_{\|}/\omega_0 = 7$, and $P_{RF} = 100\,\mathrm{kW}$. The solid line denotes the case when $\theta = \pi/2$ so that both perpendicular and parallel coupling terms are retained in the coupling coefficient. The dashed line denotes the case when $\theta = 0$ so that only the parallel coupling term contributes to the coupling coefficient.

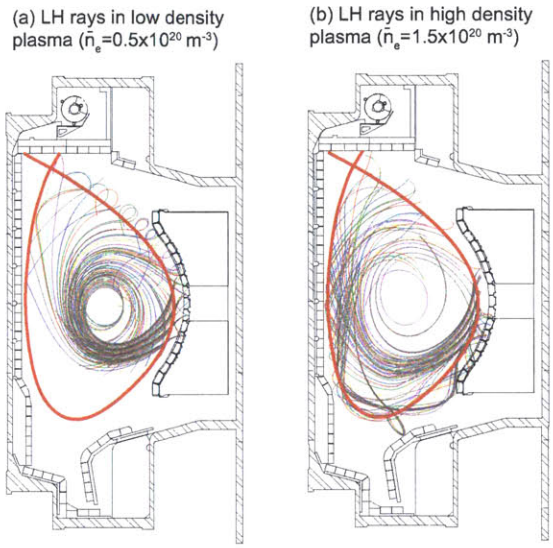

Figure 5-9: Examples of ray trajectories in low ($\overline{n}_e = 0.5 \times 10^{20}\,\mathrm{m}^{-3}$) and high-density ($\overline{n}_e = 1.5 \times 10^{20}\,\mathrm{m}^{-3}$) plasma. Limited radial penetration is seen in the high-density plasma case due to the refraction of the LH rays. This figure is adopted from [102].

enough to overcome the collisional threshold, even in the lower-density plasma where no ion cyclotron PDI is observed within the detector sensitivity. Thus, the collisional threshold is not likely to explain the observed onset of ion cyclotron PDI, suggesting that convective growth is more important in determining the observed onset of ion cyclotron PDI.

Given that edge plasma conditions are unstable to PDI in both plasmas, the change in the LH ray trajectories at the LFS edge is examined to look for a possible convective growth mechanism in the parallel coupling limit. Figure 5-9 shows the poloidal projection of the ray trajectories in the low- ($\overline{n}_e = 0.5 \times 10^{20}\,\mathrm{m}^{-3}$) and high-density ($\overline{n}_e = 1.5 \times 10^{20}\,\mathrm{m}^{-3}$) plasmas. The GENRAY [41] ray-tracing code with an edge collisional model was used. The density and temperature profile outside the LCFS is estimated based on a model with an exponentially decaying function. A relatively cold temperature ($T_{e0} \approx 2 \sim 3\,\mathrm{keV}$) results in a weak single-pass absorption of the LH rays, even in the low-density plasma. In the high-density plasma, the refraction of the LH rays limits the radial penetration to the plasma core, and the ray propagation is more aligned to the background magnetic field. This wave propagation behavior is dictated by the dispersion

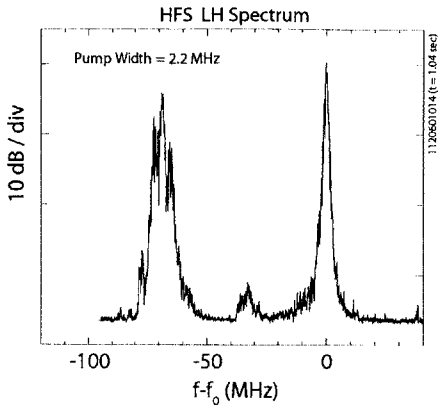

Figure 5-10: LH Spectrum measured with the inner wall probe in the plasma discharge 1120601014. Experimental parameters are listed in Table 5.1, and the contour of the LCFS is shown in Figure 5-5 (b).

relation of LH wave ($v_{g\perp}/v_{g\parallel} \approx \omega/\omega_{pe}$) in toroidal geometry. Note that this wave propagation behavior also predicts an enhanced collisional loss ($\nu \propto n_e/T_e^{3/2}$) and has been exploited [10] to explain the loss of LHCD efficiency in a wide range of $\overline{n}_e$ on Alcator C-Mod.

In our case, these trajectories imply that, as the plasma density increases, the pump LH resonance cone spends a prolonged time at the plasma edge and acts as a source to excite PDI in an extended region of the outer plasma edge. When the pump LH wave fills the plasma edge, where the homogeneous growth rate is maximized due to the parallel coupling term, the excited sideband LH wave can propagate along the pump and grow in space for a prolonged time before convecting out of the pump LH resonance cone. Therefore, the underlying cause of the observed onset of ion cyclotron PDI at the LFS edge is likely due to a weaker radial penetration of the pump LH wave in high-density plasmas. The presented experimental observations indicate that this critical $\overline{n}_e$ corresponds to approximately $\overline{n}_e \approx 1.0 \times 10^{20}\,\mathrm{m}^{-3}$ in USN plasmas.

Throughout the 2012 run campaign, no ion cyclotron PDI that is excited at the HFS edge (HFS PDI) has been observed in most of the USN plasmas with the $\vec{B} \times \nabla B$ drift direction downward. The only exception to this general observation is the plasma discharge (1120610014). In this USN plasma, strong HFS PDI is observed when $\overline{n}_e > 1.4 \times 10^{20}\,\mathrm{m}^{-3}$. Little current drive effects are observed, similar to those plasma

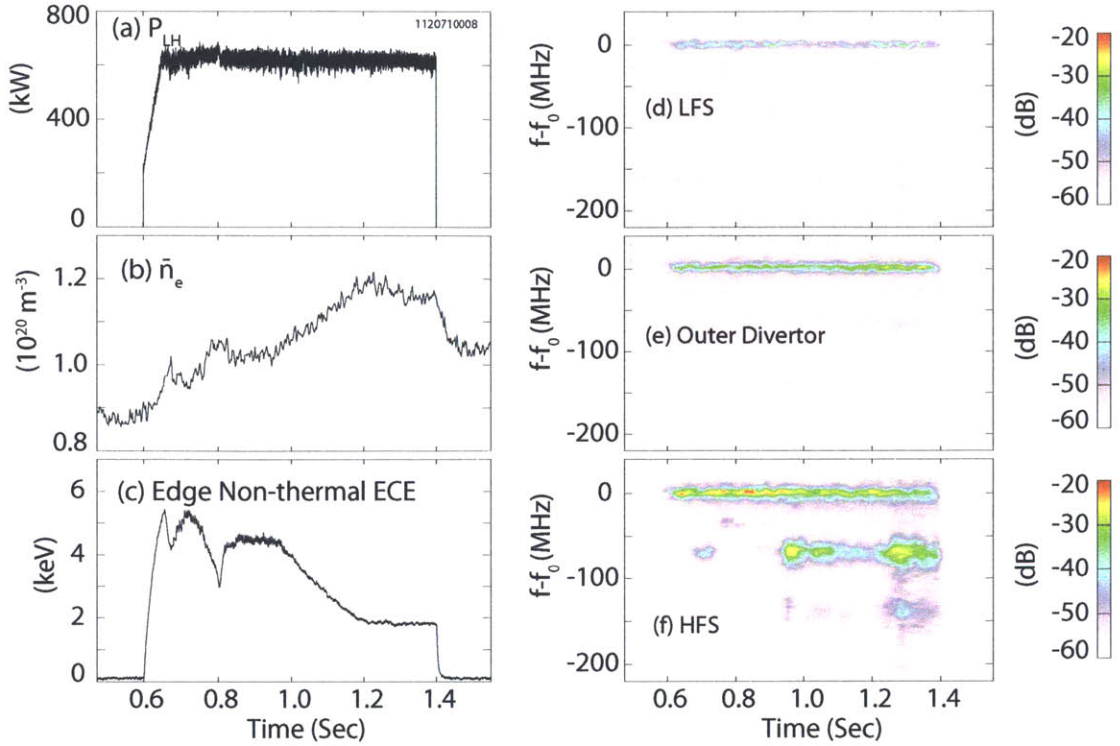

Figure 5-11: Time traces of a LSN L-mode discharge: (a) coupled LH power, (b) line averaged density, (c) edge non-thermal electron cyclotron emission, and LH frequency spectra measured with the (d) LFS probe, (e) outer divertor probe, and (f) HFS probe.

discharges at high densities. Figure 5-10 shows the LH frequency spectrum measured by the inner wall probe. Although it is not clear why HFS PDI is excited in this plasma, this plasma has a larger elongation than the other USN plasmas, and the shape of the LCFS near the HFS is similar to that of the LSN plasmas, as shown in Figure 5-5. Note that the sideband corresponding to the ion cyclotron PDI occurring at the LFS (LFS PDI) is weaker than those generally observed in typical USN plasmas. The plasma shaping may affect the PDI strength and excitation location, which will be discussed further in the following sections.

5.3.2 LSN plasma

Figure 5-11 shows the experimental observations of LH spectra in a LSN L-mode plasma. In this discharge, after LHCD turns on at 0.6 second, $\overline{n}_e$ is gradually raised from $0.9 \times 10^{20}\,\mathrm{m}^{-3}$ to $1.2 \times 10^{20}\,\mathrm{m}^{-3}$. As shown in Figure 5-11 (c), between 0.9

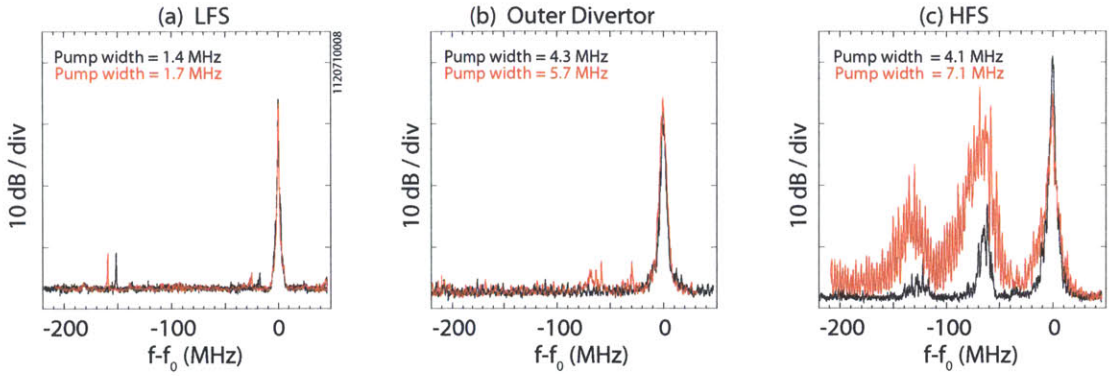

Figure 5-12: LH frequency spectra taken at t = 0.67 sec (black) and t = 1.30 sec (red) from the discharge (1120710008) shown in Figure 5-11. They are measured with the (a) LFS probe, (b) outer divertor probe, and (c) HFS probe.

second and 1.2 second, the edge non-thermal ECE drops by 50 %.

Figures 5-11 (d), (e) and (f) show the time traces of the LH frequency spectra measured at the three different locations. Three noticeable features are seen among these spectra. First, no significant ion cyclotron PDI activity is observed at the LH launcher and outer divertor even when $\overline{n}_e \approx 1.2 \times 10^{20}\,\mathrm{m}^{-3}$. Yet, the inner wall probe detects the parametrically excited ion cyclotron sidebands when the edge non-thermal ECE starts to decrease. Second, the frequency difference between the pump wave and the first down-shifted sideband (60~65 MHz) corresponds to the ion cyclotron frequency approximately evaluated near the HFS mid-plane LCFS. Third, the onset of this ion cyclotron PDI is abrupt. The peak intensity of the sidebands increases more than 20 dB within 20 ms, consistent with the non-linear nature of PDI.

Figure 5-12 compares the LH spectra of the discharge shown in Figure 5-11 before (in black) and after (in red) the onset of ion cyclotron PDI. As shown in Figure 5-12 (c), the inner wall probe measurements show the peaks of the down-shifted sidebands. In this case, the lower sideband LH waves are modulated with low frequency signals, although the reason for this is unclear. The frequency-integrated spectral power of the sideband LH wave is comparable to that of the pump. More importantly, the peak amplitude of the pump wave is observed to decrease with the increase in the spectral power of the sideband LH wave, suggesting that the pump depletion is due to ion cyclotron PDI. Furthermore, Figure 5-12 shows that the spectral shape of the

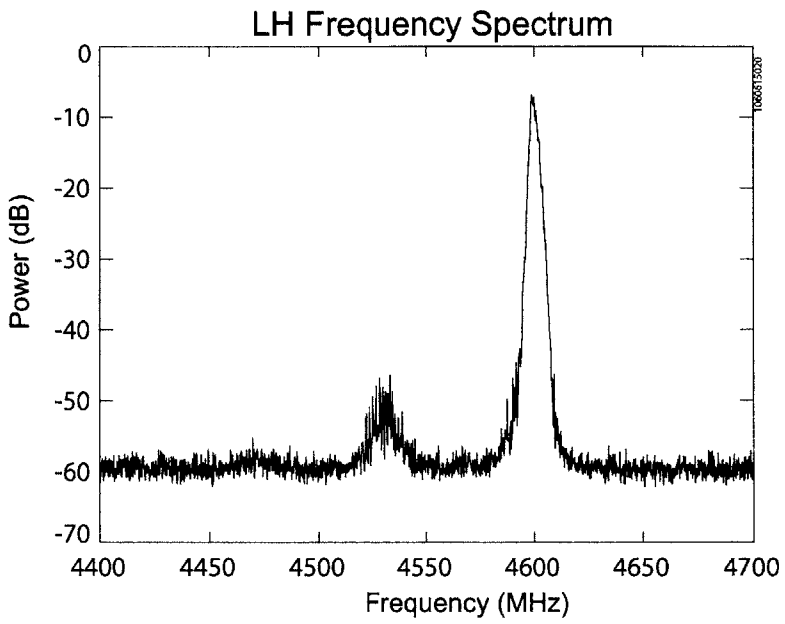

Figure 5-13: Example of the LH frequency spectrum measured with the launcher probe in a L-mode LSN plasma during the 2006 campaign. Plasma parameters are $\overline{n}_e \approx 0.8 \times 10^{20}\,\mathrm{m}^{-3}$, $B_{T0} = 5.5\,\mathrm{T}$, $I_p = 500\,\mathrm{kA}$, $P_{LH} = 400\,\mathrm{kW}$, and the launched peak $n_{\|} = 2.3$.

LH decay spectra can be dependent on the probe locations. The launcher probe does not detect these parametrically excited sideband LH waves within the detector sensitivity, implying that these decay waves are likely to be absorbed by the plasma before reaching the LFS via either Landau damping or collisional damping.

It is worth mentioning that the sideband LH waves with frequency separation of $65 \sim 70$ MHz from the pump LH wave were previously reported during the 2006 campaign [103]. Figure 5-13 shows the LH frequency spectrum that was measured with the LFS probe (the probe on the launcher) in a LSN plasma with $\overline{n}_e \approx 0.8 \times 10^{20}\,\mathrm{m}^{-3}$. The use of a commercial spectrum analyzer resulted in a higher signal to noise ratio ($\sim$ 50dB). The peak power of the observed sideband LH wave is about 40 dB weaker than the pump peak power. No obvious correlation of this signal with the LH power, reflection coefficient, or density at the surface of the launcher was reported. Note that the small bump seen between 4.45 and 4.5 GHz might be the second harmonic of the ion cyclotron sideband LH wave.

Based on the experimental observations shown here, the signals observed during

the 2006 campaign are likely to be due to the ion cyclotron PDI that is excited at the HFS edge. These results corroborate that PDI can be excited at the HFS edge even in the low density plasma and are consistent with the experimental results presented here. It also suggests that LH waves propagate around the tokamak before being fully damped; the pump propagates from the LFS edge at the launcher to the HFS edge, and the sideband LH wave that is excited at the HFS edge propagates to the LFS edge.

In addition to the presence of the ion cyclotron sideband LH waves, Figure 5-12 shows that the pump wave is broadened when measured away from the LH launcher. Pump broadening at the LH launcher is not significant, in agreement with the previous observations (e.g., Figure 3-15). Figure 5-12 shows that the pump width at 10 dB below the pump peak power is approximately 7 MHz at the HFS when ion cyclotron PDI is strongly excited. However, the measured pump width at the launcher is less than 2 MHz. In the divertor region, the pump is generally observed to be broadened by more than 2 MHz. These observations suggest that either ion sound parametric decay or turbulent scattering may also play a role away from the launcher when LH waves propagate the region in far SOL, as discussed in Chapter 4.3. However, the interaction region cannot be easily identified.

Low-frequency ion modes as a result of ion cyclotron PDI at the HFS edge have also been measured with a commercial spectrum analyzer. Figure 5-14 shows an example of the simultaneous measurement of the high-frequency spectrum near 4.6 GHz and the low-frequency spectrum from 0 to 200 MHz using the inner wall probe. A power splitter was used to split the incoming signal into two branches. The low-frequency spectrum shows the harmonic peaking at the multiples of ~60 MHz, which is also observed in the high-frequency spectrum. In this case, the line averaged density is $\overline{n}_e \approx 1 \times 10^{20}\,\mathrm{m}^{-3}$, so it is thought to be on the border of the threshold condition for the onset of strong PDI. Note that the harmonic peaking at the multiples of ~50 MHz is observed as well, which need a further experimental investigation to understand the origin of these signals. It might indicate that ion cyclotron PDI can occur on the way to the HFS edge because the pump waves

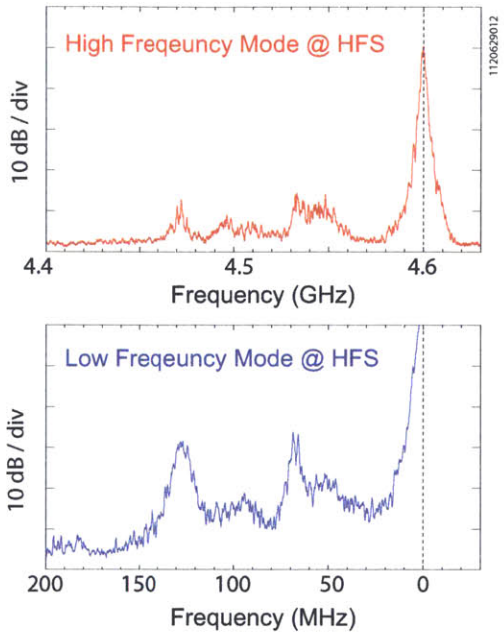

Figure 5-14: Example of simultaneous measurements of the (a) high-frequency spectrum at 4.6 GHz and (b) low-frequency spectrum from 0 to 200 MHz.

propagate along the plasma periphery on the way toward the HFS edge, but it is not conclusive yet.

The presented LH spectra in LSN plasmas show that strong ion cyclotron PDI at the HFS edge (HFS PDI) can occur below the classical limit of ion cyclotron PDI occurring at the LFS (LFS PDI) [35, 12]. The ratio ω/ω_{lh} has been used as an indicator of how close the plasma condition is to the strong PDI excitation. For the discharge shown in Figure 5-11, Figure 5-15 shows that $\omega/\omega_{lh}(0)$ is approximately 3 with $B_T(0) \approx 5.4\,\mathrm{T}$ and $n_e(0) \approx 1.8 \times 10^{20}\,\mathrm{m}^{-3}$, which is above the classical PDI limit $\omega/\omega_{lh}(0) \approx 2$.

Using the above criteria, the local condition near the HFS SOL is found to be more prone to PDI compared with the local condition near the LFS SOL, assuming the same LH power density. Figure 5-16 shows the SOL density and temperature profiles as a function of ρ (i.e., mapped along magnetic flux surfaces to the outer mid-plane: $R - R_{LCFS}$) at the LFS and HFS edge. It can be seen that the HFS edge plasma exhibits a higher density and lower temperature than the LFS edge plasma, which is attributed to the the presence of a parallel temperature gradient along the open field

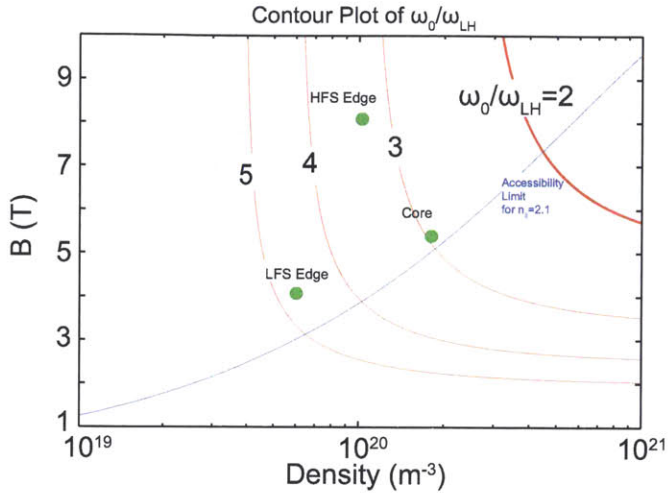

Figure 5-15: The ratio of ω/ω_{LH} at the plasma core ($B_T(0) \approx 5.4\,\mathrm{T}$ and $n_e(0) \approx 1.8 \times 10^{20}\,\mathrm{m}^{-3}$), LFS edge ($B_T \approx 4.1\,\mathrm{T}$ and $n_e \approx 0.6 \times 10^{20}\,\mathrm{m}^{-3}$), and HFS edge ($B_T \approx 8.1\,\mathrm{T}$ and $n_e \approx 1.0 \times 10^{20}\,\mathrm{m}^{-3}$). The edge plasma parameters are chosen based on the measurements shown in Figure 5-16. The blue line shows the accessibility limit when the launched $n_{\parallel}$ is 2.1.

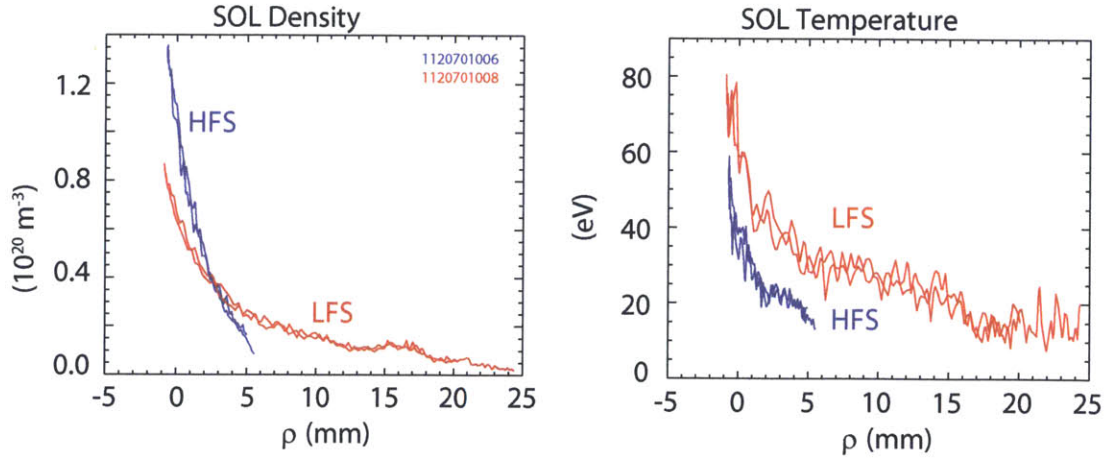

Figure 5-16: Electron density and temperature profiles (red) at the LFS SOL for the LSN discharge 1120710008 shown in Figure 5-11 at t = 1.1 sec and those (blue) at the HFS SOL for the LSN discharge 1120710006 with the similar global plasma parameters and magnetic equilibrium to the discharge 1120710008. All are plotted as a function of ρ (i.e., mapped along magnetic flux surface to the outer mid-plane: $R - R_{LCFS}$).

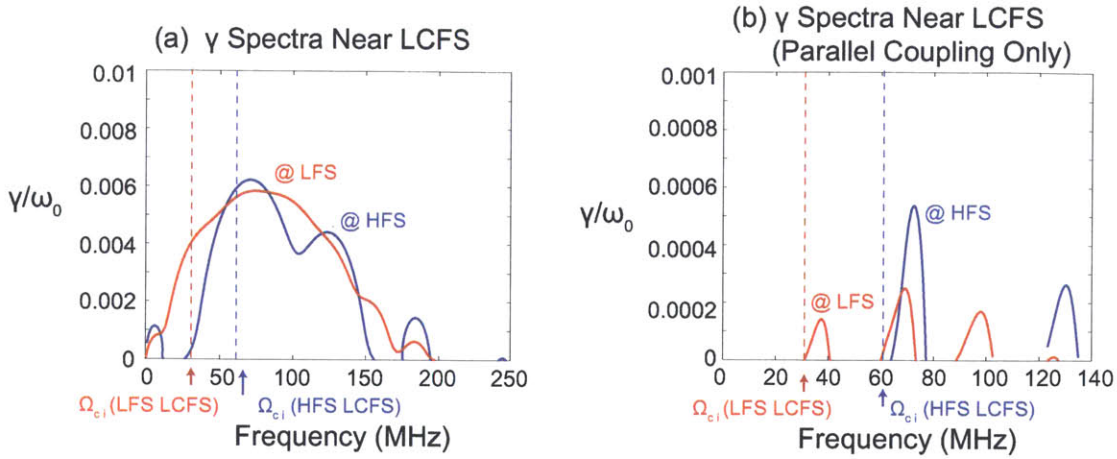

Figure 5-17: Comparison of homogeneous growth rate spectra between the LFS and HFS edge when (a) $\theta = \pi/2$ and (b) $\theta = 0$, where θ is the angle between $k_{0\perp}$ and $k_{1\perp}$. The common parameters are $f_0 = 4.6\,\mathrm{GHz}$, $P_{RF} = 100\,\mathrm{kW}$, $ck_{0\parallel}/\omega_0 = 2$, and $ck_{\parallel}/\omega_0 = 6$. Plasma parameters are taken from the measurements shown in Figure 5-16. At the LFS edge, $B = 4\,\mathrm{T}$, $n_e = n_i = 7.7 \times 10^{19}\,\mathrm{m}^{-3}$, and $T_e = T_i = 58\,\mathrm{eV}$. At the HFS edge, $B = 8\,\mathrm{T}$, $n_e = n_i = 5.9 \times 10^{19}\,\mathrm{m}^{-3}$, and $T_e = T_i = 32\,\mathrm{eV}$. Note that the homogeneous growth rate is normalized by ω_0.

lines [104]. Figure 5-15 shows that, when evaluating the local ω/ω_{lh} using the local density and magnetic field, ω/ω_{lh} at the inner mid-plane LCFS is approximately 3.3 with $B_T \approx 8.1\,\mathrm{T}$ and $n_e \approx 1.0 \times 10^{20}\,\mathrm{m}^{-3}$, whereas at the outer mid-plane LCFS with $B_T \approx 4.1\,\mathrm{T}$ and $n_e \approx 0.6 \times 10^{20}\,\mathrm{m}^{-3}$ it is about 4.7. The local ω/ω_{lh} is lower near the HFS SOL than near the LFS SOL. Moreover, the temperature at the HFS SOL tends to be lower than that at the LFS SOL. The growth rate of the ion cyclotron quasi-mode is found to decrease with increasing temperature, as shown in Chapter 4.

While the local plasma conditions at the HFS edge are favorable to PDI, the growth rate itself cannot explain the onset of ion cyclotron PDI at the HFS edge and the absence of ion cyclotron PDI at the LFS edge. Figure 5-17 (a) compares the homogeneous growth rates at the LFS and HFS LCFS when both the perpendicular and the parallel coupling terms are retained. While a higher magnetic field [34] at the HFS LCFS can lower the homogeneous growth rate in the perpendicular coupling limit, a relatively higher density and lower temperature [16, 104] cancels out the magnetic field effect. Figure 5-17 (b) compares the growth rate due to the parallel coupling term only. In this case, the difference in magnetic fields between the two

locations does not affect the growth rate; the parallel coupling term is magnetic-field independent.

Three interesting observations can be made. First, the frequencies of the ion cyclotron harmonic peaks are slightly up-shifted from the local ion cyclotron frequency, and thus care should be taken when attempting to identify the radial location based on the frequency separations in the observed spectra. Second, contrary to the peaking of the homogeneous growth rate at the higher harmonic at the LFS LCFS ($T_e \approx 60$eV), the homogeneous growth rate is peaked at the first ion cyclotron harmonic at the HFS LCFS ($T_e \approx 30$eV) due to the relatively lower temperature. Finally, the comparable growth rates are not sufficient to explain the two vastly different ion cyclotron PDI strengths between the two locations.

One caveat of these calculations is that a resonance cone propagation is assumed even at the HFS edge to calculate the local electric field there. This may not necessarily be the case, and it may be more appropriate to use the LH electric field that is evaluated from the full-wave calculations [46, 105]. Nonetheless, it is expected that the calculations presented here can be used in a representative way to understand PDI behavior because the launched LH power is weakly absorbed by the plasma on the first pass toward the HFS.

Given that both edge plasma conditions are unstable to PDI, the LH ray trajectories at the HFS edge are examined in a high-density LSN plasma to look for two possible convective growth mechanisms that may lead to the observed intense ion cyclotron PDI at the HFS edge. First is a spatial broadening of the pump LH resonance cone. Figure 5-18 (a) shows an example of the LH ray trajectories launched at the LFS plasma edge. The rays are terminated after about two toroidal turns, for an illustrative purpose. The rays propagate toward the HFS edge without being Landau-damped, due to the low plasma temperature. At the same time, Figure 5-18 (c) shows that the LH rays propagate toward the HFS edge instead of constantly radially penetrating toward the plasma core (e.g., compare to Figure 1 in [34]). As discussed in the previous section, high density plasmas prohibit the penetration of the LH rays. At the inner wall, the rays start to noticeably spread in

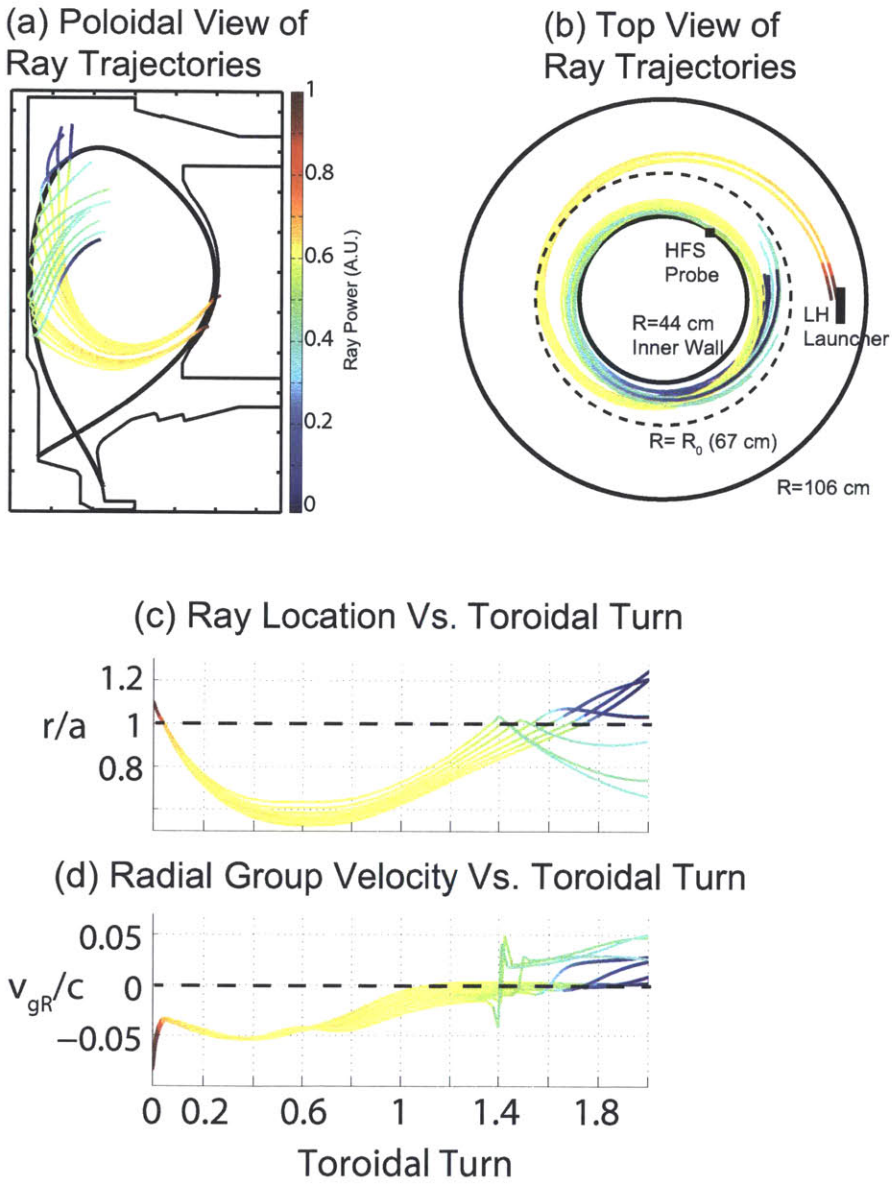

Figure 5-18: (a) Poloidal view of the LH ray trajectories in a LSN plasma at $\overline{n}_e \approx 1.3 \times 10^{20}\,\mathrm{m}^{-3}$. (b) Top view of the LH ray trajectories. (c) LH ray locations and (d) radial group velocities are shown as a function of toroidal turns.

the poloidal space after the reflection at the inner wall. While this spatial broadening of the rays can reduce the pump LH power density, it can also reduce the convective loss due to perpendicular coupling, unlike the case wherein there is a well-defined resonance cone at the LFS edge near the LH launcher. Note that this reflection behavior might not be correctly treated by the ray-tracing approach due to the violation of the WKB approximation at the plasma edge; however, full-wave simulations also show similar spatial broadening of the LH electric field at the inner wall [11, 46].

Second, a reduced radial group velocity may also enhance the convective growth. Figure 5-18 (b) shows that the rays stay near the inner part of the plasma after about a half-toroidal turn. This is because the radial LH group velocity is reduced, as shown in Figure 5-18 (d). In the parallel coupling limit ($\theta \rightarrow 0$), Δt can be defined as $\Delta t \equiv \triangle / v_{g\xi}$, where $\triangle$ is the (radial) distance across the pump resonance cone and $v_{g\xi}$ is the group velocity of the sideband LH wave in that direction. When the pump LH wave starts to propagate near the inner plasma edge, a finite growth rate, due to parallel coupling, exists, and the excited sideband LH wave propagates along the pump. Thus, except for the fact that the sideband LH wave has a higher $n_{\|}$ than that of the pump LH wave, both the pump and sideband LH wave are expected to have a similar propagation behavior. When the group velocity of the sideband LH wave is reduced, then this may significantly increase Δt, resulting in a much higher amplification factor. One can also construct a similar case in the perpendicular coupling limit because one of the perpendicular directions of the sideband LH group velocity to the pump LH group velocity can be the radial direction.

Therefore, both parallel and perpendicular coupling are expected to contribute to the convective growth of the excited sideband LH wave near the HFS edge where the resonance cone is spatially broadened and radial group velocity is slow. The latter mechanism is somewhat analogous to the case of the classical PDI limit [34]. Both the parallel and perpendicular group velocities are reduced significantly in the limit of $\omega_0/\omega_{lh}(0) \rightarrow 2$, maximizing the convective growth. One difference would be that perpendicular coupling was identified as the responsible mechanism in this PDI limit,

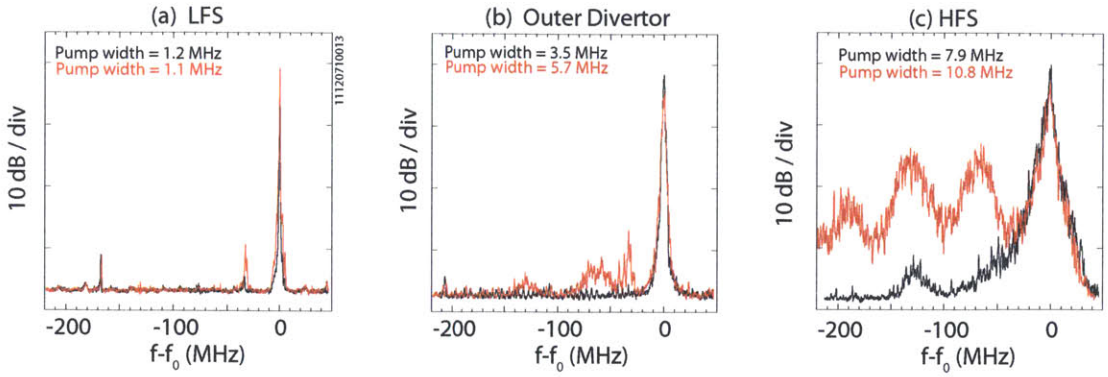

Figure 5-19: LH frequency spectra measured with the (a) LFS probe, (b) outer divertor probe, and (c) HFS probe in the IWL plasmas at $\overline{n}_e \approx 1.2 \times 10^{20}\,\mathrm{m}^{-3}$ (black) and $\overline{n}_e \approx 1.3 \times 10^{20}\,\mathrm{m}^{-3}$ (red).

while parallel coupling is thought to be more responsible for the convective growth at the plasma edge.

5.3.3 IWL plasma

IWL plasmas exhibit higher non-thermal HXR emission and ECE as compared to diverted discharges at $\overline{n}_e$ above $1.0 \times 10^{20}\,\mathrm{m}^{-3}$ [64]. The change in loop voltage during LHCD is reported to be higher as well. Note that thick-target Bremstrahlung emission is expected to contribute to the observed HXR count rate.

Figure 5-19 (c) compares the LH spectra measured at the inboard side before($\overline{n}_e \approx 1.2 \times 10^{20}\,\mathrm{m}^{-3}$) and after ($\overline{n}_e \approx 1.3 \times 10^{20}\,\mathrm{m}^{-3}$) the onset of HFS PDI. The observed PDI have a higher density threshold for the onset of ion cyclotron PDI occurring at the HFS edge. This is thought to be due to the fact that the cold SOL region at the HFS edge is eliminated in the IWL plasma. When $\overline{n}_e \approx 1.3 \times 10^{20}\,\mathrm{m}^{-3}$, the sidebands excited at the HFS edge are observed with the inner wall probe and outer divertor probe. The LH spectrum measured with the inner wall probe is dominated by the sidebands excited at the HFS edge, similar to those seen in the LSN plasmas. However, the observed density threshold to excite HFS PDI is higher in IWL plasmas than in LSN plasma; the density threshold ($\overline{n}_e \approx 1.25 \times 10^{20}\,\mathrm{m}^{-3}$) is about 20% higher as compared to that in LSN plasmas. This change in the density results in a decrease

of edge non-thermal ECE from 2 keV to 1 keV. While the outer divertor probe detects a weak sideband LH wave, the LH spectra measured with the probes at the LFS show only a relatively weaker sideband that is downshifted by about $31 \sim 33$ MHz. This mode is due to parametric excitation at the LFS edge, which is generally observed to be weak in this density range, as discussed in the previous subsection.

In addition to the observed ion cyclotron LH sideband waves, another distinct feature seen in Figure 5-19 (c) is that the width of the pump wave remains broadened down to 30 dB below the peak power, independent of the presence of the ion cyclotron sidebands. The width of the pump wave measured at the LH launcher is narrow and is similar to that observed in LSN plasmas.

5.4 Correlation between Edge Densities and PDI Strength

While the absence of ion cyclotron PDI occurring at the HFS edge in USN plasmas is not well-understood at the moment, the absence of ion cyclotron PDI occurring at the LFS edge in LSN and IWL plasmas in the density range of interest ($\overline{n}_e \approx 1.2 \times 10^{20}\, m^{-3}$) correlates with the change in edge densities in different magnetic configurations, suggesting edge plasma parameters are important in determining the onset of ion cyclotron PDI occurring at the LFS edge. The aim of this section is to understand the absence of ion cyclotron PDI at the LFS edge in LSN and IWL plasmas, even when $\overline{n}_e$ is similar to that of the USN plasma, by examining the SOL density profile in front of the launcher with different magnetic configurations. The study of edge densities is justified because the observed ion cyclotron PDI is expected to occur in a cold plasma region ($T_e \lesssim 60\,\text{eV}$) based on the observations that the dominant peak is the first ion cyclotron harmonic.

Before discussing the edge densities in the LSN and USN plasmas, Figure 5-20 (a) compares the edge densities in the USN plasmas below and above $\overline{n}_e \approx 1.0 \times 10^{20}\, m^{-3}$ as a reference. As discussed in Section 5.3, the excitation of ion cyclotron PDI at

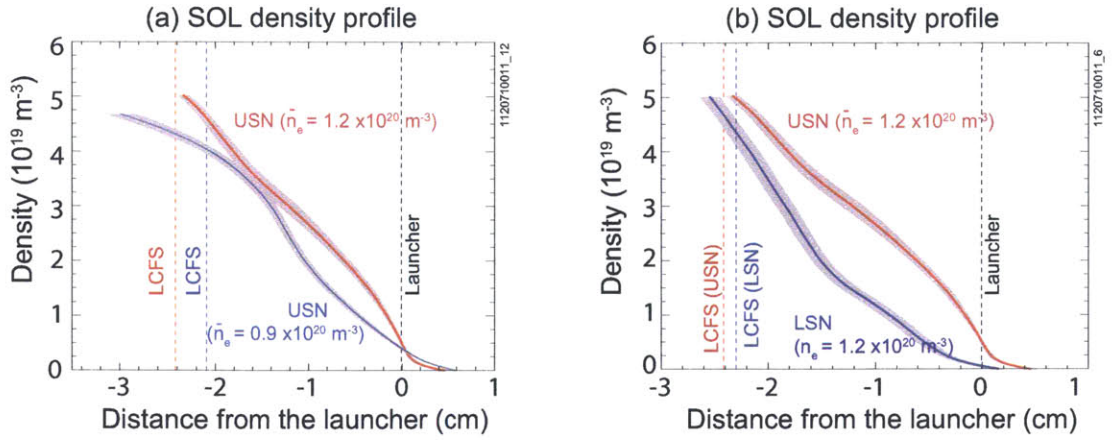

Figure 5-20: (a) SOL density profiles measured with the X-mode reflectometer in front of the LH launcher in two USN plasmas at $\overline{n}_e \approx 0.9 \times 10^{20}\,\mathrm{m}^{-3}$ and $\overline{n}_e \approx 1.2 \times 10^{20}\,\mathrm{m}^{-3}$. (b) Comparison of SOL density profiles in LSN and USN plasmas at the same $\overline{n}_e \approx 1.2 \times 10^{20}\,\mathrm{m}^{-3}$).

the LFS edge above $\overline{n}_e \approx 1.0 \times 10^{20}\,m^{-3}$ is thought to be due to the increase in edge densities, which makes the pump LH wave propagate more along the background magnetic field, minimizing the convective loss in the parallel coupling limit. The presented data in USN plasmas may indicate the necessary level of edge density to excite the observed ion cyclotron PDI in USN plasmas.

The SOL density of the LSN plasma is lower than that of the USN plasma although both plasmas have the same $\overline{n}_e \approx 1.2 \times 10^{20}\,\mathrm{m}^{-3}$, as shown in Figure 5-20 (b). Therefore, it can be argued that the SOL density in the LSN plasma at $\overline{n}_e \approx 1.2 \times 10^{20}\,\mathrm{m}^{-3}$ is not high enough to ensure the growth of ion cyclotron PDI at the LFS edge.

Nonetheless, when $\overline{n}_e$ is further raised so that edge densities are raised as well, it is expected that ion cyclotron PDI will be excited at the LFS edge. An example of the ion cyclotron PDI that is excited at the LFS edge in a LSN plasma is shown in Figure 5-21 (a). It shows the LH frequency spectra measured in the LSN plasmas at two different $\overline{n}_e$. These LH spectra were measured during the 2010 campaign. No edge density profiles are available, but the much weaker ion cyclotron sideband LH waves can be attributed to the lower edge densities at the LFS edge in the lower density plasma ($\overline{n}_e \approx 0.84 \times 10^{20}\,\mathrm{m}^{-3}$) based on our observations in the 2012 campaign. In

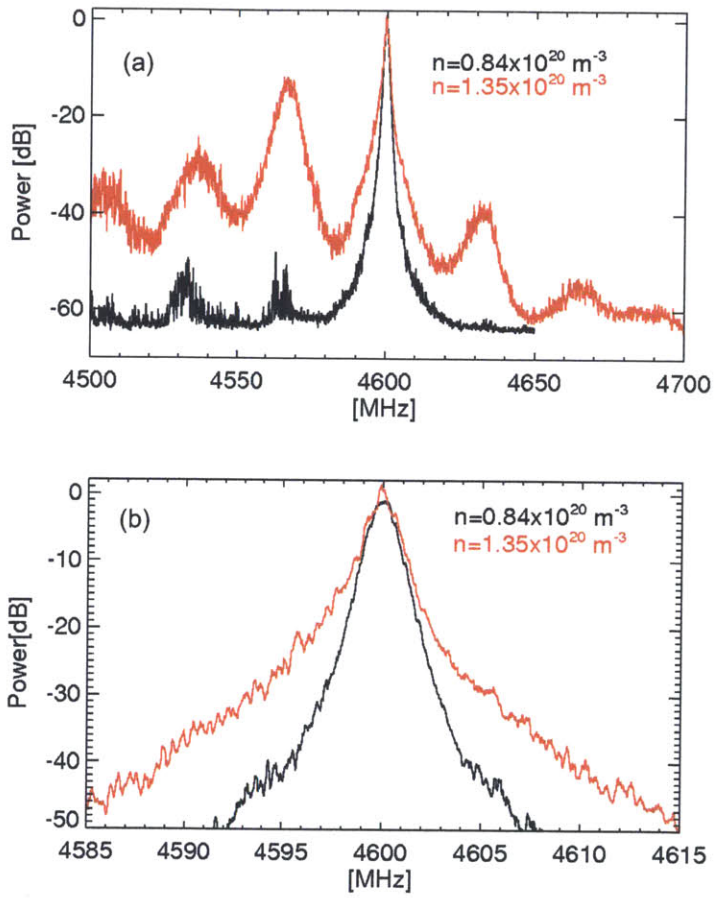

Figure 5-21: LH spectra measured with the launcher probe at two different densities of $\overline{n}_e = 0.84 \times 10^{20}$ m^{-3} (Shot No. 1100806010) and $\overline{n}_e = 1.35 \times 10^{20}$ m^{-3} (1100820031) in LSN plasmas. Plasma parameters are $B_{T0} = 5.4$ T, $I_p = 800$ kA, $P_{LH} = 600$ kW, and the launched peak $n_{\|} = 1.9$. Shown are (a) broad-band and (b) narrow-band spectra near the pump frequency.

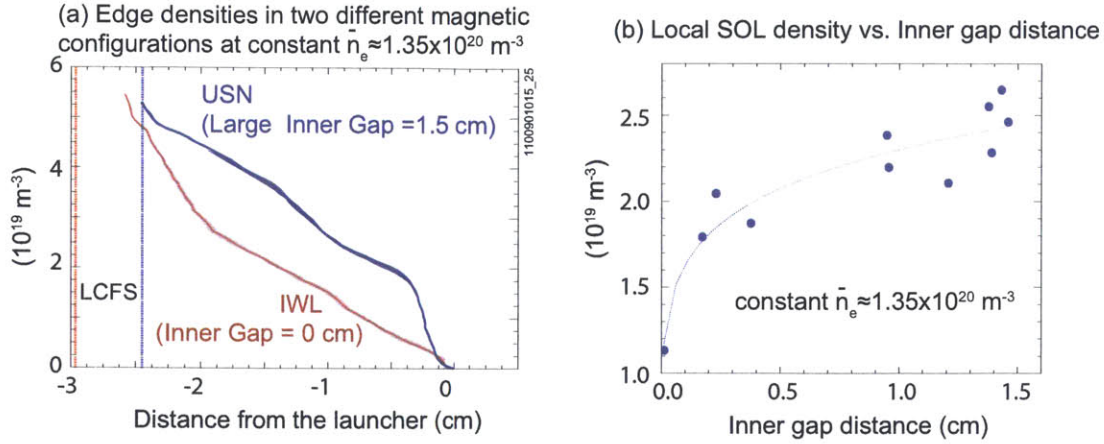

Figure 5-22: (a) SOL density profiles measured with the X-mode reflectometer in front of the LH launcher in the USN and IWL plasmas at $\overline{n}_e \approx 1.35 \times 10^{20}\,\mathrm{m}^{-3}$. (b) Dependence of the local SOL density at a radial location 1 cm in front of the LH launcher as a function of the inner gap distance that is based on EFIT calculations.

the higher density plasma at $\overline{n}_e \approx 1.35 \times 10^{20}\,\mathrm{m}^{-3}$, the integrated spectral power ratio of the sideband to the pump is about 20 % in this particular case.

In addition, Figure 5-21 (b) shows the zoomed-in spectra of the same spectra near the pump frequency. The pump broadening is symmetrical at the lower density. However, in the high-density plasma, the spectrum is clearly down-shifted starting from 10 dB below the pump peak power, persisting until the ion cyclotron side-bands dominate the spectrum. The observed downshifted asymmetric spectrum is attributed to ion sound PDI, rather than to wave scattering by turbulence.

The IWL plasma also exhibits a lower LFS edge density than that of the USN plasma. Figure 5-22 (a) compares the edge density profiles between the IWL and USN plasmas at $\overline{n}_e \approx 1.35 \times 10^{20}\,\mathrm{m}^{-3}$. Figure 5-22 (b) shows that the decrease in the inner gap distance is correlated with the decrease in the local SOL density at the radial location 1 cm away from the launcher. When the inner gap distance is 0, the plasma becomes inner-wall limited, and the local density in front of the launcher is minimized.

Figure 5-23 compares the measured LH spectra at the LH launcher in the same IWL (no inner gap) and USN (large inner gap = 1.5 cm) plasmas of Figure 5-22 (a). Only the inner gap is varied, while other plasma parameters are kept fixed. A

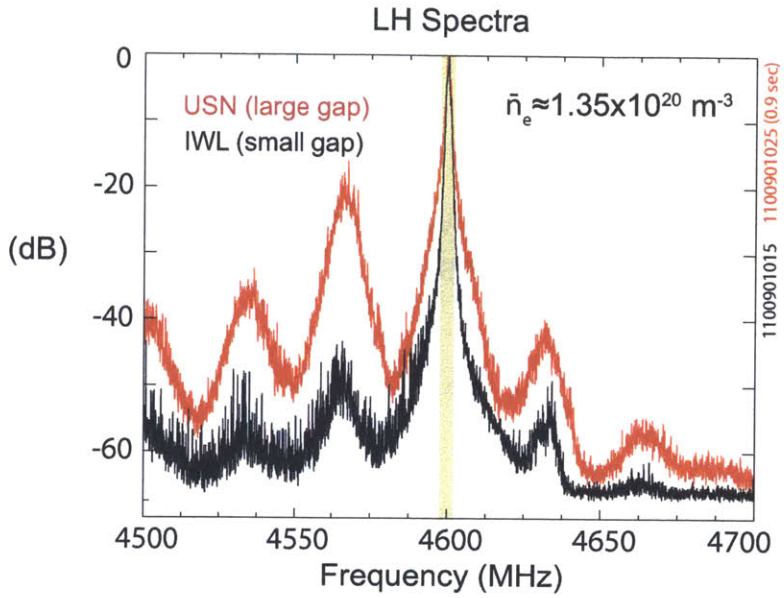

Figure 5-23: LH frequency spectra measured with the launcher probe in the USN (red) and IWL (black) plasmas at $\overline{n}_e \approx 1.35 \times 10^{20}\,\mathrm{m}^{-3}$. Plasma parameters are $B_0 = 5.4\,\mathrm{T}$, $I_p = 800\,\mathrm{kA}$, $P_{LH} = 550\,\mathrm{kW}$, and the launched peak $n_{\|} = 1.9$.

commercial spectrum analyzer was used to record the LH spectra. Two non-linear effects are observed to be weakened in the IWL plasma: ion cyclotron sideband peaks are strongly suppressed, and the spectral width of the pump LH wave is also noticeably reduced.

This magnetic-configuration-dependent PDI suggests that edge plasma parameters are more important than global plasma parameters in determining the PDI strength. The different magnetic configurations appear to affect the level of the edge density, which subsequently determines the PDI strength. Figure 5-24 summarizes the change in the pump width and the ratio of the sideband spectral power to the pump spectral power as a function of the local SOL density in front of the launcher. The measurements are made in a number of plasmas with different inner-gap distances, while $\overline{n}_e$ is kept constant. The local SOL density, at a fixed radial location from the launcher, is found to vary with the inner-gap distance. It is minimized in the IWL plasma, and maximized in the USN plasma. Interestingly, both the pump width at 30 dB below the pump peak and the sideband spectral power exhibit the threshold behavior above a certain local density. In this particular

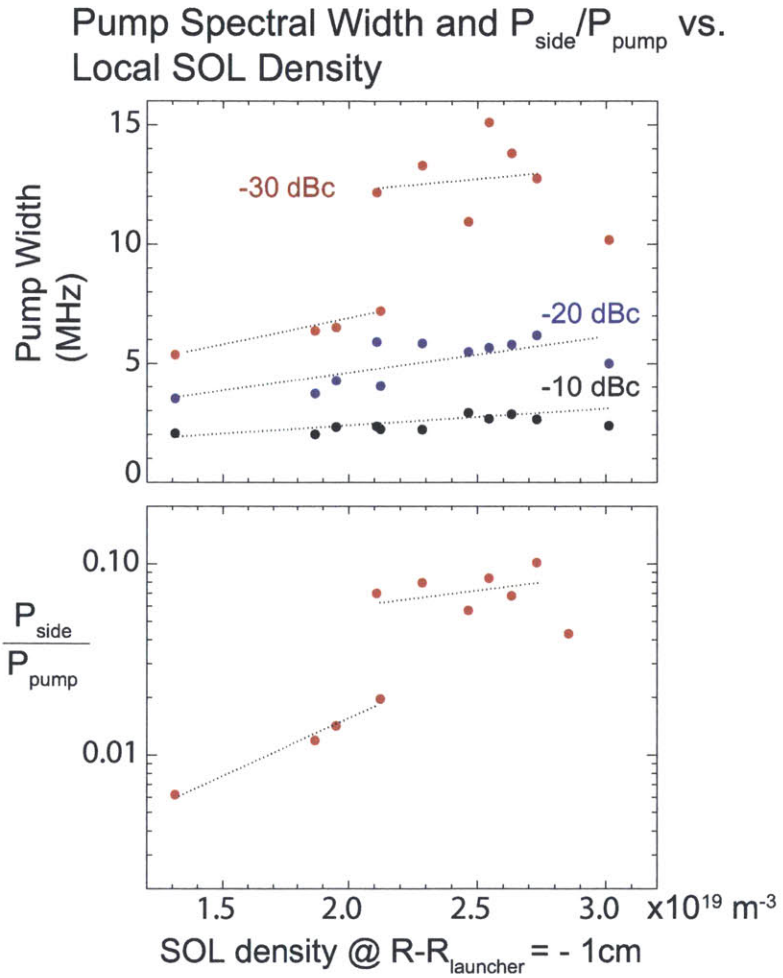

Figure 5-24: (a) Measured pump broadening at 10 dB, 20 dB, and 30 dB below the pump peak power and (b) the ratio of the sideband power to the pump power as a function of the local SOL density 1 cm radially away from the LH launcher for the same plasma parameters shown in Figure 5-23 except the inner-gap distance. Here, the pump power is defined as the integrated spectral power within the frequency range 4600 ± 2 MHz, and the sideband power is the integrated spectral power in the frequency range outside of the pump.

case, it corresponds to $n_e \approx 2.1 \times 10^{19}\,\mathrm{m}^{-3}$. The sideband power becomes about 10% of the pump power in the case shown. Here, the pump power is defined as the integrated spectral power within the frequency range $4600 \pm 2\,\mathrm{MHz}$, and the sideband power is the integrated spectral power in the remaining frequency range. Note that the spectral broadening at 30 dB below the pump peak power is reported to be an experimental signature that the LHCD performance is degraded by the ion sound PDI that occurs in front of the launcher [50, 56, 60].

5.5 Possible Role of PDI on the Loss of Lower Hybrid Current Drive Efficiency

As discussed in the previous section, the onset of PDI is observed to be in the density range where the discrepancy remains between the experimentally measured non-thermal hard X-ray count rate and the simulated hard X-ray count rate with edge loss mechanisms, such as collisional loss and full-wave effects. This suggests that PDI may be a mechanism that can explain the remaining discrepancy because no non-linear effects are considered in those simulations.

Experimental evidence of pump depletion at the HFS edge observed in LSN plasmas corroborates this hypothesis. Figure 5-25 (a) shows the frequency integrated spectral power of the pump and the first down-shifted ion cyclotron sideband at the HFS and that of the pump at the LFS as a function of $\overline{n}_e$ when $P_{LH} = 800\,\mathrm{kW}$ and peak $n_{||} = 1.6$. Lower $n_{||}$ does not significantly affect the onset of HFS PDI. The strength of the first down-shifted sideband power shows a threshold behavior above $\overline{n}_e \approx 1.0 \times 10^{20}\,\mathrm{m}^{-3}$, similar to the case when peak $n_{||} = 1.9$ (e.g., Figure 5-11). However, in contrast to the previous case, the strength of the first-downshifted sideband power decreases when $\overline{n}_e$ is raised above $\overline{n}_e \approx 1.1 \times 10^{20}\,\mathrm{m}^{-3}$. This could be due to a combination of multiple effects such as accessibility condition and different LH wave propagation behavior. We also cannot rule out the possibility that HFS PDI originates toroidally or poloidally away from

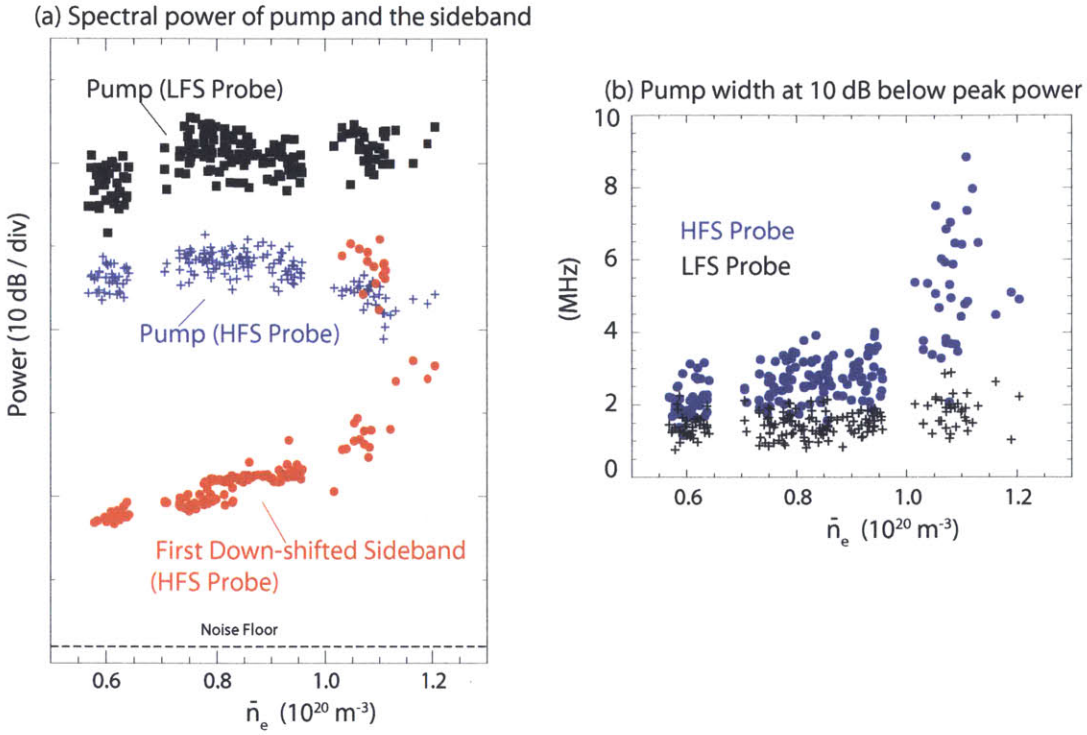

Figure 5-25: (a) Dependence of the pump spectral power measured with the launcher probe (LFS probe) and with the inner wall probe (HFS probe), and the first down-shifted sideband power measured with the HFS probe as a function of $\overline{n}_e$. Deuterium plasmas. Plasma parameters are $B_{T0} = 5.4$ T, $I_p = 550$ kA, $P_{LH} = 500$ kW, and the launched peak $n_{\|} = 1.6$. (b) Dependence of pump broadening as a function of $\overline{n}_e$ for the same plasma discharges.

the location of the probe.

Figure 5-25 (a) also implies that the observed HFS PDI is responsible for the loss of LHCD at high density. The first down-shifted sideband power becomes comparable to the pump power at $\overline{n}_e \approx 1.1 \times 10^{20}\,\mathrm{m}^{-3}$. At the same density, the pump power at the HFS starts to decrease, whereas that at the LFS remains nearly unchanged. As shown in the ray trajectory in Figure 5-9, LH waves are reflected at the HFS before being absorbed by electron Landau-damping. Thus, the observed decrease in pump power with the onset of ion cyclotron PDI at the HFS suggests that PDI can be partially responsible for the loss of current drive efficiency, especially in the multi-pass regime.

PDI occurring at the HFS edge may have also played a role in LH current drive experiments in Alcator C [106]. In this limited tokamak, ion cyclotron PDI was observed by RF probes located at the LFS edge and was characterized by the sidebands modulated by ω_{ci} at the LFS. In some circumstances, little ion cyclotron PDI was detected on the RF probes, even when the electron tail formation was already weak [107]. Ion cyclotron PDI at the HFS edge may be a key to explain those observations.

Figure 5-25 (b) shows the simultaneous pump broadening measured at the HFS edge. The fact that the pump broadening is correlated with the onset of ion cyclotron PDI suggests that it could be due to ion sound parametric decay at the HFS edge, but it is difficult at the moment to rule out the contribution of the wave-scattering effect by turbulence. Nonetheless, Figure 5-25 points out that spatially-localized measurements could be important in identifying non-linear effects because no significant change in the pump width is observed with the probes located at the LFS edge. This also suggests that the assumed spectral broadening near the launcher in FTU [56], based on the observed LH frequency spectra, can be questionable because the probe location is reported to be 180 deg toroidally away from the launcher.

Meanwhile, it is worth noting again that a similar level in the non-thermal hard X-ray count rate has been measured between USN and LSN plasmas, although a relatively weaker ion cyclotron PDI is observed to be excited at the LFS in USN

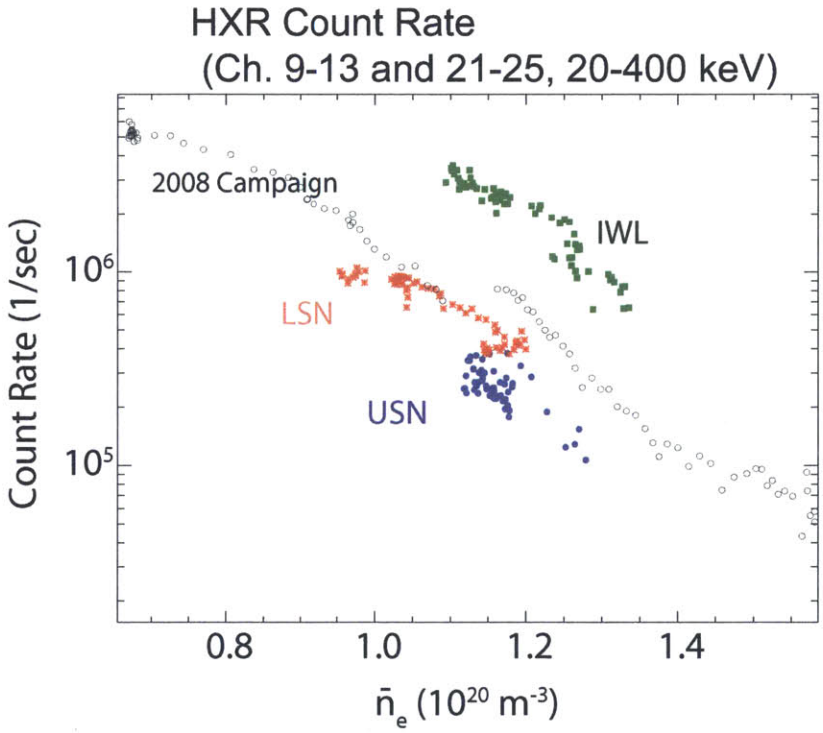

Figure 5-26: Experimentally measured non-thermal hard X-ray count rates as a function of $\overline{n}_e$ in the LSN, USN and IWL plasmas discussed in this chapter. Over-plotted are the experimental results obtained during the 2008 campaign for the purpose of comparison. The count rates are normalized to the square root of the net LH power [10].

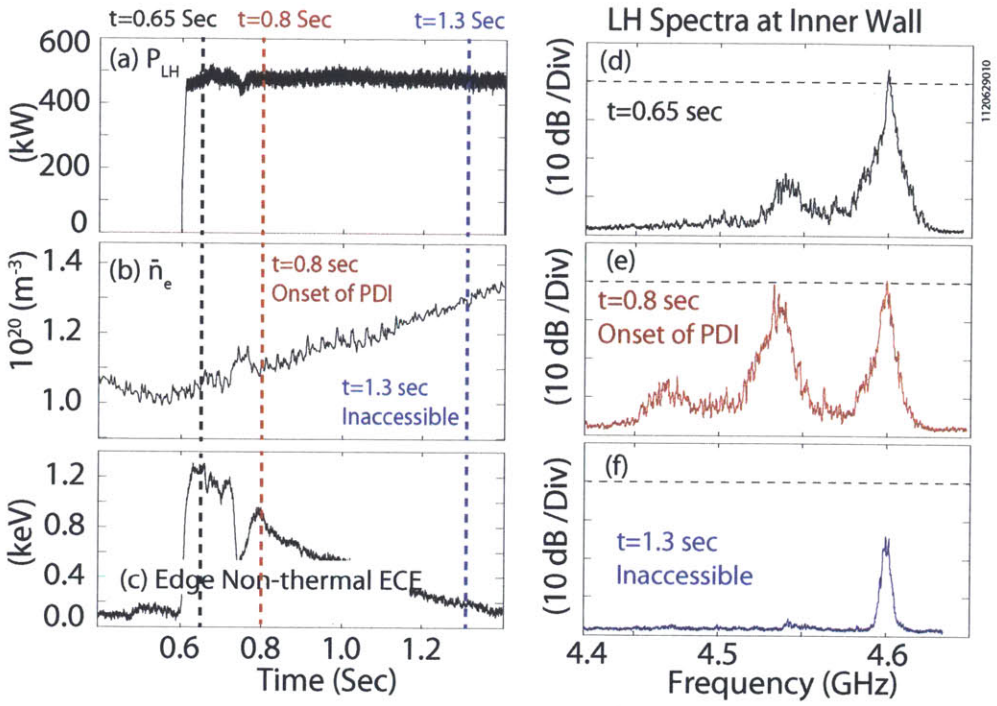

Figure 5-27: Time traces for a LSN L-mode discharge (Shot No. 1120629010): (a) coupled LH power, (b) line averaged density, (c) edge non-thermal electron emission, LH frequency spectra measured with the inner wall probe (HFS probe) at (d) t=0.65 sec, (e) t=0.8 sec, and (f) t=1.3 sec. Parameters are $B_{T0} = 5.4\,\mathrm{T}$, $I_p = 550\,\mathrm{kA}$, and the launched peak $n_{\|} = 1.6$.

plasmas. Figure 5-26 shows the non-thermal hard X-ray count rates as a function of $\overline{n}_e$ for the three discharges discussed in Section 5.3. IWL plasmas show an increase in hard X-ray count rate by an order of magnitude. The diverted discharges (LSN and USN plasmas) follow the previous experimental trend, although no clear experimental evidence of pump depletion is observed in a USN plasma in the density range of interest.

If ion cyclotron PDI happens in front of the launcher on the first pass and is significant, it is expected that the reduction of pump power would be observed with the inner wall probes. For example, when LH waves become inaccessible to plasma, inner wall probes detect little power reaching the HFS edge. For example, Figure 5-27 shows a decrease in peak pump power with the onset of HFS PDI (note the dB scale), followed by a further reduction in peak pump power by about 15 dB in an inaccessible

plasma. Note that, in this particular case, the launched peak $n_{\parallel}$ is 1.6 and the LH waves become inaccessible when $\overline{n}_e \gtrsim 1.2 \times 10^{20}\,\mathrm{m}^{-3}$. The reduction of peak pump power in inaccessible plasma indicates that LH waves now propagate in trajectories bounded by the fast and slow wave cut-offs and the mode conversion layer and that pump power does not reach the location of the HFS edge probes.

While it could be difficult to measure the pump depletion in the dB range, no apparent decrease in pump power with the onset of ion cyclotron PDI at the LFS edge is seen so far. It could be argued that the existing probes may not be sensitive to a region where strong ion cyclotron PDI occurs at the LFS edge. This is based on the observations in LSN plasmas that the probes located at the LFS did not indicate any strong onset of ion cyclotron PDI at the HFS edge. For example, the launcher probe might not be ideal to detect the propagating sideband LH waves because they are likely to propagate away from the launcher along the pump in the parallel coupling limit.

In addition to ion cyclotron PDI, it is worth noting again that pump broadening due to the ion sound quasi-mode has been used to explain the loss of current drive efficiency [56]. It was postulated that ion sound quasi-mode occurring at the mouth of the launcher could modify the launched wave-number spectrum and generate the sideband LH waves with higher $n_{\parallel}$. It was argued that a small percentage (1% $\sim$ 10%) of these LH waves could significantly interact with the pump LH waves to Landau-damp most of the LH power at the plasma periphery in a single-pass. To experimentally support this, the pump broadening at 30 dB below the peak power was presented.

However, no significant amount of pump broadening has been observed in Alcator C-Mod plasmas using the launcher probe. Although the measured pump width shows the broadening of 1 $\sim$ 2 MHz at the 10 dB level below the peak power, which is more broadened than the width measured at the output of the klystron, there is no experimental evidence that this broadening plays a critical role in understanding the loss of current drive efficiency in high-density Alcator C-Mod plasmas. As shown in Figures 3-15 and 5-25 (b), the increase in the pump width at 10 dB below the peak

pump power at the launcher is gradual without any abrupt changes as a function of $\overline{n}_e$. Figures 3-15 also shows that the change in pump width becomes apparent at 30 dB below the peak pump power across $\overline{n}_e \approx 1.0 \times 10^{20}\,\mathrm{m}^{-3}$, however, in terms of power level, the spectral power at this level, which is 0.1% of the peak pump power, is not expected to be significant enough to affect the LHCD performance.

5.6 Chapter Summary

In this chapter, the observed onset of ion cyclotron PDI is characterized in different mangetic configurations; ion cyclotron PDI is found to be excited at the HFS edge as well as at the low-field-side (LFS) edge in the Alcator C-Mod tokamak when $\overline{n}_e > 1.0 \times 10^{20}\,\mathrm{m}^{-3}$, depending on the plasma configuration in L-mode plasmas with $\vec{B} \times \nabla B$ drift direction downward. This is the density range where additional loss mechanisms are necessary to explain the observed loss of LHCD efficiency, in addition to collisional absorption or full-wave effects. Regardless of magnetic configurations, the LH sidebands are peaked at the first down-shifted ion cyclotron LH sideband, suggesting that ion modes are excited near the cold SOL region and are expected to have moderately high $ck_{\|}/\omega_0$, as presented in Chapter 4. The ray tracing analysis shows that the observed onset of ion cyclotron PDI is likely due to the minimized convective loss in the parallel coupling limit in high density plasmas. This is because the radial penetration of the pump LH wave becomes weaker with the increase in $\overline{n}_e$, which is dictated by the dispersion of LH waves ($v_{g,\perp}/v_{g,\|} \approx \omega_0/\omega_{pe}$).

LH spectra measurements in upper-single-null (USN), lower-single-null (LSN), and inner-wall-limited (IWL) plasmas are presented. Both USN and LSN plasmas show a similar level of non-thermal hard X-ray count rates, although they show different ion cyclotron PDI strengths and excitation location. In LSN plasmas, ion cyclotron PDI occurs near the HFS edge. A decrease in pump power is found to correlate with the onset of ion cyclotron PDI that is excited at the HFS edge at $\overline{n}_e \approx 1.2 \times 10^{20}\,\mathrm{m}^{-3}$. The observed ion cyclotron PDI can be strong in the density range below the classical PDI limit ($\omega_0/\omega_{LH}(0) \approx 2$) [12]. The ray tracing simulation shows that the launched

LH rays can propagate toward the HFS edge due to their limited radial penetration in multi-pass regimes. Two possible mechanisms for enhanced growth are discussed. One is the spatial broadening of the pump and the other is the slowing down of the radial group velocities of LH waves.

In USN plasmas, ion cyclotron PDI generally occurs at the LFS edge, as evidenced by frequency separations with $\omega \approx n\omega_{ci,LFSedge}$. Even the inner wall probe detects the sidebands that are excited at the LFS edge. This measurements also suggest that the parallel refractive index ($n_{\|}$) of the LH sideband is similar to that of the pump LH wave, given that the relative strength of the sideband to the pump is independent of the probe locations. The observed sideband power is not as strong as that of the sideband observed in the LSN plasmas at the same $\overline{n}_e$ ($\approx 1.2 \times 10^{20}\,\mathrm{m}^{-3}$), and no clear experimental evidence of pump depletion is observed. Given that both USN and LSN plasmas show a similar level of non-thermal hard X-ray count rates as long as $\overline{n}_e$ is similar, a possible explanation for this observation is that the location of the probe installed on the launcher is not ideal to detect ion cyclotron PDI because the LH sidebands may propagate away from the launcher along the launched LH wave when it is excited in front of the launcher. The importance of choosing the proper detection location is also evidenced by the observation that only the inner wall probe detects the strong ion cyclotron PDI that occurs at the HFS edge.

In IWL plasmas, the threshold density for ion cyclotron PDI at the HFS edge is slightly higher $\overline{n}_e \gtrsim 1.3 \times 10^{20}\,\mathrm{m}^{-3}$, but, once excited, it shows similar behavior to that observed in LSN plasmas. This higher density threshold could be due to a combined effects of different wave propagation behavior and the minimized cold SOL region at the HFS side.

These data suggest that ion cyclotron PDI may start to play a role to decrease LHCD efficiency at $\omega_0/\omega_{LH}(0) \lesssim 3$, which is a lower density threshold than the previously studied density limit ($\omega_0/\omega_{LH}(0) \approx 2$) [12]. In particular, the presented experiments imply that the HFS edge/SOL in a diverted tokamak can be potentially susceptible to non-linear effects in multi-pass regimes.

Different ion cyclotron PDI behaviors in different magnetic configurations are

correlated to different SOL characteristics depending on the magnetic configurations. For example, at $\overline{n}_e \approx 1.2 \times 10^{20}\,\mathrm{m}^{-3}$, only USN plasmas exhibit LH sidebands that are due to ion cyclotron PDI at the LFS edge. This correlates to higher edge densities in front of the launcher in USN plasmas than in LSN and IWL plasmas. It is also experimentally observed that the reducing the inner gap distance while maintaining the same $\overline{n}_e$ weakens the strength of ion cyclotron PDI that is excited at the LFS edge, implying the edge plasma-wave interaction plays an important role in determining the strength of the observed ion cyclotron PDI.

THIS PAGE INTENTIONALLY LEFT BLANK

Chapter 6

Conclusions and Future Work

6.1 Conclusions

In the present thesis, two experimental investigations are performed to understand the loss of LHCD efficiency observed in reactor-relevant high density Alcator C-Mod plasmas with $\overline{n}_e \gtrsim 1.0 \times 10^{20}\,\mathrm{m}^{-3}$. First is the detection of LH waves in the SOL using the microwave backscattering technique. Second is the LH frequency spectra measurement using probes to characterize the onset of ion cyclotron PDI in the diverted Alcator C-Mod tokamak. The new findings of this thesis include the identification of ion cyclotron PDI at the HFS edge and advancement of PDI as a candidate mechanism for the LHCD density limit at $\omega_0/\omega_{LH}(0) > 2$.

The microwave backscattering experiment presented in Chapter 3 is shown to be a viable option to study LH waves within the plasma. The modified 60 GHz O-mode reflectometer system can detect the backscattered O-mode wave as a result of the scattering of the incident O-mode wave by the LH wave at a radial location where both energy- and momentum-matching conditions are satisfied. Radially localized measurements of the LH wave electric field in the SOL are demonstrated in high density plasmas ($\overline{n}_e \gtrsim 0.9 \times 10^{20}\,\mathrm{m}^{-3}$). This experiment confirms the presence of LH waves away from the LH launcher, suggesting that the launched LH power is not completely dissipated near the LH launcher. An order of 1 MHz LH pump broadening (FWHM) is estimated in the density range of interest, suggesting that LH waves are

affected by non-linear effects, such as ion sound PDI and wave scattering. However, no apparent experimental evidence is found that the broadened width is an indication that LHCD efficiency is severely impacted due to the mechanism that is responsible for the observed broadening. This is also supported by the probe measurements presented in Chapter 5, which indicate that LH spectral width (FWHM) is already broadened below $\overline{n}_e \approx 1.0 \times 10^{20}\,\mathrm{m}^{-3}$.

Clearer experimental evidence of LH pump depletion is reported in Chapter 5 due to the ion cyclotron PDI that is excited at the HFS edge (HFS PDI). The observed onset of HFS PDI in LSN and IWL plasmas in the density range of $\overline{n}_e \approx 1.1 \sim 1.3 \times 10^{20}\,\mathrm{m}^{-3}$ shows that LH waves can be susceptible to non-linear effects at the HFS edge of the tokamak away from the launcher, unlike the conventional picture that non-linear effects are confined to the plasma edge near the LH launcher. The underlying cause of the observed HFS PDI is thought to be the weak radial penetration of the pump LH wave in a high-density multi-pass regime, which can result in reduced convective loss at the HFS edge. The ray-tracing simulations suggest that both the spatial broadening of the pump resonance cone and the slowing of the LH group velocities can be responsible for the reduced convective loss. In addition to the observed HFS PDI, the LH pump broadening is measured locally with the inner-wall probe simultaneously, implying that the plasma condition and LH wave propagation behavior at the HFS edge could be potentially susceptible to non-linear effects in general.

However, unlike in LSN and IWL plasmas, the seemingly weak ion cyclotron PDI is excited at the LFS edge (LFS PDI) in USN plasmas in the density range of interest (i.e., $\overline{n}_e \gtrsim 1.0 \times 10^{20}\,\mathrm{m}^{-3}$), which correlates with the different level of edge densities in different magnetic configurations. In USN plasmas, regardless of the position of the probes, the measured LH spectra resemble each other, and no apparent pump depletion is observed in the density range of interest. The sideband power also appears to be too weak to cause any significant degradation in the LHCD. Thus, it cannot be said that the observed ion cyclotron PDI is the remaining power loss mechanism unless the experimental evidence of pump depletion due to LFS PDI

is detected as well.

In conclusion, ion cyclotron PDI is found to be excited in the density range where additional loss mechanisms are necessary to explain the anomalous decrease of non-thermal hard X-ray count rates in Alcator C-Mod high density diverted plasmas ($\overline{n}_e \gtrsim 1.0 \times 10^{20}\,\mathrm{m}^{-3}$). In particular, evidence of pump depletion due to ion cyclotron PDI at the HFS edge is observed in LSN and IWL plasmas at densities ($\overline{n}_e \gtrsim 1.2 \sim 1.3 \times 10^{20}\,\mathrm{m}^{-3}$) below the previously studied PDI density limit. Nonetheless, the role of the observed ion cyclotron PDI on the loss of LHCD efficiency is inconclusive, unless the experimental evidence is found that ion cyclotron PDI at the LFS edge can also cause pump depletion in the density range of interest. The conjecture is that the location of the existing probes are not optimized to detect pump depletion due to ion cyclotron PDI that occurs at the LFS edge, and further experimental investigation is necessary.

Meanwhile, the observations presented corroborate that the launched LH waves are weakly absorbed on the first pass into the plasma, and support the future experimental approach [108] of Alcator C-Mod to enhance single pass absorption. Since most of the LH waves will be Landau-damped on the first pass, this approach is expected to mitigate most of the potential loss mechanisms, including ion cyclotron PDI that is excited at the HFS edge. Thus, strong single-pass absorption will help recover the expected LHCD efficiency, which is in line with the conclusions of the previous studies. No LHCD experiments to date have been conducted in single-pass absorption regime, which will be the plasma condition of future reactor-grade tokamaks, such as ITER. Such experiments on Alcator C-Mod would be an important milestone towards the realization of the steady-state tokamak operation.

6.2 Future Work

The microwave backscattering experiments in Chapter 3 can be extended to examine the radial penetration of LH waves across the LCFS. The presented backscattering

experiment has the potential to identify the radial LH field structure. However, it was not possible to find experimental signatures that the LH power was deposited at the edge because the relatively low frequency of the incident O-mode wave only allowed probing of the SOL. Therefore, the use of multi-channel higher frequency sources is highly desirable to measure the strength of LH waves both inside and outside the LCFS. In addition, measurements of the primary part of the LH resonance cone directly leaving the launcher will provide an experimental constraint on the numerical modeling and may provide additional insights into LH wave propagation behavior in high density plasmas. At the same time, it will be necessary to perform detailed 2D/3D full wave calculations to simulate the interaction between O-mode waves and LH waves in a realistic geometry, which may explain the observed power discrepancy between the 1D modeling and experiment.

Much more experimental work remains to be done to identify the role of the observed ion cyclotron PDI in the loss of LHCD efficiency. The following two important questions need to be addressed with extensive probe measurements. The first question is the toroidal and poloidal spatial extent of HFS PDI. Examinations of the poloidal and toroidal distribution of the strength of low-frequency ion-modes will also help identify the spatial region where HFS PDI occurs because they are heavily-damped modes and cannot propagate very far from the excitation location. These measurements will help identify whether or not the observed HFS PDI can globally degrade the LHCD performance.

The second question is whether or not LFS PDI is excited on the first pass, which will help evaluate its role on the loss of LHCD efficiency. This is to understand the different strength of the observed ion cyclotron PDI between USN and LSN plasmas. The radial locations of the existing probes might not be ideal to detect LFS PDI. Furthermore, LFS PDI might occur at the LFS edge toroidally and poloidally relatively far from the launcher. The installation of the microwave backscattering system near the launcher may help identify where strong LFS PDI occurs in the SOL, which may not be easily detected with the probe installed on the surface of the launcher. It would also be interesting to examine the LH spectra near

the upper divertor region where both ray-tracing and full-wave simulations predict the presence of pump LH waves after the reflection at the inner wall. Spatially localized ion cyclotron PDI might occur there as well.

Enhancing single pass absorption will also help answer the latter question. A strong single pass absorption plasma will isolate the loss mechanisms near the launcher (e.g., LFS PDI near the launcher) from the loss mechanisms away from the launcher (e.g., collisional loss, full-wave effects, and HFS PDI). Thus, it will be possible to examine whether or not LFS PDI is excited on the first pass, and determine its role on the loss of LHCD efficiency. The latter could be done by comparing the LH effects between LSN and USN plasmas because LSN plasmas do not exhibit LFS PDI in the density range of interest ($\overline{n}_e \approx 1.2 \times 10^{20}\,\mathrm{m}^{-3}$) .

Further modeling work needs to be done to quantify the LH power loss due to the observed ion cyclotron PDI. Based on the theoretical and numerical PDI study within the linear PDI theory in Chapter 4, it was argued that the parallel coupling term is important in determining the convective growth of the sideband LH wave at the plasma edge. However, the problem of pump depletion cannot be treated with this approach. The non-linear full-wave [109] or particle-in-cell [110, 111] modeling may help calculate the amount of pump depletion due to ion cyclotron PDI.

THIS PAGE INTENTIONALLY LEFT BLANK

Appendix A

Three Wave Resonant Coupling in Homogeneous, Cold Plasma

The purpose of this appendix is to derive the coupling coefficient (Equation 3.5), by adopting an approach taken by Professor R. R. Parker [112]. Resonant nonlinear scattering of the incident ordinary-mode (O-mode) wave by the lower hybrid (LH) wave, which generates the backscattered O-mode wave, will be considered. Here, the finite parallel component (to the background magnetic field) of the LH wave is included in considering the wave matching condition. Both the parallel and perpendicular components of LH waves contribute to the density fluctuation, as shown later.

These linear waves with the superscript L all have the form

$$\begin{pmatrix} \vec{E}^L \\ \vec{H}^L \\ \vec{v_i}^L \\ \vec{v_e}^L \end{pmatrix} = \begin{pmatrix} \underline{\vec{E}} \\ \underline{\vec{H}} \\ \underline{\vec{v_i}} \\ \underline{\vec{v_e}} \end{pmatrix} e^{i\Lambda} + CC, \tag{A.1}$$

where $\Lambda = \omega t - \vec{k} \cdot \vec{r}$ and the coefficients of the exponential are complex constants.

Each mode is an independent solution of the following linearized equations:

$$\nabla \times \vec{E}^L = -\mu_0 \frac{\partial \vec{H}^L}{\partial t}, \tag{A.2}$$

$$\nabla \times \vec{H}^L = \epsilon_0 \frac{\partial \vec{E}^L}{\partial t} + en_0 \vec{v}_i^L - en_0 \vec{v}_e^L, \tag{A.3}$$

$$\frac{\partial \vec{v}_i^L}{\partial t} = \frac{e}{m_i} \vec{v}_i^L \times \vec{B}_0 + \frac{e}{m_i} \vec{E}^L, \tag{A.4}$$

$$\frac{\partial \vec{v}_e^L}{\partial t} = -\frac{e}{m_e} \vec{v}_e^L \times \vec{B}_0 - \frac{e}{m_e} \vec{E}^L, \tag{A.5}$$

$$\frac{\partial n_i^L}{\partial t} = -\nabla \cdot n_0 \vec{v}_i^L, \tag{A.6}$$

$$\frac{\partial n_e^L}{\partial t} = -\nabla \cdot n_0 \vec{v}_e^L. \tag{A.7}$$

However, they become coupled due to the non-linearity presented in the following full set of equations:

$$\nabla \times \vec{E} = -\mu_0 \frac{\partial \vec{H}}{\partial t}, \tag{A.8}$$

$$\nabla \times \vec{H} = \epsilon_0 \frac{\partial \vec{E}}{\partial t} + en_i \vec{v}_i - en_e \vec{v}_e, \tag{A.9}$$

$$\frac{\partial \vec{v}_i}{\partial t} = -\vec{v}_i \cdot \nabla \vec{v}_i + \frac{e}{m_i} \vec{v}_i \times \vec{B} + \frac{e}{m_i} \vec{E}, \tag{A.10}$$

$$\frac{\partial \vec{v}_e}{\partial t} = -\vec{v}_e \cdot \nabla \vec{v}_e - \frac{e}{m_e} \vec{v}_e \times \vec{B} - \frac{e}{m_e} \vec{E}, \tag{A.11}$$

$$\frac{\partial n_i}{\partial t} = -\nabla \cdot n_i \vec{v}_i, \tag{A.12}$$

$$\frac{\partial n_e}{\partial t} = -\nabla \cdot n_e \vec{v}_e. \tag{A.13}$$

Due to the non-linearity, the three waves (e.g., the incident O-mode wave, the LH

wave, and the non-linearly scattered O-mode wave) can be coupled as follows:

$$\begin{pmatrix} \vec{E} \\ \vec{H} \\ \vec{v_i} \\ \vec{v_e} \end{pmatrix} = a_0(t,\vec{r}) \begin{pmatrix} \underline{\vec{E}} \\ \underline{\vec{H}} \\ \underline{\vec{v_i}} \\ \underline{\vec{v_e}} \end{pmatrix}_0 e^{i\Lambda_0} + CC + a_1(t,\vec{r}) \begin{pmatrix} \underline{\vec{E}} \\ \underline{\vec{H}} \\ \underline{\vec{v_i}} \\ \underline{\vec{v_e}} \end{pmatrix}_1 e^{i\Lambda_1} + CC \\ + a_2(t,\vec{r}) \begin{pmatrix} \underline{\vec{E}} \\ \underline{\vec{H}} \\ \underline{\vec{v_i}} \\ \underline{\vec{v_e}} \end{pmatrix}_2 e^{i\Lambda_2} + CC, \tag{A.14}$$

where the subscripts 0, 1, and 2 represent three linear modes, respectively, and the a's are slowly varying functions of space and time. Note that the components of each column vector are defined to within the same arbitrary constant since the linear equations A.2 - A.7 are homogeneous. This constant is determined by normalizing the mode vectors, such that

$$4\langle W_n \rangle = \epsilon_0 |\underline{\vec{E}}_n|^2 + \mu_0 |\underline{\vec{H}}_n|^2 + m_i n_0 |\underline{\vec{v}}_{i,n}|^2 + m_e n_0 |\underline{\vec{v}}_{e,n}|^2 = \omega_n, \tag{A.15}$$

where $\langle W_n \rangle$ is the time-averaged energy density stored in each mode. Thus, the action density of the mode n with the mode amplitude a_n is $\langle W_n' \rangle = \omega_n |a_n|^2/4$.

Under the assumption that only the resonant nonlinear terms are important in determining the mode amplitudes with the resonant condition ($\Lambda_0 = \Lambda_1 + \Lambda_2$), this condition implies that

$$\omega_0 = \omega_1 + \omega_2, \tag{A.16}$$

$$\vec{k}_0 = \vec{k}_1 + \vec{k}_2. \tag{A.17}$$

For example, the mode 0 refers to the nonlinearly scattered O-mode wave, the mode 1 refers to the LH wave, and the mode 2 refers to the incident O-mode wave.

The mode amplitudes can be found by applying the conservation theorem to

Equations A.2- A.13 by forming the following combinations:

$$\begin{aligned}\vec{H}^L \cdot Eq(A.8) + \vec{H} \cdot Eq(A.2) - \vec{E}^L \cdot Eq(A.9) - \vec{E} \cdot Eq(A.3) + \\ n_0(\vec{v}_i^L \cdot Eq(A.10) + \vec{v}_e^L \cdot Eq(A.11) + \vec{v}_i \cdot Eq(A.4) + \vec{v}_e \cdot Eq(A.5)).\end{aligned} \tag{A.18}$$

Using $\vec{H} \cdot \nabla \times \vec{E}^L - \vec{E}^L \cdot \nabla \times \vec{H} = \nabla \cdot (\vec{E}^L \times \vec{H})$, $\vec{H}^L \cdot \nabla \times \vec{E} - \vec{E} \cdot \nabla \times \vec{H}^L = \nabla \cdot (\vec{E} \times \vec{H}^L)$, and $\vec{H} \cdot \dfrac{\partial \vec{H}^L}{\partial t} + \vec{H}^L \cdot \dfrac{\partial \vec{H}}{\partial t} = \dfrac{\partial (\vec{H} \cdot \vec{H}^L)}{\partial t}$, and $n_{i,e} = n_0 + \delta n_{i,e}$ and $\vec{B} = \vec{B}_0 + \delta \vec{B}$, Equation A.18 can be written as follows:

$$\begin{aligned}\frac{\partial}{\partial t}(\mu_0 \vec{H}^L \cdot \vec{H} + \epsilon_0 \vec{E}^L \cdot \vec{E} + n_0 m_i \vec{v}_i^L \cdot \vec{v}_i + n_0 m_e \vec{v}_e^L \cdot \vec{v}) + \nabla \cdot (\vec{E}^L \times \vec{H} + \vec{E} \times \vec{H}^L) = \\ -e\vec{E}^L \cdot (\delta n_i \vec{v}_i - \delta n_e \vec{v}_e) + e n_0 \vec{v}_i^L \cdot (\vec{v}_i \times \delta \vec{B}) - e n_0 \vec{v}_e^L \cdot (\vec{v}_e \times \delta \vec{B}) \\ -n_0 m_i \vec{v}_i^L \cdot (\vec{v}_i \cdot \nabla \vec{v}_i) - n_0 m_e \vec{v}_e^L \cdot (\vec{v}_e \cdot \nabla \vec{v}_e).\end{aligned} \tag{A.19}$$

Substituting

$$\begin{pmatrix} \vec{E}^L \\ \vec{H}^L \\ \vec{v}_i^L \\ \vec{v}_e^L \end{pmatrix} = \begin{pmatrix} \underline{\vec{E}^*} \\ \underline{\vec{H}^*} \\ \underline{\vec{v}_i^*} \\ \underline{\vec{v}_e^*} \end{pmatrix}_0 e^{-i\Lambda_0}, \tag{A.20}$$

for the linear mode 0, and

$$\begin{pmatrix} \vec{E} \\ \vec{H} \\ \vec{v}_i \\ \vec{v}_e \end{pmatrix} = a_0(t, \vec{r}) \begin{pmatrix} \underline{\vec{E}} \\ \underline{\vec{H}} \\ \underline{\vec{v}_i} \\ \underline{\vec{v}_e} \end{pmatrix}_0 e^{i\Lambda_0}, \tag{A.21}$$

for mode 0, and only those that drive the mode 0 [i.e., those with exponent $i\Lambda_0 = i(\Lambda_1 + \Lambda_2)$], the following mode equation for mode 0 can be obtained:

$$\frac{\partial}{\partial t} a_0 + \vec{v}_{g0} \cdot \nabla a_0 = \frac{K_0}{\omega_0} a_1 a_2, \tag{A.22}$$

where $\vec{v}_{g0}$ is the group velocity of mode 0 and K_0 is given by

$$K_0 = -e\underline{\vec{E}}_0^* \cdot (\underline{\delta n}_{i,1}\underline{\vec{v}}_{i,2} - \underline{\delta n}_{e,1}\underline{\vec{v}}_{e,2}) + en_0\underline{\vec{v}}_{i,0}^* \cdot (\underline{\vec{v}}_{i,1} \times \underline{\delta \vec{B}}_2) - en_0\underline{\vec{v}}_{e,0}^* \cdot (\underline{\vec{v}}_{e,1} \times \underline{\delta \vec{B}}_2)$$
$$-n_0 m_i \underline{\vec{v}}_{i,0}^* \cdot (\underline{\vec{v}}_{i,1} \cdot \nabla \underline{\vec{v}}_{i,2}) - n_0 m_e \underline{\vec{v}}_{e,0}^* \cdot (\underline{\vec{v}}_{e,1} \cdot \nabla \underline{\vec{v}}_{e,2}) + (1 \Leftrightarrow 2). \tag{A.23}$$

Similarly, by recalling that they are driven respectively by the modes 0 and 2 CC, and modes 0 and 1 CC, the mode equations for modes 1 and 2 can be obtained as follows:

$$\frac{\partial}{\partial t} a_1 + \vec{v}_{g1} \cdot \nabla a_1 = \frac{K_1}{\omega_1} a_0 a_2^*, \tag{A.24}$$

$$\frac{\partial}{\partial t} a_2 + \vec{v}_{g2} \cdot \nabla a_2 = \frac{K_2}{\omega_2} a_0 a_1^*, \tag{A.25}$$

where

$$K_1 = -e\underline{\vec{E}}_1^* \cdot (\underline{\delta n}_{i,0}\underline{\vec{v}}_{i,2}^* - \underline{\delta n}_{e,0}\underline{\vec{v}}_{e,2}^*) + en_0\underline{\vec{v}}_{i,1}^* \cdot (\underline{\vec{v}}_{i,0} \times \underline{\delta \vec{B}}_2^*) - en_0\underline{\vec{v}}_{e,1}^* \cdot (\underline{\vec{v}}_{e,0} \times \underline{\delta \vec{B}}_2^*)$$
$$-n_0 m_i \underline{\vec{v}}_{i,1}^* \cdot (\underline{\vec{v}}_{i,0} \cdot \nabla \underline{\vec{v}}_{i,2}^*) - n_0 m_e \underline{\vec{v}}_{e,1}^* \cdot (\underline{\vec{v}}_{e,0} \cdot \nabla \underline{\vec{v}}_{e,2}^*) + (0 \Leftrightarrow 2^*), \tag{A.26}$$

and

$$K_2 = -e\underline{\vec{E}}_2^* \cdot (\underline{\delta n}_{i,0}\underline{\vec{v}}_{i,1}^* - \underline{\delta n}_{e,0}\underline{\vec{v}}_{e,1}^*) + en_0\underline{\vec{v}}_{i,2}^* \cdot (\underline{\vec{v}}_{i,0} \times \underline{\delta \vec{B}}_1^*) - en_0\underline{\vec{v}}_{e,2}^* \cdot (\underline{\vec{v}}_{e,0} \times \underline{\delta \vec{B}}_1^*)$$
$$-n_0 m_i \underline{\vec{v}}_{i,2}^* \cdot (\underline{\vec{v}}_{i,0} \cdot \nabla \underline{\vec{v}}_{i,1}^*) - n_0 m_e \underline{\vec{v}}_{e,2}^* \cdot (\underline{\vec{v}}_{e,0} \cdot \nabla \underline{\vec{v}}_{e,1}^*) + (0 \Leftrightarrow 1^*). \tag{A.27}$$

It can be shown that for a system conserving energy and momentum, the coupling constants are related as follows:

$$K = \frac{K_0}{\omega_0} = -\frac{K_1^*}{\omega_1} = -\frac{K_2^*}{\omega_2}, \tag{A.28}$$

and the coupled mode equations can be put in the following form:

$$\frac{\partial}{\partial t}a_0 + \vec{v}_{g0}\cdot\nabla a_0 = K a_1 a_2 \tag{A.29a}$$

$$\frac{\partial}{\partial t}a_1 + \vec{v}_{g1}\cdot\nabla a_1 = -K^* a_0 a_2^* \tag{A.29b}$$

$$\frac{\partial}{\partial t}a_2 + \vec{v}_{g2}\cdot\nabla a_2 = -K^* a_0 a_1^* \tag{A.29c}$$

To calculate coupling constants in the presented case, an 1D slab geometry with the background magnetic field $\vec{B}_0 = B_0\hat{z}$ is considered with the following three modes: mode 0 is the scattered O-mode with $\omega = \omega_0$ and $\vec{k} = -k_0\hat{x} + k_{0,\|}\hat{z}$ where $k_0 > 0$, mode 1 is the LH mode with $\omega = \omega_1$ and $\vec{k} = k_1\hat{x} + k_{1,\|}\hat{z} = -|k_1|\hat{x} + k_{1,\|}\hat{z}$, and mode 2 is the incident O-mode with $\omega = \omega_2$ and $\vec{k} = k_2\hat{x}$ where $k_2 > 0$. Note again that the resonant condition implies that $\omega_0 = \omega_1 + \omega_2$ and $\vec{k}_0 = \vec{k}_1 + \vec{k}_2$. $\vec{k}_{0,\|} = \vec{k}_{1,\|}$, and $\vec{k}_{0,\perp} = \vec{k}_{1,\perp} + \vec{k}_{2,\perp}$. Thus, the scattered O-mode is assumed to gain a finite $k_\|$. Note also that higher order correction terms will be neglected in this calculation, which is discussed in detail in Chapter 3.2.2.

The complex amplitudes of mode 0 (i.e., the scattered O-mode) are given as follows:

$$\underline{\vec{E}}_0 = E_0\hat{z}, \tag{A.30a}$$

$$\underline{\delta\vec{B}}_0 = \sqrt{\mu_0\epsilon_0}E_0\hat{y}, \tag{A.30b}$$

$$\underline{\vec{v}}_{e,0} = -\frac{e}{i\omega_0 m_e}E_0\hat{z}, \tag{A.30c}$$

$$\underline{\vec{v}}_{i,0} = 0, \tag{A.30d}$$

$$\delta n_{i,0} = 0, \tag{A.30e}$$

$$\delta n_{e,0} = 0. \tag{A.30f}$$

The complex amplitudes of mode 1 (i.e., the LH mode) with the assumption that ions

are magnetized are given as follows:

$$\underline{\vec{E}_1} \approx E_1\hat{x}, \tag{A.31a}$$

$$\underline{\delta\vec{B}_1} \approx 0, \tag{A.31b}$$

$$\underline{\vec{v}_{e,1}} = -i\frac{\omega_1 e}{m_e\omega_{ce}^2}E_1\hat{x} + \frac{ieE_{1,z}}{m_e\omega_1}\hat{z}, \tag{A.31c}$$

$$\underline{\vec{v}_{i,1}} = -i\frac{e}{m_i\omega_1}E_1\hat{x}, \tag{A.31d}$$

$$\delta n_{i,1} = -i\frac{n_0 e}{m_i\omega_1^2}k_1E_1, \tag{A.31e}$$

$$\delta n_{e,1} = -i\frac{n_0 e}{m_e\omega_{ce}^2}k_{1,x}E_{1,x} + i\frac{n_0 e}{m_e\omega_{pe}^2}k_{1,x}E_{1,x}. \tag{A.31f}$$

Note also that the density fluctuation by the LH wave can be approximated to be

$$\begin{aligned}\delta n_{e,1} &= \frac{n_0}{\omega_1}(k_{1,x}v_{1,x} + k_{1,z}v_{1,z}) \\ &= -\frac{ien_0}{m_e\omega_{ce}^2}k_{1,x}E_{1,x} + \frac{ien_0}{m_e\omega_{pe}^2}k_{1,x}E_{1,x} \\ &\approx \frac{ien_0}{m_e\omega_{pe}^2}k_{1,x}E_{1,x},\end{aligned} \tag{A.32}$$

with the relations $k_{1,z} = -k_{1,x}\omega_1/\omega_{pe}$ and $E_{1,z} = (k_{1,z}/k_{1,x})E_{1,x}$.

The complex amplitudes of mode 2 (i.e., the incident O-mode) are given as follows:

$$\underline{\vec{E}_2} = E_2\hat{z}, \tag{A.33a}$$

$$\underline{\delta\vec{B}_2} = -\sqrt{\mu_0\epsilon_2}E_2\hat{y}, \tag{A.33b}$$

$$\underline{\vec{v}_{e,2}} = -\frac{e}{i\omega_2 m_e}E_2\hat{z}, \tag{A.33c}$$

$$\underline{\vec{v}_{i,2}} = 0, \tag{A.33d}$$

$$\delta n_{i,2} = 0, \tag{A.33e}$$

$$\delta n_{e,2} = 0. \tag{A.33f}$$

Using these complex amplitudes, the coupling coefficient K_1 is given by

$$\begin{aligned}
K_1 &= -n_0 m_e \vec{v}^*_{e,1} \cdot (\vec{v}^*_{e,2} \cdot \nabla \vec{v}_{e,0}) - e n_0 \underline{\vec{v}}^*_{e,1} \cdot (\underline{\vec{v}}_{e,0} \times \delta \underline{\vec{B}}^*_2 + \underline{\vec{v}}^*_{e,2} \times \underline{\vec{B}}_0) \\
&= -\frac{n_0 e^3}{m_e^2 \omega_{pe}^2} \frac{\omega_1}{\omega_0 \omega_2} |k_1| E_0 - e n_0 \underline{\vec{v}}^*_{e,1} \cdot \hat{x} \left[\frac{e}{i m_e} \left(\frac{\sqrt{\mu_0 \epsilon_2}}{\omega_0} - \frac{\sqrt{\mu_0 \epsilon_0}}{\omega_2} \right) \right] E_0 E_2^* \\
&= -\frac{n_0 e^3}{m_e^2 \omega_{pe}^2} \frac{\omega_1}{\omega_0 \omega_2} |k_1| E_0 + \frac{n_0 e^3}{m_e^2 \omega_{ce}^2} \frac{\omega_1}{\omega_0 \omega_2} (k_2 - k_0) E_0 E_1^* E_2^* \\
&= -\frac{n_0 e^3}{m_e^2 \omega_{pe}^2} \frac{\omega_1}{\omega_0 \omega_2} |k_1| E_0 + \frac{n_0 e^3}{m_e^2 \omega_{ce}^2} \frac{\omega_1}{\omega_0 \omega_2} |k_1| E_0 E_1^* E_2^* \\
&\approx -\frac{n_0 e^3}{m_e^2 \omega_{pe}^2} \frac{\omega_1}{\omega_0 \omega_2} |k_1| E_0 E_1^* E_2^*.
\end{aligned} \tag{A.34}$$

K_2 can be found by identifying that the three terms involving the electrons are nonzero while the ion terms vanish:

$$\begin{aligned}
K_2 &= e \underline{\vec{E}}^*_2 \cdot \delta n^*_{e,1} \underline{\vec{v}}_{e,0} - e n_0 \underline{\vec{v}}^*_{e,2} \cdot (\underline{\vec{v}}^*_{e,1} \times \underline{\delta \vec{B}}_0 + \frac{m_e}{e} \underline{\vec{v}}^*_{e,1} \cdot \nabla \underline{\vec{v}}_{e,0}) \\
&= \underline{\vec{E}}^*_2 \cdot \delta n^*_{e,1} \underline{\vec{v}}_{e,0} \\
&\approx -\frac{n_0 e^3}{m_e^2 \omega_{pe}^2} \frac{|k_1|}{\omega_0} E_0 E_1^* E_2^*.
\end{aligned} \tag{A.35}$$

Note that the two terms in the parenthesis cancel each other.

K_0 can be also found in a similar way that K_2 is found:

$$\begin{aligned}
K_0 &= e \vec{E}^*_0 \delta n_{e,1} \vec{v}_{e,2} \\
&\approx \frac{n_0 e^3}{m_e^2 \omega_{pe}^2} \frac{|k_1|}{\omega_2} E_0^* E_1 E_2.
\end{aligned} \tag{A.36}$$

It can be seen that the coupling constants are related as follows:

$$K = \frac{K_0}{\omega_0} = -\frac{K_1^*}{\omega_1} = -\frac{K_2^*}{\omega_2} = \frac{n_0 e^3}{m_e^2 \omega_{pe}^2} \frac{|k_1|}{\omega_0 \omega_2} E_0^* E_1 E_2. \tag{A.37}$$

To calculate the electric fields appearing in Equation A.37, they are assumed to be real quantities without loss in generality although they were assumed to be complex

in calculating K's. E_0 can be found from Equation A.15:

$$\epsilon_0 E_0^2 + \mu_0 \epsilon(\omega_0)\frac{E_0^2}{\mu_0} + m_e n_0 \frac{e^2}{\omega_0^2 m_e^2} E_0^2 = \omega_0 \Leftrightarrow E_0 = \sqrt{\frac{\omega_0}{2\epsilon_0}} \tag{A.38}$$

E_2 is found in a similar way and $E_2 = \sqrt{\frac{\omega_2}{2\epsilon_0}}$. To calculate E_1, it should be noted that the parallel electric field also contributes to the energy density. While E_1 can be found in the similar way, E_1 can be also found from the following expression that relates the energy density to the electric field:

$$\langle W_1 \rangle = \frac{1}{4}\epsilon_0 E_1^* \frac{\partial}{\partial \omega}(\omega\epsilon)E = \frac{1}{4}\epsilon_0 E_{1x}^2 (2 + 2\frac{\omega_{pe}^2}{\omega_{ce}^2}), \tag{A.39}$$

where ϵ is

$$\epsilon \approx \begin{pmatrix} 1 - \frac{\omega_{pi}^2}{\omega_1^2} + \frac{\omega_{pe}^2}{\omega_{ce}^2} & 0 & 0 \\ 0 & 0 & 0 \\ 0 & 0 & 1 - \frac{\omega_{pe}^2}{\omega_1^2} \end{pmatrix}, \tag{A.40}$$

and it is assumed that $\vec{E}_1 = E_{1x}\hat{x} + E_{1z}\hat{z}$ and $k_z^2/k_x^2 = -\epsilon_{xx}/\epsilon_{zz}$. Then E_1 becomes

$$E_{1x} = \sqrt{\frac{\omega_1}{\epsilon_0}} \frac{1}{\sqrt{2 + 2\omega_{pe}^2/\omega_{ce}^2}}. \tag{A.41}$$

Substituting these E's into Equation A.37, K is finally calculated to be

$$K \simeq \omega_{pe} \sqrt{\frac{\omega_1}{\omega_0 \omega_2}} \frac{|k_1|}{\sqrt{n_0 m_e}} \frac{1}{2\sqrt{2 + 2\omega_{pe}^2/\omega_{ce}^2}}. \tag{A.42}$$

THIS PAGE INTENTIONALLY LEFT BLANK

Appendix B

Analytic Backscattering Power in 1D Inhomogeneous Plasma

The purpose of this Appendix is to derive the 1D backscattering power shown in Equation 3.9.

B.0.1 Analytic Solution of Mode Amplitudes

Equation 3.7 can be rewritten in the following form

$$\frac{\mathrm{d}}{\mathrm{d}\xi}a_0 = -l\frac{K}{v_{g0}}a_1 a_2 \exp(-i\xi^2) \tag{B.1a}$$

$$\frac{\mathrm{d}}{\mathrm{d}\xi}a_2 = -l\frac{K^*}{v_{g2}}a_1^* a_0 \exp(i\xi^2) \tag{B.1b}$$

with the following normalization

$$\xi \equiv \sqrt{\frac{\kappa'}{2}}x \equiv x/l. \tag{B.2}$$

Eliminating a_0, the second order differential equation for a_2 is obtained

$$a_2'' - 2i\xi a_2' - Za_2 = 0, \tag{B.3}$$

where $Z = l^2 K K^* a_1 a_1^* / (v_{g0} v_{g2})$. By substituting a trial solution of the form

$$a_2 = \exp\left(i\frac{\xi^2}{2}\right) u(\xi), \tag{B.4}$$

Equation B.3 becomes

$$u'' + (\xi^2 + (i - Z))u = 0. \tag{B.5}$$

It is shown in Gradshteyn and Ryzhik [83] that the differential equation of the form

$$u'' + (\xi^2 + \lambda)u = 0 \tag{B.6}$$

has solutions in terms of parabolic cylinder functions

$$u = D_{-\frac{1+i\lambda}{2}}(\pm(1+i)\xi). \tag{B.7}$$

Since we are interested in the propagation from the left ($\xi \to -\infty$) to right ($\xi \to +\infty$), we choose the one with the positive argument of Equation B.7 as a physically relevant solution of a_2 for our case and neglect the second. We construct a general solution of a_2 as follows:

$$a_2 = c_2 e^{i\xi^2/2} D_{iZ/2}(\sqrt{2}e^{i\pi/4}\xi) \tag{B.8}$$

where c_2 is a coefficient which depends on a boundary condition. Without loss of generality, we set this value to $c_2 = 1$ because we are interested in the ratio between a_2 and a_0, which will cancel out c_2.

The mode amplitude of the backscattered wave a_0 can be then found from Equation B.1 (b)

$$a_0 = -\frac{\exp(-i\xi^2)}{lK^* a_1^* / v_{g2}} \frac{\mathrm{d}}{\mathrm{d}\xi} a_2. \tag{B.9}$$

To express a_0 in a simple form, we first differentiate a_2 with respect to ξ

$$\frac{\mathrm{d}}{\mathrm{d}\xi} e^{i\xi^2/2} D_{iZ/2}(\sqrt{2}e^{i\pi/4}\xi) = i\xi e^{i\xi^2/2} D_{iZ/2}(\sqrt{2}e^{i\pi/4}\xi) + e^{i\xi^2/2} \frac{\partial}{\partial\xi} D_{iZ/2}(\sqrt{2}e^{i\pi/4}\xi), \tag{B.10}$$

and use the relation [83]

$$\frac{\mathrm{d}}{\mathrm{d}z}D_\nu(z) = \nu D_{\nu-1}(z) - \frac{1}{2}zD_\nu(z) \tag{B.11}$$

to obtain the following relation:

$$\frac{\mathrm{d}}{\mathrm{d}\xi}e^{i\xi^2/2}D_{iZ/2}(\sqrt{2}e^{i\pi/4}\xi) = e^{i\xi^2/2}e^{i\pi/4}\frac{iZ}{\sqrt{2}}D_{iZ/2-1}(\sqrt{2}e^{i\pi/4}\xi). \tag{B.12}$$

Using this, we obtain the analytic solution of a_0 as follows:

$$a_0 = -ie^{i\pi/4}e^{-i\xi^2/2}\frac{lKa_1/v_{g0}}{\sqrt{2}}D_{iZ/2-1}(\sqrt{2}e^{i\pi/4}\xi). \tag{B.13}$$

The absolute magnitudes of the model amplitudes (a_2 and a_0) are plotted in Figure 3-3. The non-oscillatory behavior of both mode amplitudes in the region $\xi > 0$ is observed when taking the complex amplitude of the solutions and has been checked independently by numerically solving Equation B.1.

B.0.2 Asymptotic Expansion of Mode Amplitudes

To evaluate the ratio of scattered power density to incident power density, we are interested in the mode amplitudes at $\xi \to -\infty$: $a_0|_{\xi\to-\infty}$ and $a_2|_{\xi\to-\infty}$. The asymptotic expansions [82, 83] for $D_p(z)$, when $|z| \gg 1$ and $|z| \gg |p|$, is given by the following:

$$D_p(z) \approx e^{-z^2/4}z^p\left(1 - \frac{p(p-1)}{2z^2} + \cdots\right) \quad \text{when } |\arg(z)| < \frac{3}{4}\pi. \tag{B.14}$$

From the asymptotic expression for $D_{iZ/2}$ at $\xi \to -\infty$

$$\begin{aligned} D_{iZ/2}(\sqrt{2}e^{i\pi/4}\xi)|_{\xi\to-\infty} &\approx (-\sqrt{2}e^{i\pi/4}\xi)^{iZ/2}e^{-i\xi^2/2} \\ &= \exp\left(\frac{3\pi}{8}Z\right)\exp\left(-i\frac{\xi^2}{2} + i\frac{Z}{2}\ln(\sqrt{2}|\xi|)\right), \end{aligned} \tag{B.15}$$

the asymptotic expression for a_2 at $\xi \to -\infty$ becomes

$$a_2|_{\xi\to-\infty} \approx \exp\left(\frac{3\pi}{8}Z\right)\exp\left(i\frac{Z}{2}\ln(\sqrt{2}|\xi|)\right). \tag{B.16}$$

To obtain the asymptotic expression for a_0, we first use the following relation [83]

$$D_p(z) = e^{p\pi i}D_p(-z) + \frac{\sqrt{2\pi}}{\Gamma(-p)}e^{\pi(p+1)i/2}D_{-p-1}(-iz) \tag{B.17}$$

to find the asymptotic form of $D_{iZ/2-1}$ at $\xi \to -\infty$

$$D_{iZ/2-1}(\sqrt{2}e^{i\pi/4}\xi)|_{\xi\to-\infty} \approx \frac{e^{-\pi i}e^{-i\xi^2/2}}{\sqrt{2}e^{i\pi/4}|\xi|} \tag{B.18}$$

$$+ \frac{\sqrt{2\pi}}{\Gamma(1-iZ/2)}\exp\left(\frac{\pi}{8}Z\right)\exp\left(i\frac{\xi^2}{2} - i\frac{Z}{2}\ln(\sqrt{2}|\xi|)\right). \tag{B.19}$$

Neglecting the first term at $\xi \to -\infty$, we find the asymptotic expression for a_0 at $\xi \to -\infty$

$$a_0|_{\xi\to-\infty} \approx -i\exp\left(i\frac{\pi}{4}\right)\exp\left(\frac{\pi Z}{8}\right)\frac{lKa_1/v_{g0}}{\sqrt{2}}\frac{\sqrt{2\pi}}{\Gamma(1-iZ/2)}\exp\left(-i\frac{Z}{2}\ln(\sqrt{2}|\xi|)\right). \tag{B.20}$$

Finally, the absolute amplitude ratio of backscattered wave to incident waves at $\xi \to -\infty$ is

$$\left|\frac{a_0}{a_2}\right|_{\xi\to-\infty} \approx \sqrt{\pi}\frac{lKa_1}{v_{g0}}, \tag{B.21}$$

where the approximation $Z \ll 1$ is used for our case.

B.0.3 Scattering Power Density

From the definition of the time averaged energy density

$$\langle W_j\rangle = \frac{1}{4}a_j^2\omega_j, \tag{B.22}$$

and the power density

$$S_j = v_{gj}\langle W_j \rangle, \tag{B.23}$$

the ratio of the scattered power density to the incident power density becomes

$$\left.\frac{S_0}{S_2}\right|_{\xi\to-\infty} = \pi\frac{\omega_0}{\omega_2}\frac{v_{g0}}{v_{g2}}\frac{l^2K^2}{v_{g0}^2}a_1^2. \tag{B.24}$$

The energy density of the LH mode is given by $\langle W_1 \rangle \approx \epsilon_0 E_1^2(2 + \omega_{pe}^2/\omega_{ce}^2)/4$. Substituting this and rewriting the right hand side of Equation B.24 in terms of δn (i.e., Equation 3.10) yields the following form:

$$\begin{aligned}\left.\frac{S_0}{S_2}\right|_{\xi\to-\infty} &= G\pi l^2 r_e^2(\delta n)^2\lambda_0^2 \\ &\approx \pi r_e^2\lambda_0^2 l^2(\delta n)^2,\end{aligned} \tag{B.25}$$

where G is the term responsible for the dielectric effect, the so-called geometrical factor for the coupling from O-mode to O-mode [113] in the scattering process

$$G = \frac{\omega_0^2}{\omega_2^2}\frac{1}{\sqrt{1-\omega_p^2/\omega_0^2}\sqrt{1-\omega_p^2/\omega_2^2}}. \tag{B.26}$$

This term at the scattering layer is about 1.5, when using $f_0 = 60\,\mathrm{GHz}$, $f_2 = 64.6\,\mathrm{GHz}$, and $n_e \approx 2\times10^{19}\,\mathrm{m}^{-3}$ (e.g., Figure 3-9). Away from the scattering layer, this will be closer to ω_0^2/ω_2^2, and we have set it to 1 in our case. In addition to the dielectric effect, the de-phasing effect is introduced in the term l, replacing the interaction length L in the conventional scattering formula [89].

THIS PAGE INTENTIONALLY LEFT BLANK

Appendix C

2D time-dependent full-wave simulation of scattering process between the ordinary-mode wave and lower hybrid wave

This appendix is to describe a two-dimensional time-dependent simulation of the scattering process between the ordinary-mode (O-mode) wave and the lower hybrid (LH) wave, using a finite-element-method solver, COMSOL [87]. Figure C-1 shows a simulation domain in the 2D space and the assumed background density distribution. The geometry of the top and bottom antennas is based on the actual horn antennas for the 60 GHz O-mode reflectometer system installed on Alcator C-Mod [85]. The electric field is polarized in the z-direction (out of the page). The distance between the horn antennas and the boundary of the plasma, where the density is 0, is assumed to be 20 cm at the midplane (i.e., at $y = 0$ in Figure C-1).

COMSOL solves the following coupled Maxwell's equations [114]:

$$\nabla \times \vec{E} = -\frac{\partial \vec{B}}{\partial t}, \tag{C.1}$$

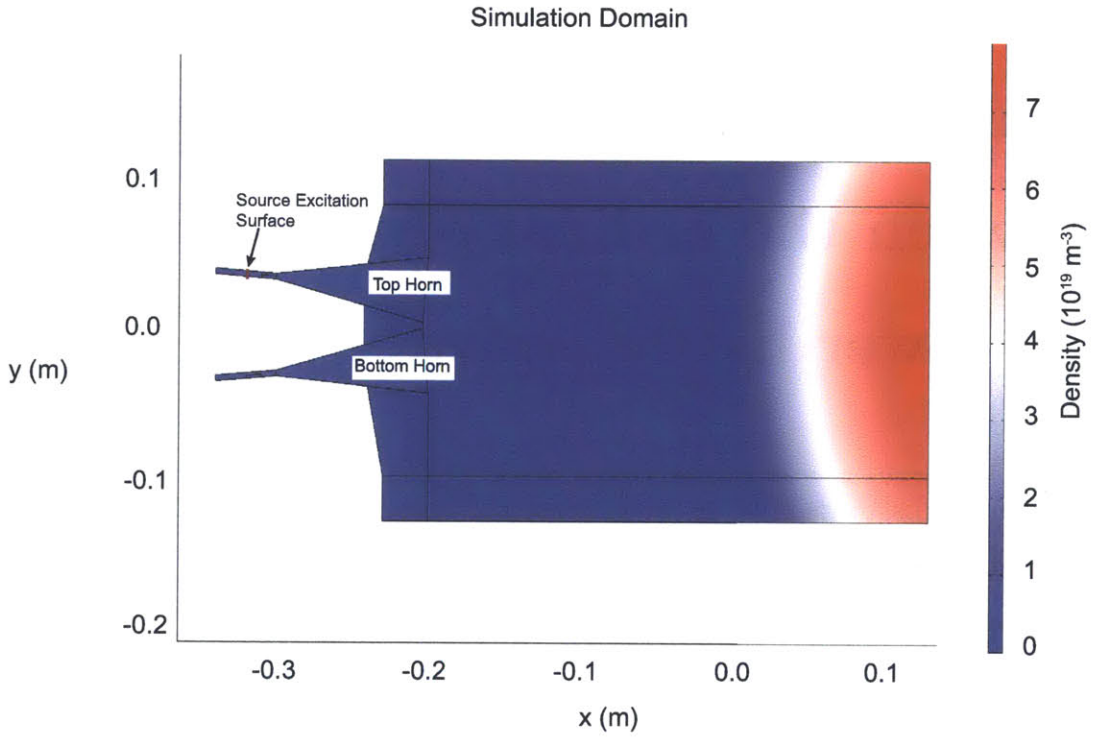

Figure C-1: 2D simulation domain in COMSOL and the background density distribution.

and

$$\nabla \times \vec{B} = \mu_0 \vec{J} + \epsilon_0 \mu_0 \frac{\partial \vec{E}}{\partial t}. \tag{C.2}$$

The plasma response is included in the following expression that relates the current density to the electric field:

$$\frac{\partial \vec{J}_z}{\partial t} = \frac{e^2 n_e}{m_e} \vec{E}_z, \tag{C.3}$$

where n_e is the total electron density, which is assumed to be the sum of the background density n_{bg} and the perturbed density n_{lh} due to the LH wave:

$$n_e = n_{bg} + n_{lh} \tag{C.4}$$

Here, the background plasma density is assumed to have the following spatial distribution:

$$n_{bg} = n_{e0} \left(1 - \frac{(x - 0.2)^2 + (y/1.5)^2}{r_{minor}^2} \right). \tag{C.5}$$

in the region where $x > 0$. Here, $n_{e0} = 9 \times 10^{19}\,\mathrm{m}^{-3}$ and $r_{minor} = 0.2\,\mathrm{m}$. In addition, the density fluctuation due to the presence of the LH wave is assumed to be present in the 2D space where $0\,m < x < 0.06\,m$ and $-0.06\,m < y < 0.06\,m$ (in order to limit the computational domain) with the following spatial distribution:

$$n_{lh} = 0.001\, n_{bg} \cos(k_{lh} x - \omega_{lh} t). \tag{C.6}$$

Here, $k_{lh} = -\sqrt{P/S} k_{\|}$ and ω_{lh} is the angular frequency of the LH wave ($= 2\pi \times 4.6 \times 10^9$ rad/s). $n_{\|}$ is assumed to be 2 in this simulation. The density fluctuation is assumed to be 0.1% of the background density (Equation 3.10). In order to calculate P and S, the background magnetic field is assumed to be present only in the z-direction with the spatial distribution $B_t = 5.4 r_{minor}/[r_{minor} - (x - r_{minor})]\,\mathrm{T}$ in the region $x > 0$.

The source current is excited at the inner surface of the top horn (refer to

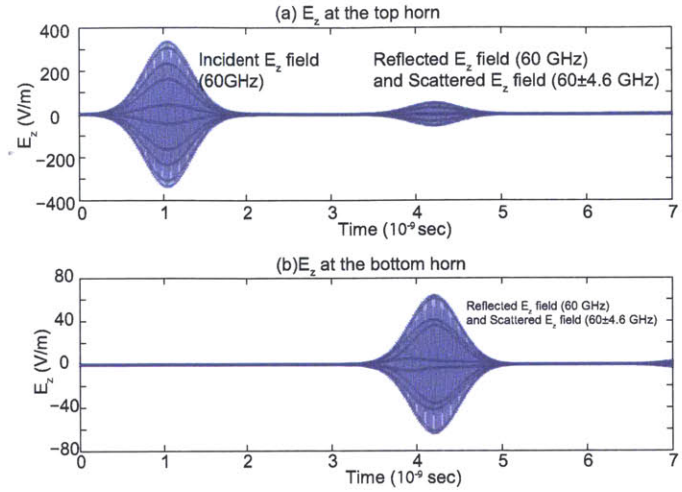

Figure C-2: (a) Launched E_z and detected E_z with the top and bottom horns as a function of time.

Figure C-1) with the following time distribution:

$$J_z = J_0 \exp(i\omega_{lh}t) \exp\left(\frac{-(t-t_1)^2}{t_{width}^2}\right), \tag{C.7}$$

where $t_1 = 30t_0$, $t_{width} = 12t_0$, and $t_0 = 1/(60 \times 10^9)$ sec..

Figure C-2 (a) shows the time evolution of the electric field at the inner surface of the top horn. Up to $t \approx 2$ nsec, the launched electric field is recorded. Due to a combined effect of the presence of the cut-off layer of the incident 60 GHz O-mode wave and the scattering interaction, the bottom horn detects the electric fields that are originated from the the reflection (60 GHz) and scattering process (60±4.6 GHz). Figure C-3 shows an example of the electric field distribution when $t = 3.6$ nsec. Figure C-2 also shows the time evolution of the received signals measured with the top and bottom horns after $t \approx 3$ ns.

Figure C-4 shows the frequency spectra of the launched signal that is measured with the top horn and the received signal that is measured with the bottom horn. The magnitudes of the both spectra are normalized by the maximum magnitude of the launched signal that is measured at the top horn. While the launched signal contains only the 60 GHz component, the received signal contains frequency-shifted scattered signals, in addition to the reflected 60 GHz O-mode signal. The frequency up-shifted

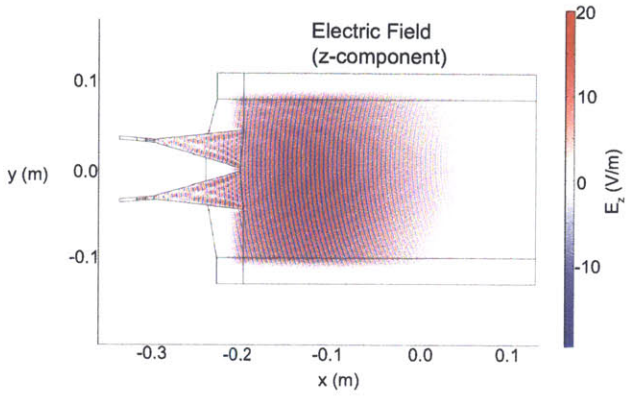

Figure C-3: Total electric field distribution in the 2D space when $t = 3.6 \times 10^{-9}$ sec.

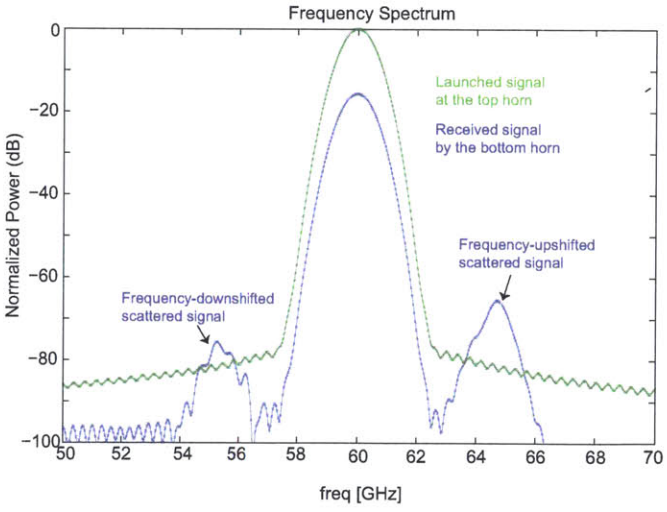

Figure C-4: Frequency spectrum of the launched signal at the top horn (green) and the detected signal at the bottom horn (blue).

signal is about 60~70 dB below the launched peak power, which is in line with the result of the analytic calculation in Chapter 3.2.2. This figure also shows that the reflected signal is reduced by about 20 dB due to the 2D spatial effect, suggesting that, in reality, scattered signals might have also been affected by these 2D (and 3D) spatial effects.

Appendix D

Development of Power Detector

The power detector consists of a logarithmic amplifier (AD8307), an operational amplifier (AD8031) for buffered output, and an operational amplifier (ALD2702) as a low-pass filter to eliminate any unwanted ripples from the output. Figure D-1 shows the schematic of the circuit of the power detector. Because of its sensitivity to very low power ($\sim$ -80 dBm), this module has been installed inside the RF-shielded box to minimize spurious signal pick-up. The logarithmic amplifier (AD8307) is an integral part of this measurement system, which compresses the dynamic power range of an input signal into a decibel equivalent DC output. The DC output of this system is then digitized, transferred through an optical fiber, and stored at a computer cluster.

Of the several benefits of using logarithmic amplifiers, it can save system space and cost. For example, an analog-to-digital converter available for O-mode reflectometery system can sample signals at 2MHz, leading to a Nyquist frequency of 1 MHz. Digitizing a 1.1 GHz signal requires either another set of high bit digitizers or multiple commercial spectrum analyzers.

While the low pass corner frequency is set by the low pass filter outside of this circuit, the high pass 3 dB corner frequency is determined by the capacitor in front of the logarithmic amplifier. It was set to be 3 kHz to eliminate direct DC coupling and low frequency noise. The resulting bandwidth of this power detector system is then approximately 97 kHz. The output of the logarithmic amplifier is the output voltage

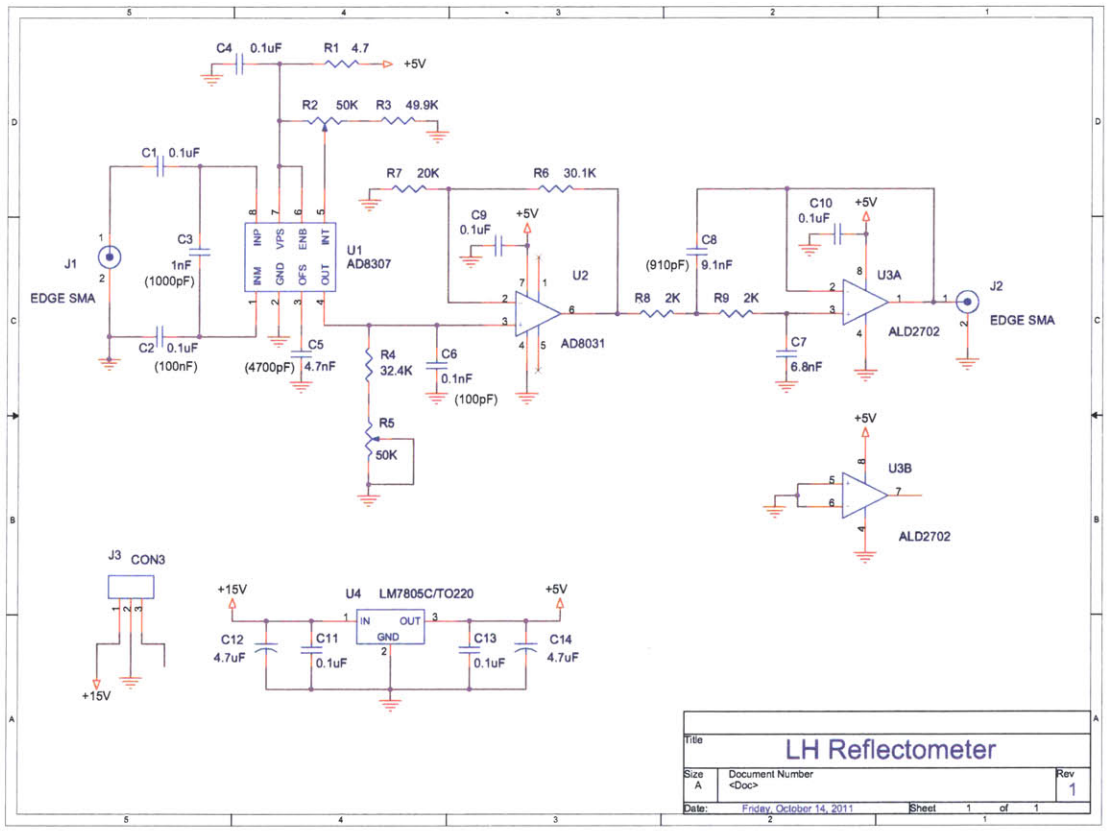

Figure D-1: Schematic of the circuit of the power detector.

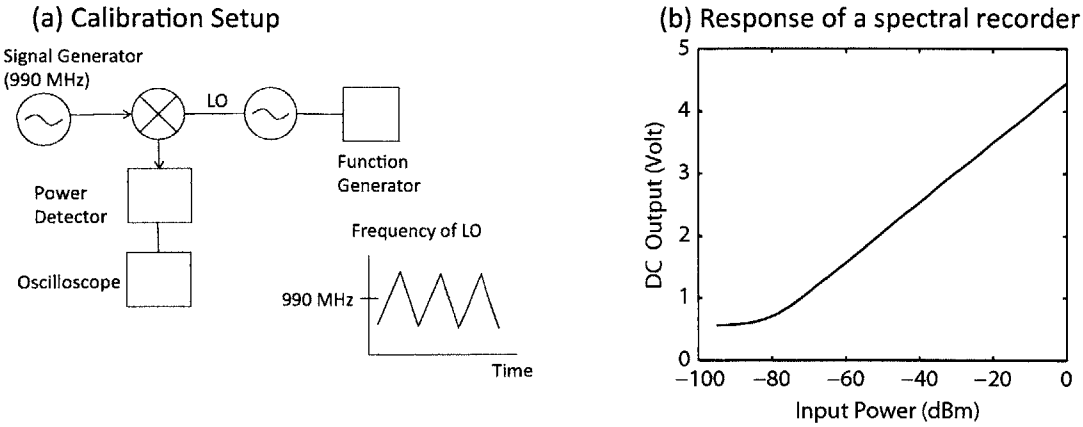

Figure D-2: Calibration setup and calibration curve of the power detector.

proportional to the power of the input signals. The operational amplifier (AD8031) after the logarithmic amplifier allows changing the slope of the response with the use of variable resistors. Currently, it is adjusted to set the slope at 50 mV/dB. The last operational amplifier eliminates high frequency ripples embedded in the DC output. It removes the frequency components above 10 kHz.

A typical calibration curve of the spectral recorder as a function of input power is shown in Figure D-2 (b). An HP 8685B signal generator was used to simulate a 990 MHz RF source. The frequency of the LO sweeps at around 990 MHz with sweeping rate of 10 Hz by controlling a tuning voltage of the LO with a function generator. An oscilloscope was connected to the spectral recorder to monitor the output DC voltage. A linear relation between the input power and the output peak DC voltage is observed over the range from -80 - 0 dBm. During experiments, detected scattered signals are converted into DC output voltage in the power detecting staging, output signals are digitized, transferred over an optical fiber, and stored on the computer cluster of Alcator C-Mod.

THIS PAGE INTENTIONALLY LEFT BLANK

Bibliography

[1] J. Wesson. *Tokamaks*, volume 149. Oxford University Press, 2011.

[2] N. J. Fisch. Theory of current drive in plasmas. *Reviews of Modern Physics*, 59(1):175, 1987.

[3] J. P. Freidberg. *Plasma physics and fusion energy.* Cambridge University Press, 2007.

[4] F. X. Söldner and JET Team. Shear optimization experiments with current profile control on JET. *Plasma Physics and Controlled Fusion*, 39:353, 1997.

[5] S. Ide, O. Naito, T. Oikawa, et al. 17th IAEA conference on fusion energy. *IAEA, Vienna*, page 567, 1998.

[6] A. A. Tuccillo, Y. Baranov, R. Cesario, B. J. Ding, M. Goniche, G. M. Wallace, L. Amicucci, J. F. Artaud, S. G. Baek, E. Barbato, V. Basiuk, G. Berger-By, P. T. Bonoli, G. Calabrò, A. Cardinali, C. Castaldo, S. Ceccuzzi, J. Decker, A. Ekedahl, J. Gunn, J. Hillairet, A. E. Hubbard, K. Kirov, J. Mailloux, O. Meneghini, F. C. Mirizzi, F. Napoli, R. R. Parker, V. Pericoli-Ridolfini, Y. Peysson, F. Santini, S. Shiraiwa, and B. N. Wan. On the use of lower hybrid waves at ITER relevant density. In *Proceedings of the 24th IAEA Fusion Energy Conference*, pages ITR/P1–09, San Diego, USA, October 2012.

[7] G. M. Wallace, I. C. Faust, O. Meneghini, R. R. Parker, S. Shiraiwa, S. G. Baek, P. T. Bonoli, A. E. Hubbard, J. W. Hughes, B. L. LaBombard, et al. Lower hybrid current drive at high density in the multi-pass regime. *Physics of Plasmas*, 19:062505, 2012.

[8] F. M. Poli, C. E. Kessel, M. S. Chance, S. C. Jardin, and J. Manickam. Ideal MHD stability and performance of ITER steady-state scenarios with ITBs. *Nuclear Fusion*, 52(6):063027, 2012.

[9] F. Najmabadi, C. G. Bathke, M. C. Billone, J. P. Blanchard, L. Bromberg, E. Chin, F. R. Cole, J. A. Crowell, D. A. Ehst, L. A. El-Guebaly, et al. Overview of the ARIES-RS reversed-shear tokamak power plant study. *Fusion Engineering and Design*, 38(1):3, 1997.

[10] G. M. Wallace, R. R. Parker, P. T. Bonoli, A. E. Hubbard, J. W. Hughes, B. L. LaBombard, O Meneghini, E. Schmidt, A, S. Shiraiwa, D. G. Whyte, J. C. Wright, S. J. Wukitch, R. W. Harvey, A. P. Smirnov, and Wilson J. R. Absorption of lower hybrid waves in the scrape off layer of a diverted tokamak. *Physics of Plasmas*, 17:082508, 2010.

[11] O. Meneghini. *Full-wave modeling of lower hybrid waves on Alcator C-Mod.* PhD thesis, Massachusetts Institute of Technology, 2012.

[12] Y. Takase, M. Porkolab, J. J. Schuss, R. L. Watterson, C. L. Fiore, R. E. Slusher, and C. M. Surko. Observation of parametric instabilities in the lower-hybrid range of frequencies in the high-density tokamak. *Physics of Fluids*, 28:983, 1985.

[13] S. G. Baek, S. Shiraiwa, R. R. Parker, A. Dominguez, G. J. Kramer, and E . S. Marmar. Modification of ordinary-mode reflectometry system to detect lower-hybrid waves in Alcator C-Mod. *Review of Scientific Instruments*, 83:10E325, 2012.

[14] S. G. Baek, S. Shiraiwa, R. R. Parker, P. T. Bonoli, E. S. Marmar, G. M. Wallace, A. Dominguez, G. J. Kramer, and C. Lau. Detection of lower hybrid waves in the scrape-off layer of tokamak plasmas with microwave backscattering. *Submitted to Physics of Plamsas.*

[15] S. G. Baek, R. R. Parker, C. Lau, S. Shiraiwa, and G. M. Wallace. Observation of spectral broadening of lower hybrid waves in Alcator C-Mod. *Plasma Fusion Research*, 7:2402031, 2012.

[16] S. G. Baek, R. R. Parker, S. Shiraiwa, G. M. Wallace, P. T. Bonoli, D. Brunner, I. C. Faust, A. E. Hubbard, B. LaBombard, and M. Porkolab. Measurements of ion cyclotron parametric decay of lower hybrid waves at the high-field side of Alcator C-Mod. *Plasma Physics and Controlled Fusion*, 55(5):052001, 2013.

[17] S. G. Baek, R. R. Parker, S. Shiraiwa, G. M. Wallace, M. Porkolab, Y. Takase, I. C. Faust, D. Brunner, A. E. Hubbard, B. LaBombard, and C. Lau. Characterization of the onset of ion cyclotron parametric decay instability of lower hybrid waves in a diverted tokamak. *Submitted to Physics of Plamsas.*

[18] I. H. Hutchinson, R. Boivin, F. Bombarda, P. Bonoli, S. Fairfax, C. Fiore, J. Goetz, S. Golovato, R. Granetz, M. Greenwald, S. Horne, A. Hubbard, J. Irby, B. LaBombard, B. Lipschultz, E. Marmar, G. McCracken, M. Porkolab, J. Rice, J. Snipes, Y. Takase, J. Terry, S. Wolfe, C. Christensen, D. Garnier, M. Graf, T. Hsu, T. Luke, M. May, A. Niemczewski, G. Tinios, J. Schachter, and J. Urbahn. First results from Alcator C-Mod. *Physics of Plasmas*, 1(5):1511, 1994.

[19] J. Irby, D. Gwinn, W. Beck, B. LaBombard, R. Granetz, and R. Vieira. Alcator C-Mod design, engineering, and disruption research. *Fusion science and technology*, 51(3):460, 2007.

[20] Y. Shimomura, R. Aymar, V. A. Chuyanov, M. Huguet, H. Matsumoto, T. Mizoguchi, Y. Murakami, A. R. Polevoi, M. Shimada, ITER Home Teams, et al. ITER-FEAT operation. *Nuclear fusion*, 41(3):309, 2001.

[21] G. T. Hoang, A. Bécoulet, J. Jacquinot, J. F. Artaud, Y. S. Bae, B. Beaumont, J. H. Belo, G. Berger-By, J. P. Bizarro, P. Bonoli, et al. A lower hybrid current drive system for ITER. *Nuclear Fusion*, 49(7):075001, 2009.

[22] P. T. Bonoli, J. Ko, R. R. Parker, A. E. Schmidt, G. M. Wallace, J. C. Wright, C. L. Fiore, A. E. Hubbard, J. Irby, E. Marmar, et al. Lower hybrid current drive experiments on Alcator C-Mod: Comparison with theory and simulation. *Physics of Plasmas*, 15(5):056117, 2008.

[23] P. T. Bonoli, R. R. Parker, M. Porkolab, J. J. Ramos, S. J. Wukitch, Y. Takase, S. Bernabei, J. C. Hosea, G. Schilling, and J. R. Wilson. Modelling of advanced tokamak scenarios with LHCD in Alcator C-Mod. *Nuclear Fusion*, 40(6):1251, 2000.

[24] P. T. Bonoli, R. Parker, S. J. Wukitch, Y. Lin, M. Porkolab, J. C. Wright, E. Edlund, T. Graves, L. Lin, J. Liptac, A. Parisot, A. E. Schmidt, V. Tang, W. Beck, R. Childs, M. Grimes, D. Gwinn, D. Johnson, J. Irby, A. Kanojia, P. Koert, S. Marazita, E. Marmar, D. Terry, R. Vieira, G. Wallace, J. Zaks, S. Bernabei, C. Brunkhorse, R. Ellis, E. Fredd, N. Greenough, J. Hosea, C. C. Kung, G. D. Loesser, J. Rushinski, G. Schilling, C. K. Phillips, J. R. Wilson, R. W. Harvey, C. L. Fiore, R. Granetz, M Greenwald, A. E. Hubbard, I. H. Hutchinson, B LaBombard, B. Lipschultz, J Rice, J. A. Snipes, J. Terry, S. M. Wolfe, and the Alcator C-Mod Team. Wave-particle studies in the ion cyclotron and lower hybrid ranges of frequencies in Alcator C-Mod. 51(3):401, 2007.

[25] S. Shiraiwa, O. Meneghini, R. R. Parker, G. M. Wallace, J. Wilson, I. Faust, C. Lau, R. Mumgaard, S. Scott, S. Wukitch, et al. Design, and initial experiment results of a novel LH launcher on Alcator C-Mod. *Nuclear Fusion*, 51(10):103024, 2011.

[26] G. M. Wallace et al. *Nuclear Fusion* to appear, 2013.

[27] A. Dominguez. *Study of density fluctuations and particle transport at the edge of I-mode plasmas*. PhD thesis, Massachusetts Institute of Technology, 2012.

[28] R. J. Briggs and R. R. Parker. Transport of RF energy to the lower hybrid resonance in an inhomogeneous plasma. *Physical Review Letters*, 29(13):852, 1972.

[29] P. M. Bellan and M. Porkolab. Propagation and mode conversion of lower-hybrid waves generated by a finite source. *Physics of Fluids*, 17:1592, 1974.

[30] D. G. Swanson. *Plasma waves.* CRC Press, 2003.

[31] T. H. Stix. *Waves in plasmas.* Springer, 1992.

[32] Y. Takase. *A study of parametric instabilities during the Alcator C lower hybrid wave heating experiments.* Sc.D. Thesis, Massachusetts Institute of Technology, 1983.

[33] M. Porkolab. Survey of lower hybrid experiments. *Plasma Science, IEEE Transactions on*, 12(2):107, 1984.

[34] M. Porkolab. Parametric instabilities due to lower-hybrid radio frequency heating of tokamak plasmas. *Physics of Fluids*, 20:2058, 1977.

[35] M. Porkolab, S. Bernabei, W. M. Hooke, R. W. Motley, and T. Nagashima. Observation of parametric instabilities in lower-hybrid radio-frequency heating of tokamaks. *Physical Review Letters*, 38:230, 1977.

[36] P. L. Andrews and F. W. Perkins. Spectral broadening of lower-hybrid waves by time-dependent density fluctuations. *Physics of Fluids*, 26:2546, 1983.

[37] P. L. Andrews and F. W. Perkins. Scattering of lower-hybrid waves by drift-wave density fluctuations: Solutions of the radiative transfer equation. *Physics of Fluids*, 26:2537, 1983.

[38] P. T. Bonoli and E. Ott. Toroidal and scattering effects on lower-hybrid wave propagation. *Physics of Fluids*, 25:359, 1982.

[39] N. J. Fisch. Confining a tokamak plasma with RF-driven currents. *Physical Review Letters*, 41(13), 1978.

[40] N. J. Fisch and A. H. Boozer. Creating an asymmetric plasma resistivity with waves. *Physical Review Letters*, 45(9):720, 1980.

[41] A.P. Smirnov and R. Harvey. *Bulletin of the American Physical Society*, 40, 1995.

[42] R. W. Harvey and C. McCoy. In *Proceedings of the IAEA Technical Committee Meeting on Simulation and Modeling of Thermonuclear Plasmas*, page 489, Montreal, 1992. International Atomic Energy Agency.

[43] C. F. Kennel and F. Engelmann. Velocity space diffusion from weak plasma turbulence in a magnetic field. *Physics of Fluids*, 9:2377, 1966.

[44] Nicholas A Krall and Alvin W Trivelpiece. Principles of plasma physics. *International Student Edition-International Series in Pure and Applied Physics, Tokyo: McGraw-Hill Kogakusha, 1973*, 1, 1973.

[45] P. T. Bonoli and R. C. Englade. Simulation model for lower hybrid current drive. *Physics of Fluids*, 29:2937, 1986.

[46] J. C. Wright, P. T. Bonoli, A. E. Schmidt, C. K. Phillips, E. J. Valeo, R. W. Harvey, and M. A. Brambilla. An assessment of full wave effects on the propagation and absorption of lower hybrid waves. *Physics of Plasmas*, 16(7):072502, 2009.

[47] S. Shiraiwa, J. Ko, O. Meneghini, R. Parker, A. E. Schmidt, S. Scott, M. Greenwald, A. E. Hubbard, J. Hughes, Y. Ma, et al. Full wave effects on the lower hybrid wave spectrum and driven current profile in tokamak plasmas. *Physics of Plasmas*, 18:080705, 2011.

[48] N. Bertelli, G. M. Wallace, P. T. Bonoli, R. W. Harvey, A. P. Smirnov, S. G. Baek, R. R. Parker, C. K. Phillips, E. J. Valeo, J. R. Wilson, et al. The effects of the scattering by edge plasma density fluctuations on lower hybrid wave propagation. *Plasma Physics and Controlled Fusion*, 55(7):074003, 2013.

[49] Y. Takase and M. Porkolab. Parametric excitation of ion-sound quasimodes during lower-hybrid heating experiments in tokamaks. *Physics of Fluids*, 26(10):2992, 1983.

[50] R. Cesario, A. Cardinali, C. Castaldo, F. Paoletti, and D. Mazon. Modeling of a lower-hybrid current drive by including spectral broadening induced by parametric instability in tokamak plasmas. *Physical review letters*, 92(17):175002, 2004.

[51] M. Porkolab, J. J. Schuss, B. Lloyd, Y. Takase, S. Texter, P. Bonoli, C. Fiore, R. Gandy, D. Gwinn, B. Lipschultz, et al. Observation of lower-hybrid current drive at high densities in the Alcator C tokamak. *Physical Review Letters*, 53:450, 1984.

[52] R. R. Parker, S. G. Baek, O. Meneghini, C. Lau, Y. Podpaly, M. Porkolab, J. E. Rice, A. E. Schmidt, S. Shiraiwa, G. M. Wallace, et al. Recent results from lower hybrid current drive experiments on Alcator C-Mod. *Bulletin of the American Physical Society*, 55:TP9.80, 2010.

[53] F. Alladio, E. Barbato, G. Bardotti, R. Bartiromo, G. Bracco, G. Buceti, P. Buratti, F. Crisanti, R. De Angelis, F. De Marco, et al. Density limit for lower hybrid wave-electron interaction and minority hydrogen absorption in FT. *Nuclear fusion*, 24(6):725, 1984.

[54] C. Gormezano, F. De Marco, G. Mazzitelli, A. Pizzuto, G. B. Righetti, and F. Romanelli. The FTU program. *Fusion science and technology*, 45:297, 2004.

[55] V. Pericoli Ridolfini, G. Calabro, L. Panaccione, et al. Study of lower hybrid current drive efficiency over a wide range of FTU plasma parameters. *Nuclear fusion*, 45(11):1386, 2005.

[56] R. Cesario, L. Amicucci, A. Cardinali, C. Castaldo, M. Marinucci, L. Panaccione, F. Santini, O. Tudisco, M. L. Apicella, G. Calabrò, et al. Current drive at plasma densities required for thermonuclear reactors. *Nature Communications*, 1:55, 2010.

[57] V. K. Tripathi, C. S. Liu, and C. Grebogi. Parametric decay of lower hybrid waves in a plasma: Effect of ion nonlinearity. *Physics of Fluids*, 22:301, 1979.

[58] R. Cesario and A. Cardinali. Parametric instabilities excited by ion sound and ion cyclotron quasi-modes during lower hybrid heating of tokamak plasmas. *Nuclear fusion*, 29(10):1709, 1989.

[59] R. Cesario, L. Amicucci, C. Castaldo, M. Kempenaars, S. Jachmich, J. Mailloux, O. Tudisco, A. Galli, A. Krivska, et al. Plasma edge density and lower hybrid current drive in JET. *Plasma Physics and Controlled Fusion*, 53(8):085011, 2011.

[60] R. Cesario, A. Cardinali, C. Castaldo, F. Paoletti, W. Fundamenski, S. Hacquin, et al. Spectral broadening of lower hybrid waves produced by parametric instability in current drive experiments of tokamak plasmas. *Nuclear fusion*, 46(4):462, 2006.

[61] E. Barbato. The role of non-resonant collision dissipation in lower hybrid current driven plasmas. *Nuclear Fusion*, 51(10):103032, 2011.

[62] V. Ridolfini-Pericoli, M. L. Apicella, G. Calabrò, C. Cianfarani, E. Giovannozzi, and L. Panaccione. Lower hybrid current drive efficiency in tokamaks and wave scattering by density fluctuations at the plasma edge. *Nuclear Fusion*, 51(11):113023, 2011.

[63] M. Goniche, J. Mailloux, Y. Demers, V. Fuchs, P. Jacquet, C. Boucher, A. Côté, C. Côté, J. Gunn, B. Terreault, et al. Strong toroidal asymmetries in power deposition on divertor and first wall components during LHCD on TdeV and Tore Supra. *Journal of nuclear materials*, 241:745, 1997.

[64] G. M. Wallace, A. E. Hubbard, P. T. Bonoli, I. C. Faust, R. W. Harvey, J. W. Hughes, B. L. LaBombard, O. Meneghini, R. R. Parker, A. E. Schmidt, S. Shiraiwa, A. Smirnov, D. Whyte, J. Wilson, J. Wright, S. Wukitch, and the Alcator C-Mod Team. Lower hybrid current drive at high density in Alcator C-Mod. *Nuclear Fusion*, 51:083032, 2011.

[65] R. E. Slusher, C. M. Surko, J. J. Schuss, R. R. Parker, I. H. Hutchinson, D. Overskei, and L. S. Scaturro. Study of driven lower-hybrid waves in the Alcator A tokamak using CO2 laser scattering. *Physics of Fluids*, 25:457, 1982.

[66] G. A. Wurden, K. L. Wong, and M. Ono. Lower-hybrid wave resonance cone detection via CO-laser scattering. *Physics of Fluids*, 28:716, 1985.

[67] F. Orsitto and D. Frigione. Detection of lower-hybrid waves in a tokamak by use of CO2-laser scattering. *Physical Review A*, 38(1):335, 1988.

[68] R. W. Motley, F. J. Paoloni, S. Bernabei, and W. M. Hooke. Detection of lower hybrid waves within a plasma by microwave scattering. *Review of Scientific Instruments*, 49(8):1143, 1978.

[69] G. Ichtchenko, M. Moresco, A. Vendramin, and E. Zilli. Detection of lower hybrid waves by coherent scattering of microwaves: Preliminary results in Wega. *International Journal of Infrared and Millimeter Waves*, 2(4):713–737, 1981.

[70] Y. Uesugi, T. Itoh, S. Takamura, and T. Okuda. Heterodyne detection of lower hybrid waves in a plasma by microwave scattering. *Plasma Physics*, 25:875, 1983.

[71] R. Rohatgi, K. I. Chen, G. Bekefi, P. Bonoli, S. C. Luckhardt, M. Mayberry, M. Porkolab, and J. Villasenor. Experimental measurements of lower-hybrid wave propagation in the Versator II tokamak using microwave scattering. *Physics of Fluids B: Plasma Physics*, 3:2101, 1991.

[72] J. B. Wilgen, P. M. Ryan, G. R. Hanson, D. W. Swain, S. I. Bernabei, N. Greenough, S. DePasquale, C. K. Phillips, J. C. Hosea, and J. R. Wilson. Reflectometer sensing of RF waves in front of the high harmonic fast wave antenna on NSTX. *Review of scientific instruments*, 77(10):10E933, 2006.

[73] J. H. Lee, E. J. Doyle, N. C. Luhmann Jr, W. A. Peebles, C. C. Petty, R. I. Pinsker, and T. L. Rhodes. Determination of internal radio frequency electric field profiles via millimeter wave reflectometry in the DIII-D tokamak. *Review of scientific instruments*, 68(1):462, 1997.

[74] X. L. Zou, L. Laurent, and J. M. Rax. Scattering of an electromagnetic wave in a plasma close to a cut-off layer. Application to fluctuation measurements. *Plasma Physics and Controlled Fusion*, 33:903, 1991.

[75] N. Bretz. One-dimensional modeling of the wavelength sensitivity, localization, and correlation in reflectometry measurements of plasma fluctuations. *Physics of Fluids B: Plasma Physics*, 4:2414, 1992.

[76] I. H. Hutchinson. One-dimensional full-wave analysis of reflectometry sensitivity and correlations. *Plasma physics and controlled fusion*, 34:1225, 1992.

[77] B. B. Afeyan, A. E. Chou, and B. I. Cohen. The scattering phase shift due to Bragg resonance in one-dimensional fluctuation reflectometry. *Plasma Physics and Controlled Rusion*, 37:315, 1995.

[78] C. Fanack, I. Boucher, F. Clairet, S. Heuraux, G. Leclert, and XL Zou. Ordinary-mode reflectometry: modification of the scattering and cut-off responses due to the shape of localized density fluctuations. *Plasma physics and controlled fusion*, 38:1915, 1996.

[79] S. Shiraiwa, S. Baek, A. Dominguez, E. Marmar, R. R. Parker, and G. J. Kramer. Direct detection of lower hybrid wave using a reflectometer on Alcator C-Mod. *Review of Scientific Instruments*, 81:10D936, 2010.

[80] A. Bers. Basic plasma physics I. *Handbook of Plasma Physics*, 1, 1983.

[81] A. D. Piliya. Nonstationary theory of decay instability in a weakly inhomogeneous plasma. *Soviet Journal of Experimental and Theoretical Physics*, 37:629, 1973.

[82] E. Z. Gusakov, S. Heuraux, and A. Y. Popov. Strong Bragg backscattering in reflectometry. *Plasma Physics and Controlled Fusion*, 51:065018, 2009.

[83] I. S. Gradshteyn, I. M. Ryzhik, and A. Jeffrey. *Table of Integrals, Series, and Products*. Academic Press, 1980.

[84] C. Lau, G. Hanson, Y. Lin, J. Wilgen, S. Wukitch, B. Labombard, and G. M. Wallace. First results of the SOL reflectometer on Alcator C-Mod. *Review of Scientific Instruments*, 83(10):10E309, 2012.

[85] P. C. Stek. *Reflectometry measurements on Alcator C-Mod.* PhD thesis, Massachusetts Institute of Technology, 1997.

[86] N. P. Basse, A. Dominguez, E. M. Edlund, C. L. Fiore, R. S. Granetz, A. E. Hubbard, J. W. Hughes, I. H. Hutchinson, J. H. Irby, B. LaBombard, et al. Diagnostic systems on Alcator C-Mod. *Fusion science and technology*, 51(3):476, 2007.

[87] `http://www.comsol.com`.

[88] G. M. Wallace, R. R. Parker, P. T. Bonoli, R. W. Harvey, A. E. Schmidt, A. P. Smirnov, D. G. Whyte, J. R. Wilson, J. C. Wright, and S. J. Wukitch. Observations of lower hybrid wave absorption in the scrape off layer of a diverted tokamak. In *AIP Conference Proceedings*, volume 1187, page 395, 2009.

[89] I. H. Hutchinson. *Principles of plasma diagnostics*. Cambridge University Press, 2002.

[90] I. Faust, J. L. Terry, M. L. Reinke, O. Meneghini, S. Shiraiwa, G. M. Wallace, R. R. Parker, A. E. Schmidt, and J. R. Wilson. Lower hybrid wave induced SOL emissivity variation at high density on the Alcator C-Mod tokamak. volume 1406, page 231, 2011.

[91] M. Porkolab. Theory of parametric instability near the lower-hybrid frequency. *Physics of Fluids*, 17:1432, 1974.

[92] V. K. Tripathi, C. Grebogi, and C. S. Liu. Unified formalism of lower hybrid parametric instabilities in plasmas. *Physics of Fluids*, 20:1525, 1977.

[93] C. S. Liu, V. K. Tripathi, V. S. Chan, and V. Stefan. Density threshold for parametric instability of lower-hybrid waves in tokamaks. *Physics of Fluids*, 27:1709, 1984.

[94] J. J. Schuss, M. Porkolab, Y. Takase, D. Cope, S. Fairfax, M. Greenwald, D. Gwinn, I. H. Hutchinson, B. Kusse, E. Marmar, et al. Lower hybrid heating in the Alcator A tokamak. *Nuclear Fusion*, 21(4):427, 1981.

[95] L. Chen and R. L. Berger. Spatial depletion of the lower hybrid cone through parametric decay. *Nuclear Fusion*, 17(4):779, 1977.

[96] J. Wersinger and I. Park. Nonlinear lower hybrid wave depletion. In *AIP Conference Proceedings*, volume 129, page 194, 1985.

[97] N. Smick and B. LaBombard. Wall scanning probe for high-field side plasma measurements on Alcator C-Mod. *Review of Scientific Instruments*, 80(2):023502, 2009.

[98] G. M. Wallace. *Behavior of lower hybrid waves in the scrape off layer of a diverted tokamak.* PhD thesis, Massachusetts Institute of Technology, 2010.

[99] R. Cesario and V. Pericoli-Ridolfini. Study of the parametric instabilities in the lower hybrid frequency range in the FT tokamak. *Nuclear Fusion*, 27(3):435, 1987.

[100] J. W. Hughes, D. A. Mossessian, A. E. Hubbard, E. S. Marmar, D. Johnson, and D. Simon. High-resolution edge Thomson scattering measurements on the Alcator C-Mod tokamak. *Review of Scientific Instruments*, 72(1):1107, 2001.

[101] C. Lau, G. Hanson, J. Wilgen, Y. Lin, and S. Wukitch. Scrape-off layer reflectometer for Alcator C-Mod. *Review of Scientific Instruments*, 81:10D918, 2010.

[102] G. M. Wallace. Lower hybrid current drive at high density in the multi-pass regime. *Bulletin of the American Physical Society*, page YI2.6, 2011. `http://meetings.aps.org/link/BAPS.2011.DPP.YI2.6`.

[103] G. Wallace, P. Bonoli, J. Liptac, R. R. Parker, A. E. Schmidt, and J. R. Wilson. Lower hybrid coupling studies on Alcator C-Mod. In *APS Meeting Abstracts*, volume 1, page QP1.49, 2006.

[104] B. LaBombard, J. E. Rice, A. E. Hubbard, J. W. Hughes, M. Greenwald, J. Irby, Y. Lin, B. Lipschultz, E. S. Marmar, C. S. Pitcher, N. Smick, S. M. Wolfe, S. J. Wukitch, and the Alcator Group. Transport-driven scrape-off-layer flows and the boundary conditions imposed at the magnetic separatrix in a tokamak plasma. *Nuclear Fusion*, 44(10):1047, 2004.

[105] S. Shiraiwa, O. Meneghini, R. R. Parker, P. T. Bonoli, M. Garrett, M. C. Kaufman, J. C. Wright, and S. J. Wukitch. Plasma wave simulation based on a versatile finite element method solver. *Physics of Plasmas*, 17:056119, 2010.

[106] Y. Takase, S. Knowlton, S. McDermott, M. Porkolab, S. Texter, C. Fiore, S. McCool, P. Pribyl, and J. Rice. Lower hybrid current ramp-up experiments and density limit on Alcator C. In *AIP Conference Proceedings*, volume 129, page 186, 1985.

[107] Y. Takase. private communication, 2012.

[108] S. Shiraiwa, S. G. Baek, P. T. Bonoli, I. C. Faust, A. E. Hubbard, O. Meneghini, R. R. Parker, G. M. Wallace, J. R. Wilson, R. W. Harvey, A. P. Smirnov, D. Brunner, B. LaBombard, C. Lau, R. Mumgaard, S. Scott, N. Tsujii, and S. Wolfe. Progress towards steady-state regimes in Alcator C-Mod. *Nuclear Fusion*, 53:113028, 2013.

[109] F. Napoli, C. Castaldo, R. Cesario, and G. Schettini. Modeling of the nonlinear mode coupling of lower hybrid waves in tokamak plasmas. *Plasma Physics and Controlled Fusion*, 55(9):095004, 2013.

[110] A. A. Hussein. *Simulation Studies of Parametric Processes Associated with Ionospheric Stimulated Electromagnetic Radiation.* PhD thesis, Virginia Polytechnic Institute and State University, 1997.

[111] T. G. Jenkins, T. M. Austin, D. N. Smithe, J. Loverich, and A. H. Hakim. Time-domain simulation of nonlinear radiofrequency phenomena. *Physics of Plasmas*, 20:012116, 2013.

[112] R. R. Parker. private communication, 2012.

[113] T. P. Hughes and S. R. P. Smith. Effects of plasma dielectric properties on Thomson scattering of millimetre waves in tokamak plasmas. *Journal of Plasma Physics*, 42:215, 1989.

[114] J. H. Irby, S. Horne, I. H. Hutchinson, and P. C. Stek. 2d full-wave simulation of ordinary mode reflectometry. *Plasma physics and controlled fusion*, 35(5):601, 1993.